

**PRESSURE SIGNATURE IN ADVERSE-
PRESSURE-GRADIENT WALL BOUNDED
TURBULENT FLOWS**

Julie You-Hee Han

A thesis

submitted in total fulfillment
of the requirements for the degree of
Master of Engineering

School of the Built Environment – Mechanical Engineering
Victoria University of Technology

Footscray Campus
PO BOX 14428 MCMC
Melbourne, Victoria 8001

Australia

September, 2000



23125133

FTS THESIS
532.0527 HAN
30001006995379
Han, Julie You-Hee
Pressure signature in
adverse-pressure-gradient
wall bounded turbulent flows

Abstract

This thesis represents a first step towards generating experimental data of increasing adverse pressure gradient turbulent flows in a systematical methodical. For this purpose, a flexible setup has been prepared in an open-return wind tunnel. The setup can be used in generating different increasing and decreasing adverse pressure gradient cases. Although such flows are commonly encountered in engineering applications, lack of experimental data exists in the literature especially of increasing adverse pressure gradient turbulent flows. Hence, such cases are needed both to deepen the existing understanding of this class of flows and for verification of numerical prediction methods.

In addition to the main setup in the wind tunnel, a calibration rig has been prepared, consisting of a fully-developed turbulent pipe flow setup. This rig has been used for Preston tube calibrations. Subsequently, the mean flow characteristics of one increasing adverse pressure gradient case have been examined in the wind tunnel.

The mean flow profiles obtained in the present study have been compared with those of nine decreasing and one other increasing adverse pressure gradient flows from the literature. This comparison has shown that two half-power regions exist in these flows, extending from within the inertial sublayer to the velocity defect region. The half-power parameters scale with the pressure parameter and friction velocity. The resulting prediction of the mean flow profiles is consistent with the moving equilibrium concept.

Acknowledgements

First and foremost, I would like to express my sincerest thanks to my supervisor, Associate Professor, Özden Turan, for her expert guidance, kind support, never ending encouragement and caring, similar to parents, throughout this work. I was fortunate enough to have her as my supervisor. Her approach to scientific and engineering investigation as well as her enthusiasm will always be an inspiration to me.

I would like to thank all the teaching and technical staff of the School of the Built Environment – Mechanical engineering, especially to Michael Sek, Vincent Rouillard, Tien Do, Leszlo Kovacs, Ray McIntosh, Harry Friedrich, Norman Welgus, Laurence Martin, Joseph Angelone, Glenda Geyer and Lyn Allis for their interest and friendly help and assistance and technical support at all times. The Dean's Research Scholarship Scheme in Faculty of Science and Engineering for financial support is also gratefully acknowledged.

My gratitude must be extended to my fellow postgraduate students and friends, Katya Nyankina, Suzana Klopovic, Davis Ip, Li Tao, Jeremy Anderson, Seyit Ayranci and Mehesh Prakash who helped me keep my sanity.

Finally, I want to express my deep gratitude to my parents, parents-in-law, my brothers, Tae-Hee and Do-Hee, my husband, our daughter Hae-Young, sister-in-law and all family and friends in Korea for all of their support and understanding. For this I will be forever indebted.

Julie You-Hee Han

September, 2000

TABLE OF CONTENTS

Abstract	ii
Acknowledgements	iii
Table of Contents	iv
List of Tables	vi
List of Figures	vii
Chapter 1. Introduction	1
1.1. Wall-Bounded Adverse Pressure Gradient Turbulent Flows	1
1.2. Objective and Thesis Structure	3
Chapter 2. Literature Review	5
2.1. Basic turbulence Characteristics	5
2.2. Closure Problem	7
2.3. Known Effects due to Wall and Adverse Pressure Gradient	9
2.4. Major Accomplishments to Date in Adverse Pressure Gradient Research	16
Chapter 3. Experimental Setup	20
3.1. Introduction	20
3.2. Wind Tunnel	20
3.3. Velocity Traverses and the Traversing Mechanism	22
3.4. The Fully-Developed Pipe Flow Setup: Calibration Rig	24
3.5. Preston Tube Calibration	25
3.5.1. Calibration by Patel's Correction	26
3.5.2. An Alternate Calibration with Correction Factor	28
3.5.3. Frei and Thomann Correction	29
Chapter 4. Results and Discussion	37
4.1. Flexible Top Preparation	37
4.2. Pressure Distribution	37

4.3. Mean Velocity Traverse	39
4.4. Friction Velocity	39
4.5. Logarithmic Profiles	41
Chapter 5. Similarity of Adverse Pressure Gradient Boundary Layers and Half Power Laws	58
5.1. Introduction	58
5.2. Brief Description of the Eleven Adverse Pressure Gradient Flows	58
5.2.1. Pressure Parameter, Δ	59
5.2.2. Kinematic Pressure Gradient, α	60
5.2.3. Further Flow Characteristics	60
5.3. Log-Law Profiles	63
5.4. Half Power Profiles	64
5.5. Half Power Slops and Intercepts: C_i , D_i , C_o and D_o	65
5.6. Moving Equilibrium	67
5.7. Length Scales	69
5.8. Other Velocity Scales	72
Chapter 6. Conclusions	103
References	106
Appendix A. Flexible top shapes and the corresponding pressure distributions in the test section	114
Appendix B. Experimental y^+, U^+, y/δ and U/U_e values of Flow Han	135
Appendix C. The procedure to get the inner and outer parameters, C_i, C_o, D_i and D_o	147
Appendix D Streamwise length scale distribution in the eleven flows	149

List of Tables

	page
Table 3.1. Calculated x^* and y^* ranges for various sizes of Preston tubes.	30
Table 3.2. Various sizes of Preston tubes x^* , u_{*p} and u_{*t} .	30
Table 3.3. Correction factors for 1 mm and 2 mm Preston tubes at three Reynolds numbers.	30
Table 4.1. Flexible top coordinates.	43
Table 4.2. C_p , dC_p/dx , d^2C_p/dx^2 .	44
Table 4.3. Streamwise values of the pressure gradient parameter, Δ .	45
Table 4.4. u_* values from Clauser chart.	45
Table 4.5 Streamwise values of the friction velocity as obtained with Preston's method	46
Table A. 20 trial cases of preliminary tests in the wind tunnel.	115
Table B. Mean velocity profiles at 12 stations	135

List of Figures

	page
Figure 2.1. Flow past a blunt-body (White, 1994).	9
Figure 2.2. Boundary-layer separation in diffuser (White, 1994).	11
Figure 2.3. The law of the wall (Tennekes and Lumley, 1972).	12
Figure 3.1. Schematic representation of the bent Pitot-static and Preston tubes.	31
Figure 3.2 Wind tunnel.	32
Figure 3.3. Static pressure tap insert.	33
Figure 3.4. Traversing mechanism.	34
Figure 3.5. Calibration rig.	35
Figure 3.6. Preston tube traverses in the calibration rig.	36
Figure 4.1. Flexible top shape.	47
Figure 4.2. (a) Wall static pressure.	48
(b) First streamwise derivatives.	48
(c) Second streamwise derivatives.	48
Figure 4.3. Mean velocity measurements.	49
Figure 4.4. Clauser plots at 12 stations.	50
Figure 4.5. Streamwise distribution of the friction velocity.	54
Figure 4.6. Logarithmic law.	55
Figure 4.7. Mean velocity profile at U/U_e against y/δ scale.	56
Figure 4.8. Wake strength, Π	57
Figure A. 20 trial cases of preliminary tests in the wind tunnel.	115
Figure C. U_c^+ and definitions.	148
Figure D. Length scales of 11 flows.	150

Chapter 1. INTRODUCTION

1.1 Wall-Bounded Adverse Pressure Gradient Turbulent Flows

Adverse pressure gradient turbulent flows and subsequent flow separation from a plane or curved wall are encountered frequently in engineering applications in both internal and external flows. Common examples of such internal flows can be seen in diffuser flows in turbomachinery applications, in the flow passages of vehicles and appliances, and in the flow passages inside a confining structure during a fire. Some examples of adverse pressure gradient external flows are, the flow over an aerofoil, a fuselage or a passenger car. In both internal and external cases, separation causes momentum and energy losses, and due to the complexity of the resulting flow physics, flow prediction becomes difficult for design purposes or performance optimisation. In most cases, turbulent separation reduces performance efficiency. There is a definite lack of turbulence data in the literature for adverse pressure gradient flows with and without separation. Hence, thorough experimental investigation is valuable in developing a fundamental understanding of such complex turbulent flows leading to practical turbulence modelling.

Although empirical and semi-empirical prediction and experimental investigation of these turbulent flows have been looked at starting even before Stratford (1959), to Kader and Yaglom (1978) and to the present (e.g. by Granville (1989), Stropky et al. (1990), Pauley et al. (1990), and Skåre and Krongstad (1994)) due to their common occurrences, more work is still needed for two reasons. Firstly, from an experimental point of view,

systematic variation of the adverse pressure gradient must be accomplished in a flexible experimental rig to examine “the pressure signature” on the flow. Secondly, from a computational point of view, practical schemes need to be developed for the numerical prediction of these complex yet common flows. Especially “increasing” adverse pressure gradient cases need to be examined experimentally and compared with the existing “decreasing” adverse pressure cases. Therefore, a more thorough experimental investigation needs to be conducted than is available in the literature.

It is possible to predict some simple geometries, such as boundary layer and pipe flows, with k - ϵ type of turbulence closures without having to resort to direct numerical simulation. Although direct numerical simulation studies from Kim et al.’s (1987) to Moser et al.’s (1999), are possible academically, they are not yet practical with the common computational power available even in the industry with considerable financial means for design. The presence of extra strain rates and the resulting complex turbulent flows require fine-tuning of simpler approaches (Lai et al. 1989; Chukkapalli and Turan, 1995). Unfortunately, this fine-tuning seems to be completely flow dependent. Therefore, it lacks universality, and hence, it is not sufficiently practical. On the other hand, it is often not easy to check the universality of some semi-empirical and practical prediction techniques due to lack of experimental data. Experimental efforts in this area are mostly on the investigation of turbulent boundary layer separation (Simpson and Shivaprasad, 1983; Simpson, 1981) or on backward facing step geometries (Selby et al., 1990; Simpson, 1983).

The significance of this thesis lies in its potential to provide a fundamental understanding of complex adverse pressure gradient flows with direct practical applications resulting from this understanding. One increasing adverse pressure gradient case has been prepared for systematic examination. The resulting mean flow patterns have been compared with those of adverse pressure gradient flows from the literature. The experimental setup can be used for further investigation of the chosen case. Equivalently, by varying the adverse pressure gradient through a set range, the same setup can be utilized to study different cases. With this understanding, the possibility of unifying such flows can be widened.

1.2 Objective and Thesis Structure

The general objective of this thesis is to contribute to the recognition of universal patterns in wall-bounded adverse pressure gradient turbulent flows. For this purpose, the experimental work has been carried out towards further understanding of this class of flows, especially when the pressure gradient is increasingly adverse.

In this thesis, a general Literature Review is given next in Chapter 2 to briefly summarize the author's understanding of relevant basic physics. In the absence of an oral thesis defense, it is felt that Chapter 2 is needed. In Chapter 3, the Experimental Setup is discussed in detail. The increasing adverse pressure gradient case examined using this experimental setup is presented next in Chapter 4. Chapter 4, Results and Discussion, contains a complete description of the mean flow characteristics of this particular flow. In Chapter 5, the present results are examined along with available experimental data

from the literature towards the Similarity of Adverse Pressure Gradient Boundary Layers and Half-Power Laws. In Chapter 6, the conclusions are presented, and the significance of the work is summarized. In addition to the literature review in Chapter 2, the review of relevant literature is included in Chapters 3 to 5.

Chapter 2. LITERATURE REVIEW

2.1 Basic Turbulence Characteristics

Turbulent flows can be described by seven general characteristics (Hinze, 1975; Tennekes and Lumley, 1972). The first of these is irregularity, or randomness, of all turbulent flows. Turbulent motion is impossible to describe in detail as a function of time and space coordinates because of its irregularity. However, irregular turbulent motion can be described if laws of probability are applied. Hence, turbulence is an irregular condition of flow in which various quantities show a random variation with time and space coordinates, but it is possible to calculate statistically distinct average values (Hinze, 1975).

The second outstanding characteristic of turbulent motion is the diffusivity of turbulence. Diffusivity enables turbulent flows to rapidly transport and mix vector and scalar quantities such as momentum, heat and mass. The diffusivity of turbulence can prevent boundary layer separation on aerofoils at large angles of attack, increase heat transfer rates in machinery and increase momentum transfer between winds and ocean currents.

The Reynolds number of a turbulent flow can be interpreted as the ratio of a turbulence time scale to a molecular time scale. The molecular time scale prevails in the absence of turbulence in a problem with the same length scale. This description is often more reliable than thinking of Reynolds number as a ratio of inertia terms to viscous

terms in the governing equations. As a third characteristic, turbulent flows occur at high Reynolds numbers. Diffusion due to viscosity and other effects occurs at smaller length scales than inertia effects at high Reynolds numbers (Tennekes and Lumley, 1972). Turbulent flows at high Reynolds numbers are characterized by the existence of several length scales, some of which assume very specific roles in the description and analysis of flows. Because of this reason, spectral analysis of turbulent motion is useful. As a fourth characteristic, a wide range of length scales exists in turbulent flows characterising them as broadband phenomena.

Fifthly, turbulence is rotational and three-dimensional. Turbulent flows are characterized by high levels of fluctuating vorticity. In order to describe turbulent flows, vorticity dynamics is essential. Random waves on the surface of oceans are in turbulent motion, and they are highly rotational.

As a sixth characteristic, turbulent flows are always dissipative. In all flows of real viscous fluids, viscosity effects result in the conversion of kinetic energy of flow into heat. Viscous shear stress increases at the expense of the kinetic energy of turbulence and performs deformation work. If no energy is supplied into turbulence, the viscous losses can not be compensated for, and turbulence decays rapidly. Hence, the rate of dissipation of turbulence kinetic energy is an important parameter in defining characteristics of a class of turbulent flows.

As indicated previously, when Reynolds numbers are large enough, the major characteristics of turbulent flows are not controlled by the molecular properties of the fluid. As a result, turbulence is a flow property, and it is a continuum phenomenon. However, as a seventh characteristic, turbulence theory suffers from the absence of sufficiently powerful mathematical methods. This particular characteristic of turbulence can be further described as the closure problem.

2.2 Closure Problem

For engineering purposes, turbulent fluid motion can be described using statistically averaged continuity (mass conservation) and momentum conservation equations. However, after such averaging (time, space or ensemble averaging), the resulting set of equations does not form a closed set, because the number of unknowns exceeds the number of equations.

The reason is the appearance of averaged second order correlations of fluctuating velocities (Reynolds stresses) in the mean momentum equations as a result of averaging. If an additional transport equation is written for each of these nine Reynolds stresses, additional third order correlations appear. On the other hand, transport equations for third order correlations include fourth order correlations. Hence, the statistically averaged governing equations of motion do not close, although statistically averaging the continuity and momentum equations is the most practical way to treat them in turbulence. *The closure problem* hence described leads to *turbulence modelling*. The governing

equations of motion need to be closed at one stage through modelling of the additional terms, second, third or higher order correlations of the fluctuating velocities, in terms of the lower order terms, such as the mean velocity gradients, or turbulence kinetic energy, k , and its rate of dissipation, ϵ . Depending on the level of closure different turbulence models exist (Wilcox, 1993). A turbulence model is a set of equations that are algebraic or differential, and it requires empirical input.

A modified k - ϵ turbulence model was introduced by Chukkapalli and Turan (1992, 1995). Similar to the basic k - ϵ turbulence model, their model is based on closing the system of governing equations consisting of mass and momentum conservation. Conventionally, the Reynolds stress terms (second order fluctuating velocity correlations) which appear in the mean flow equations after averaging, are related directly to the mean flow gradients. In the modified model of Chukkapalli and Turan, structural parameters are used to relate Reynolds stresses to turbulence kinetic energy, k , instead. The third order correlations which appear in the k -equation are modelled in terms of the second order correlations. As a result of these modifications, successful application of the resulting k - ϵ model was obtained in decreasing adverse pressure gradient flows. This modified model can be assessed with increasing adverse pressure gradient data from the experimental setup described in Chapter 3.

2.3 Known Effects due to Wall and Adverse Pressure Gradient

Ludwig Prandtl first formulated the boundary-layer theory in 1904. Boundary layer is a flow region where viscous forces and inertia forces are approximately equal. According to his boundary layer hypothesis, viscous effects are limited to a thin region near a solid surface at high Reynolds numbers. If there is a blunt-body in the flow, the boundary layer is thin in the front, or windward side of the body, where the pressure gradient decreases along the surface. In the rear of the boundary layer, the flow encounters increasing pressure gradients and breaks off, or separates, into a broad, pulsating wake. This flow pattern is illustrated in Figure 2.1 below.

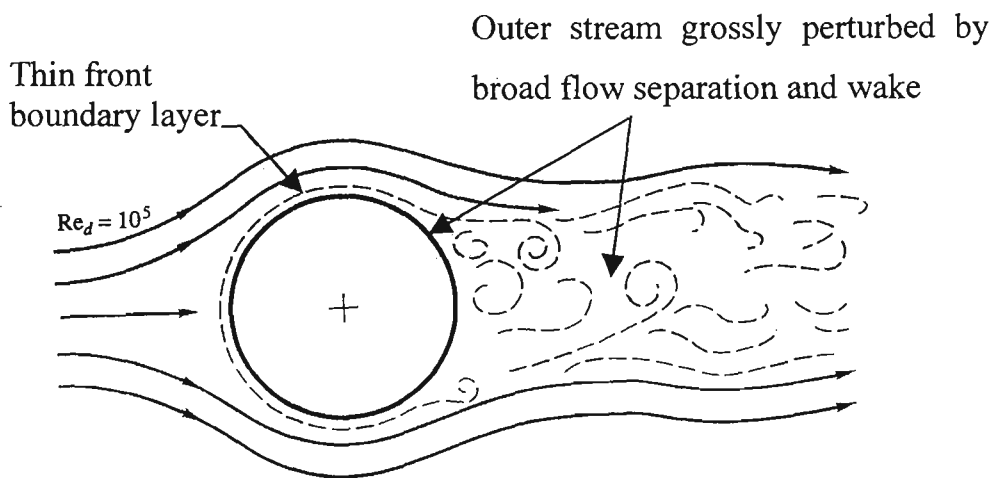


Figure 2.1 Flow past a blunt-body (White, 1994).

Separation is caused by excessive momentum loss near the wall in a boundary layer trying to move downstream against increasing pressure, $\partial P / \partial x > 0$ where P is the static pressure, and x is the main longitudinal flow direction parallel to the wall.

In adverse pressure gradient flows, static pressure increases in the flow direction, in comparison with zero and favorable pressure gradient flows, where $\partial P/\partial x = 0$ and $\partial P/\partial x < 0$, respectively. Adverse pressure gradient flows are more difficult to predict, because they are much more complex, according to the definition of Bradshaw (1976). Adverse pressure gradient turbulent flows can be classified into two groups, as increasing and decreasing adverse pressure gradient cases. In Chukkapalli and Turan (1995), depending on the second longitudinal derivative of the static pressure, flows with $\partial^2 P/\partial x^2 < 0$ were defined as decreasing adverse pressure gradient, and those with $\partial^2 P/\partial x^2 > 0$ as increasing adverse pressure gradient flows. As indicated in Chapter 5, this definition is used here, too.

In general, the main reasons for the complexity of turbulent flow problems are wall effects and the adverse pressure gradient effects. The effect of wall on turbulence structure is two-fold. Firstly, the viscous effects surface due to reduced local turbulence Reynolds number. Secondly, transverse normal Reynolds stresses are preferentially suppressed, and turbulent eddies are distorted in the wall vicinity. The latter effect makes the turbulence structure anisotropic. If statistical features of turbulence have no preference for any direction, meaning that perfect disorder reigns, turbulence is called isotropic.

As a result of adverse pressure gradients, the assumption of self-preservation in the longitudinal direction becomes questionable (Chukkapalli and Turan, 1995). Turbulence activities such as additional mechanisms of production, dissipation, and

transport of turbulence (lateral vortex stretching) are greatly enhanced. Most prominent physical phenomena responsible for this additional activity are irrotational strains and lateral divergence. The additional strain rate makes the mean flow field and turbulent eddying interaction more complex.

Figure 2.2 shows a converging-diverging conduit consisting of a nozzle, throat and diffuser. The nozzle flow is a favorable gradient flow where pressure is decreasing, and velocity is increasing. The flow never separates in this region. At the throat, the pressure gradient is approximately zero and velocity is constant. The diffuser flow is an adverse gradient flow where pressure is increasing, and velocity is decreasing. The boundary layers become thicker in this region. Flow separation and backflow can appear in the diffuser flow.

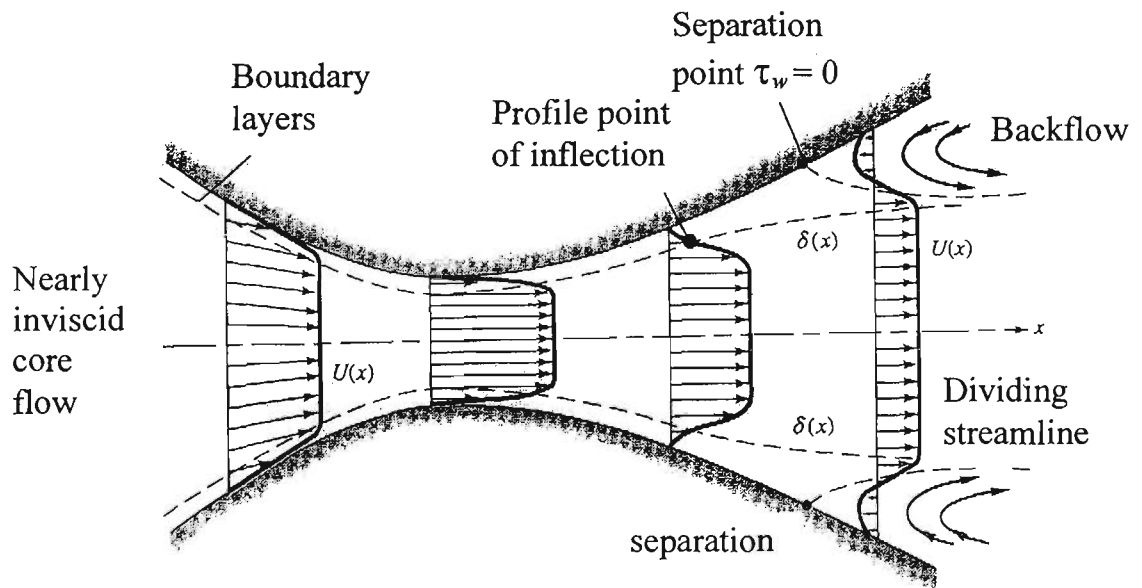


Figure 2.2 Boundary-layer separation in a diffuser (White, 1994).

Figure 2.3 shows the basic mean velocity regions next to a wall in turbulent flows. In this figure, the horizontal axis is the non-dimensional distance from the wall, y^+ ($y^+ = yu^*/\nu$, where u^* is the friction velocity; ν is the fluid kinematic viscosity, $\nu = \mu / \rho$; μ and

dimensionless velocity, U^+ ($U^+ = U/u_*$, where U is the longitudinal mean velocity). The mean velocity regions shown in Figure 2.3 are the viscous sublayer next to the wall (where the dimensionless mean velocity varies linearly with dimensionless distance from the wall), inertial sublayer further away from the wall (where the dependence becomes logarithmic) and buffer layer in between (Gerhart and Gross, 1985). The total shear stress distribution in a turbulent flow near a smooth surface can be divided in three regions. The wall layer is where turbulent stress is very small, and viscous stress is large. This region is next to the wall. Further away from the wall is the fully turbulent layer where viscous stress is negligible, and turbulent stress is large. The overlapping layer is where both stresses are significant (Gerhart and Gross, 1985).

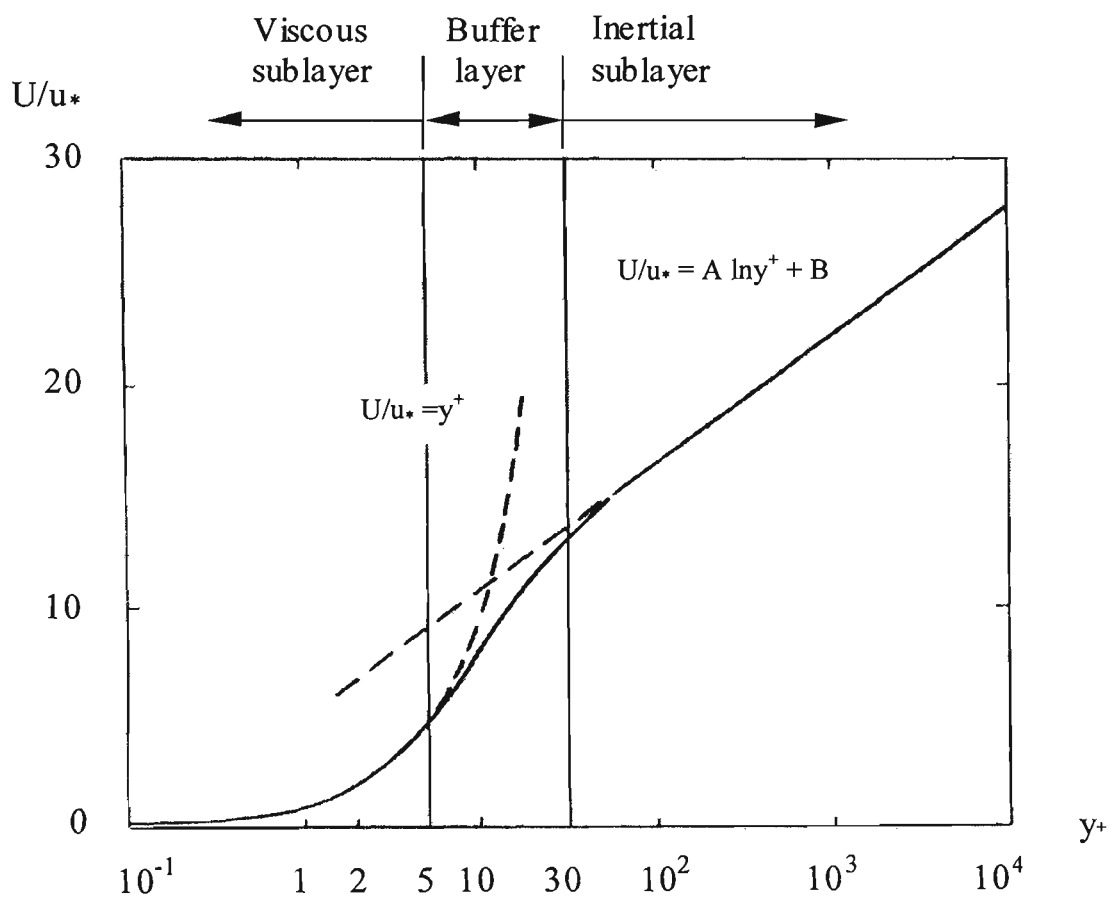


Figure 2.3 Mean velocity behaviour in wall vicinity. $A = 1/\kappa$, $\kappa = 0.41$ is von Kármán's constant from his classical 1930 work (Tennekes and Lumley, 1972). The intercept of $B = 5.2$ is from Coles (1956). This figure is taken from Figure 5.6 of Tennekes and Lumley (1972).

The viscous sublayer, located within the wall layer, is another name for the thin layer next to the wall where turbulence effects begin to develop. The average thickness of this layer is up to about $y^+ = 5$ in favorable and zero pressure gradient flows. In order to describe the velocity profile accurately, each layer should be examined in detail, and then the layers can be patched together. With this approach, the buffer layer is where the logarithmic law and the linear law of the wall overlap. Similarly, the logarithmic law is where the law of the wall next to the wall and the law of the wake at the edge of the boundary layer overlap. This derivation is illustrated next (Gerhart and Gross, 1985).

The law of the wall,

$$U^+ = f(y^+) \quad (2.1)$$

is applicable in the viscous sublayer.

The shear stress at the wall is defined as follows:

$$\tau_w = \mu \left(\frac{dU}{dy} \right) \Big|_{y=0} \quad (2.2)$$

Integrating the above expression and using no-slip condition at the wall, leads to the following equation:

$$U = (\tau_w / \mu) y. \quad (2.3)$$

Therefore,

$$U^+ = y^+, \quad (2.4)$$

if $\tau_w = \rho u_*^2$ (and hence, this expression defines the friction velocity, u_* , in terms of the wall shear stress, τ_w). Equation (2.4) is valid within the viscous sublayer of the wall layer (near the wall), and U^+ and y^+ are the appropriate dimensionless velocity and distance, respectively, within this region.

The longitudinal mean velocity, U , in a pipe or boundary layer flow is governed by the centre-line or core velocity at the boundary layer edge, U_e , inner pipe radius, R , or the boundary layer thickness, δ , wall shear stress, τ_w , fluid density, ρ , and distance from the wall, y :

$U = F(U_e, R, \tau_w, \rho, y)$ in a developing or fully-developed pipe flow, or

$U = F(U_e, \delta, \tau_w, \rho, y)$ in a developing boundary layer flow. (2.5)

von Kármán re-wrote the Equation (2.5) as follows:

$(U_e - U) = F(R, \tau_w, \rho, y)$, or

$(U_e - U) = F(\delta, \tau_w, \rho, y)$, (2.6)

where $(U_e - U)$ is a single parameter, and it is called velocity defect.

Equation 2.6 can be rewritten in dimensionless form, and the equation is called the velocity defect law or the law of the wake (Coles, 1955).

$U^+ = (U_e / u_*) + G(y / R)$, or

$U^+ = (U_e / u_*) + G(y / \delta)$. (2.7)

The function G requires experimental data or a specific theory.

Both Equation (2.1), the law of the wall, and Equation (2.7), the velocity defect law, are applied in the inertial sublayer to obtain the logarithmic velocity profile (Coles, 1956):

$$U^+ = A \ln y^+ + B,$$

where $A = 1/\kappa$, $\kappa = 0.41$ and B is a Reynolds number dependent constant (Turan et al. 1987).

The flow in the wall region is determined by the condition at the wall as expressed by the wall shear stress and wall roughness. The two regions next to the wall, the viscous sublayer and the buffer layer are called the wall region. The roughness height, k does not occur as an additional parameter in flows over a smooth surface.

The mean flow profiles described so far are present only in zero and favorable pressure gradient wall-bounded turbulent flows, such as regular flat plate boundary layers (zero-pressure gradient) and pipe flows (favorable pressure gradient). With the presence of decreasing adverse pressure gradients, the law of the wall remains unchanged, but the logarithmic law region tends to get pushed towards the wall (to smaller y^+ values) in addition to being shorter in length as the pressure gradient increases (Turan et al. 1987). It has been shown that with decreasing adverse pressure gradients, two half-power regions start in the flow (Kopp and Turan, 1992). The extent of these regions increases in the flow direction. Both of these ideas have been investigated in increasing and decreasing adverse pressure gradient flows in this thesis.

2.4 Major Accomplishments to Date in Adverse Pressure Gradient Research

Only two increasing adverse pressure gradient experiments have been reported in the literature, those of Samuel and Joubert (1974) and Sandborn and Slogar (1955), although increasing adverse pressure gradients are as common in turbulent flows as decreasing adverse pressure gradient ones. On aircraft wing sections, ship hulls and bodies of revolution, part of the adverse pressure gradient is increasing, as shown by Abbott and Von Doenhoff (1949) and Goldstein (1965). The region of increasing adverse pressure gradient was limited to the first two stations in the experiment of Sandborn and Slogar; and hence, limited information is available from their work. On the other hand, the data of Samuel and Joubert lack third and fourth order turbulence quantities and the rate of dissipation measurements. These missing turbulence quantities are essential both to understand the flow physics and for turbulence modelling purposes. The experimental setup described in Chapter 3 has been made available to enable such thorough experimental analysis.

Most of the available works on adverse pressure gradient flows are on decreasing adverse pressure gradient experiments. In fact, equilibrium boundary layers are used commonly to study decreasing adverse pressure gradient effects. In the Ph. D. thesis of Skåre (1994), an equilibrium boundary layer is examined, which develops under strong decreasing adverse pressure gradient. Clauser (1954) and Townsend (1976) defined equilibrium flows. An equilibrium flow is where the flow profiles are similar at different longitudinal stations, and the skin friction coefficient, C_f , and the shape factor, H , remain

constant (Here, $C_f = \tau_w / (1/2 \rho U_e^2)$, where τ_w is shear stress at the wall, and U_e is the free stream velocity outside the boundary layer; and $H = \delta^* / \theta$, where δ^* is the displacement thickness, and θ is the momentum thickness). Clauser (1954) defined equilibrium boundary layers to have profiles of $(U_e - U) / u^*$ versus y / δ which are invariant of the streamwise direction (δ is the boundary layer thickness). An equilibrium boundary layer can be established when a constant ratio is kept between the streamwise pressure gradient and the shear stress. Clauser presented two boundary layers in adverse pressure gradient, and Bradshaw (1967) studied the turbulent structure of two layers very similar to Clauser's. None of their boundary layers was near separation. Stratford (1959) was the first person who presented an equilibrium boundary layer with zero skin friction.

The simplest turbulent equilibrium boundary layer is a zero pressure gradient flow. According to Townsend (1976), a zero pressure gradient flow is not a true equilibrium flow, because the skin friction coefficient, C_f and the shape factor, H are not constant. However, the equilibrium conditions are satisfied due to slow decrease in both C_f and H downstream. In order to get the constant values of C_f and H , the flow should develop on a rough surface or in well-defined pressure gradient.

The reason for the common preference for equilibrium flows is two-fold. Firstly, the profiles of mean velocity and fluctuating velocity moments remain unchanged in the streamwise direction when scaled with the similarity parameters. Therefore, experimentally, equilibrium flows are easier to deal with due to their repetitive patterns. This characteristic also makes gradients easier to evaluate. Secondly, from a turbulence

modelling point of view, the adverse pressure gradient cases with long streamwise stretches are more challenging than the adverse pressure gradient flows that separate quickly. In the later case, modelling the adverse pressure gradient details can be omitted, since flow separation dominates the flow. This point was shown clearly at the 1968 Stanford Conference (Cockrell et al. 1968). The moderately decreasing adverse pressure gradient equilibrium boundary layer of Clauser (1954) was determined to be the most difficult case to predict at this conference.

Skåre's (1994) results are also reported in Skåre and Krogstad (1994). In the recognition of the need for high order turbulence quantities, this work is similar to the present thesis, but in a decreasing adverse pressure gradient flow. Rate of dissipation measurements are missing in Skåre's thesis. In Skåre's thesis, the experimental data were obtained with single and x-wire probes. Skåre used an array of eight x-wire probes aligned in the horizontal and vertical planes to measure large-scale motions. His use of multiple x-wire probes was similar to the works of Hayakawa and Hussain (1989) and Bisset et al. (1990) in the wake of a cylinder, and Antonia et al. (1990) in zero pressure gradient boundary layers.

Prior to Skåre's work, Clauser (1954), Stratford (1959), and East and Sawyer (1979) had examined decreasing adverse pressure gradient equilibrium boundary layers. Skåre's work is different both in maintaining a higher decreasing adverse pressure gradient for a longer streamwise distance and in measuring higher order moments. Turan and Azad (1993) reported rate of dissipation measurements both in favorable and adverse

pressure gradient flows. The adverse pressure gradient measurements were carried out in an eight-degree conical diffuser where a strong decreasing adverse pressure gradient existed. Chukkapalli and Turan (1995) collated adverse pressure gradient data of different authors to develop a modified k - ϵ turbulence model. The only increasing adverse pressure gradient data they could use for this purpose was that of Samuel and Joubert (1974), also known as Flow 141 of the 1981 Stanford Conference (Kline et al. 1981). The three decreasing adverse pressure gradient flows were Flows 142 and 143 of the same conference, and the data of Turan (1988). A modified model was developed based on the decreasing adverse pressure gradient data, in spite of the differences among the three sets used: Flow 142 is a planar diffuser flow with a developing inlet. Flow 143 is a conical diffuser flow with a similar inlet and high core turbulence. The experimental data of Turan is from a conical diffuser with a fully-developed inlet. Although the modified model was successful in decreasing adverse pressure gradient flows, the limited data of Flow 141 was not sufficient to show conclusive agreement or disagreement. The present thesis is a step towards filling this gap in the literature of lack of increasing adverse pressure gradient data.

Chapter 3. EXPERIMENTAL SETUP

3.1 Introduction

In order to facilitate the complete experimental investigation of an increasing adverse pressure gradient turbulent flow, a pressure gradient distribution similar to that of Flow 141 (Samuel and Joubert, 1974) was generated in a wind tunnel. Only the mean flow characteristics of this flow have been investigated experimentally in this thesis. For calibration purposes, a fully-developed turbulent pipe flow setup has been prepared. In this chapter, the wind tunnel and pipe flow rigs are described in detail, along with instrumentation. Friction velocities were measured with calibrated Preston tubes. Different diameter Preston tubes were calibrated in the fully developed pipe flow, and this calibration was compared with Patel's correction (1965). Pitot-static tubes were used for mean velocity measurements.

In the wind tunnel, bent Preston and Pitot-static tubes were used. Schematic views of both types of probes are shown in Figure 3.1. In the fully-developed pipe flow, only straight Preston tubes were needed.

3.2 Wind Tunnel

Mean velocity measurements were carried out in the Research Wind Tunnel located in the Fluid Mechanics Laboratory at the School of the Built Environment, Victoria University. A schematic view of the wind tunnel is given in Figure 3.2. The

wind tunnel is open-return type with a centrifugal blower at the inlet. The fan diameter is 1.3 m, driven by a 60.4-hp motor. The flow then goes through a 1.1-m long wide angle diffuser followed by a 0.55 m-long setting chamber of cross sectional area $1.9 \text{ m} \times 1.9 \text{ m}$.

Two layers of honeycomb of nominal diameter of 7 mm are inserted in the setting chamber in 5-cm lengths. Fine mesh screens cover each end of the honeycomb. A third screen is located just before the end of contraction cone. The honeycomb and three layers of the fine mesh straighten the flow at low velocity. Before entering the test section, the flow passes through a 1.94-m long contraction cone which has an area ratio of 9.4 : 1.

The test section dimensions are 0.9 m by 0.9 m by 4.5 m long. At the inlet, the test section area is closed partly with a flexible top leaving an effective area of $0.9 \text{ m} \times 0.425 \text{ m}$. There are three windows to place the probes easily in the flow, especially the hot-wire probes without breaking the wire. The test section is designed to generate different ranges of pressure gradients by changing a flexible top. The flexible top is made from 3-mm thick lexan, and it is adjusted by means of nine pairs of screws. 48 9-mm diameter holes were drilled at the centre of the flexible top to fit probe holders for vertical traverses.

The wall static pressure distribution was measured over the false bottom. The false bottom is made of plywood, and 32 static pressure taps exist to monitor the static pressure change along the bottom wall. The diameter of the static pressure holes is 1mm,

and they are at 150 mm intervals. A schematic view of a static pressure tap insert is shown in Figure 3.3.

In the test section, the flexible top was set to produce the desired pressure gradient, as described in Chapter 4. However, before any measurements could start, the gaps between the leading edge of the flexible top and the top wall of the contraction cone and between the leading edge of the false bottom and the bottom wall of the contraction cone had to be taken care of first. To cover these gaps, 0.1-mm thick plexiglass sheets are used, thinner than the flexible top. The top covering was a gentle curve of 62-cm arc length in streamwise direction and 44-cm arc length in normal direction. Similarly, the bottom covering had 64-cm arc length in streamwise direction and 8-cm arc length in normal direction.

There are a total of 16 cone pressure holes, 8 at upstream and 8 at downstream of the contraction cone (two holes each at the bottom, top and on each side per station). For the present measurements, only 12 cone pressure holes were used, since 4 holes (2 holes on top and 1 hole at each side) at the downstream station were covered with the flexible top.

3.3 Velocity Traverses and the Traversing Mechanism

All pressure measurements were conducted with home made Preston and Pitot-static tubes connected to a FCO12-micromanometer from Furness Controls Limited. A traversing mechanism operated by a stepping motor and an electric controller was used

for this purpose. The controller contained an 8-digit Add/Subtract Totalising Counter from RS Components Limited. A schematic view of the traversing mechanism is presented in Figure 3.4.

A stepping motor is mounted on a shaft which has a pitch diameter of 1.5 mm. A disk with 50 slots is mounted with the stepping motor and the controller. The purpose of the disk is to control the stepping motor. The slots in the disk are read by Slotted Opto Switches from RS Components Limited. This information is then fed to the 8-digit Add/Subtract Totalising Counter.

The traversing mechanism traverses 1.5 mm in the vertical direction when the disk rotates by one revolution. Hence, a stepping motor that can traverse 0.03 mm increments was used to operate the traversing mechanism for all measurements. The accuracy of the traversing mechanism was governed by two factors, the stepping motor and the power screw in the traversing mechanism.

The traversing accuracy was tested by operating the stepping motor many times. The stepping motor proved to be extremely accurate, since the motor steps matched the distance by which the carriage holding the probe holder advanced. The backlash in the power screw holding the carriage has been estimated to be less than ± 0.015 mm corresponding to one half of the slot advancement of 0.03 mm.

3.4 The Fully-Developed Pipe Flow Setup: Calibration Rig

A calibration rig was built to provide fully-developed turbulent pipe flow at its exit. A schematic view of this setup is given in Figure 3.5. A 3.6-hp motor drives a centrifugal fan. A settling chamber pipe of 203-mm outer diameter, 3-mm wall thickness and 3-m length is placed before a contraction of 3.8 : 1 area ratio. The contraction cone is followed by 3 lengths of 6-m long stainless steel piping of 101.6-mm (4-in.) inner diameter and 3-mm wall thickness. The pipe sections are connected by externally adjusted sleeves to maintain better contact and to avoid steps where two pipes meet.

One of the three stainless-steel pipe sections has four static pressure taps at five stations. These stations are 1 m apart. In order to decide whether or not to use all four of the pressure taps in obtaining an average reading from a given section, all taps were tested individually. The anomalous readings were used to eliminate some of the taps. The pipe section with the static pressure taps showed the same pressure drop when used in the middle or at the end of the three-pipe assembly.

The flow speed is controlled by a damper at the inlet of the fan. A flexible coupling separates the fan from the settling chamber in order to prevent fan vibration travelling to the pipe exit. The settling chamber is filled with two layers of the same honeycomb as used in the settling chamber of the wind tunnel.

Three Reynolds numbers were used for the present experiments, corresponding to the fully, three quarter and quarter open cases of the damper. These were, 281,000,

274,000, 146,000, respectively, corresponding to the centre line velocities of 39 m/s, 38 m/s and 20 m/s. Here, Reynolds number is defined as follows:

$$\text{Re} = \frac{U_{CL} d}{\nu}$$

where U_{CL} is the centre line velocity; d is the inner pipe diameter ($d = 101.6$ mm) and ν is the kinematic viscosity (of air, $\nu = 1.5 \times 10^{-5}$ m²/s).

This calibration rig is meant for Preston tube and x-wire calibrations. In the present thesis, in the absence of hot-wire measurements, it has been used for Preston tube calibration, only.

3.5 Preston Tube Calibration

Home made total head tubes of diameters 1 mm, 2 mm, 2.5 mm, 3 mm, 4 mm, 5 mm, 6 mm, were used in the fully-developed turbulent pipe flow, both to check on the velocity profile in the pipe and also to calibrate them as Preston tubes. All total head tube measurements were obtained at one radius from the pipe exit as suggested by Preston (1950). As shown in Figure 3.6, all velocity traverses obtained with the largest to smallest diameter Preston tubes collapse on to one curve. In order to check if the pipe flow is fully developed, up to second and third order fluctuating velocity correlations need to be measured axially to show that they do not change (Dang, 1987). Since no hot wire measurements have been taken in this study, such a rigorous check has not been applied. However, as indicated before, it has been observed that the pressure gradient is constant over the last 12 m pipe length (a necessary but insufficient condition). In

addition, as described next, all Preston tubes have been calibrated with respect to Patel's (1965) fully-developed pipe flow correlations.

3.5.1 Calibrating by Patel's Correction

In a turbulent boundary layer, Preston's method (1950 and 1954) of measuring skin friction is based on putting a fine circular total head tube on the wall. Preston corrected such readings with respect to measurements in a fully-developed pipe flow. Patel (1965) revised Preston (1954)'s original calibration curve which was erroneous.

Friction velocity, u_* , is defined as follows:

$$u_*^2 = \nu \left. \frac{\partial \bar{U}}{\partial y} \right|_{y=0} = \frac{\tau_w}{\rho}, \quad (3.1)$$

where τ_w is the shear stress at the wall.

In a fully-developed pipe flow, the pressure drop and friction velocity are related as follows (Hinze, 1975, p. 712):

$$u_*^2 = -\frac{R}{2} \frac{1}{\rho} \frac{\partial P}{\partial x}. \quad (3.2)$$

Patel kept Preston's non-dimensional relationship between the dynamic pressure reading from a Preston tube, ΔP_p , and wall shear stress, τ_w :

$$\frac{\tau_w d^2}{4\rho\nu^2} = F\left(\frac{\Delta P_p d^2}{4\rho\nu^2}\right), \quad (3.3)$$

where d is the Preston tube diameter, and ρ and ν are the fluid density and kinematic viscosity, respectively. He defined three calibration ranges based on a variable y^* . y^* can be related to a Reynolds number based on u_* , $Re_* = u_* d / \nu$. y^* is defined as follows:

$$y^* = \log_{10} \left(\frac{\tau_w d^2}{4\rho\nu^2} \right) = \log_{10} \left(\frac{1}{4} \left[\frac{u_* d}{\nu} \right]^2 \right). \quad (3.5)$$

The corresponding independent variable, x^* , is defined as follows:

$$x^* = \log_{10} \left(\frac{\Delta P_p d^2}{4\rho\nu^2} \right). \quad (3.6)$$

To use Patel's correction curves, first x^* is calculated with the dynamic pressure, ΔP_p , obtained with each diameter, d , Preston tube. Then, y^* value is obtained from the appropriate range, and u_* is calculated from y^* . The x^* and y^* values at the three Reynolds numbers of this study are listed in Table 3.1. Subsequently, values obtained from y^* , u_{*p} , are compared with u_* obtained from Equation 3.2. This comparison is given in Table 3.2 for the three Reynolds numbers of this study. As indicated in Table 3.1, the calibration range used here is,

$$2.8 \leq y^* \leq 4.4 \text{ for } Re = 146,000,$$

$$3.4 \leq y^* \leq 5.0 \text{ for } Re = 274,000, \text{ and}$$

$$3.4 \leq y^* \leq 5.0 \text{ for } Re = 281,000.$$

These ranges correspond to the following two equations:

$$y^* = 0.8287 - 0.1381x^* + 0.1437x^{*2} - 0.0060x^{*3} \quad (3.7)$$

for $2.9 < x^* < 5.6$, and

$$x^* = y^* + 2\log_{10} (1.95y^* + 4.10) \quad (3.8)$$

for $5.6 < x^* < 7.6$.

In Table 3.2, at the lowest Reynolds number, friction velocity after Patel's correction, u_{*p} , and the "true" friction velocity from Equation 3.2, u_* , agree as measured by the seven Preston tubes of diameters 1 to 6 mm. As Reynolds number increases, the agreement ceases for $d \geq 3$ mm at $Re = 274,000$ and for $d \geq 2.5$ mm at $Re = 281,000$. This result indicates insensitivity of the instrumentation at the lowest Reynolds number. More importantly, it indicates that Preston tubes of 1-mm and 2-mm diameter can be used in the wind tunnel with Patel's calibration.

3.5.2 An Alternate Calibration with Correction Factor

As an alternative to Patel's calibration, an attempt was made to develop a correction factor for each Preston tube. For this purpose, friction velocity to be corrected, u_{*m} , was measured as follows:

$$\Delta P_p = \frac{1}{2} \rho U^2 \text{ from Preston tube.}$$

$$\tau_w = \nu \left. \frac{\partial U}{\partial y} \right]_{y=0} \approx \nu \frac{\Delta U}{\Delta y} = \nu \frac{U - 0}{\left(\frac{d}{2}\right) - 0} = \rho u_{*m}^2$$

The "true" friction velocity from Equation 3.2 was then used to obtain a correction factor,

C:

$$\frac{u_*}{u_{*m}} = C$$

The correction factors hence obtained for 1 mm and 2 mm Preston tubes are listed in Table 3.3 for three Reynolds numbers. As indicated in this table, a constant value was not obtained for one diameter, and hence this approach was dropped.

3.5.3 Frei and Thomann Correction

Frei and Thomann (1980) suggested further correcting u_* after Patel's calibration for adverse pressure gradient. Their correction is based on comparison of Preston tube measurements after Patel's correction with independent wall shear stress measurements.

The Frei and Thomann correction curves are based on $P_p = \frac{dP}{dx} \frac{\nu}{\rho u_{*p}^2}$, where $dP/dx > 0$.

As described in detail in Chapter 4 next, with the dP/dx values from the increasing adverse pressure case of the present study, the required correction was less than 5 % and hence, it was not applied. The u_* values quoted in Chapter 4 next are obtained with Patel's calibration, only.

Preston tube diameter [mm]	Re = 146,000		Re = 274,000		Re = 281,000	
	x*	y*	x*	y*	x*	y*
1.0	4.83	2.84	5.43	3.36	5.45	3.37
2.0	5.54	3.45	6.10	3.95	6.11	3.96
2.5	5.75	3.64	6.32	4.15	6.35	4.16
3.0	5.93	3.80	6.50	4.30	6.52	4.31
4.0	6.22	4.05	6.78	4.55	6.85	4.56
5.0	6.43	4.24	6.99	4.75	7.05	4.76
6.0	6.60	4.40	7.15	4.91	7.18	4.92
x* ranges	4.8 < x* < 6.6		5.4 < x* < 7.2		5.5 < x* < 7.2	
y* ranges	2.8 < y* < 4.4		3.4 < y* < 5.0		3.4 < y* < 5.0	

Table 3.1 Calculated x* and y* ranges for various size Preston tubes.

d [mm]	Re = 146,000			Re = 274,000			Re = 281,000		
	x*	u* _p	u*	x*	u* _p	u*	x*	u* _p	u*
1.0	4.83	0.79	0.79	5.43	1.42	1.42	5.45	1.44	1.44
2.0	5.54	0.80	0.79	6.10	1.42	1.42	6.11	1.44	1.44
2.5	5.75	0.80	0.79	6.32	1.42	1.42	6.35	1.47	1.44
3.0	5.93	0.80	0.79	6.50	1.40	1.42	6.52	1.45	1.44
4.0	6.22	0.79	0.79	6.78	1.41	1.42	6.85	1.52	1.44
5.0	6.43	0.80	0.79	6.99	1.41	1.42	7.05	1.47	1.44
6.0	6.60	0.79	0.79	7.15	1.38	1.42	7.18	1.43	1.44

Table 3.2 Preston tube calibration. In this table, u*_p is the friction velocity after Patel's correction, and u* is the actual value from Equation 3.2.

Preston tube diameter [mm]	Re = 146,000	Re = 274,000	Re = 281,000
1	2.23	2.39	2.38
1	2.25	2.27	2.34
2	2.25	2.39	2.40
2	2.18	2.29	2.31

Table 3.3 Correction factors for 1 mm and 2 mm Preston tubes at three Reynolds numbers.

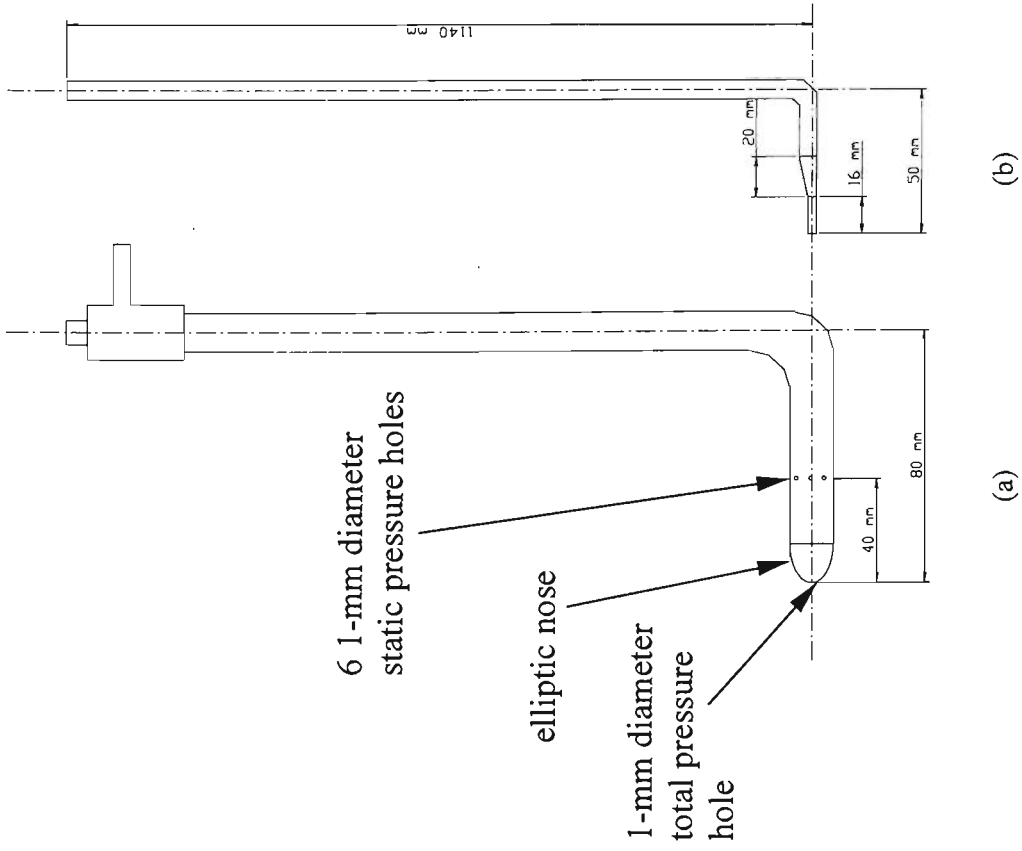


Figure 3.1 Schematic representation of the bent Pitot-static (a) and Preston (b) tubes used in the wind tunnel. Only straight Preston tubes are used in the fully-developed pipe flow. The diameter of the Pitot-static tube is 5 mm. The tip of the Preston tube is 1-mm outer and 0.6 mm inner diameter, and the rest is made of stainless-steel tubing.

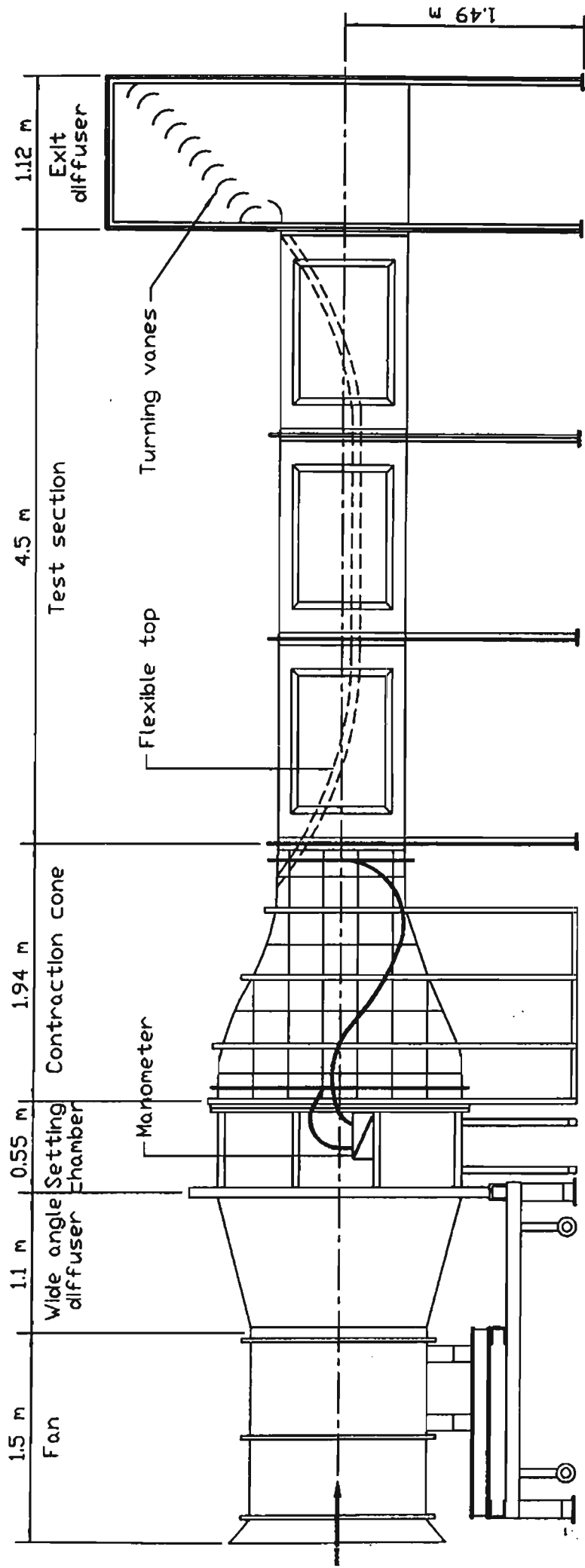


Figure 3.2 Wind tunnel (not to scale).

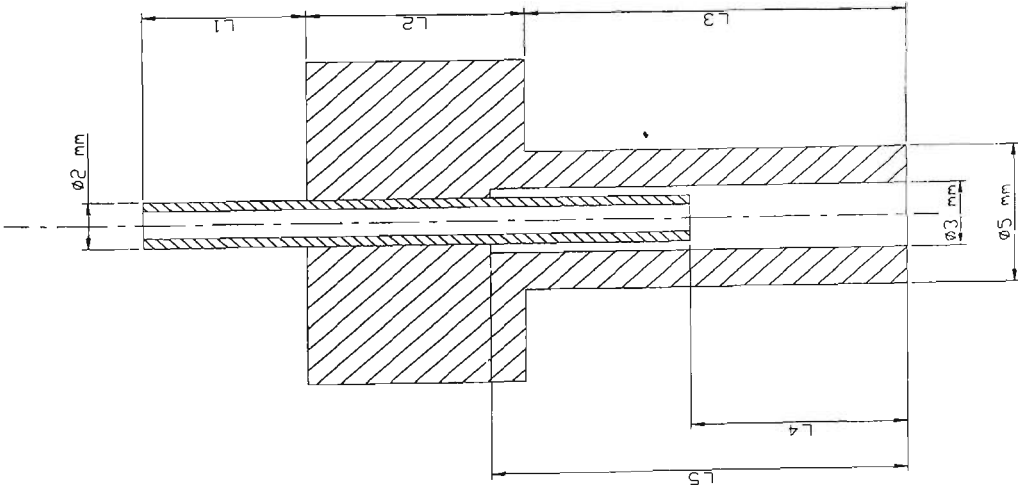


Figure 3.3 Static pressure tap insert. L1, L2, L3, L4 and L5 are 17.5 mm, 16.5 mm, 19 mm, 18 mm and 24 mm, respectively for the wind tunnel, and 3.0 mm, 10 mm, 15 mm, 24 mm and 24 mm, respectively for the calibration rig. The 2-mm outer diameter stainless steel tubing has a wall thickness of 0.25 mm.

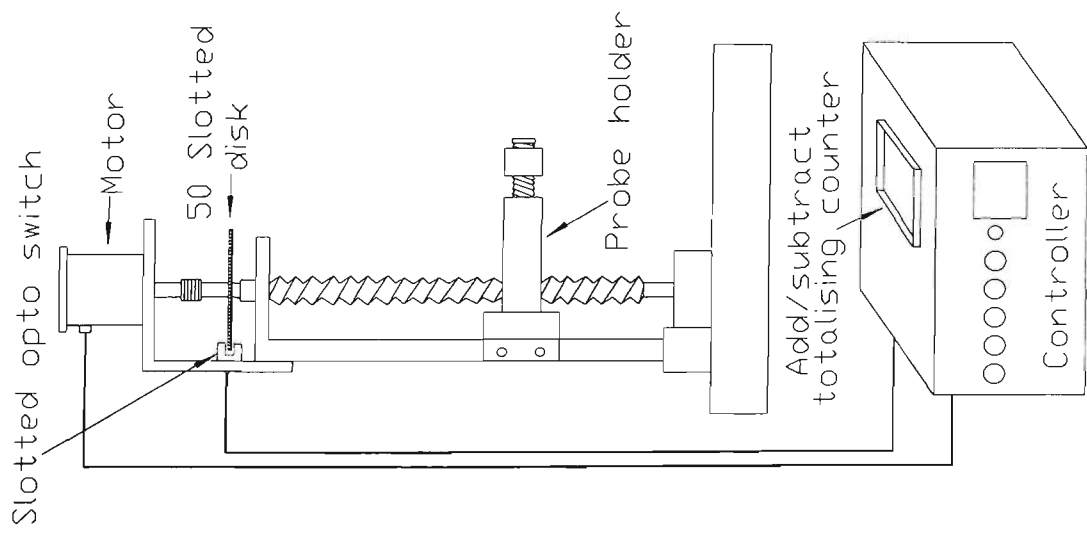


Figure 3.4 Traversing mechanism.

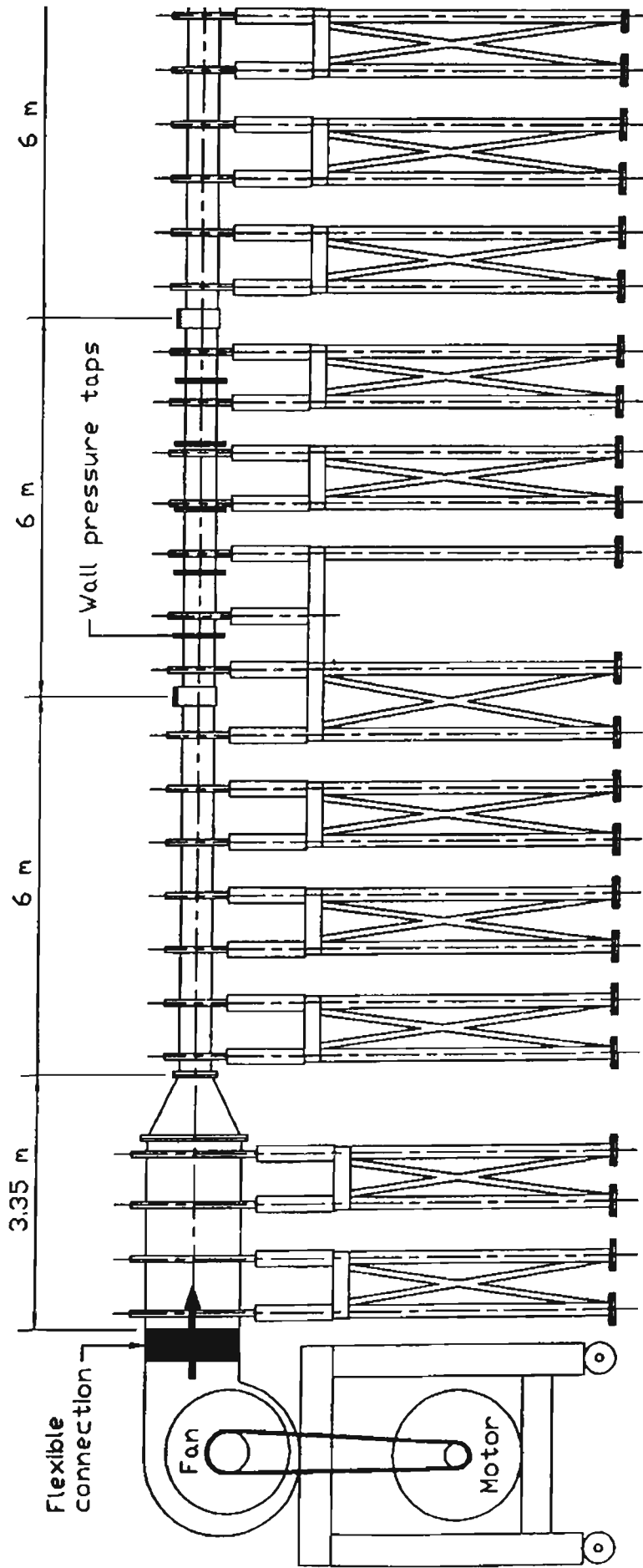


Figure 3.5 Calibration rig (not to scale).

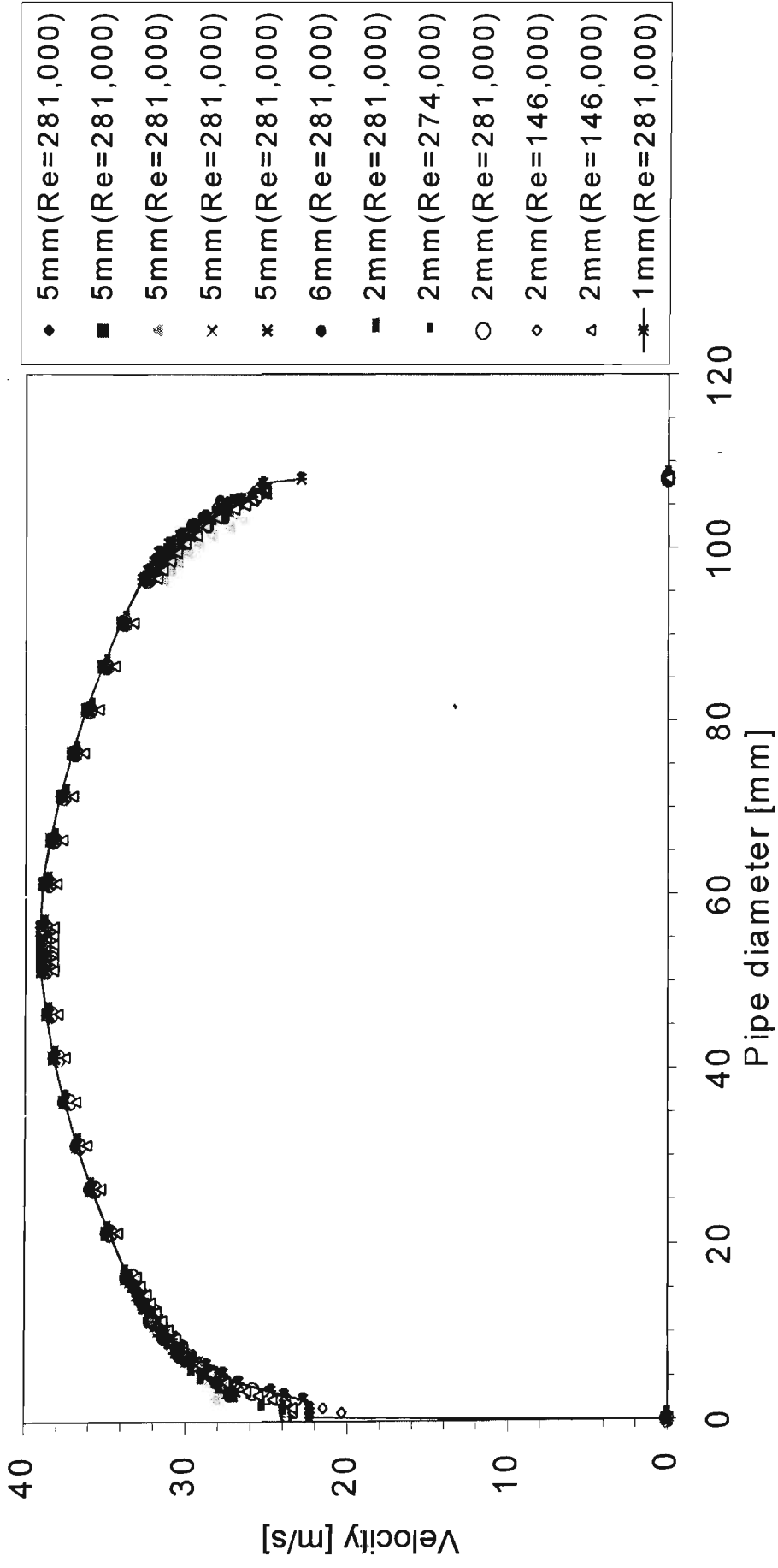


Figure 3.6 Preston tube traverses in the calibration rig with 4 different Preston tubes. Tube diameters are listed in the legend.

Chapter 4. RESULTS AND DISCUSSION

4.1 Flexible Top Preparation

Before starting the mean velocity measurements, it was necessary to set the flexible top to generate a long region of increasing adverse pressure gradient. It was decided to use Flow 141 characteristics as a guide. The flexible top had to be given as gentle a curve as possible starting from the top wall of the contraction cone, all the way to the exit of the test section. As described in Section 3.2, the flexible top was connected at its leading edge to the top wall of the contraction cone with a thinner plexiglass sheet for this purpose. At the test section exit, the trailing edge of the flexible top was connected to the exit diffuser, again with as continuous a curve as it was at the inlet.

The final shape of the flexible top is shown in Figure 4.1. The corresponding coordinates are listed in Table 4.1. In Appendix A, a range of trial shapes and the corresponding pressure distributions are given. The chosen shape for further measurements is Case 19 of the 20 cases given in Appendix A.

4.2 Pressure Distribution

The final choice of the flexible top shape given in Figure 4.1 was based on the similarity of the resulting streamwise pressure distribution to that of Flow 141. This comparison is given in Figure 4.2. In Figures 4.2 (a), (b) and (c), respectively, the streamwise distribution of the wall static pressure and its first and second streamwise derivatives are shown along with those of Flow 141. The first and second derivatives

were obtained through central differencing after smoothing the values of the previous step. The values of C_p and its first two streamwise gradients are listed in Table 4.2 for the present study. In Table 4.2 and Figures 4.2 (b) and (c), the non-dimensional pressure coefficient, C_p is defined as follows:

$$C_p = \frac{P - P_{ref}}{\frac{1}{2} \rho U_{ref}^2}, \quad (4.1)$$

where P_{ref} is the reference static pressure measured at a streamwise distance of 262 mm from the start of the test section. The reference velocity, U_{ref} , was 21m/s in the free stream, measured at the same location as P_{ref} .

The pressure gradient parameter, Δ , is defined as follows:

$$\Delta = \frac{\alpha \nu}{u_*^3}, \quad (4.2)$$

where $\alpha = \frac{1}{\rho} \frac{\partial P}{\partial x} \cong \frac{1}{\rho} \frac{dP}{dx}$; ν is the kinematic viscosity, and u_* is the friction velocity.

Patel (1965) gave a limit of $\Delta < 0.015$ for Preston tube measurements with 6 % accuracy. The values of the pressure gradient parameter for the present study are shown in Table 4.3. Brown & Joubert (1969) suggested that Preston tubes should be used when the pressure gradient parameter is less than or equal to 0.05. The Δ values were not higher than this limit in the present study.

4.3 Mean Velocity Traverses

Mean velocity was measured at 23 streamwise locations with normal traverses from the false bottom to the flexible top at each station. For this purpose, a 5-mm diameter home-made Pitot static tube and 1-mm diameter home-made Preston tube were used. For Preston tube traverses, static pressure was measured with the wall static pressure taps on the false bottom in the test section. These traverses are presented in Figure 4.3. For further analysis, the experimental data from every other station have been utilized, resulting in 12 stations for the rest of this chapter and Chapter 5.

4.4 Friction Velocity

For the experiments in the wind tunnel, the friction velocity was obtained using two different approaches, namely, Clauser charts and Preston tube measurements (along with Patel's and Frei and Thomann's corrections). These two approaches are described next.

Clauser (1954) charts are shown in Figure 4.4 where the measured velocity profiles are plotted as U/U_e against yU_e/ν . Here, y is measured perpendicular to the bottom wall (the false bottom with the static-wall-pressure taps). U_e is the core velocity at each section. In Table 4.3, the core velocity values are listed (along with U_{ref} for comparison).

The following is the expected equation for the straight line in the logarithmic region.

$$\frac{U}{U_e} = \sqrt{\frac{C_f}{2}} \left(A \times \log_{10} \left(\frac{yU_e}{\nu} \right) + A \times \log_{10} \left(\sqrt{\frac{C_f}{2}} \right) + B \right) \quad (4.3)$$

In Equation (4.3), C_f is the skin friction coefficient, A and B are constants. C_f is defined as follows:

$$C_f = \frac{\tau_w}{\frac{1}{2}\rho U_e^2} = \frac{\rho u_*^2}{\frac{1}{2}\rho U_e^2} = \frac{2u_*^2}{U_e^2} \quad (4.4)$$

Clauser used a gradient with $A = 5.6$ and a y intercept with $B = 4.9$. In the present study, the local skin friction coefficient was calculated by using the gradient of the log-law fit, from Figure 4.4 with $A = 5.6$, since the gradient can be expressed as, $(\log_{10} e) \frac{Au_*}{U_e}$.

Then, B was calculated by using the y intercept value of the best fit. These values are listed in Table 4.4. The average B value is calculated to be 5.1.

After obtaining u_* as listed in Table 4.4 from Clauser charts, u_* was also measured with a 1 mm Preston tube. The resulting measurements were corrected with Patel's correction using the x^* and y^* values listed in Table 4.5. As indicated in Section 3.5.3, Frei and Thomann's correction indicated less than 5 % error in these values. Hence, the Frei and Thomann correction was not used. The resulting u_* values are presented in Table 4.5.

As indicated in Tables 4.4 and 4.5, the two methods of obtaining u_* led to similar results, as expected. The reason is that the use of Clauser's charts relies on the presence of the logarithmic law within the boundary layer, whereas Preston's method is based on the presence of the law of the wall. Both profiles were present within the boundary layer

developing on the false bottom in the test section. In Figure 4.5, the resulting streamwise distribution of the friction velocity is presented. The streamwise decrease can be interpreted to mean that had the test section been longer, the flow would have separated from the bottom wall further downstream.

4.5 Logarithmic Profiles

In Figure 4.6, the mean velocity profiles at the 12 streamwise stations of the present study, are plotted in a semi-logarithmic scale in the inner variables to see the scaling close to the wall, with U^+ against y^+ . Here, $U^+ = U/u_*$ and $y^+ = yu_*/\nu$. The straight line in Figure 4.6 is to emphasize the logarithmic overlap from $y^+ = 100$ to $y^+ = 1000$. In Figure 4.6 (a), all stations are presented. In Figure 4.6 (b), the same data are plotted with the exception of the values obtained at $x = 2.335$ m. The data from this station were eliminated, since as seen in Figure 4.6 (a), there was a mis-match with the profiles from other stations (although this profile is used for half-power considerations). In Figure 4.7, the same data are plotted with the outer variables as U/U_e against y/δ . The experimental values y^+ , u^+ , y/δ and U/U_e are listed in Appendix B, along with u_* , δ and U_e at each station.

In Figure 4.6, the logarithmic law line is given by the following expression:

$$\frac{U}{u_*} = \frac{1}{\kappa} \ln\left(\frac{yu_*}{\nu}\right) + 5.2. \quad (4.5)$$

In Equation (4.5), $\kappa = 0.41$ is a universal constant. The best fit to the present profiles indicated that 5.2 is the intercept. The experimental results are seen to collapse onto the classical logarithmic law of the wall. As indicated in Figure 4.8, the logarithmic region tends to the law of the wall, $U^+ = y^+$, after a buffer region towards the wall. Towards the core, it connects to Coles's (1956) universal wake function. Musker's (1979) inner function represents the wake strength. The definition of the wake strength, Π is shown in Figure 4.8. The wake strength Π is calculated as 2.26 in present work. The expression for the wake strength is as follows:

$$2\Pi / \kappa = 2\Pi / 0.41 . \quad (4.6)$$

In Chapter 5, the mean velocity profiles from the 12 streamwise stations identified in this chapter are compared with the mean velocity data from 10 increasing and decreasing adverse pressure gradient flows from the literature.

x [mm]	y [mm]
0	425
143	425
615	430
1193	440
1703	448
2226	457
2765	480
3280	511
3865	571
4470	700
4640	751

Table 4.1 Flexible top coordinates. $x = 0$ corresponds to the test section inlet.

x [m]	C_p	dC_p/dx [1/m]	d^2C_p/dx^2 [1/m ²]
0.100	0.001109		
0.250	0.001109	-0.005544	
0.300	0.000000	0.000000	0.066533
0.400	0.001109	0.004436	0.049284
0.550	0.001109	0.012321	0.026285
0.700	0.004805	0.012321	-0.123210
0.850	0.004805	-0.024642	-0.123210
1.000	-0.002587	-0.024642	0.205350
1.150	-0.002587	0.036963	0.287490
1.300	0.008501	0.061605	0.123210
1.450	0.015894	0.073926	0.041070
1.600	0.030679	0.073926	-0.082140
1.750	0.038072	0.049284	0.000000
1.900	0.045464	0.073926	0.123210
2.050	0.060250	0.086247	-0.042430
2.200	0.071339	0.061197	0.038636
2.352	0.078731	0.097915	0.205341
2.502	0.100909	0.123210	0.084316
2.652	0.115694	0.123210	0.123210
2.802	0.137872	0.160173	0.123210
2.952	0.163746	0.160173	-0.123210
3.102	0.185924	0.123210	-0.082140
3.252	0.200709	0.135531	0.123210
3.402	0.226583	0.160173	0.123210
3.552	0.248761	0.172494	0.123210
3.702	0.278331	0.197136	0.123210
3.852	0.307901	0.209457	0.000000
4.002	0.341168	0.197136	-0.164280
4.152	0.367042	0.160173	-0.164280
4.302	0.389220	0.147852	-0.164280
4.452	0.411398	0.110889	-0.287490
4.602	0.422487	0.061605	-0.063613
4.752	0.429879	0.091805	0.013387

Table 4.2 C_p , dC_p/dx , d^2C_p/dx^2 .

x [m]	U_e [m/s]	Δ
0.262	20.80	-0.001000
1.089	20.60	0.000146
1.245	20.60	0.000201
1.867	20.20	0.000496
2.335	19.80	0.000704
2.412	19.70	0.000952
2.669	19.50	0.001057
2.825	19.00	0.001428
3.317	18.15	0.002599
3.702	17.50	0.004554
3.902	16.90	0.005797
4.346	15.80	0.005466

Table 4.3 Streamwise values of the pressure gradient parameter, Δ . $U_{ref} = 20.80$ m.

x [m]	C_f	U_e [m/s]	u* [m/s]	B
0.262	4.00×10^{-3}	20.80	0.93	5.16
1.089	3.12×10^{-3}	20.60	0.81	5.18
1.245	2.86×10^{-3}	20.60	0.78	5.81
1.867	2.41×10^{-3}	20.20	0.70	5.87
2.335	2.18×10^{-3}	19.80	0.65	5.65
2.412	2.60×10^{-3}	19.70	0.71	4.80
2.669	2.50×10^{-3}	19.50	0.69	5.20
2.825	2.70×10^{-3}	19.00	0.70	3.69
3.317	2.25×10^{-3}	18.15	0.61	4.86
3.702	1.91×10^{-3}	17.50	0.54	5.09
3.902	1.96×10^{-3}	16.90	0.53	4.43
4.346	1.44×10^{-3}	15.80	0.42	5.52
				average B = 5.105

Table 4.4 u_* from Clauser plots ($A = 5.6$).

x [m]	x*	y*	u* [m/s]
0.262	4.98	3.00	0.95
1.089	4.85	2.87	0.82
1.245	4.84	2.86	0.81
1.867	4.77	2.80	0.75
2.335	4.76	2.79	0.74
2.422	4.68	2.71	0.68
2.669	4.69	2.72	0.69
2.825	5.33	3.26	0.64
3.317	4.52	2.57	0.58
3.702	4.40	2.50	0.53
3.902	4.32	2.42	0.49
4.346	4.18	2.31	0.43

Table 4.5 Streamwise values of the friction velocity as obtained with Preston's method (after Patel's correction).

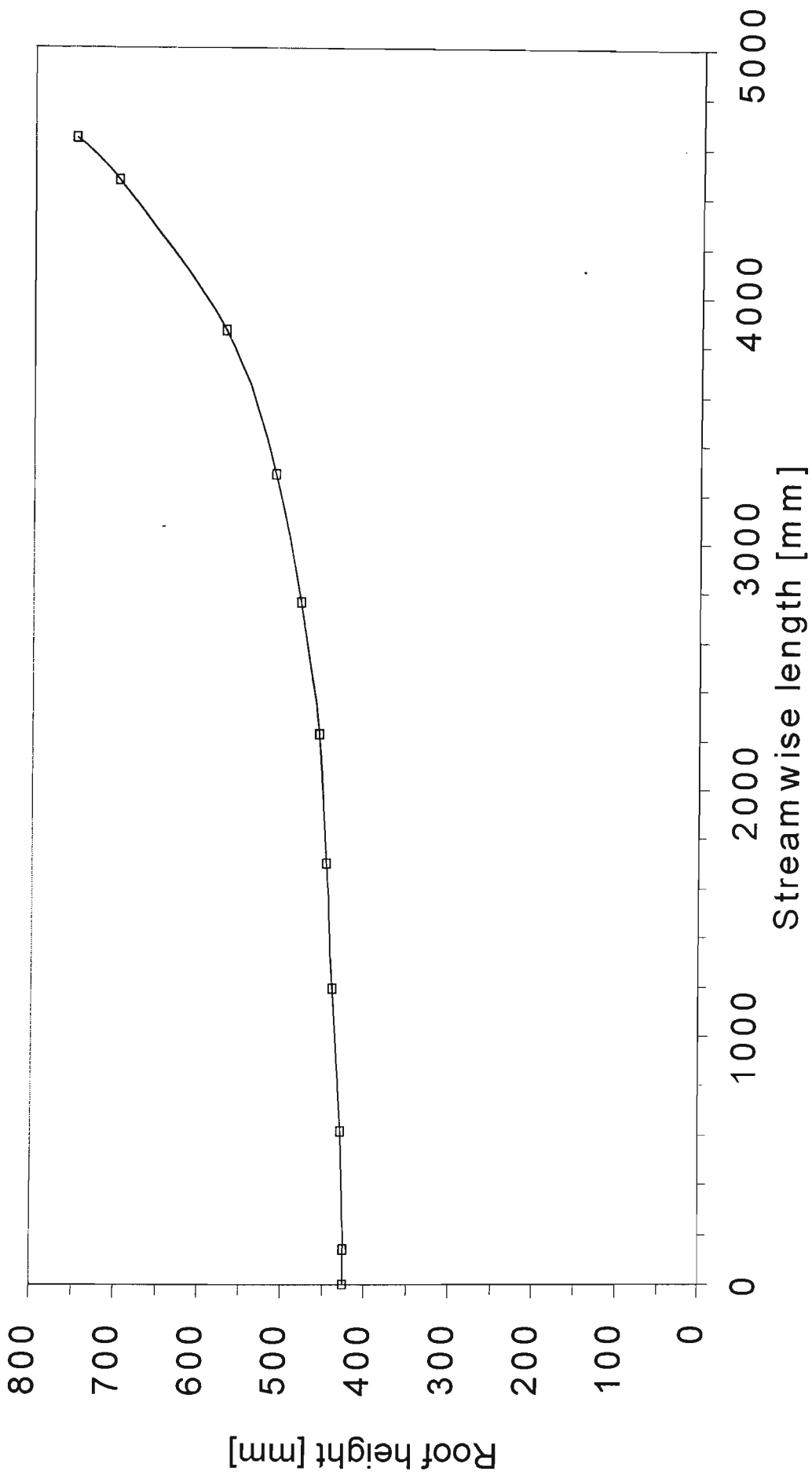
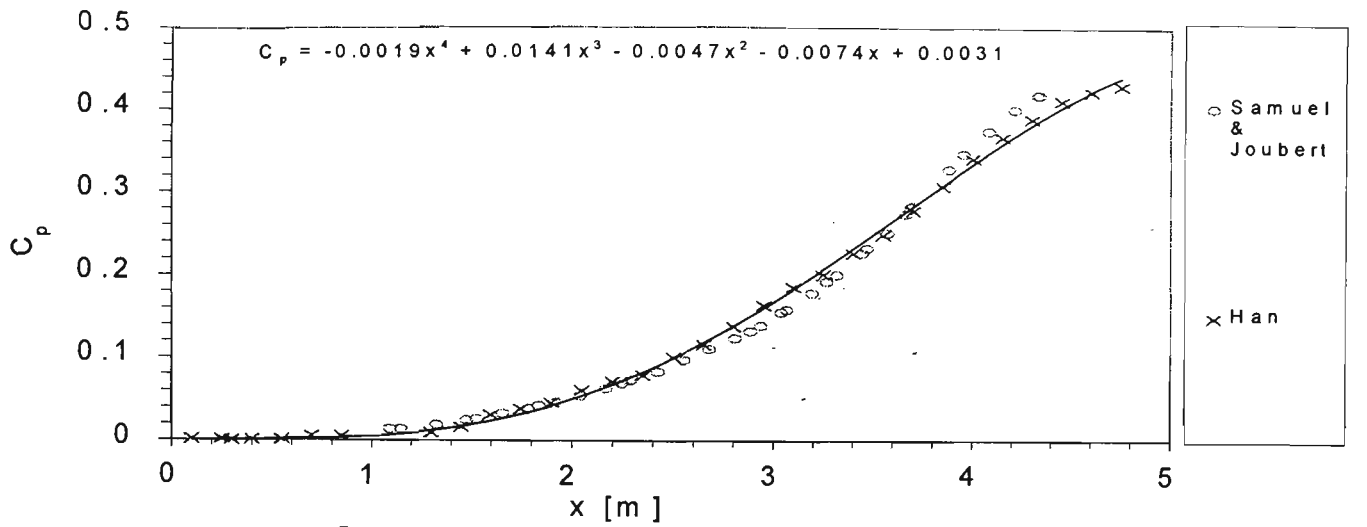
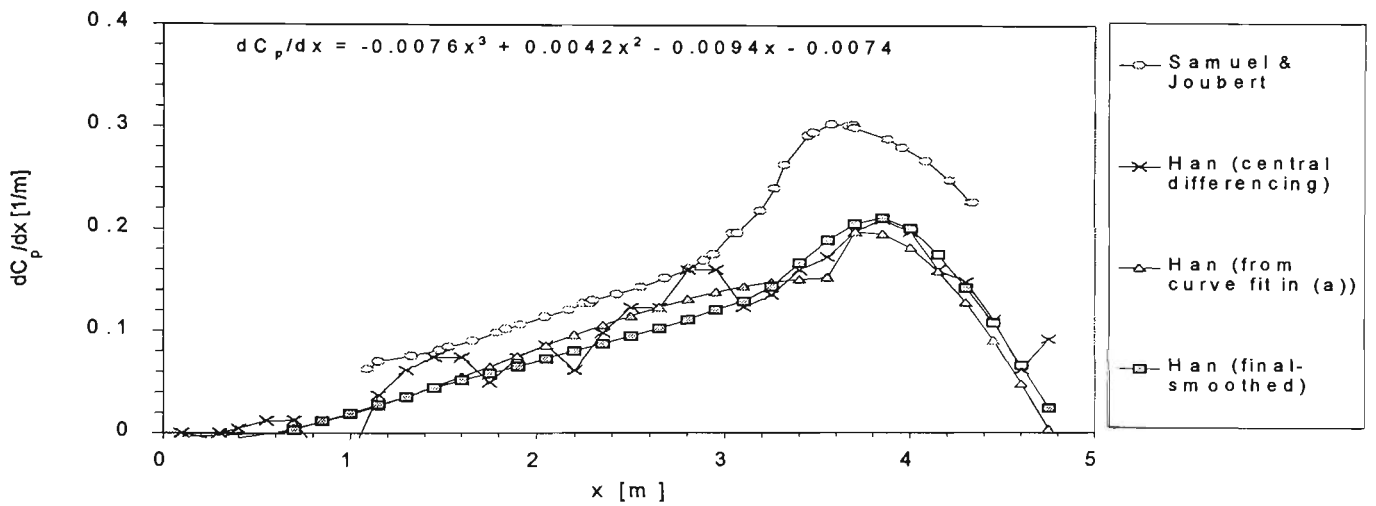


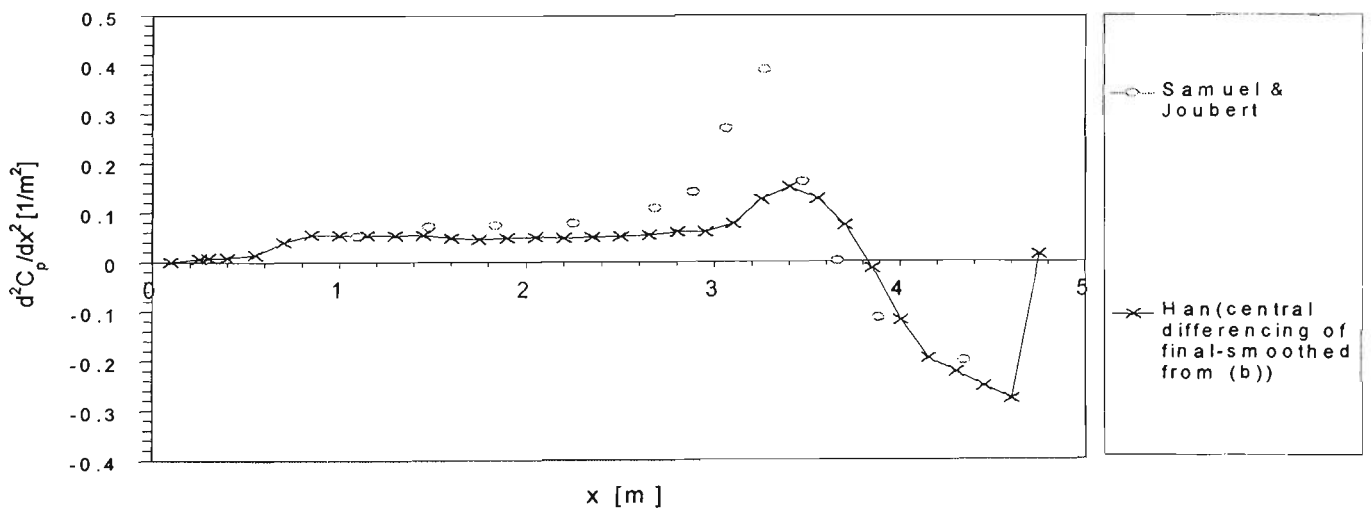
Figure 4.1 Flexible top shape.



(a)



(b)



(c)

Figure 4.2 (a) Wall static pressure coefficient, and its (b) first and (c) second streamwise derivatives.

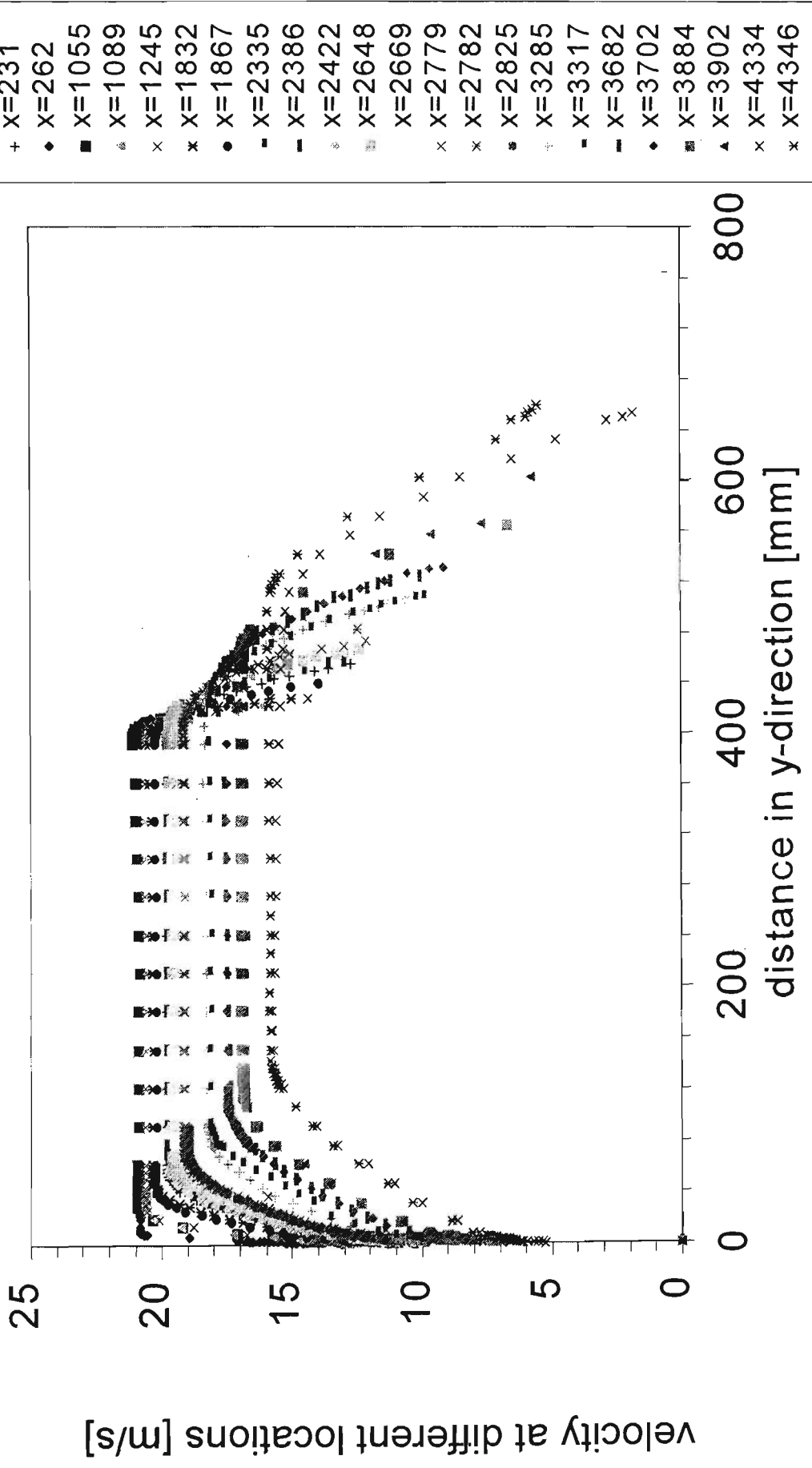
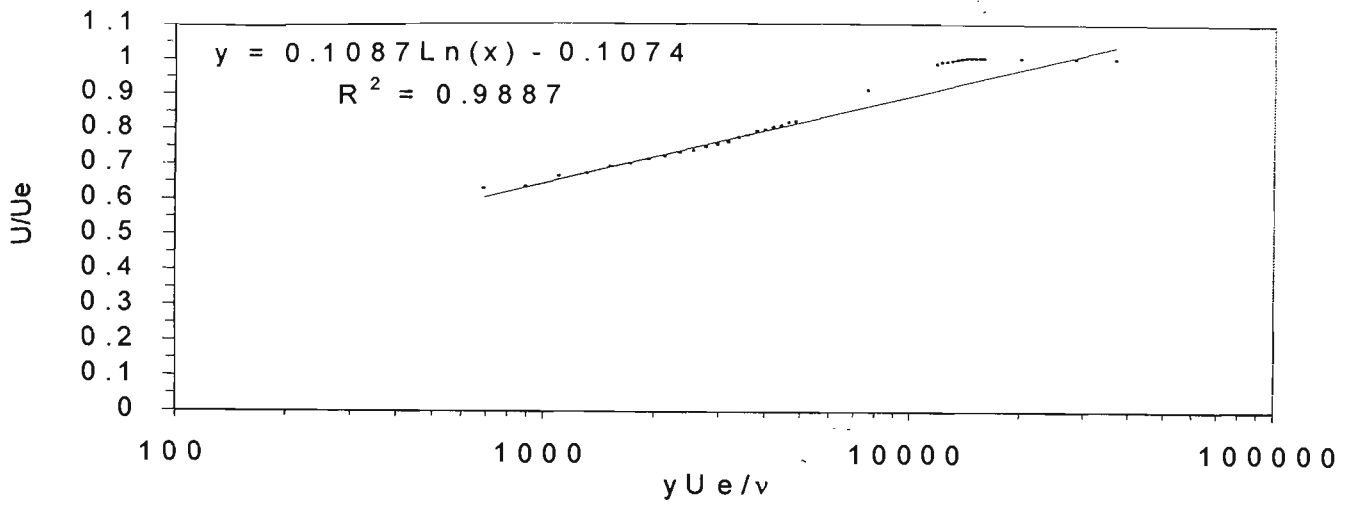
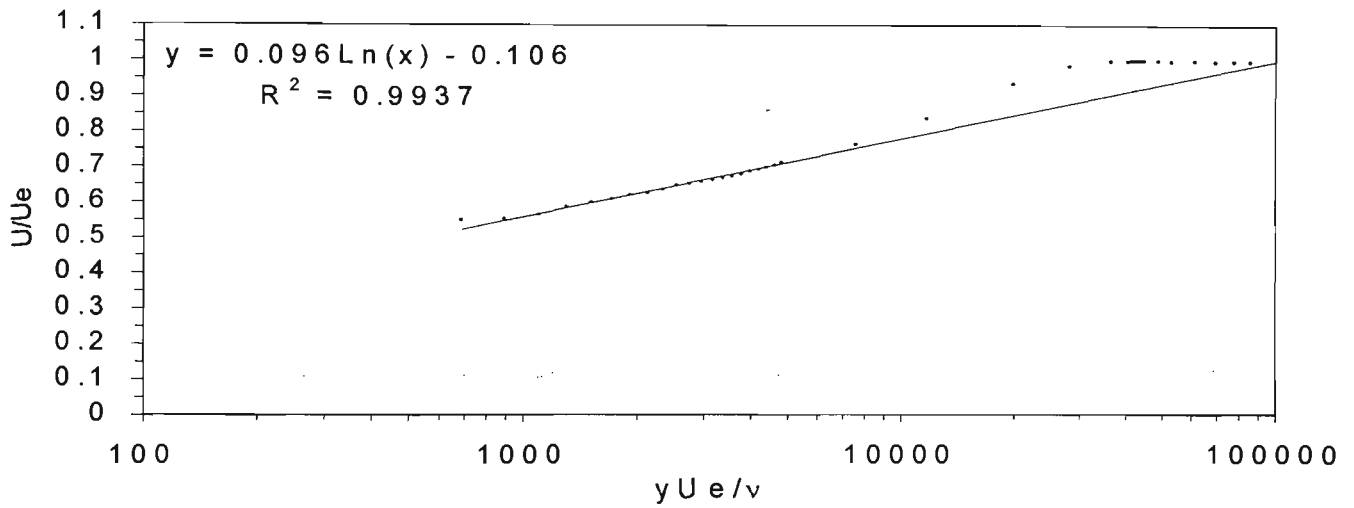


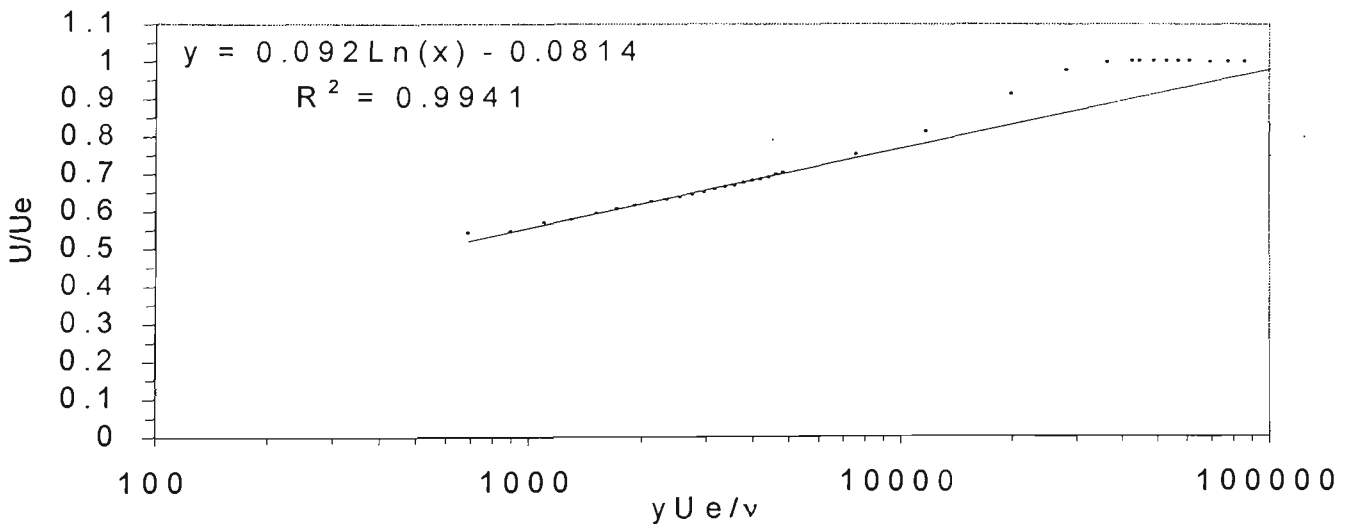
Figure 4.3 Mean velocity measurements.



(a) $x = 0.26$ m.

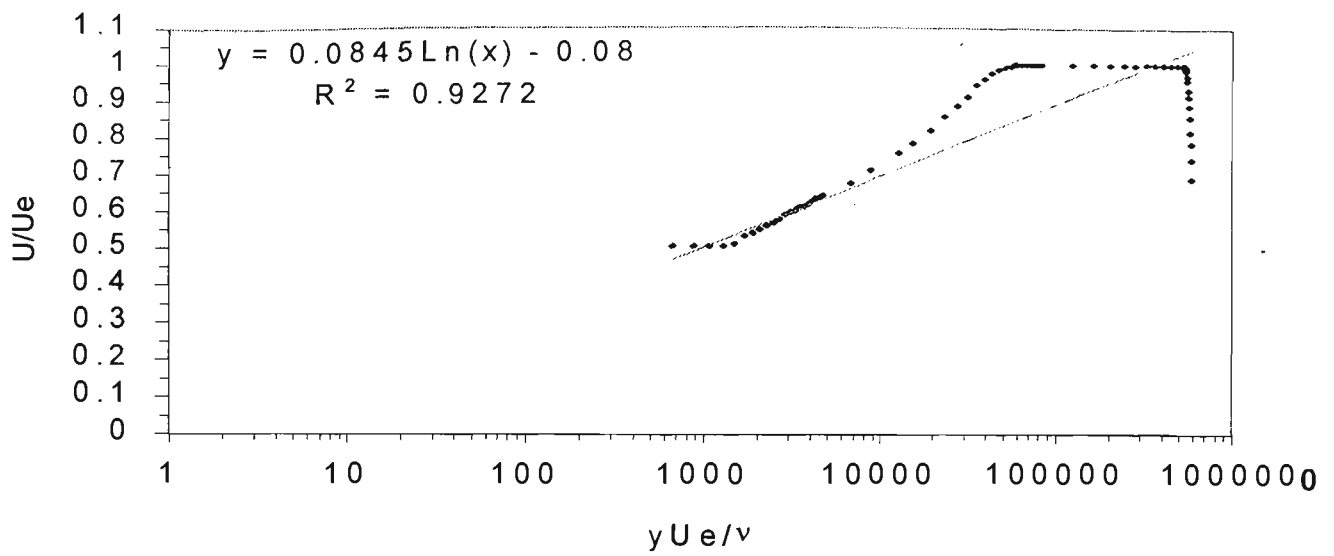


(b) $x = 1.09$ m.

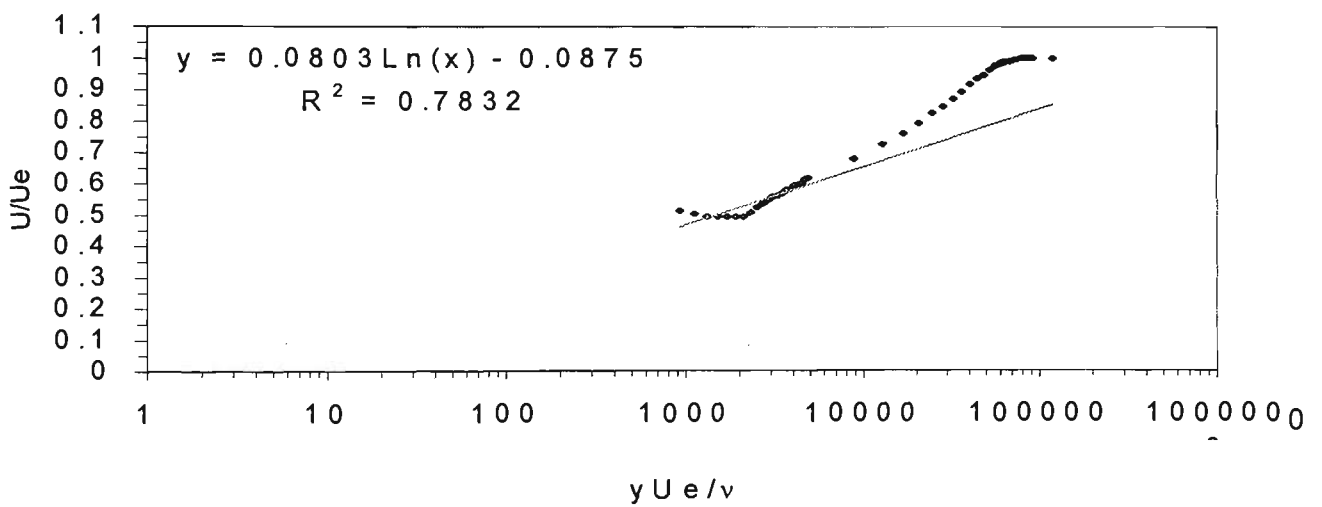


(c) $x = 1.25$ m.

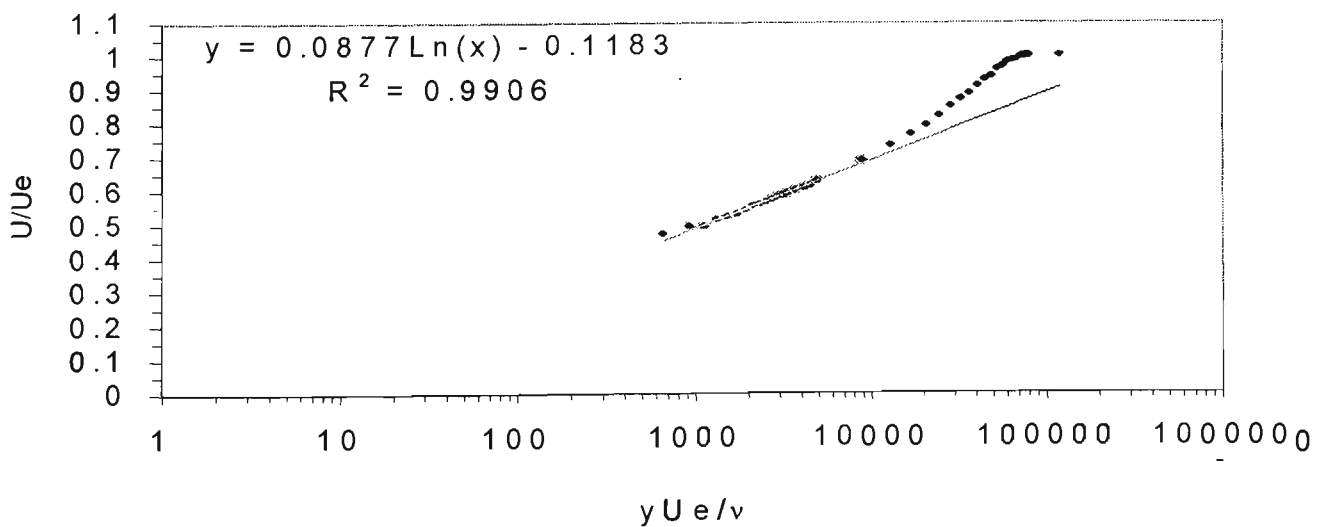
Figure 4.4 Clauser plots. In the equation given in each frame, $y = U/U_e$ and $x = yU_e/\nu$. R represents the goodness of fit for the given logarithmic expression.



(d) $x = 1.87$ m.

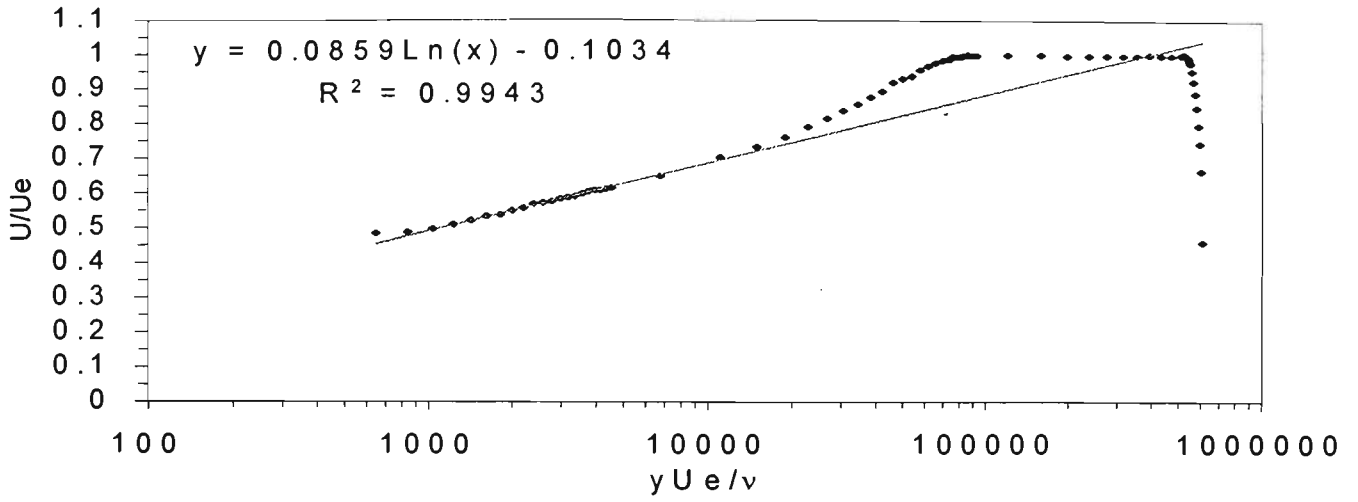


(e) $x = 2.34$ m.

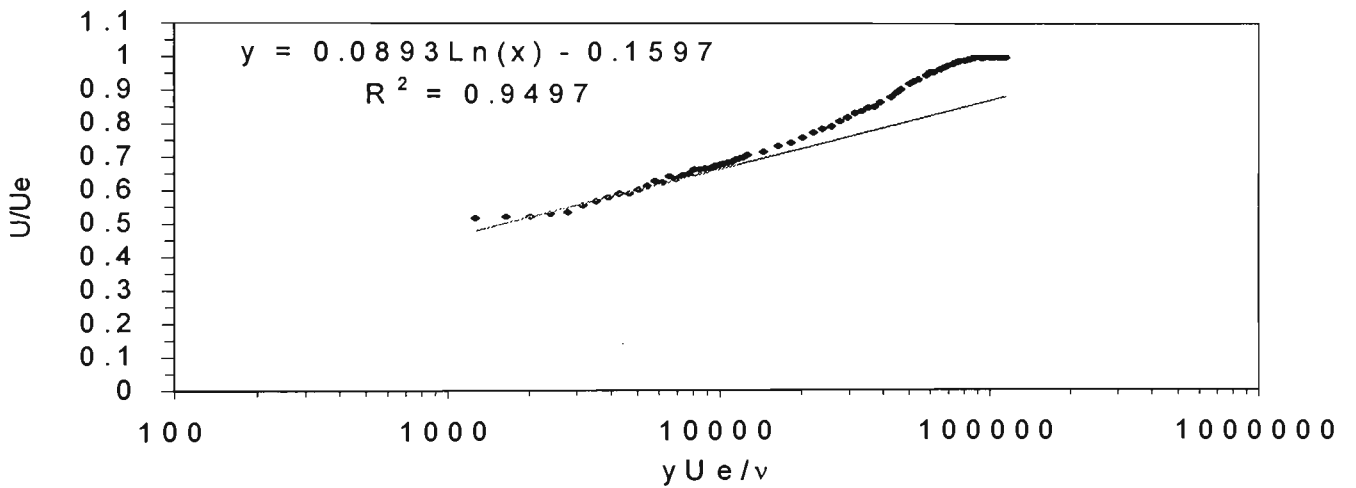


(f) $x = 2.42$ m.

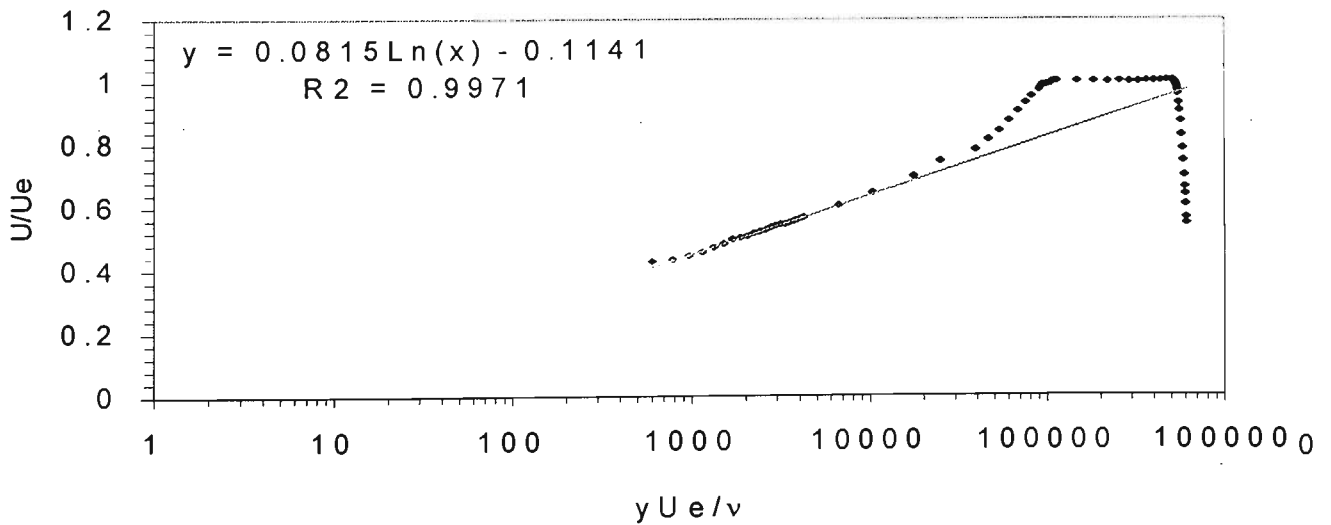
Figure 4.4 Clouser plots. In the equation given in each frame, $y = U/U_e$ and $x = yU_e/\nu$. R represents the goodness of fit for the given logarithmic expression.



(g) $x = 2.67$ m.

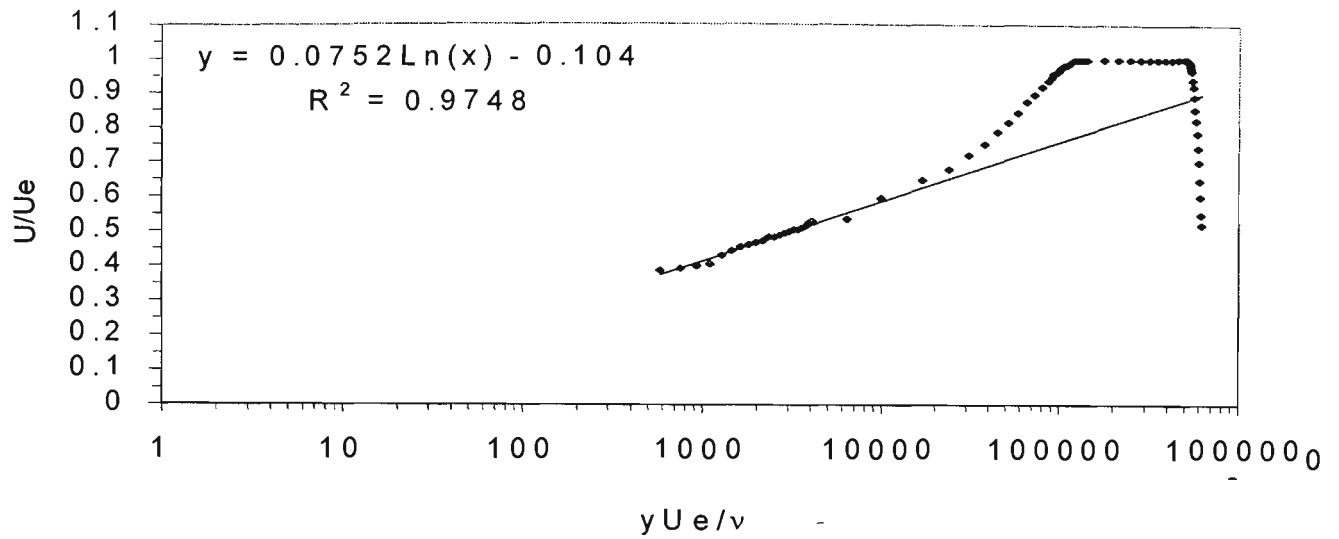


(h) $x = 2.83$ m.

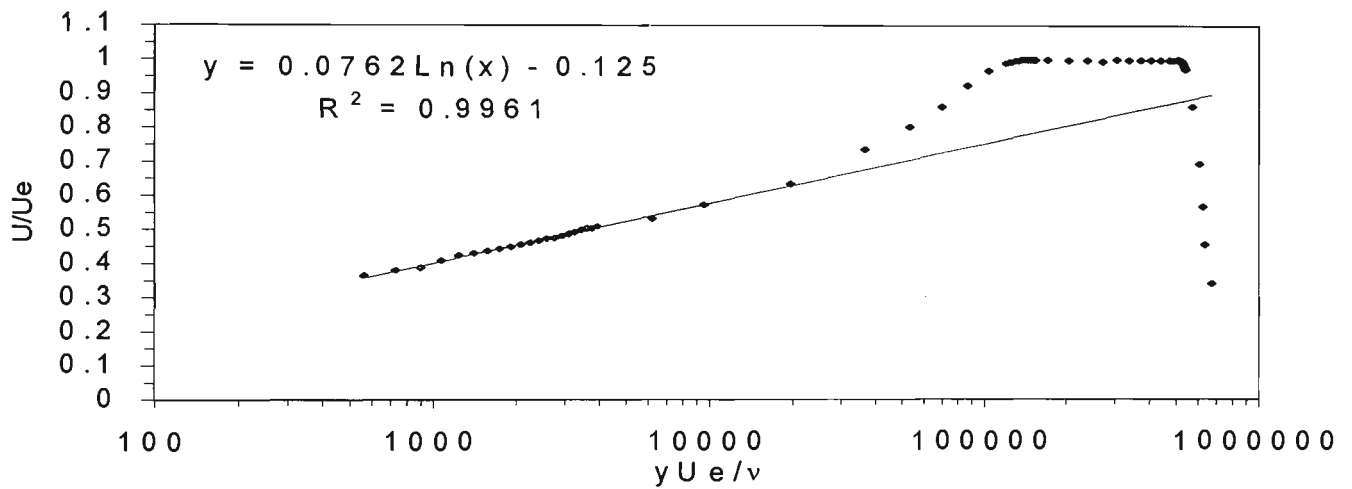


(i) $x = 3.32$ m.

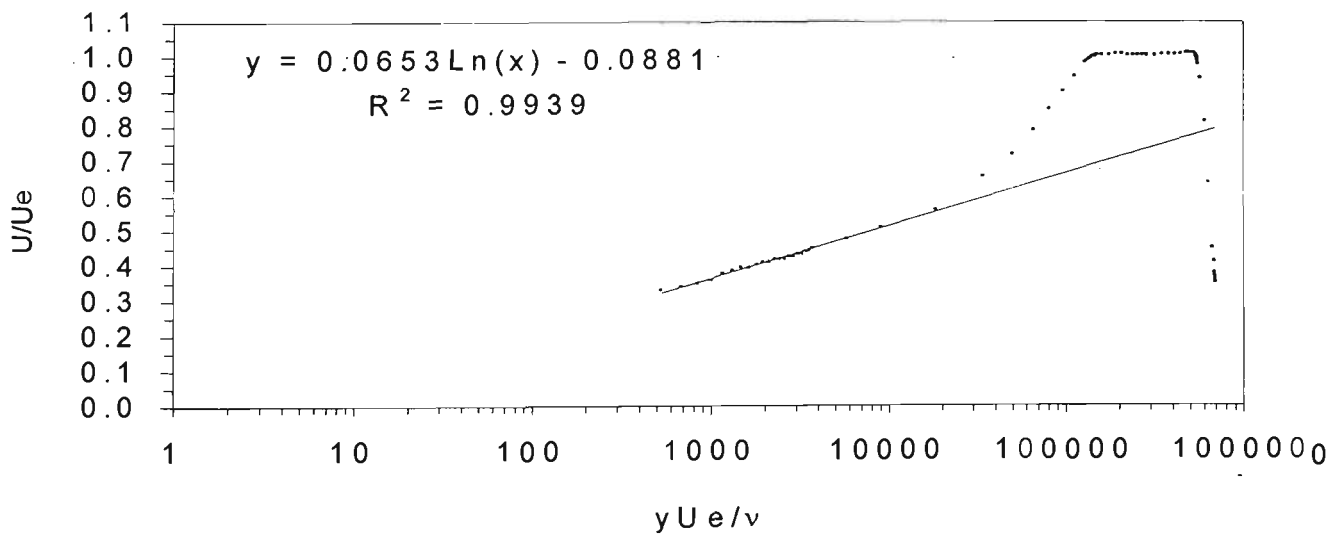
Figure 4.4 Clouser plots. In the equation given in each frame, $y = U/U_e$ and $x = yU_e/\nu$. R represents the goodness of fit for the given logarithmic expression.



(j) $x = 3.70$ m.



(k) $x = 3.90$ m.



(l) $x = 4.35$ m.

Figure 4.4 Clauser plots. In the equation given in each frame, $y = U/U_e$ and $x = yU_e/\nu$. R represents the goodness of fit for the given logarithmic expression.

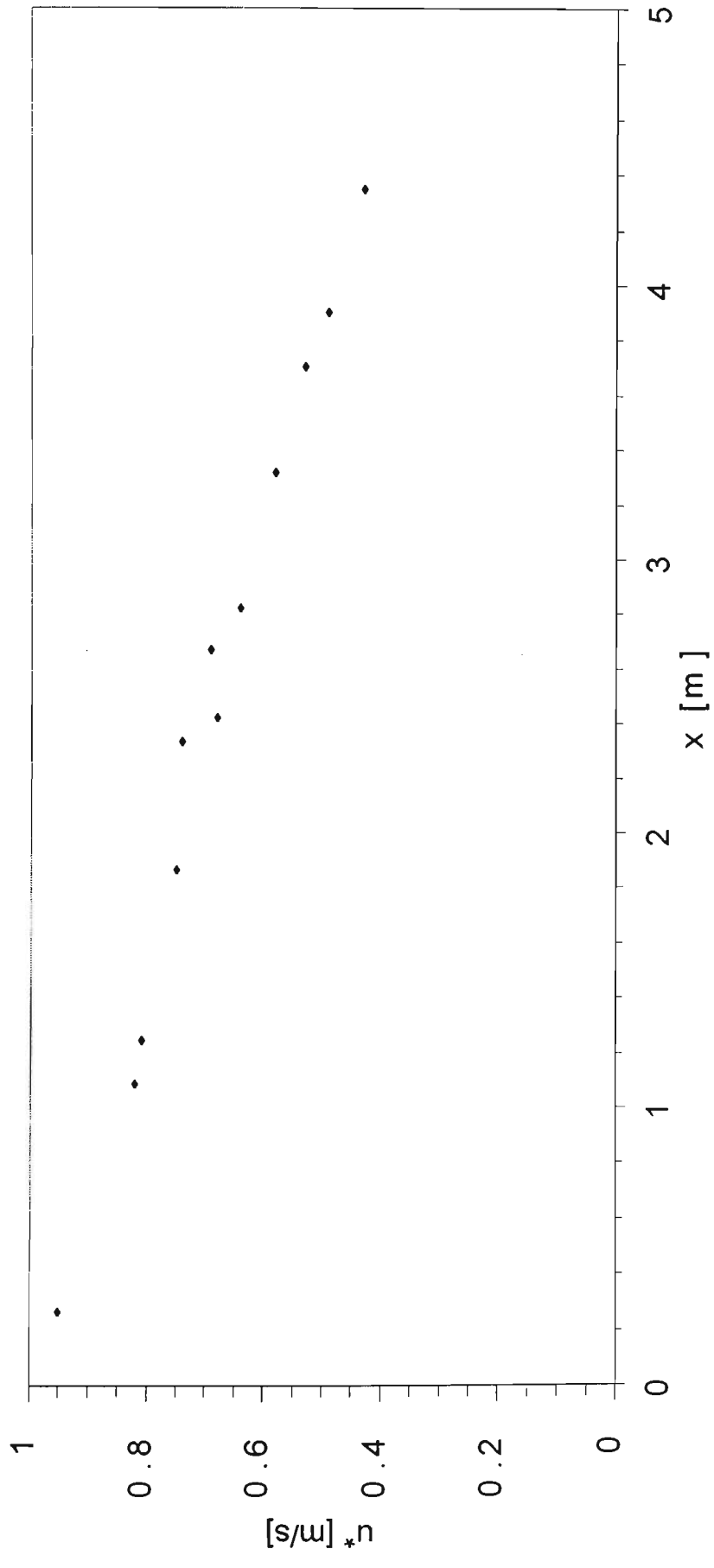
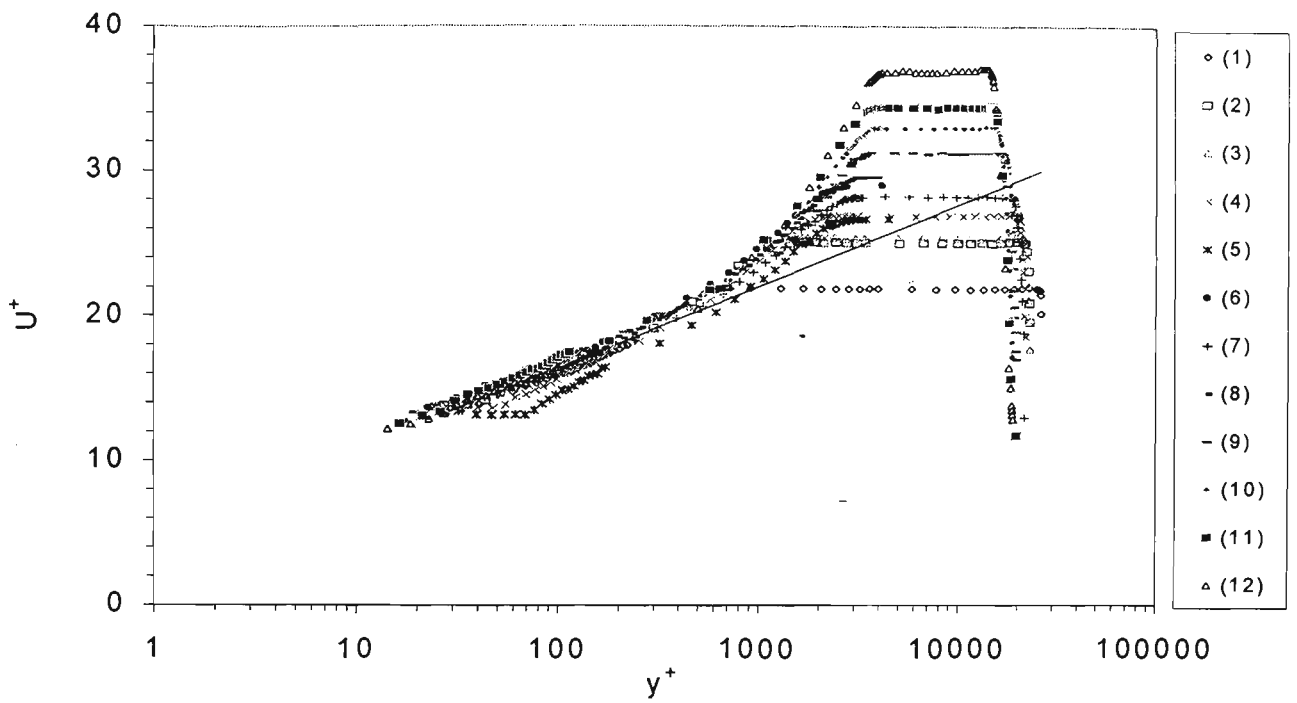
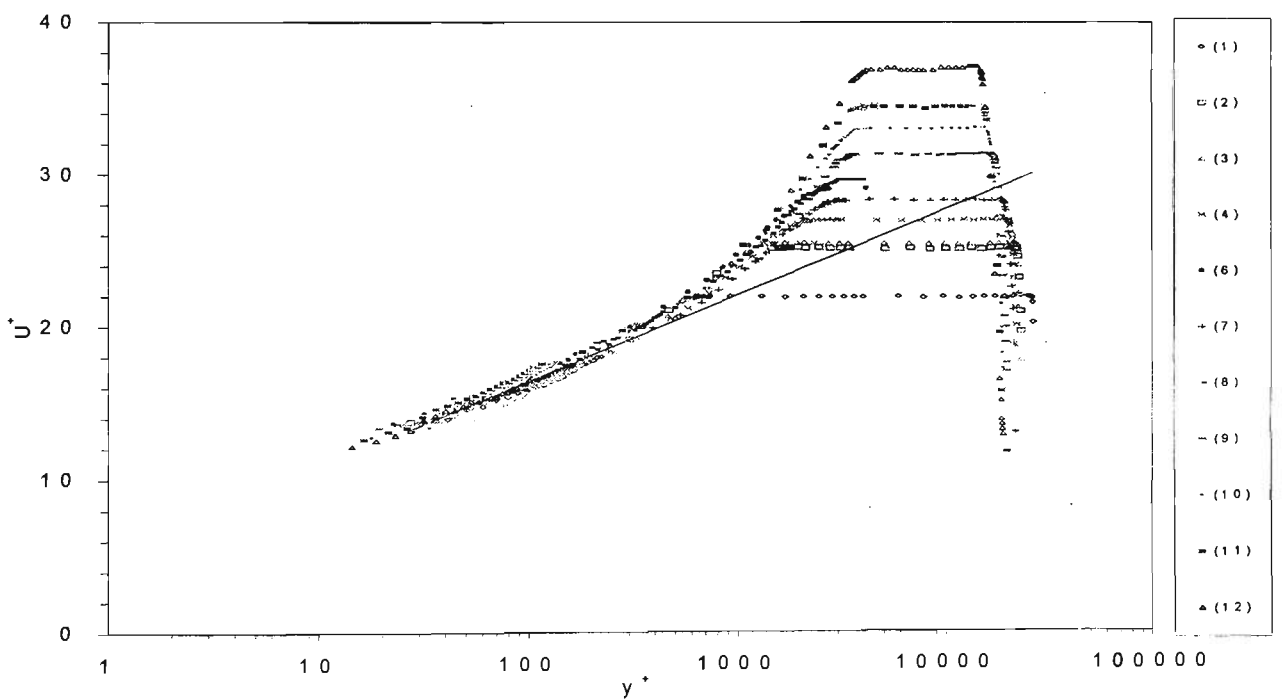


Figure 4.5 Streamwise distribution of the friction velocity.



(a)



(b)

Figure 4. 6 Logarithmic law. (a) Mean velocity profiles in semi-logarithmic scale at all the stations. (b) Same as in (a) excluding data from $x = 2.34$ m. Stations 1 to 12 correspond to 0.26, 1.09, 1.25, 1.87, 2.34, 2.42, 2.67, 2.83, 3.32, 3.70, 3.90, 4.35 m from the inlet, respectively. The straight line represent $U/u_* = 1/\kappa \ln(yu_*/\nu) + 5.2$, where $\kappa = 0.41$.

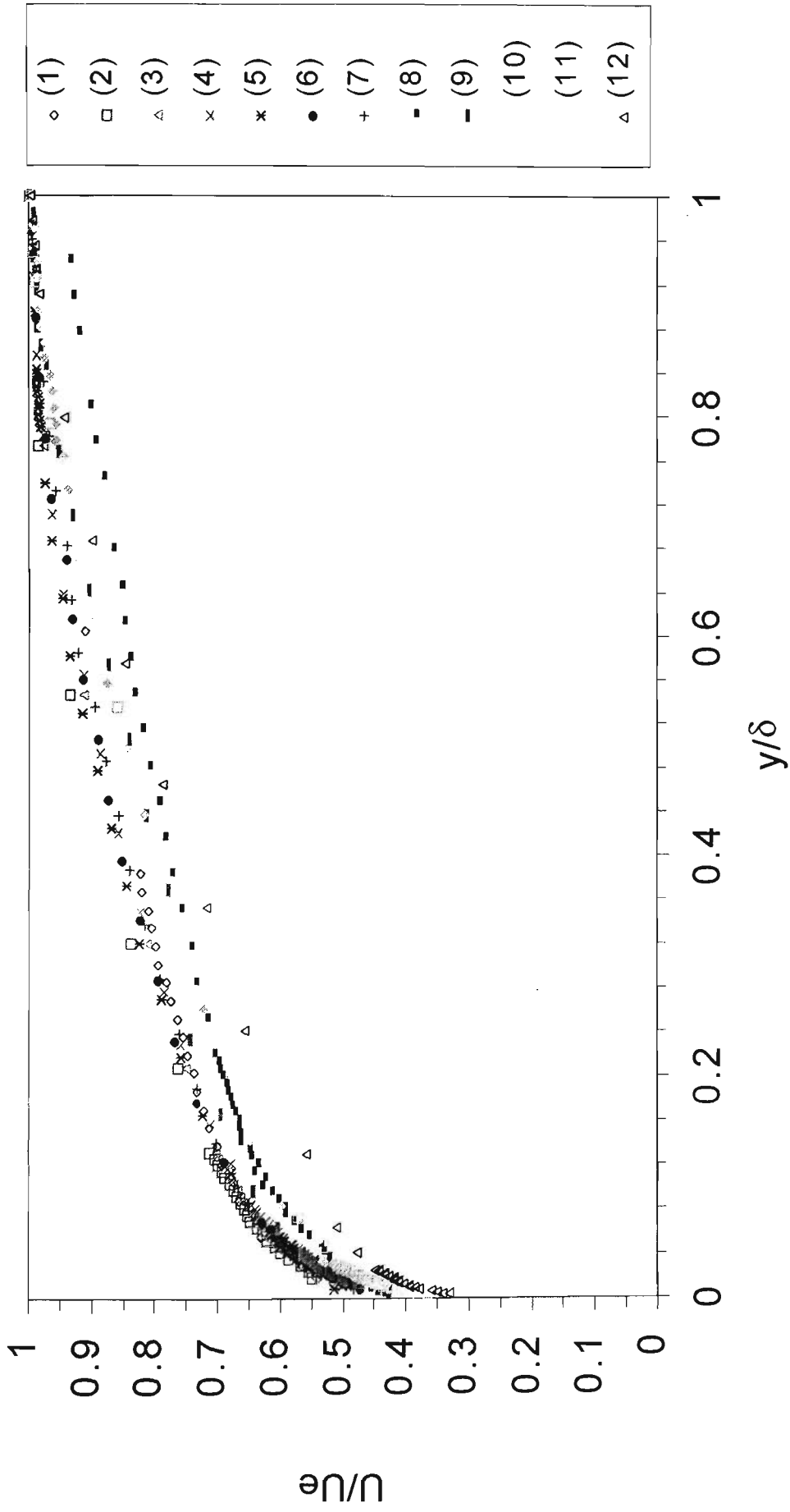


Figure 4.7 Mean velocity profiles with outer scaling. Stations 1 to 12 correspond to 0.26, 1.09, 1.25, 1.87, 2.34, 2.42, 2.67, 2.83, 3.32, 3.70, 3.90, 4.35 m for the inlet, respectively.

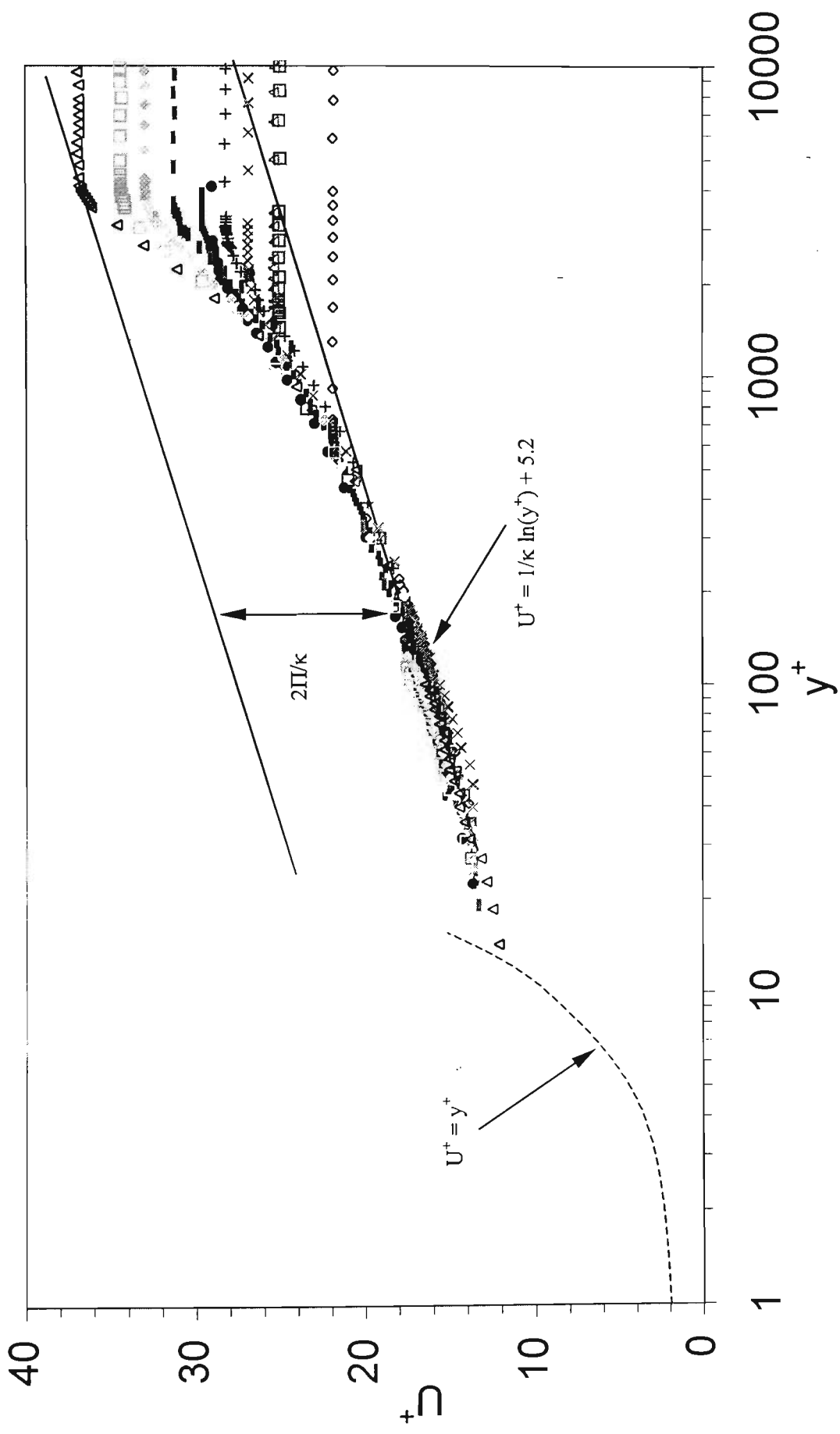


Figure 4.8 Wake strength, Π

Chapter 5. SIMILARITY OF ADVERSE PRESSURE GRADIENT BOUNDARY LAYERS AND HALF-POWER LAWS

5.1 Introduction

In this chapter, the experimental mean velocity data from eleven adverse pressure gradient turbulent flows, including the data presented in Chapter 4, are used to assess the presence of half-power regions. Flows 1100, 1200, 2900, 5000 and 5100 are from the 1968 AFOSR-IFP-Stanford Conference (Coles and Hirst, 1968) and Flows 141, 142, 143 are from the 1980-81 AFOSR-HTTM-Stanford Conference (Kline et al., 1981). An eight-degree conical diffuser flow, referred here as Flow 8-degree, from Turan (1988), Kassab (1986) and Ozimek (1985), is also used. An equilibrium boundary layer flow is taken from Skåre (1994). Flow Han represents the increasing adverse pressure gradient flow described in Chapter 4, that is similar to Flow 141.

5.2 Brief Description of the Eleven Adverse Pressure Gradient Flows

Flows 1100, 1200, 2900, 141, Skåre and Han are plane diffuser flows. Flows 5000, 5100, 142, 143 and 8-degree are conical diffuser flows. Two of the plane diffusers, Flow 141 and Han, have increasing adverse pressure gradients, and the rest of the flows have decreasing adverse pressure gradients except for a short region at their entrances. The diffuser flows have either a developing channel (or boundary layer) or pipe flow at their inlet, except for the eight-degree conical diffuser which has a fully-developed pipe flow at its inlet. In Figures 5.1 to 5.11, the mean velocity profiles are plotted of these eleven flows. Figures (a), (b) and (c), respectively, in each figure represent the profiles of

U^+ against y^+ , U^+ against $(y/\delta)^{1/2}$ and U/U_e against $(y/\delta)^{1/2}$. These mean velocity profiles are discussed further both in this section, following the description of the pressure gradient behaviours of these flows next, and in Sections 5.3 and 5.4 to follow.

5.2.1 Pressure Parameter, Δ

In Figure 5.12, the pressure parameter, $\Delta = \frac{\alpha v}{u_*^3}$, distribution in the streamwise direction is presented for each of these flows. As seen in Figure 5.12 (a), all five of the conical diffuser flows, Flows 142, 143, 5000, 5100 and 8-degree, have higher values of the pressure parameter than the remaining plane diffuser flows. In order to examine the Δ distribution for the plane diffuser flows, Figure 5.12 (b) has been prepared by zooming in to the region $0 \leq \Delta \leq 0.05$ in Figure 5.12 (a). As seen in 5.12 (b), Flows 1100, 1200 and Han have similar streamwise distributions of Δ , and $\Delta < 0.005$ mostly for these flows. Although Flow 141 also starts out to be similar to this group, Δ increases more rapidly to 0.01. For Flow Skåre, Δ varies between 0.01 and 0.015. For Flow 2900, the Δ behaviour is in between those of flat and conical diffusers.

Δ exceeds 0.02 for all stations of Flow 8-degree, and for some stations of Flows 5000, 5100, 142 and 143. For these conical diffuser flows, the logarithmic law region shortens with increasing Δ , as expected (Kader and Yaglom, 1978). This behaviour can be observed in Figures 5.4 (a), 5.5 (a), 5.7 (a), 5.8 (a) and 5.9 (a). In addition, in the case

of Flow 8-degree, the logarithmic law region disappears close to the diffuser inlet at $x = 0.06$ m to reappear at $x = 0.18$ m (Turan et al., 1987).

5.2.2 Kinematic Pressure Gradient, α

The kinematic pressure gradient, $\alpha = \left(\frac{1}{\rho}\right)\frac{dP}{dx}$, is plotted against streamwise distance, x in Figure 5.13 for the eleven flows. As illustrated in Figure 5.14, three different kinds of α behaviour is shown in Figure 5.13. Most flows with decreasing adverse pressure gradients, specifically, Flows 1100, 2900, 5000, 5100, 142, 143, 8-degree, and Skåre, have the concave up shape shown in Figure 5.14 (a). The concave down shape shown in Figure 5.14 (b) is also for decreasing adverse pressure gradient cases. Among the flows considered in this thesis, only Flow 1200 has this behaviour. Flows 141 and Han are increasing adverse pressure gradient flows. These two flows have the increasing concave up shape shown in the Figure 5.14 (c).

5.2.3 Further Flow Characteristics

Flow 1100 is Ludwig and Tillmann's boundary layer in "mild" adverse pressure gradient. 12 profiles given in Figure 5.1 are from a diverging channel. The Reynolds number of the flow is 2.2×10^6 m^{-1} , defined as the reference velocity divided by kinematic viscosity. Flow 1200 is a boundary layer in "strong" adverse pressure gradient, as defined by Ludwig and Tillmann. As seen in Figure 5.13 (b), the kinematic pressure gradient, α , is higher than that of Flow 1100, although the pressure parameter, Δ , values

are similar for $x < 5$ m. The experimental data of Flow 1200 are from 10 stations with eventual separation in the diverging channel. These profiles are presented in Figure 5.2. The Reynolds number of this flow is the same as that of Flow 1100.

Flow 2900 is Perry's boundary layer at the entrance in a straight-walled diffuser. 10 velocity profiles are available, as shown in Figure 5.3. The Reynolds number of this flow is $2.5 \times 10^6 \text{ m}^{-1}$. Flows 5000 and 5100 are from Fraser's 10-degree conical diffuser. 11 and 12 profiles are available, respectively, as shown in Figures 5.4 and 5.5. The Reynolds numbers are $3.3 \times 10^6 \text{ m}^{-1}$ and $3.6 \times 10^6 \text{ m}^{-1}$, respectively.

Flow 141 is Samuel and Joubert's increasingly adverse pressure gradient flow in a return circuit boundary-layer tunnel. The test section had a $1 \text{ m} \times 0.36 \text{ m}$ inlet with a 3.5 m long region of a flexible roof in the streamwise direction. The Reynolds number was kept at $1.7 \times 10^6 \text{ m}^{-1}$. The data were collected at 12 stations. These profiles are presented in Figure 5.6.

Flow 142 is Pozzorini's low-core turbulence flow in a 6-degree conical diffuser with an area ratio of 4. With the thin boundary layer at the inlet, the potential core extended to the exit of the diffuser. The Reynolds number of this flow was $2.7 \times 10^6 \text{ m}^{-1}$. 10 profiles are available for this flow, as shown in Figure 5.7. Flow 143 is Pozzorini's high-core turbulence flow in the same 6-degree conical diffuser as Flow 142 with a developing boundary layer. The Reynolds number is $1.2 \times 10^6 \text{ m}^{-1}$. 5 velocity profiles are plotted in Figure 5.8 from this flow.

The Reynolds number of the 8-degree conical diffuser flow is $1.4 \times 10^6 \text{ m}^{-1}$, and the data are from 6 stations. These profiles are presented in Figure 5.9. Skåre's flow is an equilibrium boundary layer in strong adverse pressure gradient. The skin friction coefficient was kept low at a constant level in a closed return wind tunnel. The inlet cross section was $1.40 \text{ m} \times 0.28 \text{ m}$ with a 6 m long region of an adjustable roof in the streamwise direction. The Reynolds number was $1.6 \times 10^6 \text{ m}^{-1}$ with a reference velocity of 23.6 m/s. 12 profiles of the data are considered in this chapter, as shown in Figure 5.10. Equilibrium was established for $4 \text{ m} \leq x \leq 5 \text{ m}$. Within this region, the skin friction coefficient was kept as low as $0.5 \times 10^{-3} < C_f < 0.6 \times 10^{-3}$ with an almost constant value of the shape factor, $H \sim 2.0$, $H = \frac{\delta^*}{\theta}$, where δ^* and θ are the displacement and momentum thicknesses, respectively.

Flow Han is an increasing adverse pressure gradient flow that is similar to Flow 141, as discussed in Chapter 4. The test section dimensions are $0.9 \text{ m} \times 0.9 \text{ m} \times 4.5 \text{ m}$ long, as stated in Chapter 3. Similar to Flow 141, the test section is equipped with a flexible top to generate different pressure gradients on the boundary layer developing over the false bottom. The false bottom refers to the raised plywood floor in the test section on which 32 static pressure taps exist to monitor the static pressure change along the bottom wall, as described in detail in Chapter 3. The Reynolds number is $1.4 \times 10^6 \text{ m}^{-1}$.

5.3 Log-Law Profiles

From the semi-logarithmic plots in Figures 5.1 to 5.11 parts (a), it can be seen that none of the flows has as full a collapse of the velocity profiles throughout the flow as Skåre's (Skåre, 1994). In fact, in obtaining Skåre's experimental mean velocity data, the values corresponding to $x = 4$ m are used only in the present thesis. Therefore, Figure 5.10 (a) does not show his experimental scatter. The 8-degree conical diffuser flow profiles given in Figure 5.9 show reasonable collapse up to about $y^+ = 100$, then they start to separate. The experimental data of the last station of the 8-degree conical diffuser flow do not show a logarithmic law intercept similar to that of other stations. This result may be due to this station's being too close to the exit of the diffuser, and consequently, the measurements being affected by possible back-flow. Another reason for this behaviour may be the high value of Δ as discussed previously in Section 5.2.1. Flows 1100, 1200, 2900, 141 and Han show collapse of the velocity profiles up to about $y^+ = 1000$, Flows 142 and 143 up to about $y^+ = 300$, and Flows 5000 and 5100 up to about $y^+ = 100$ before the profiles started to separate. As in Chapter 4, the following form of the logarithmic law is used here:

$$U^+ = \frac{1}{\kappa} \ln y^+ + B, \text{ where } \kappa = 0.41.$$

$B = 5.2$ for Flows 1100, 1200, 2900, 5000, 5100, 141, Skåre and Han. $B = 3.0$ for Flow 142, $B = 4.0$ for Flow 143 and $1 \leq B \leq 4.4$ for Flow 8-degree.

5.4 Half-Power Profiles

The U^+ against $(y/\delta)^{1/2}$ plots in parts (b) of Figures 5.1 to 5.11 show a behaviour similar to that of the log-law plots. $(y/\delta)^{1/2}$ scale opens up the horizontal axis away from the wall. Hence, the separation in the outer layer can be seen more clearly than in the log-law plots. In parts (c) of Figures 5.1 to 5.11, the half-power development in the eleven flows is seen more clearly from the U/U_e against $(y/\delta)^{1/2}$ plots than from parts (b) of the same figures. It has been observed that there are two regions at each measuring station where the mean velocity varies with the square root of the distance from the wall, namely, an inner half-power region and an outer half-power region (Kopp and Turan, 1992).

The inner half-power profile is defined as follows:

$$\frac{U}{u_*} = \frac{C_i}{u_*} \sqrt{\frac{y}{\delta}} + \frac{D_i}{u_*}, \quad (5.1)$$

The outer half-power profile is given as follows:

$$\frac{U}{U_e} = \frac{C_o}{U_e} \sqrt{\frac{y}{\delta}} + \frac{D_o}{U_e}. \quad (5.2)$$

In Equations 5.1 and 5.2, C_i and C_o are the gradients and D_i and D_o are the intercepts of the inner and outer half power expressions, respectively. The inner and outer regions are shown by straight lines in the half-power plots, parts (c) of Figures 5.1 to 5.11. In Appendix C, a procedure is given to describe how these lines are drawn to extract C_i , D_i , C_o and D_o from experimental data.

5.5 Half Power Slopes and Intercepts: C_i , D_i , C_o and D_o

The intercepts of the inner and outer regions of Flows 1100, 141, 143 and Han are all greater than zero. The intercepts of the outer regions of the other flows start from greater than zero, and then, they become negative. The two straight line regions first form a concave down overall pattern initially at the inlet of the flows ($C_i > C_o$ where $D_i < D_o$). Then, this pattern changes to concave up while the flow develops ($C_i < C_o$ where $D_i > D_o$). The change occurs mostly at a U^+ of about 20 ± 5 .

In Figures 5.15 to 5.18, the half-power slopes and intercepts of the eleven flows are plotted. In Figures 5.15 and 5.16, respectively, the inner half-power parameters, C_i and D_i , are presented. The following form of Equation 5.1 is used for this purpose:

$$\left[\frac{\frac{U}{u_*}}{\frac{\sqrt{\alpha\delta}}{u_*}} = \frac{\frac{C_i}{u_*}}{\frac{\sqrt{\alpha\delta}}{u_*}} \left(\frac{y}{\delta} \right)^{\frac{1}{2}} + \frac{\frac{D_i}{u_*}}{\frac{\sqrt{\alpha\delta}}{u_*}} \right] \quad (5.3)$$

$$\Rightarrow \frac{U}{\sqrt{\alpha\delta}} = \frac{C_i}{\sqrt{\alpha\delta}} \left(\frac{y}{\delta} \right)^{\frac{1}{2}} + \frac{D_i}{\sqrt{\alpha\delta}}.$$

The reason for this choice of scaling was to better reflect the effect of the pressure gradient on the inner half power region. Hence, $\frac{C_i}{\sqrt{\alpha\delta}}$ and $\frac{D_i}{\sqrt{\alpha\delta}}$ are plotted against

$\frac{u_*}{\sqrt{\alpha\delta}}$ in Figures 5.15 and 5.16, respectively, for the eleven flows examined here. As

indicated in Section 5.7, u_* is the expected velocity scale for the inner half power region, since it coincides with the inertial sublayer. The data from all flows collapse onto the

following straight lines within 97 % and 99 % confidence limits, respectively, for

$$C_i/\sqrt{\alpha\delta} \text{ and } D_i/\sqrt{\alpha\delta}.$$

$$\frac{C_i}{\sqrt{\alpha\delta}} = m_1 \frac{u_*}{\sqrt{\alpha\delta}} + b_1, \quad (5.4)$$

where $m_1 = 15.278$ and $b_1 = 1.518$, and

$$\frac{D_i}{\sqrt{\alpha\delta}} = m_2 \frac{u_*}{\sqrt{\alpha\delta}} + b_2 \quad (5.5)$$

where $m_2 = 12.568$ and $b_2 = -0.133$.

In Figures 5.17 and 5.18, respectively, the outer half-power parameters, C_o and D_o , are plotted. Equation 5.2 is used in the following form for this purpose:

$$\left[\frac{\frac{U}{U_e}}{\left(\frac{U_e}{u_*}\right)^{-1}} = \frac{\frac{C_o}{U_e}}{\left(\frac{U_e}{u_*}\right)^{-1}} \left(\frac{y}{\delta}\right)^{\frac{1}{2}} + \frac{\frac{D_o}{U_e}}{\left(\frac{U_e}{u_*}\right)^{-1}} \right] \quad (5.6)$$

$$\Rightarrow \frac{U}{u_*} = \frac{C_o}{u_*} \left(\frac{y}{\delta}\right)^{\frac{1}{2}} + \frac{D_o}{u_*}.$$

The reason for using this form is the expectation that the outer half power region merges into the velocity defect law which scales with u_* as $(U_e-U)/u_*$, as indicated in Equation

2.7. Hence, in Figures 5.17 and 5.18, respectively, C_o/u_* and D_o/u_* are plotted against

U_e/u_* . For the eleven flows studied here, the data collapse onto the following straight

lines within 99 % and 96 % confidence limits, respectively, for C_o/u_* and D_o/u_* .

$$\frac{C_o}{u_*} = m_3 \frac{U_e}{u_*} + b_3, \quad (5.7)$$

where $m_3 = 2.056$ and $b_3 = -44.215$, and

$$\frac{D_o}{u_*} = m_4 \frac{U_e}{u_*} + b_4, \quad (5.8)$$

where $m_4 = -0.921$ and $b_4 = 41.135$.

In Figure 5.19, the half-power expressions developed in this section, namely, Equations 5.4, 5.5 and 5.1 for the inner half power, and Equations 5.7, 5.8 and 5.2 for the outer half-power profiles are compared with the experimental data from the 11 flows examined here. In general, the predicted velocity profiles given by the straight lines follow the experimental trends, except for Flows 143 and 8-degree as shown in Figures 5.19 (h) and (i). This result is explained next based on the moving equilibrium behaviour.

5.6 Moving Equilibrium

In Figure 5.20, $U_e/\sqrt{\alpha\delta}$ is plotted against U_e/u_* to examine Kader and Yaglom's (1978) moving equilibrium concept. Moving equilibrium indicates that both the free stream velocity, U_e , and kinematic pressure gradient, α , change slowly with x .

Consequently, the flow adjusts to these changes, and its structure depends mainly on the relevant local parameters rather than their upstream history.

When plotted in this form, the data from the 11 flows considered here collapse onto one curve, with the exception of the last two stations of Flow 1200, and Flows 143 and 8-degree. For the remaining flows, for $U_e/u_* > 30$, $6 \leq U_e/\sqrt{\alpha\delta} \leq 7$ condition is reached, as seen in Figure 5.20. In this region, $U_e/\sqrt{\alpha\delta}$ becomes almost constant, and this is the region where the data from Flow Skåre, an equilibrium boundary layer flow, are located. Hence, in agreement with Kader and Yaglom (1978)'s assertion, that $U_e/\sqrt{\alpha\delta} < 6.3$ corresponds to loss of moving equilibrium, the mean velocity profiles of Flows 143 and 8-degree were not predicted with the half-power profiles in Figure 5.19. Therefore, it is expected that Equations 5.4, 5.5, 5.7 and 5.8 can be used when $U_e/\sqrt{\alpha\delta} > 6$.

In the case of Flow 143, the high core turbulence may be the reason for the lack of moving equilibrium. In the case of Flow 8-degree, both the high values of the pressure parameter, Δ , and the different inlet conditions can be the reason for the different behaviour observed in Figures 5.19 and 5.20. Amongst the 11 flows examined here, flow 8-degree is the only one with a fully-developed inlet.

Flow 1200 has a pattern different than all other flows in Figure 5.20, in the sense that $U_c/\sqrt{\alpha\delta}$ starts to increase for $U_c/u_* > 30$. Only three data points are available in this range. Hence, although it is suspected that the unique α behaviour shown in Figure 5.14 (b) may be the reason for the different pattern of Flow 1200, it is not possible to conclude further. The predicted half-power profiles fit Flow 1200 data not differently than other flows. Since $U_c/\sqrt{\alpha\delta} > 7$, this flow is expected to be in moving equilibrium.

5.7 Length Scales

Through dimensional analysis, Kader and Yaglom (1978) proposed the following three universal functions, Φ_1 to Φ_3 , to represent the mean velocity gradient, dU/dy , for an arbitrary value of α :

$$\frac{dU}{dy} = \frac{u_*}{y} \Phi_1 \left(\frac{yu_*}{\nu}, \frac{u_*^3}{|\alpha|\nu}, \frac{\delta u_*}{\nu} \right) \quad \text{for } \delta_v \sim y \ll \delta_p, \quad (5.9)$$

$$\frac{\partial U}{\partial y} = \frac{|\alpha|^{1/2}}{y^{1/2}} \Phi_2 \left(\frac{y|\alpha|}{u_*^2}, \frac{\delta|\alpha|}{u_*^2}, \frac{\delta u_*}{\nu} \right) \quad \text{for } \delta_v \ll y \ll \delta_p, \quad (5.10)$$

$$\frac{\partial U}{\partial y} = \frac{|\alpha|^{1/2}}{\delta^{1/2}} \Phi_3 \left(\frac{y}{\delta}, \frac{\delta|\alpha|}{u_*^2}, \frac{\delta u_*}{\nu} \right) \quad \text{for } y \sim \delta, \quad (5.11)$$

where the corresponding three length scales are the viscous length scale, $\delta_v = \nu/u_*$, pressure gradient length scale, $\delta_p = u_*^2/\alpha$ ($\alpha > 0$, only, in the present case), and boundary layer thickness, δ .

For $y \ll \delta_p$, δ_p and δ do not have a significant effect on dU/dy . Hence, Equation 5.9 leads to the law of the wall. Similarly, for $y \gg \delta_v$, the logarithmic profile is obtained from Equation 5.9. On the other hand, Equation 5.10 leads to a half-power profile. Equation 5.11 results in a velocity defect law which has $\delta^{1/2}$ dependence. When φ_2 and φ_3 are matched at the interface of the two regions, the half-power relationship is obtained again.

Next, the three length scales mentioned above, δ_v , δ_p and δ , are compared with the beginning and end of the logarithmic region (denoted as $y_{\log,b}$ and $y_{\log,e}$, respectively), the inner half-power region (denoted as $y_{i,b}$ and $y_{i,e}$, respectively) and the outer half-power region (denoted as $y_{o,b}$ and $y_{o,e}$, respectively). For the eleven flows studied here, when these nine length scales are plotted in the streamwise direction, the three patterns shown in Figure 5.21 are obtained. Flows 1100, 1200, 2900, 5000, 5100, 142, 143, 8-degree and Skåre, have the behaviour given in Figure 5.21 (a). The remaining flows, Flows 141 and Han have the characteristics given in Figures 5.21 (b) and (c), respectively. The corresponding scaled plots are presented in Appendix D for each flow.

The patterns presented in Figure 5.21 (a) indicate that the inner half-power profile starts within the logarithmic region, and extends beyond it in decreasing adverse pressure gradient flows. In the two increasing adverse pressure gradient flows, as seen in Figures 5.21 (b) and (c), the same pattern develops after the pressure gradient changes character and begins to decrease. Initially, the logarithmic region extends well into the outer half-power profile in these two flows.

In general, the patterns summarized in Figure 5.21 (a) indicate that the overall mean velocity profile is composed of the following segments for an adverse pressure gradient flow:

$$U^+ = y^+ \quad \text{for } y < \delta_v \text{ and}$$

$$U^+ = \frac{1}{\kappa} \ln y^+ + 5.2 \quad \text{for } \delta_v < y \sim \delta_p,$$

with a blending (buffer) region in between.

$$\frac{U}{U_e} = \frac{C_i}{U_e} \left(\frac{y}{\delta} \right)^{\frac{1}{2}} + \frac{D_i}{U_e} \quad \text{for } \delta_v < y \text{ and } y > \delta_p,$$

continuing from the logarithmic profile without a blending region.

$$\frac{U}{U_e} = \frac{C_o}{U_e} \left(\frac{y}{\delta} \right)^{\frac{1}{2}} + \frac{D_o}{U_e} \quad \text{for } \delta_p < y < \delta,$$

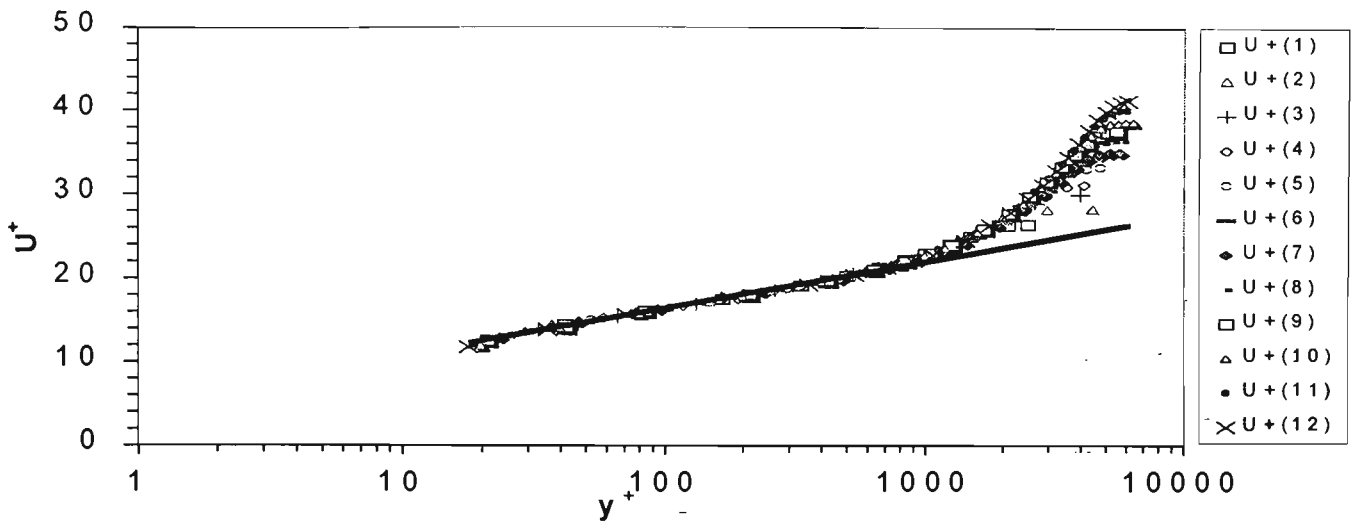
with a blending region after the inner half power profile, but continuing to the velocity defect profile without another blending region.

With an increasing adverse pressure gradient, the blending region between the inner and outer half-power profiles shifts into the logarithmic region. Otherwise, the overall pattern remains the same as for decreasing adverse pressure gradient cases.

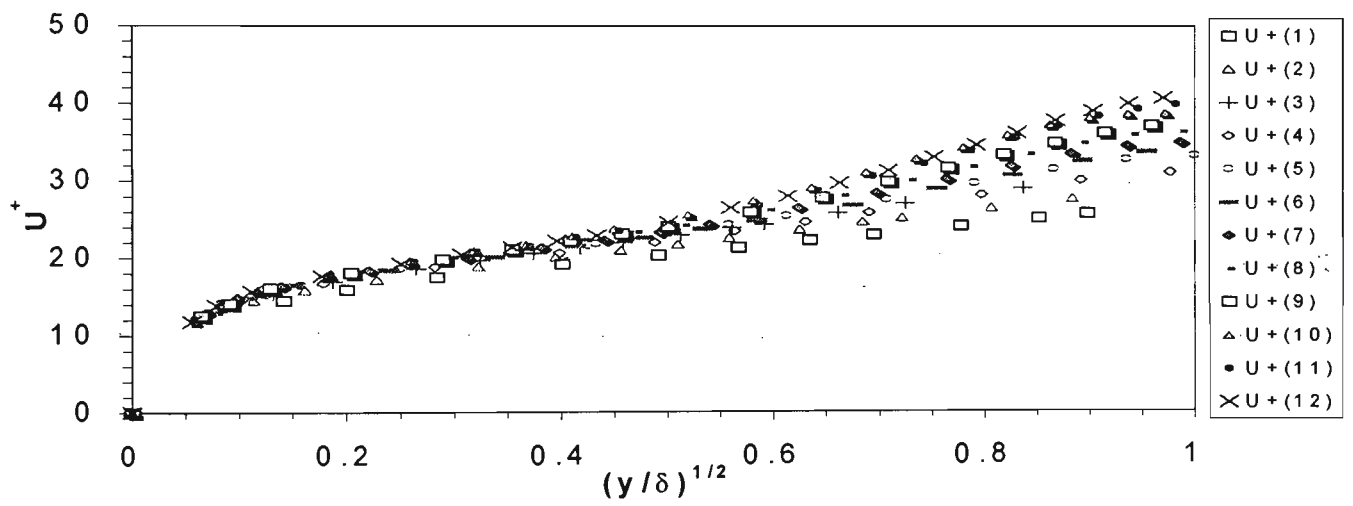
5.8 Other Half Power Profiles and the Present Work

As indicated earlier, the presence of inner and outer half-power profiles was observed by Kopp and Turan (1992). However, the conclusive functional forms given here with Equations 5.4, 5.5, 5.7 and 5.8 were not obtained in that study.

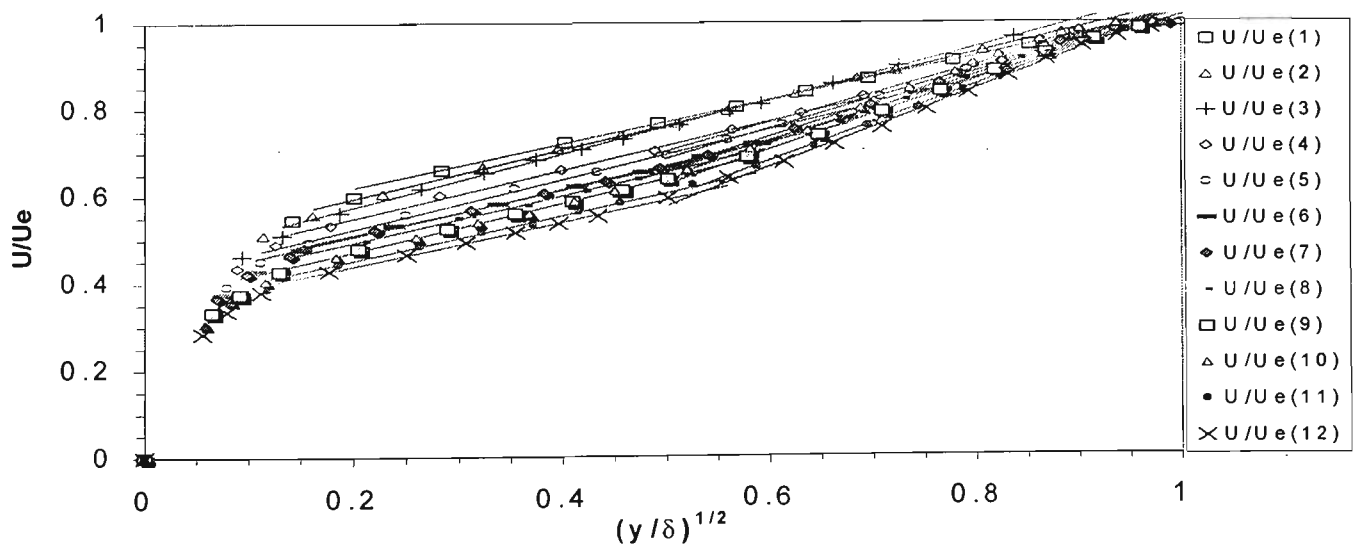
It is known that the first suggestion of a half-power velocity profile dates back to the work of Solodkin and Mezhirov in 1956 (Kader and Yaglom, 1978). Subsequently, Stratford (1959), Townsend (1960), Perry et al. (1966), Perry (1966), Perry and Schofield (1973), McDonald (1969) and Kader and Yaglom (1978) proposed half power profiles. In all these works, one half-power profile is proposed extending between the logarithmic and velocity defect regions. As indicated in Section 5.7 in relation to Figure 5.21, a more complete mean velocity profile is provided here by using two inner half-power regions. The resulting profile has the minimum possible logarithmic region right after the law of the wall. Hence, even when the logarithmic profile is destroyed due to large Δ , the resulting composite profile can be used with the slope and intercept expressions given in Equations 5.4, 5.5, 5.7 and 5.8, provided $U_e / \sqrt{\alpha \delta} > 6$.



(a)

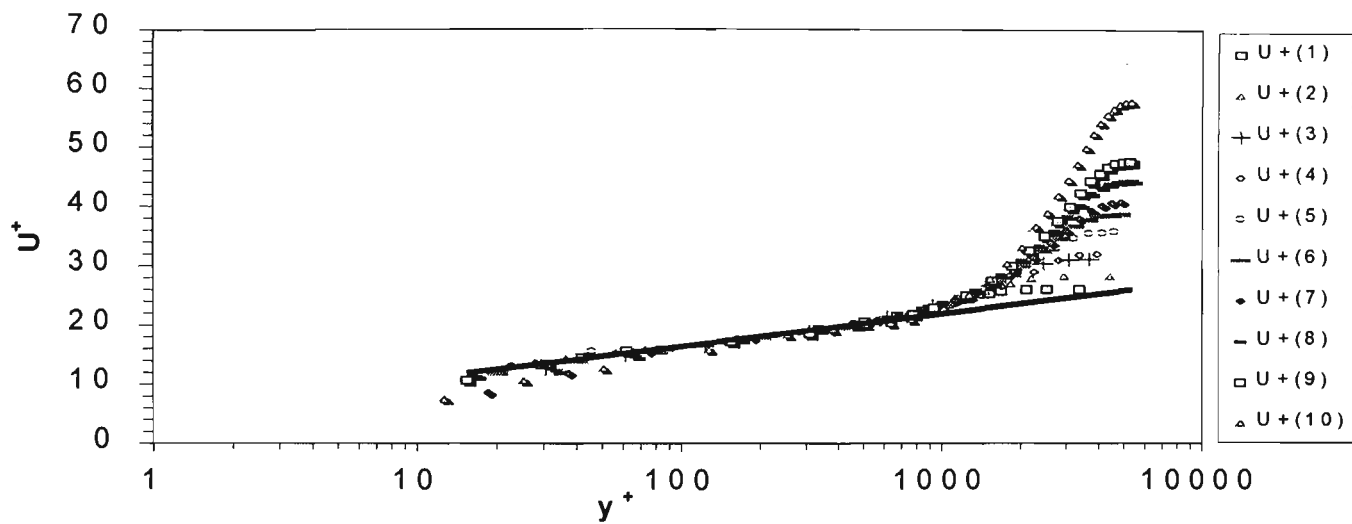


(b)

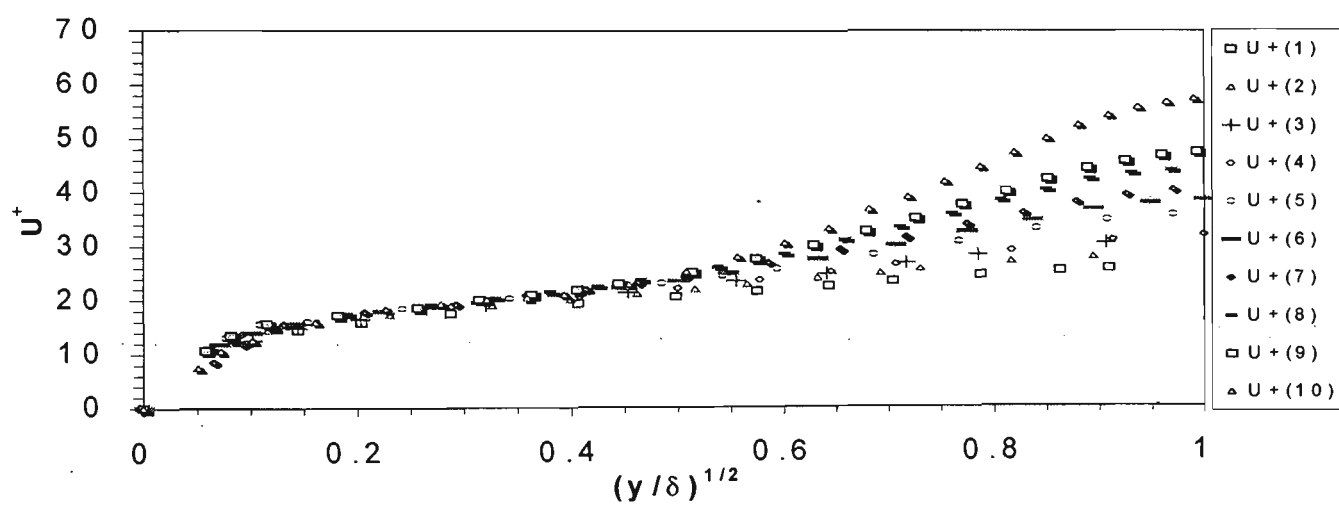


(c)

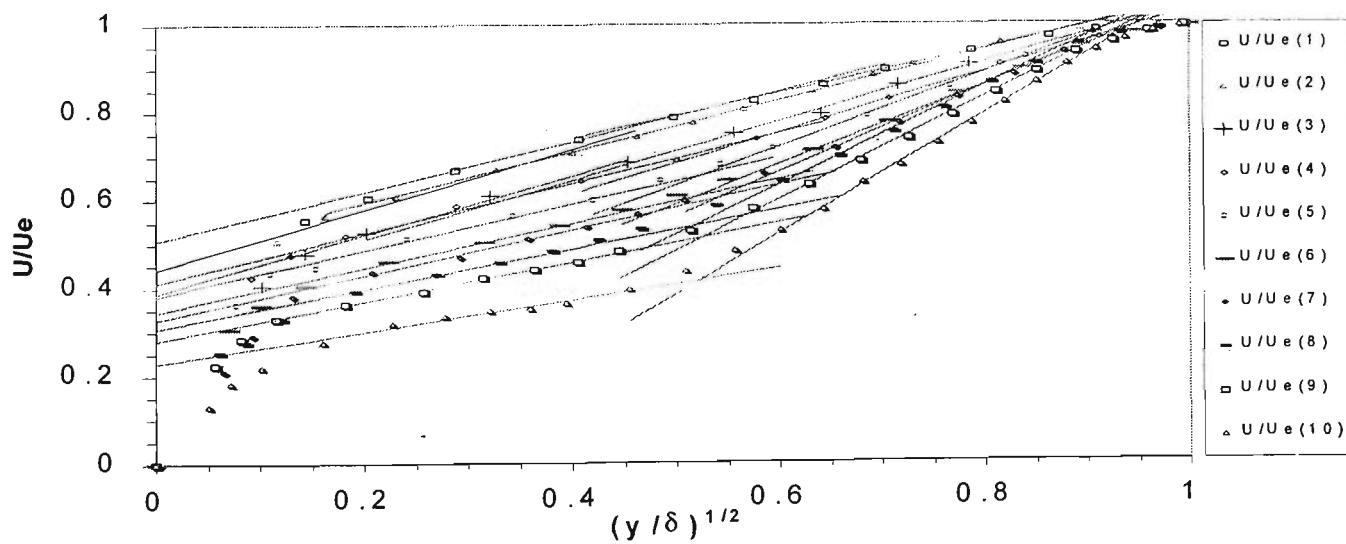
Figure 5.1 Flow 1100. Stations 1 to 12 correspond to 0.78, 1.28, 1.78, 2.28, 2.78, 3.13, 3.33, 3.53, 3.73, 3.93, 4.12, 4.33 m for the inlet, respectively.



(a)

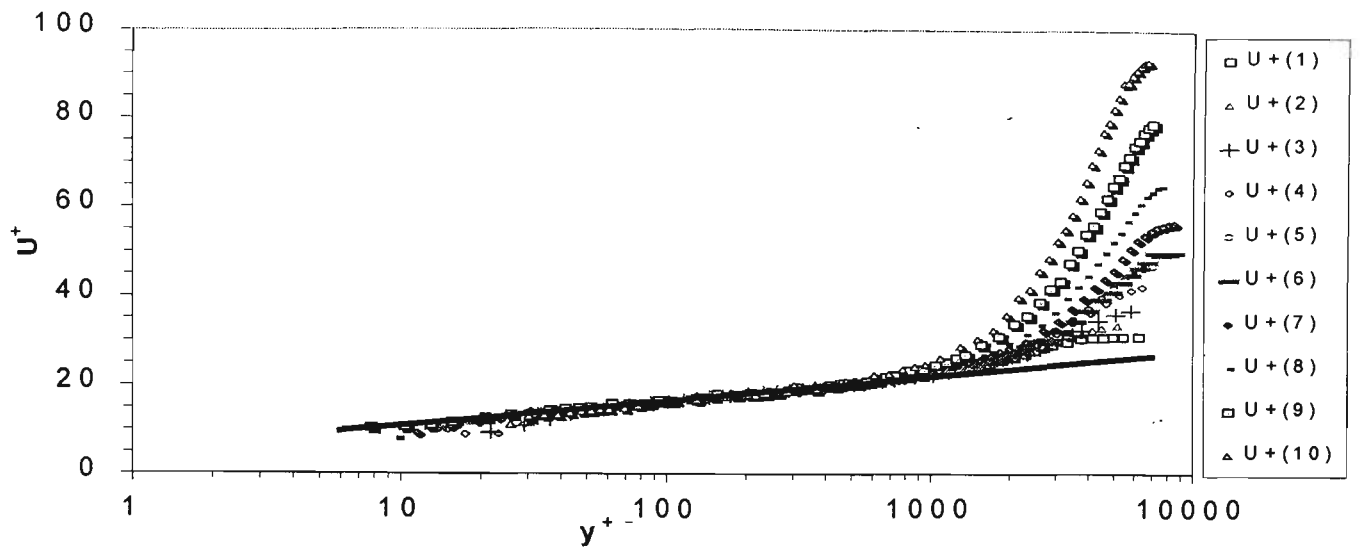


(b)

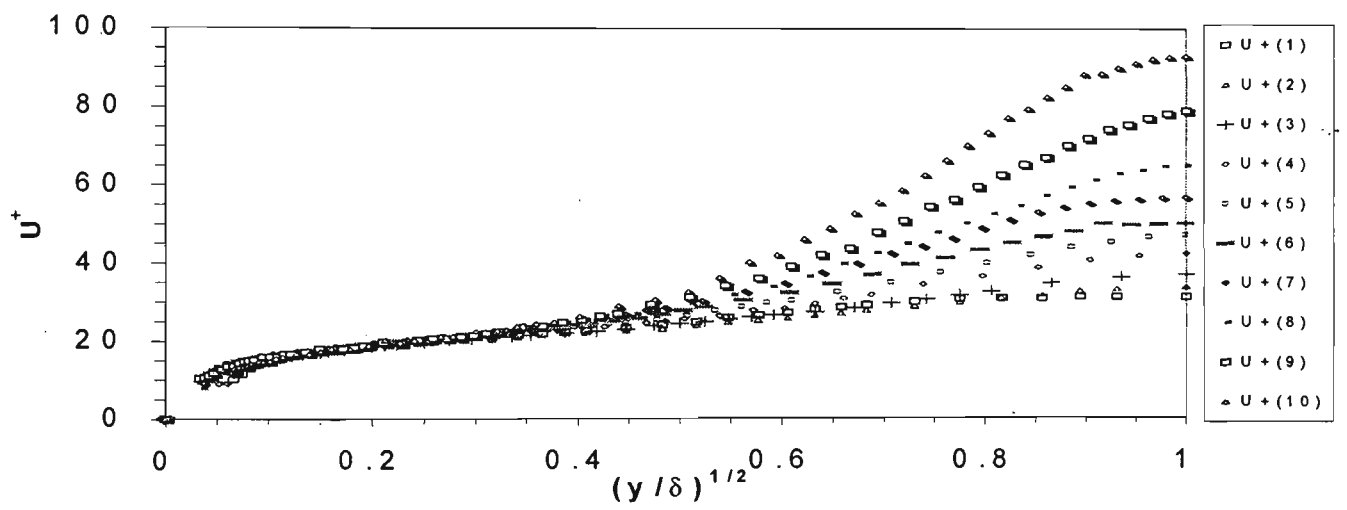


(c)

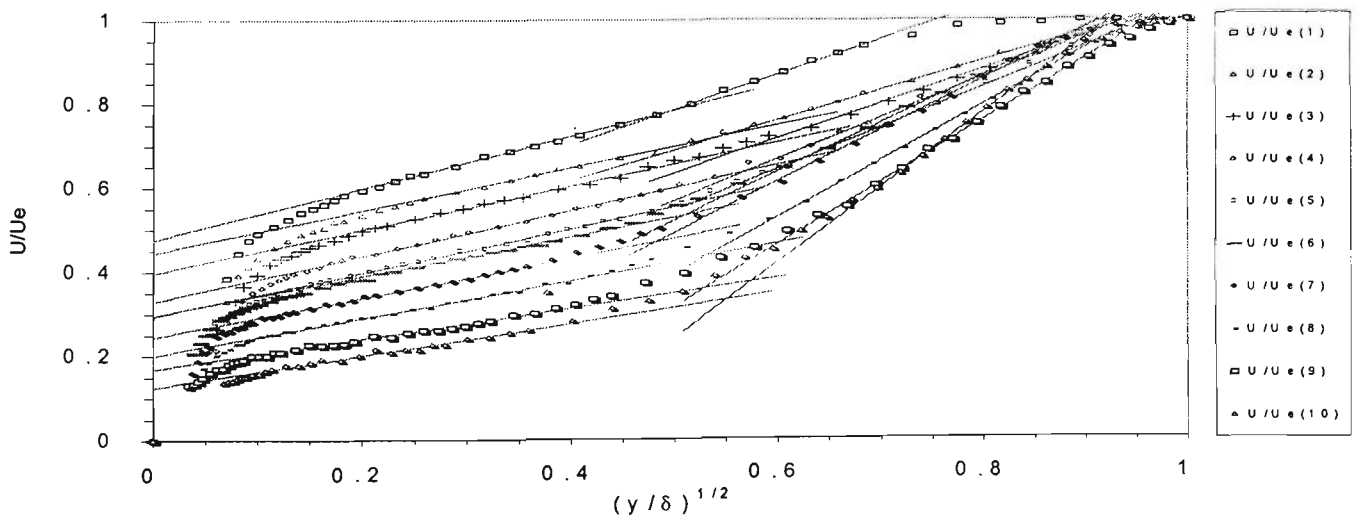
Figure 5.2 Flow 1200. Stations 1 to 10 correspond to 0.78, 1.28, 1.78, 2.28, 2.78, 3.13, 3.33, 3.53, 3.73, 3.93 m for the inlet, respectively.



(a)



(b)



(c)

Figure 5.3 Flow 2900. Stations 1 to 10 correspond to 0.76, 1.22, 1.68, 2.13, 2.60, 3.05, 3.35, 3.81, 4.27, 4.57, m for the inlet, respectively.

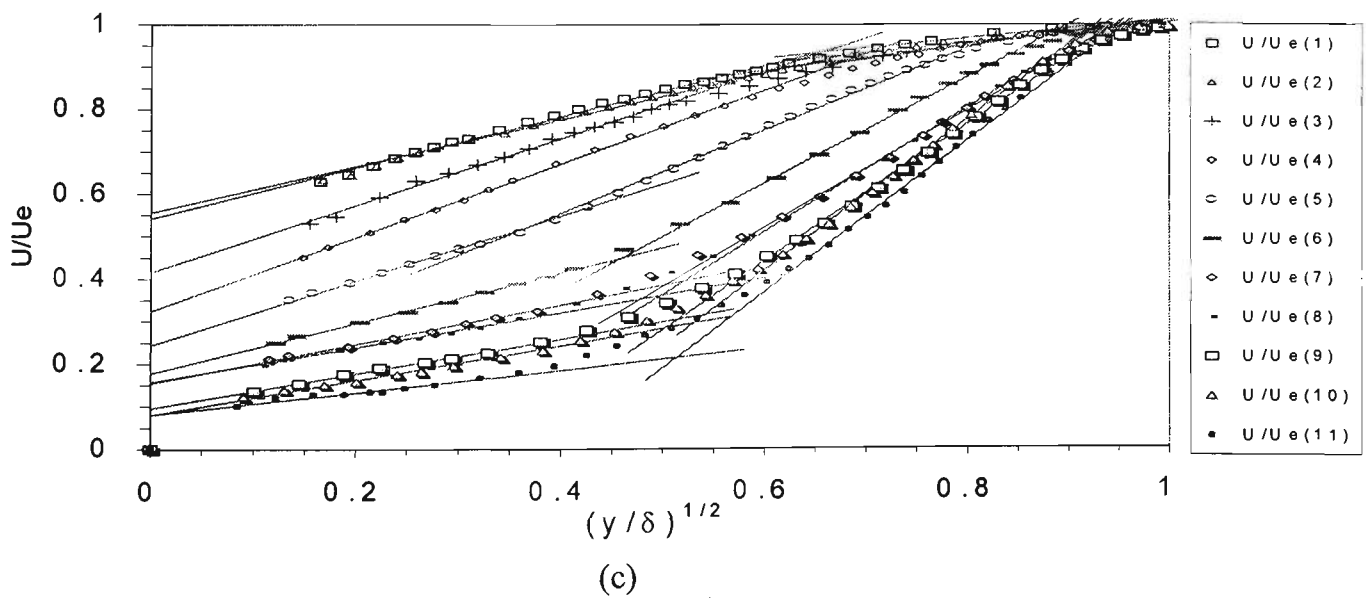
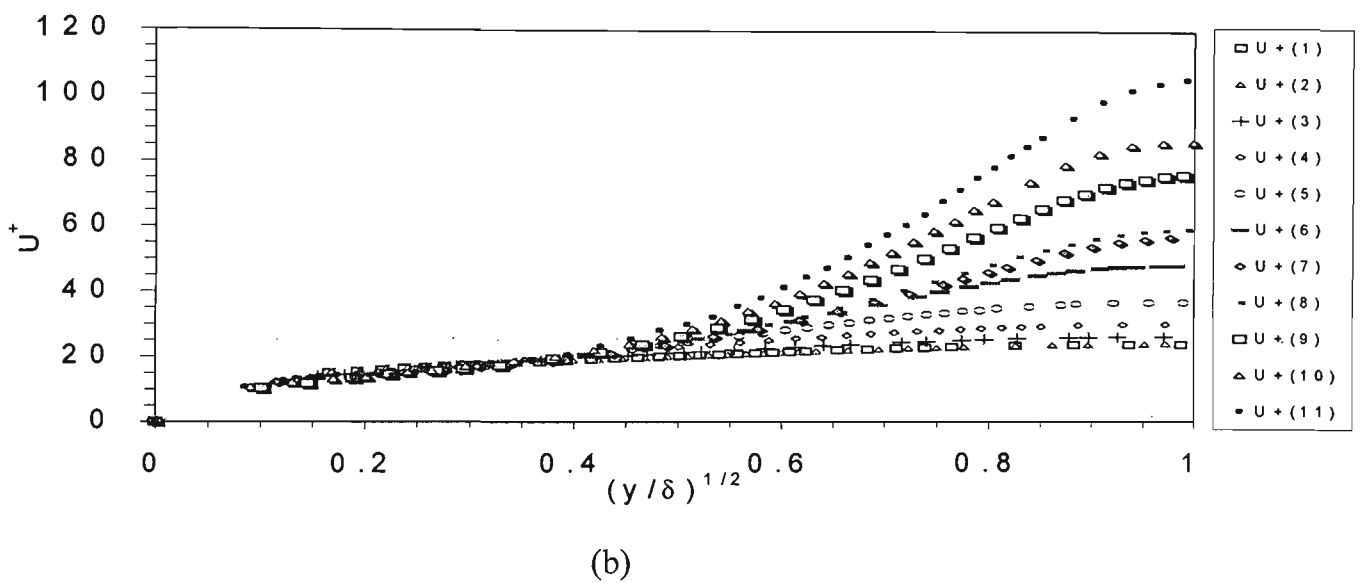
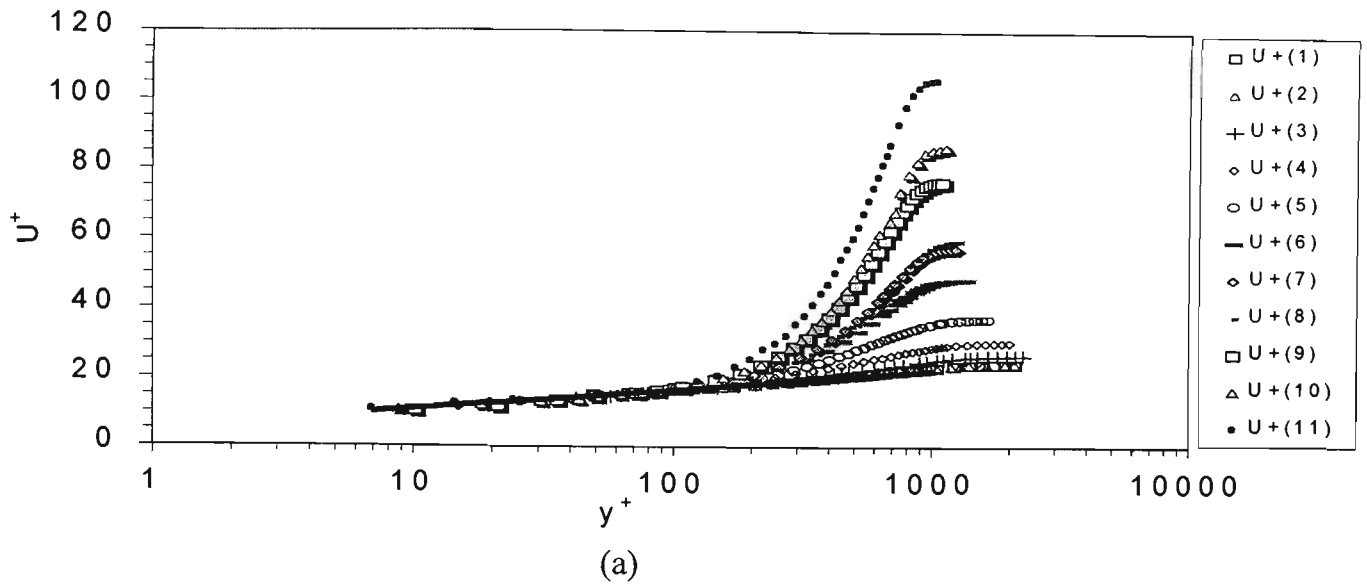


Figure 5.4 Flow 5000. Stations 1 to 11 correspond to 0.12, 0.16, 0.21, 0.24, 0.30, 0.38, 0.44, 0.47, 0.53, 0.58, 0.64 m for the inlet, respectively.

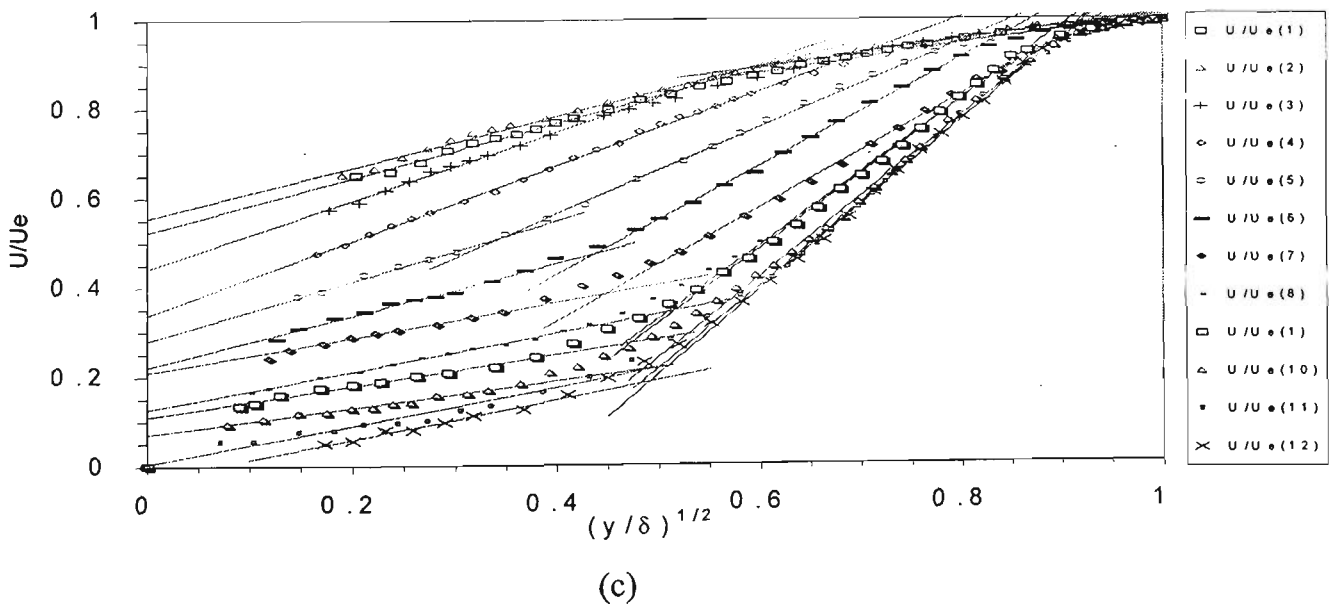
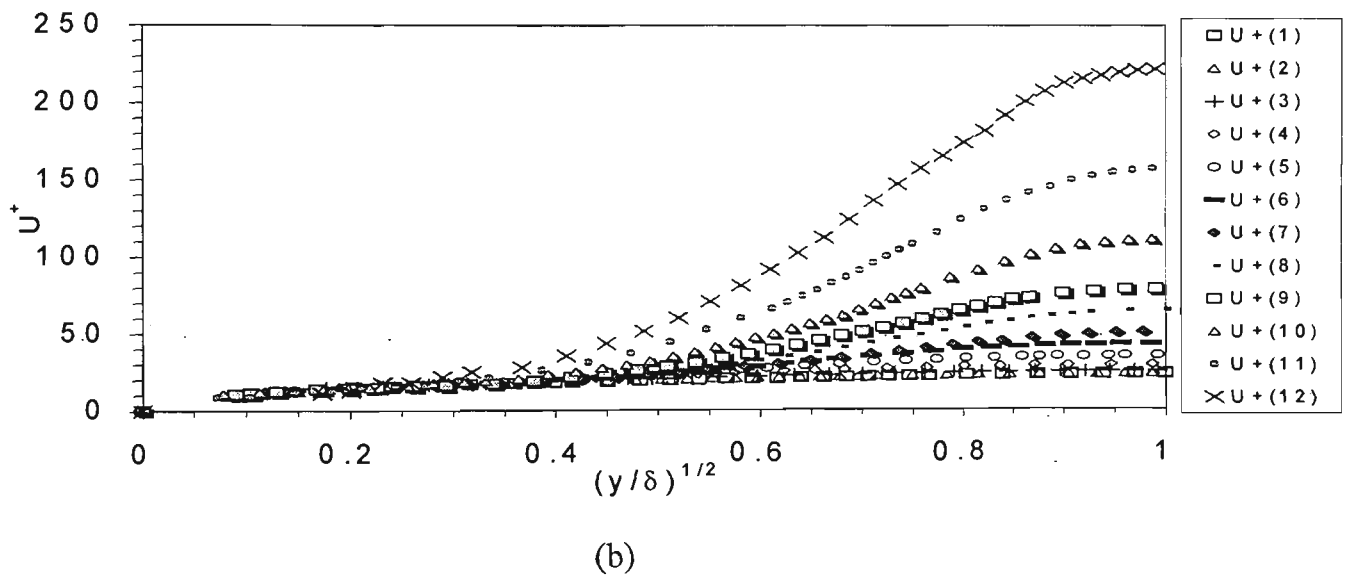
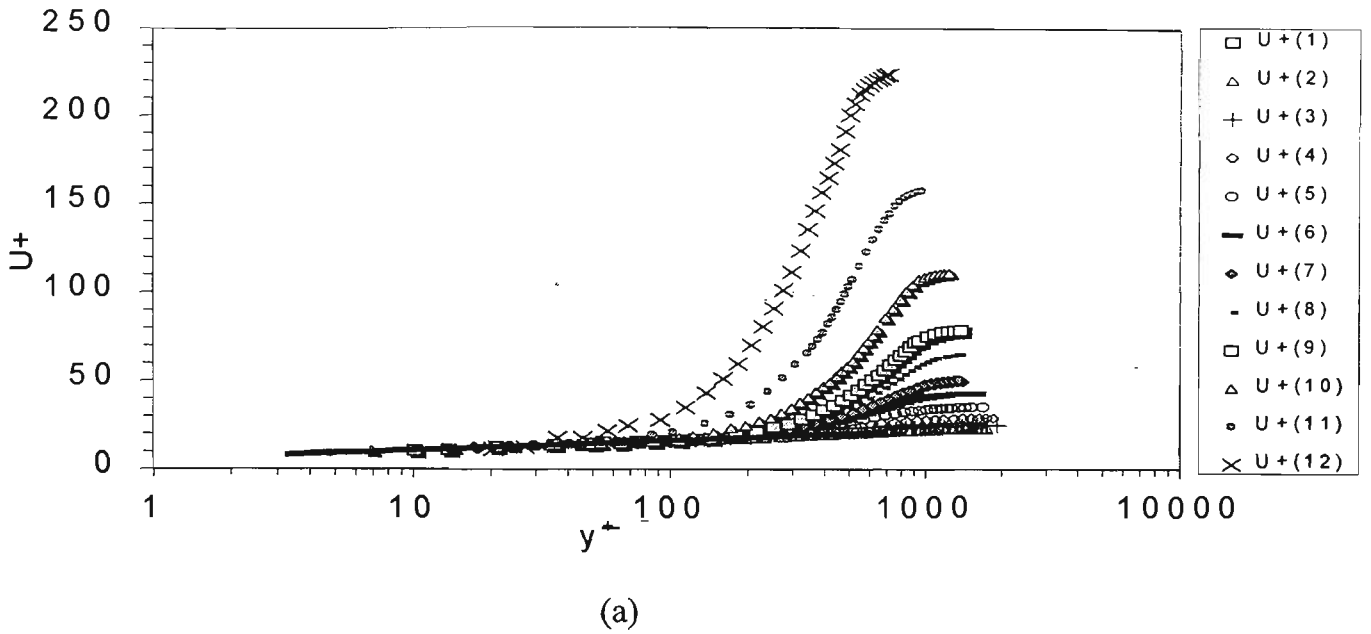
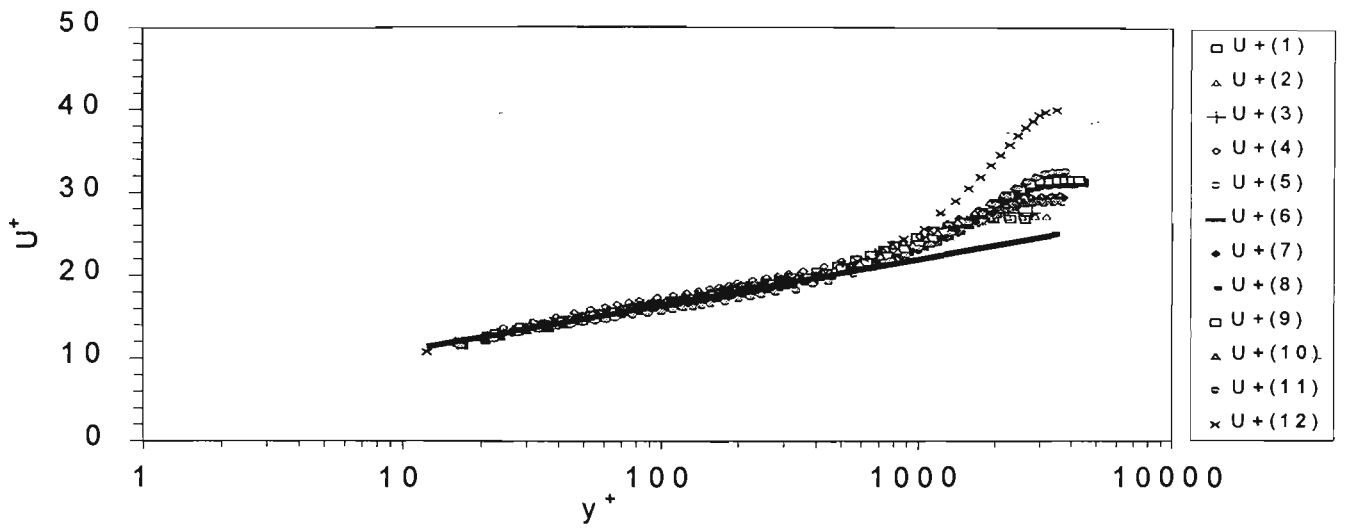
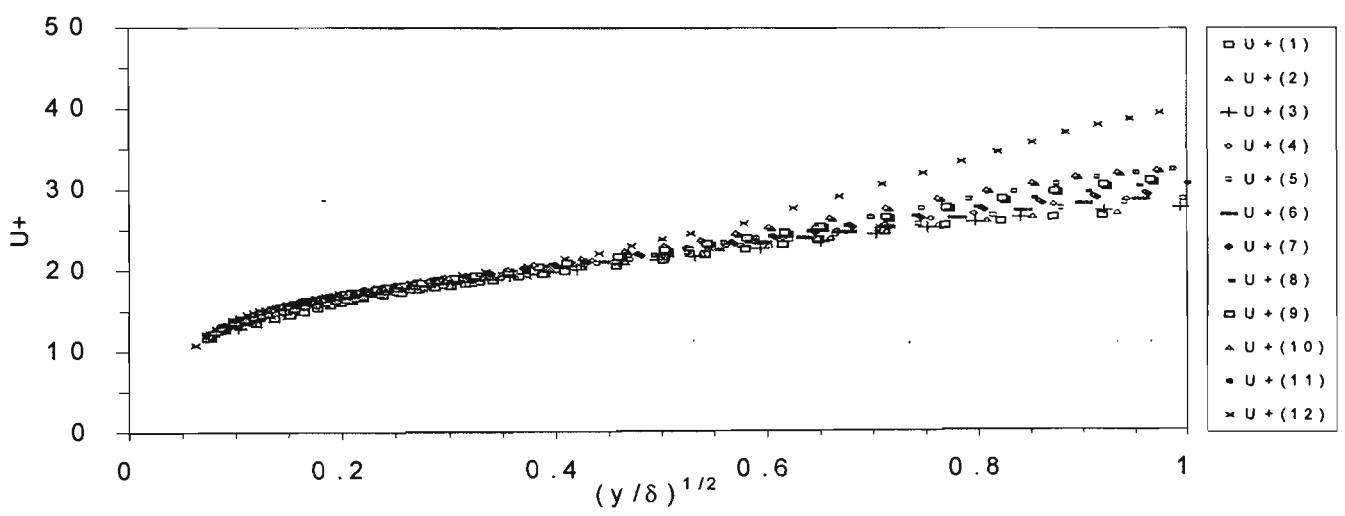


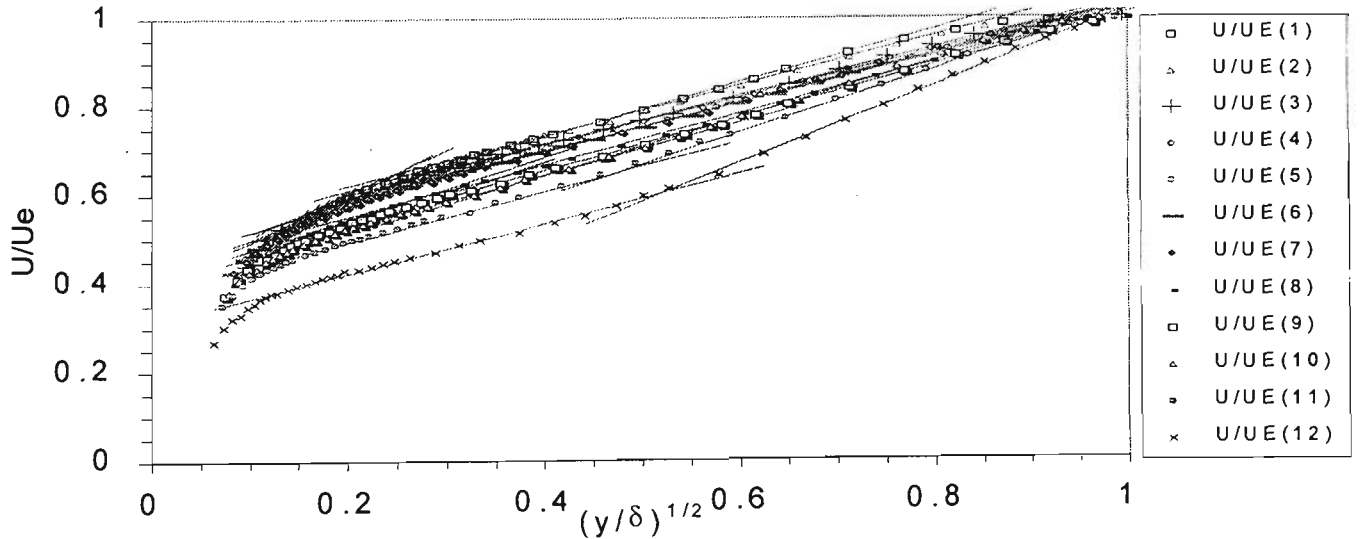
Figure 5.5 Flow 5100. Stations 1 to 12 correspond to 0.12, 0.16, 0.20, 0.24, 0.30, 0.38, 0.44, 0.52, 0.58, 0.68, 0.74, 0.78 m for the inlet, respectively.



(a)

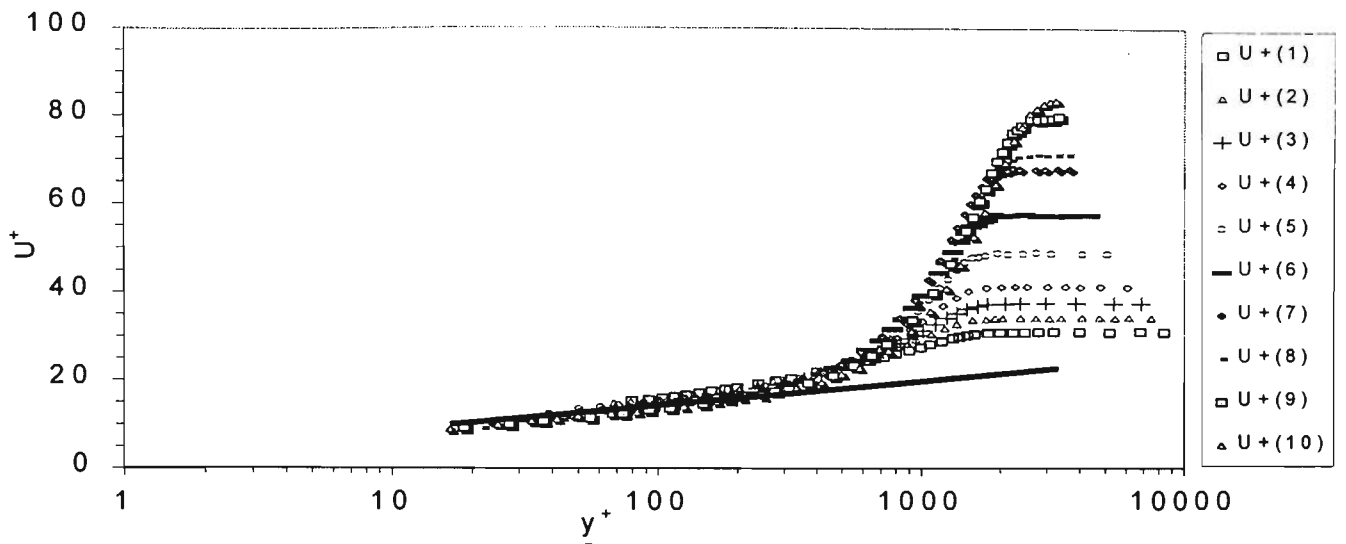


(b)

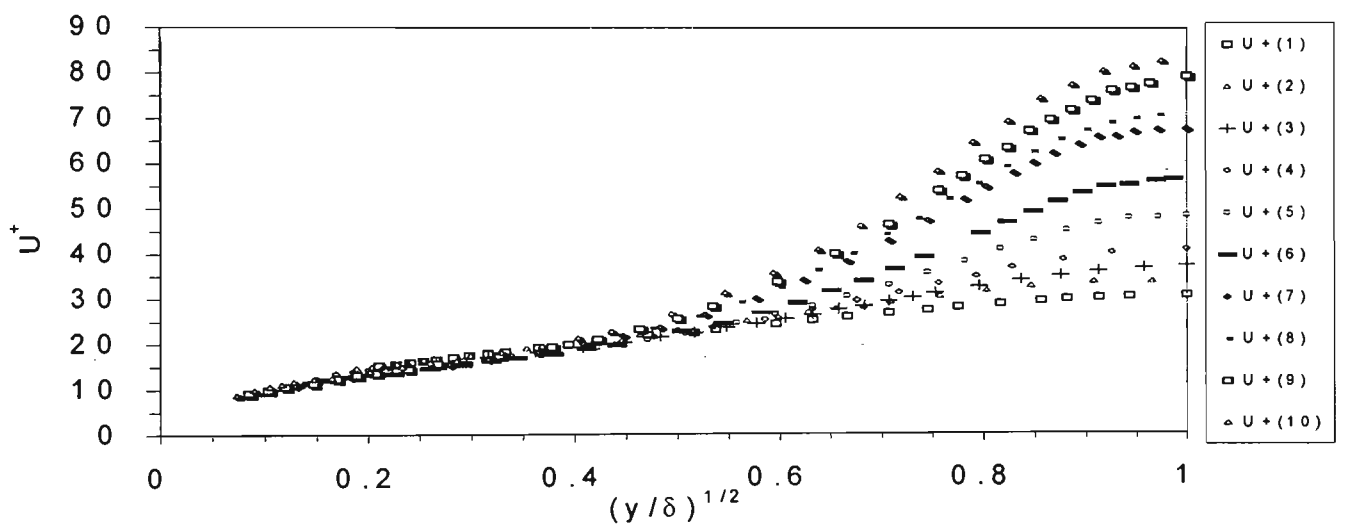


(c)

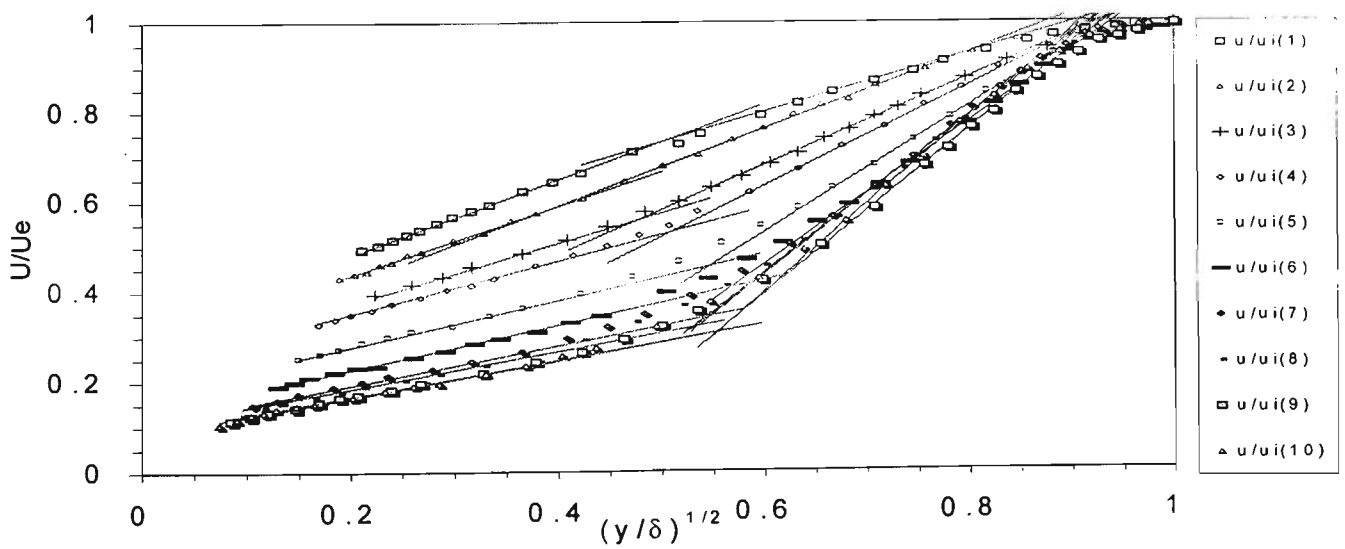
Figure 5.6 Flow 141. Stations 1 to 12 correspond to 0.86, 1.16, 1.44, 1.76, 2.10, 2.26, 2.40, 2.56, 2.72, 2.87, 3.04, 3.40 m for the inlet, respectively.



(a)

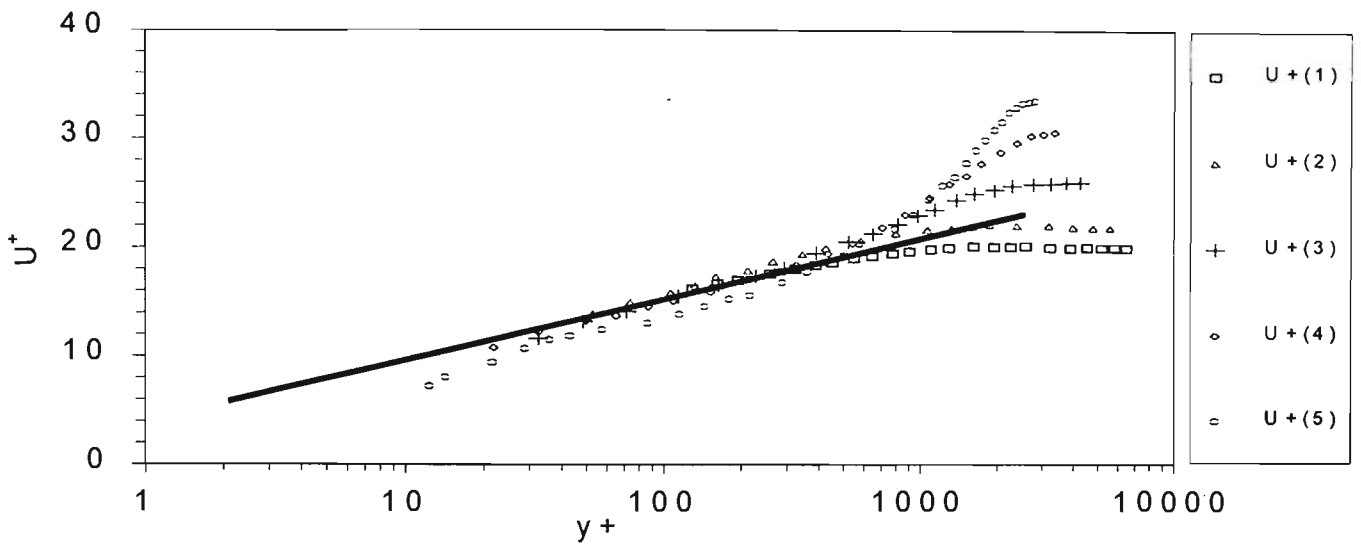


(b)

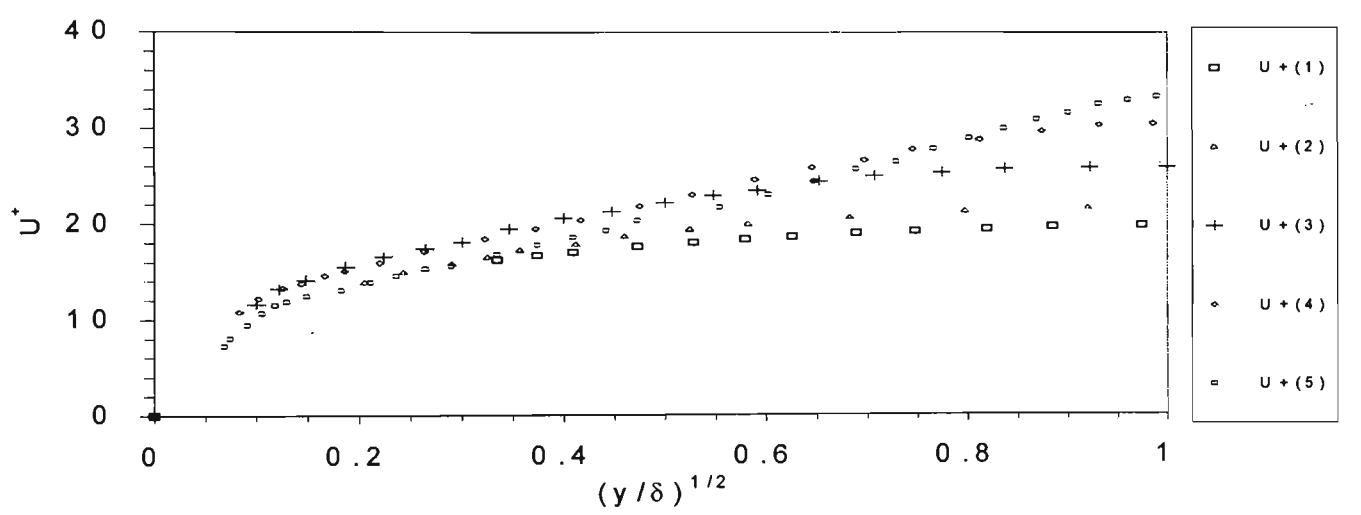


(c)

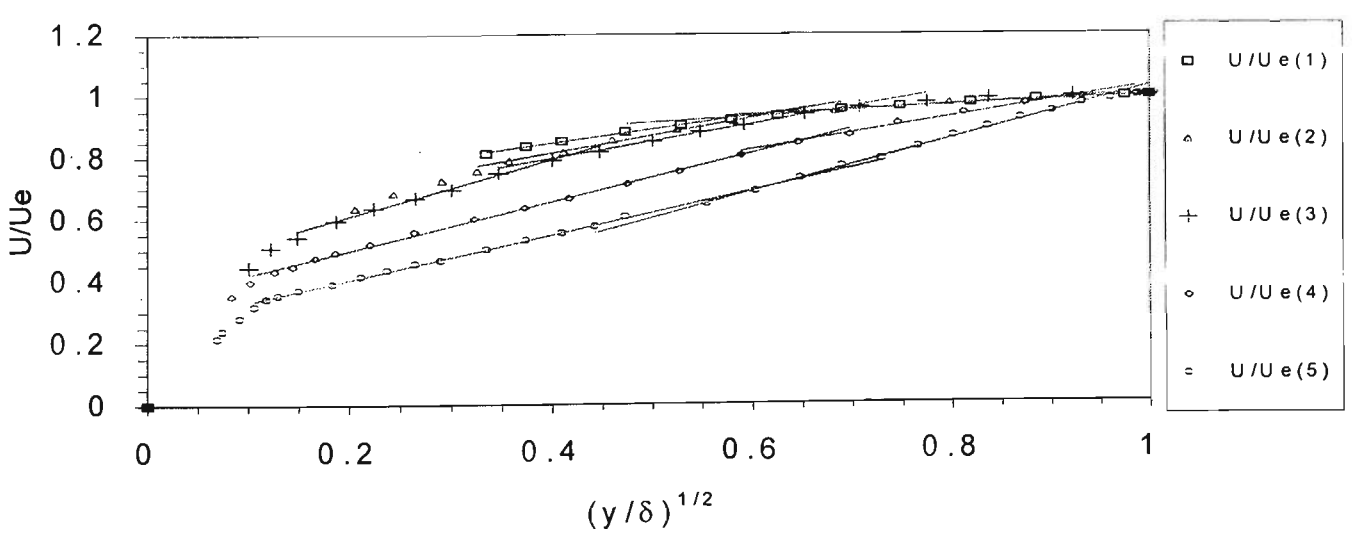
Figure 5.7 Flow 142. Stations 1 to 10 correspond to 0.1, 0.19, 0.29, 0.38, 0.57, 0.76, 1.05, 1.24, 1.53, 1.81 m for the inlet, respectively.



(a)

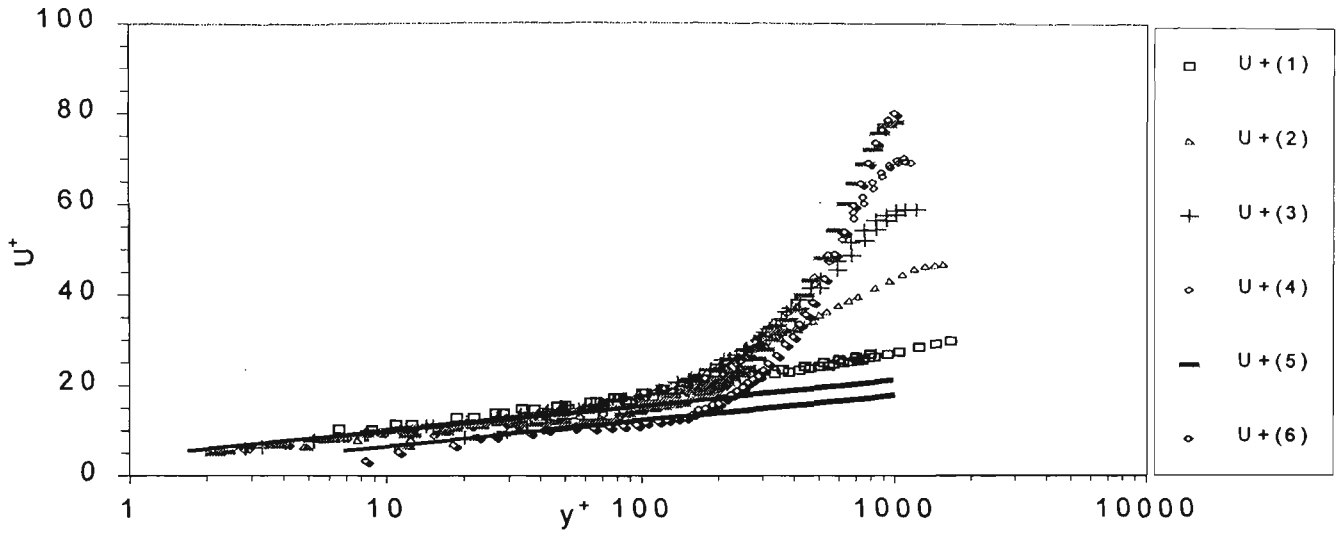


(b)

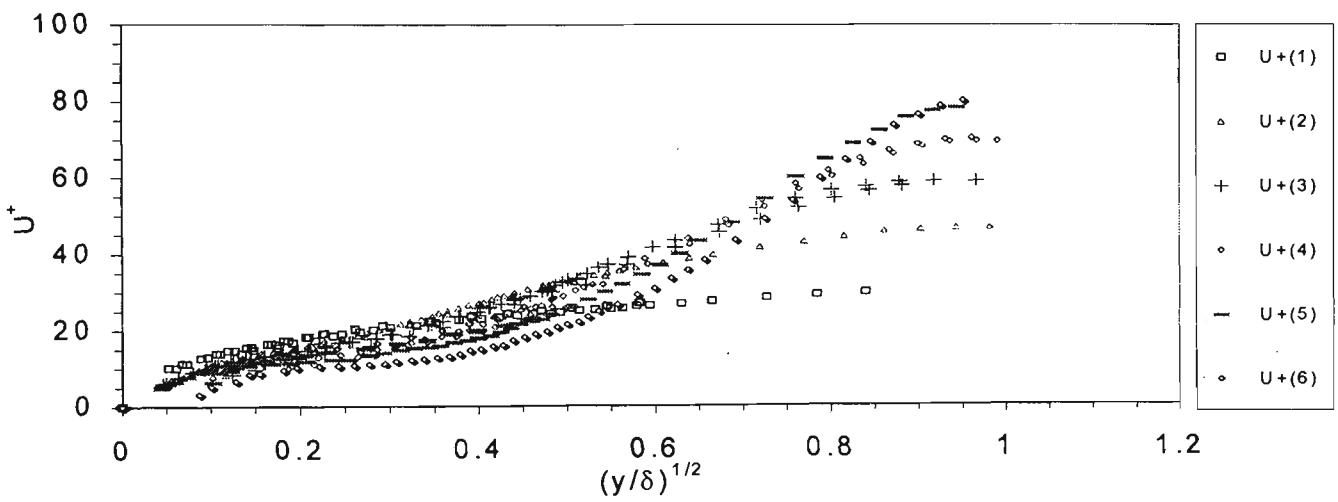


(c)

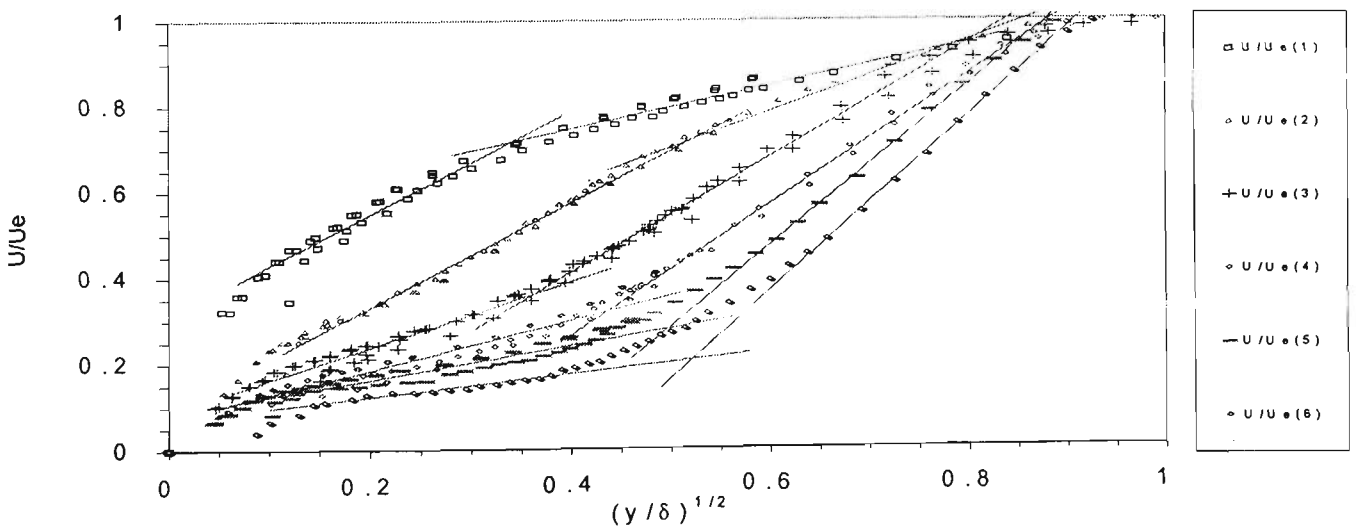
Figure 5.8 Flow 143. Stations 1 to 5 correspond to -0.06, 0.10, 0.57, 1.05, 1.81 m for the inlet, respectively.



(a)

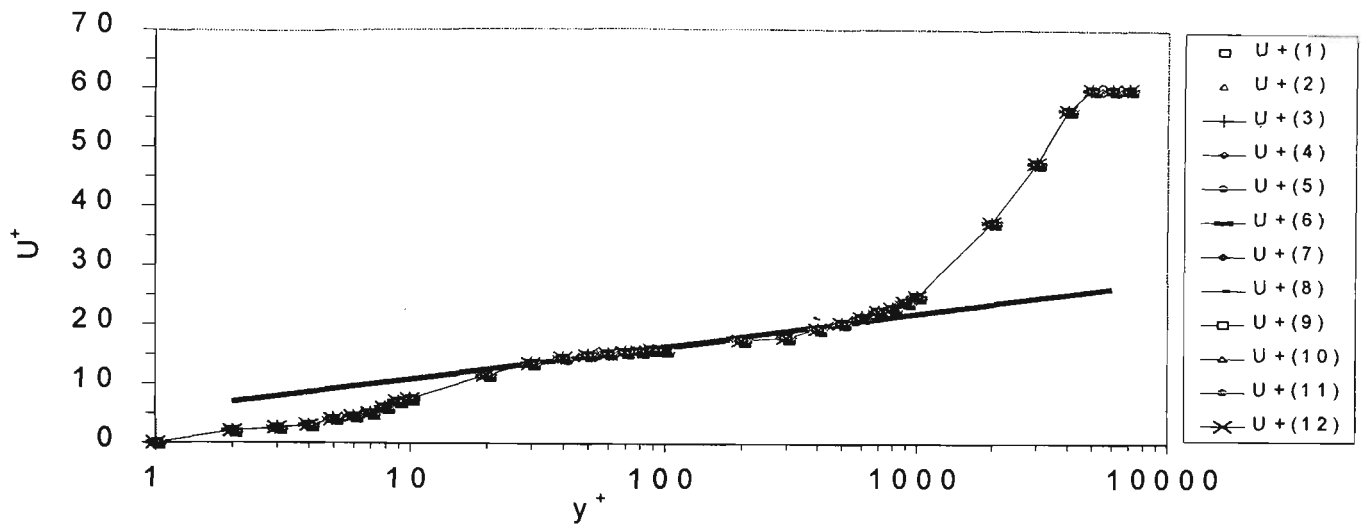


(b)

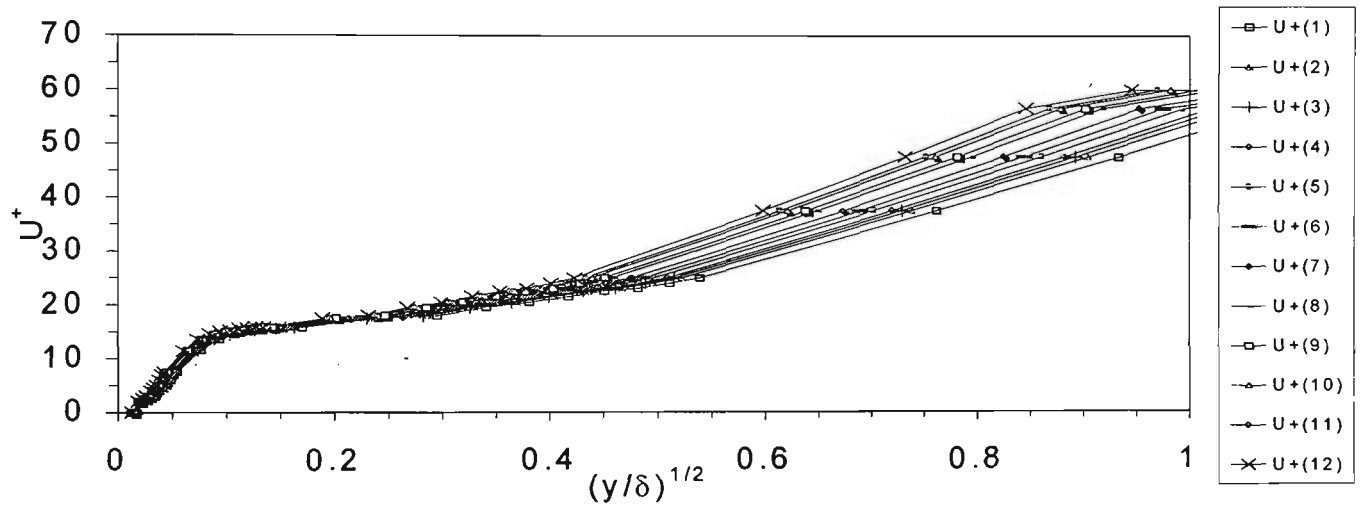


(c)

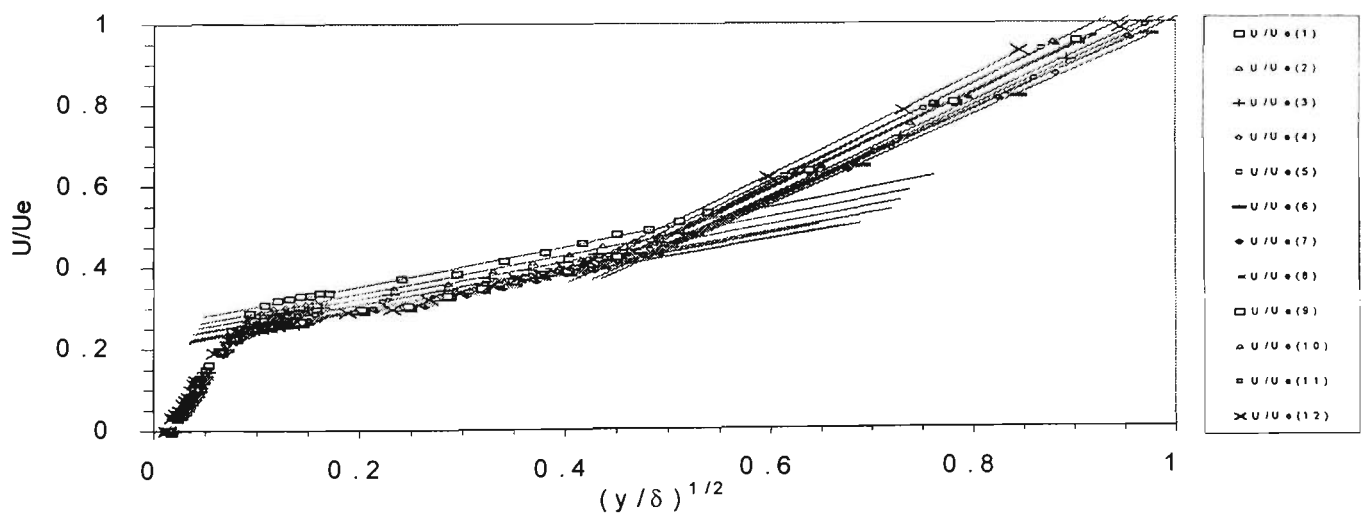
Figure 5.9 Flow 8-degree. Stations 1 to 6 correspond to 0.06, 0.18, 0.30, 0.42, 0.54, 0.66 m for the inlet, respectively.



(a)



(b)



(c)

Figure 5.10 Flow Skåre. Stations 1 to 12 correspond to 3.0, 3.2, 3.4, 3.6, 4.0, 4.2, 4.4, 4.6, 4.8, 5.0, 5.2 m for the inlet, respectively.

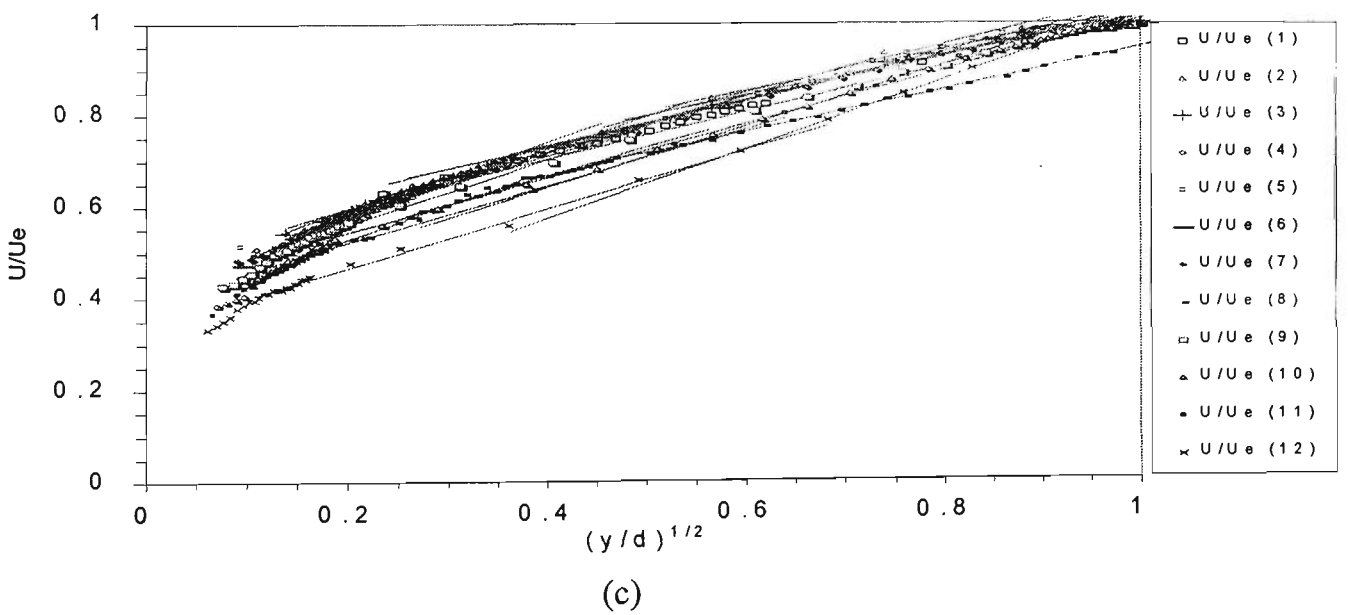
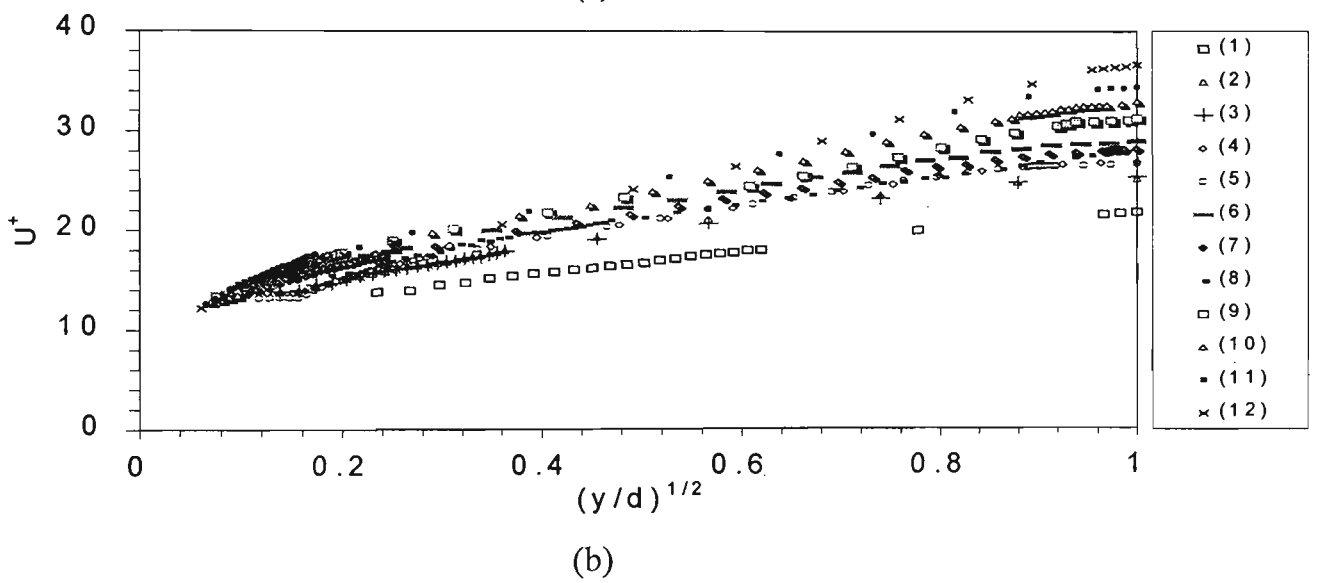
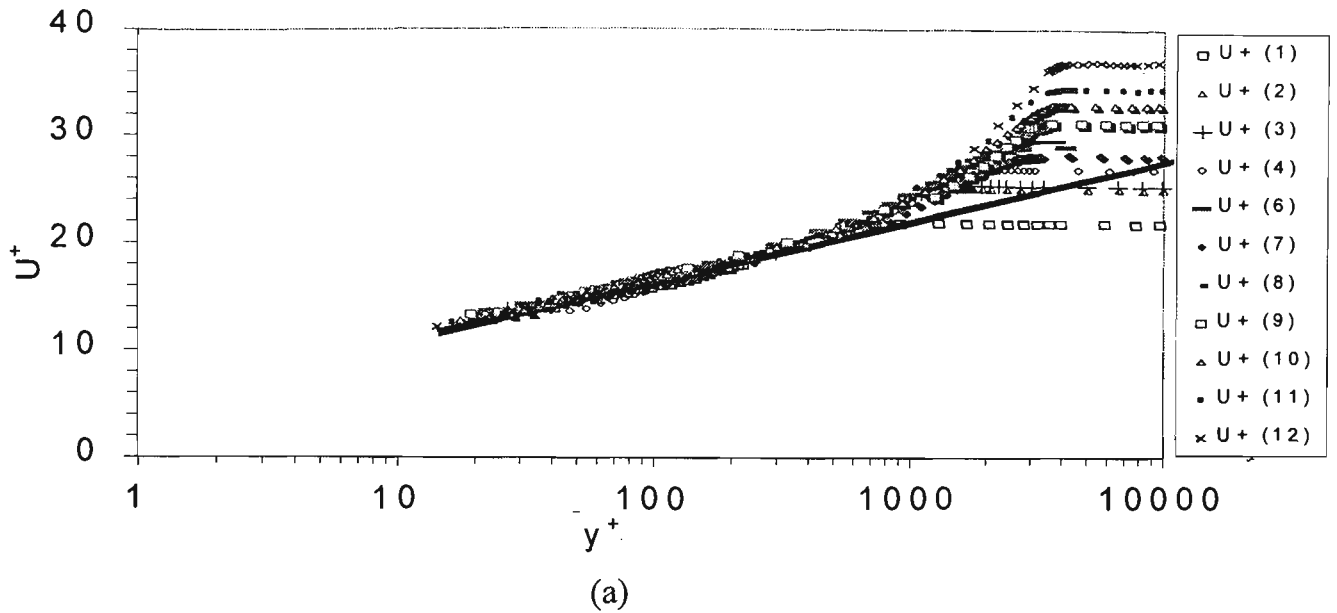
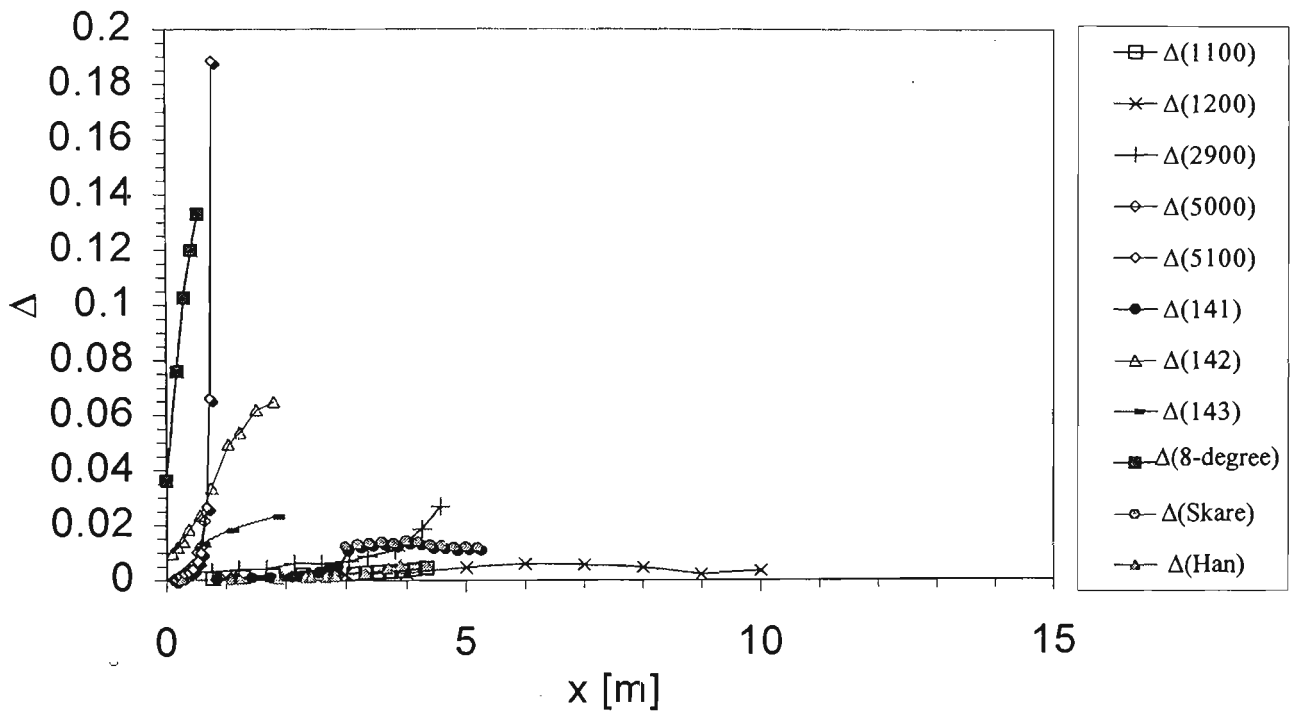
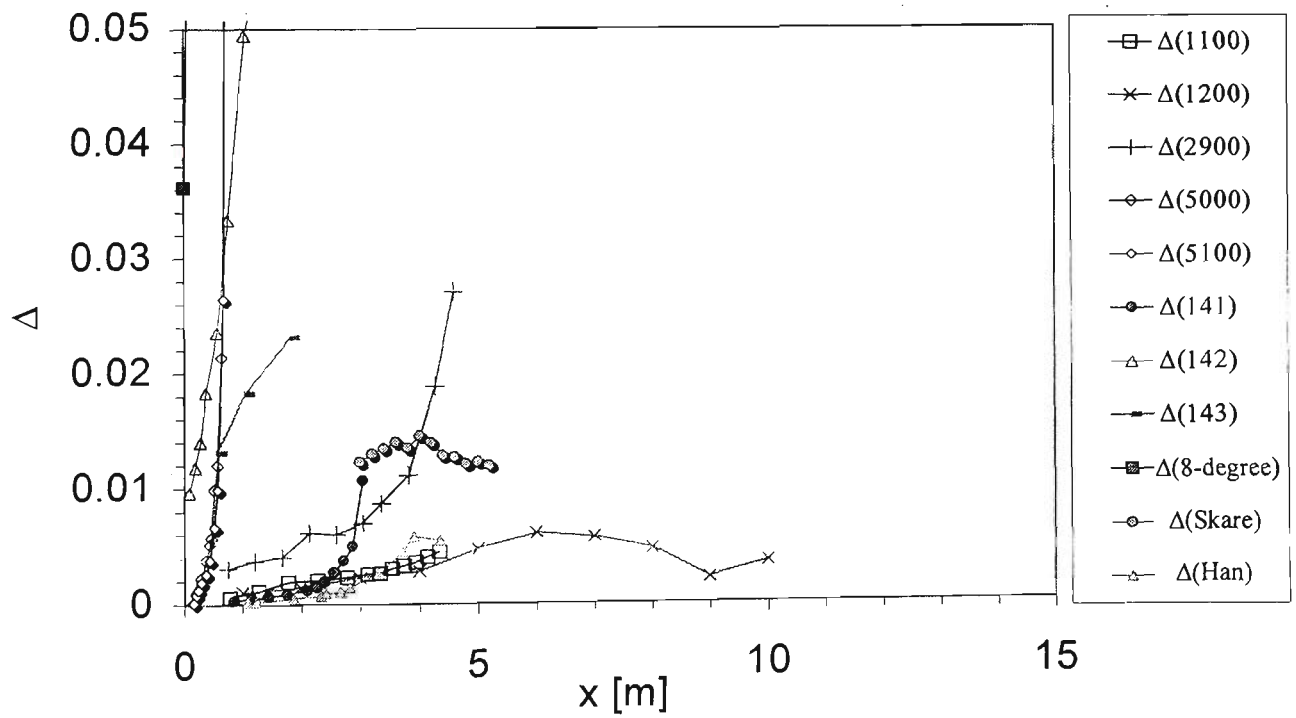


Figure 5.11 Flow Han. Stations 1 to 12 correspond to 0.26, 1.09, 1.25, 1.87, 2.34, 2.42, 2.67, 2.83, 3.32, 3.70, 3.90, 4.35 m for the inlet, respectively.

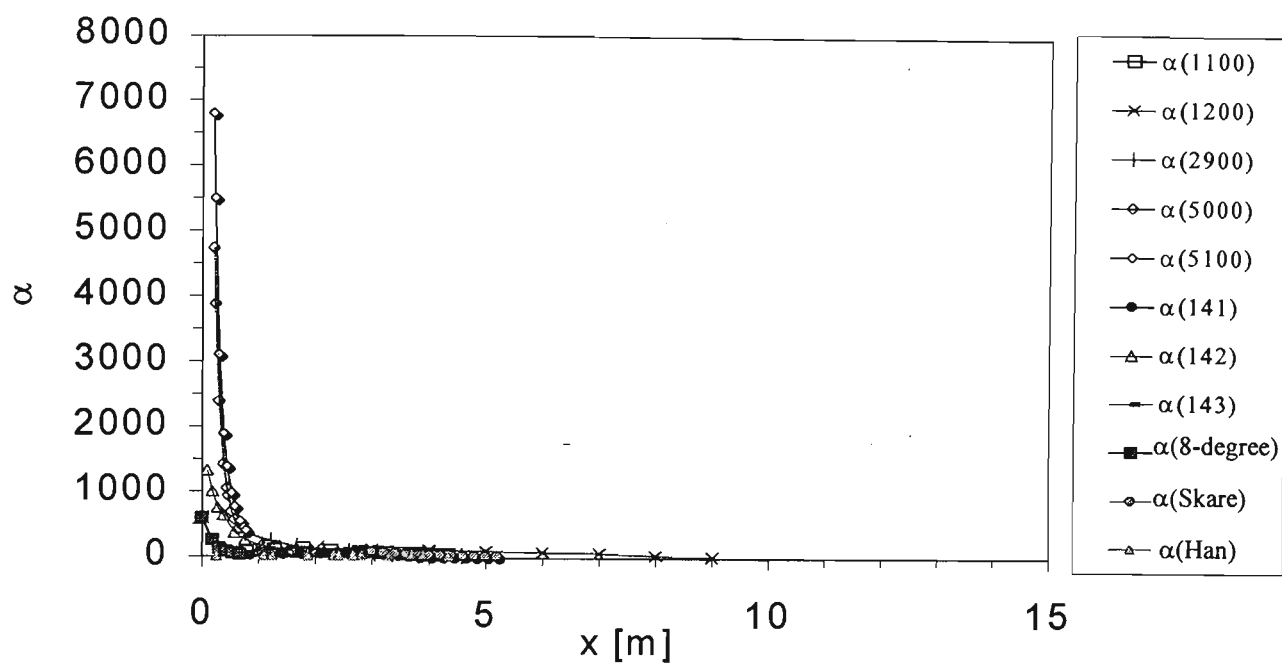


(a)

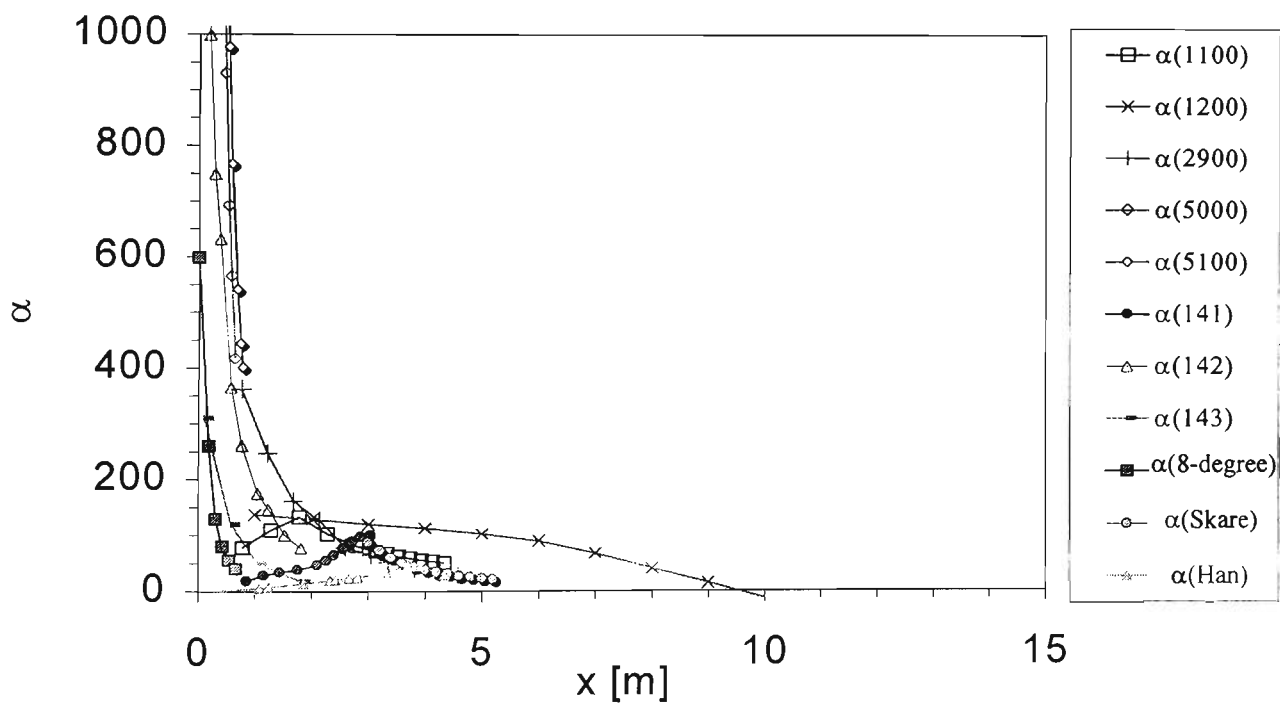


(b)

Figure 5.12 Pressure parameter. (a) All flows, (b) Plane diffusers.

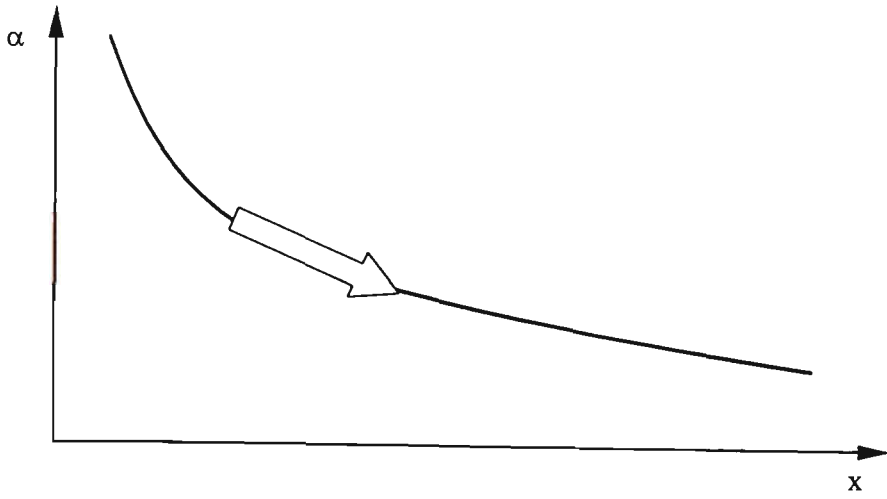


(a)

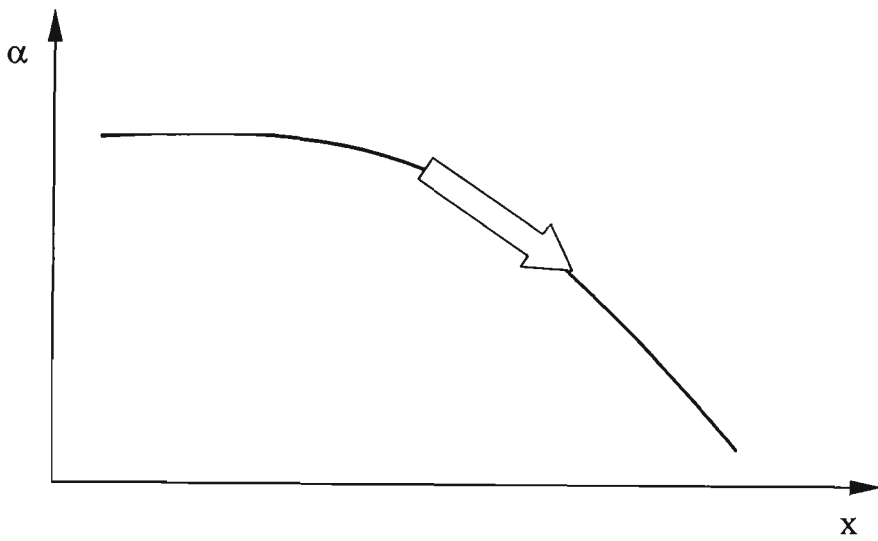


(b)

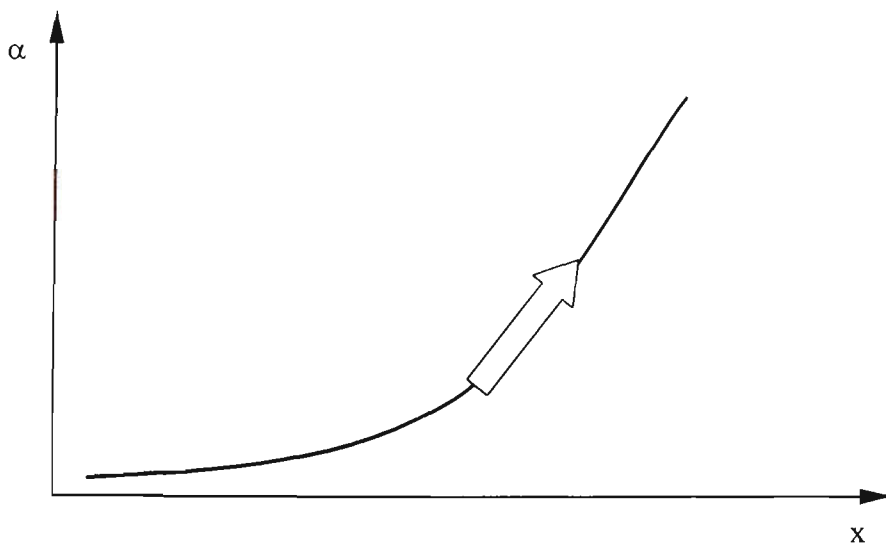
Figure 5.13 Kinematic Pressure gradient. (a) All flows, (b) $\alpha < 1000$ behaviour.



(a) Flow 1100, 2900, 5000, 5100, 142, 143, 8-degree and Skåre.



(b) Flow 1200.



(c) Flow 141 and Han.

Figure 5.14 Variation of α .

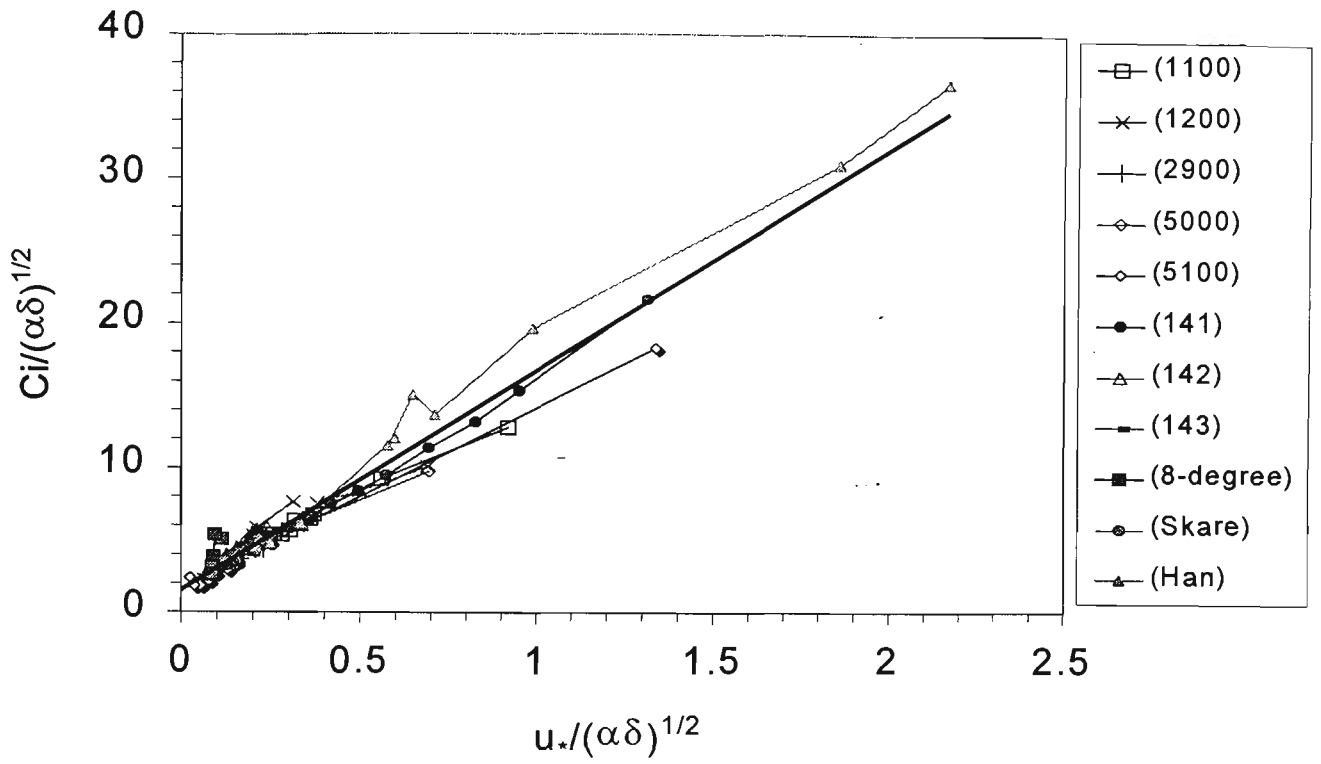


Figure 5.15 Inner half-power slope. The solid line represents Equation 5.4.

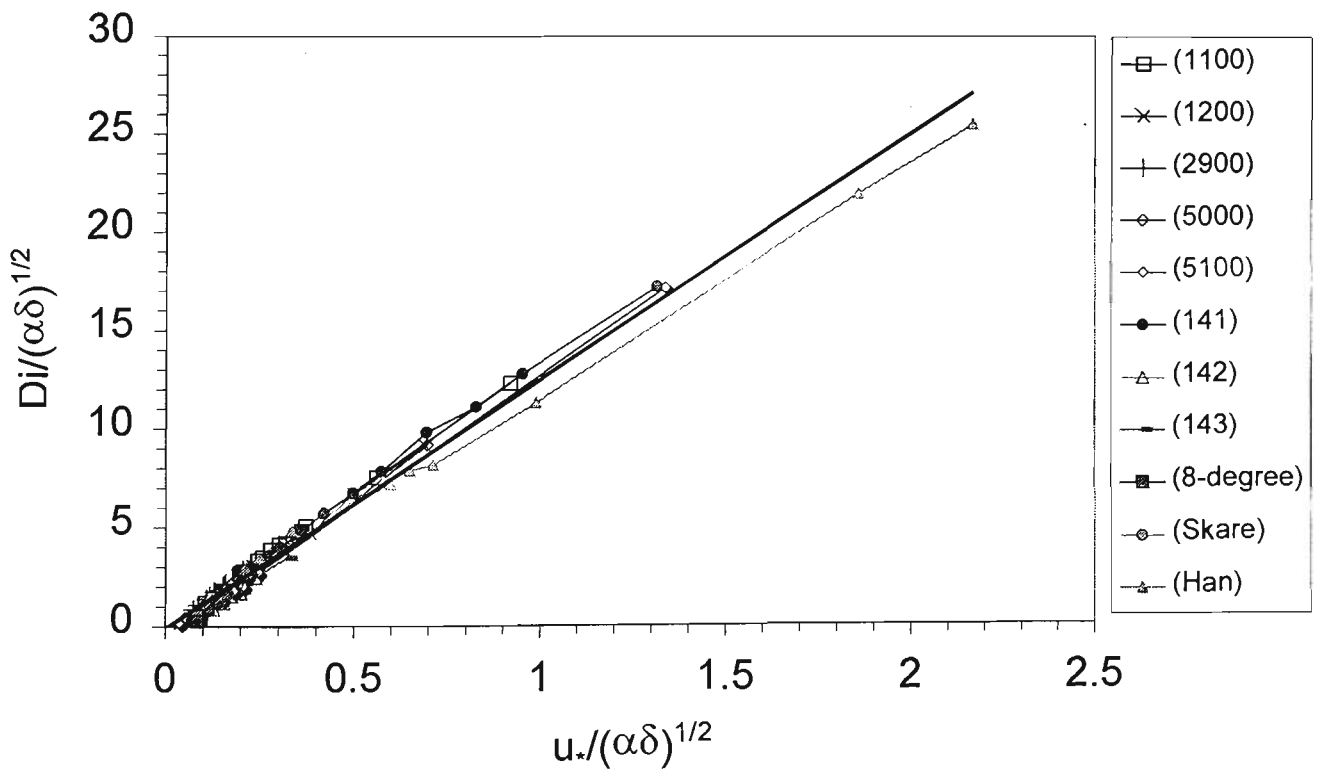


Figure 5.16 Inner half-power intercept. The solid line represents Equation 5.5.

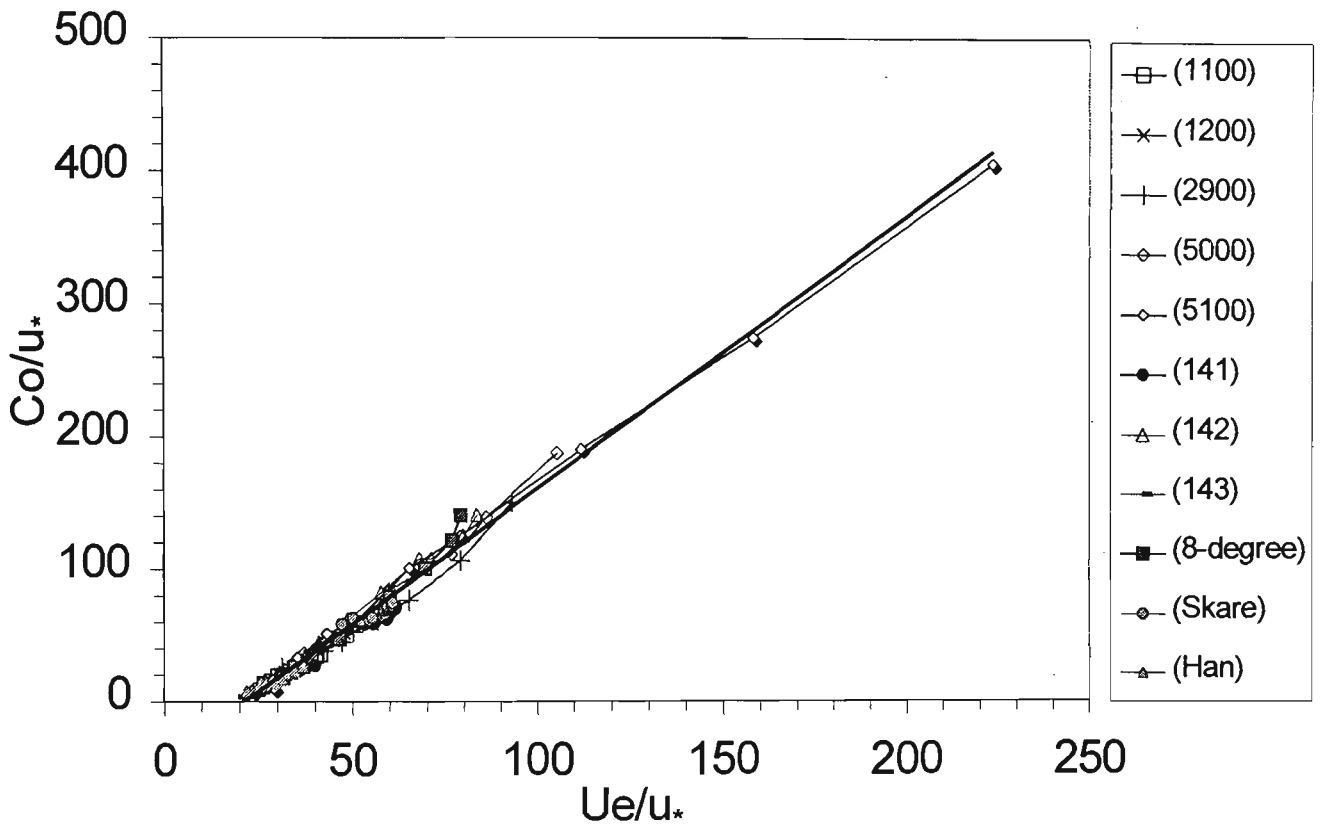


Figure 5.17 Outer half-power slope. The solid line represents Equation 5.7.

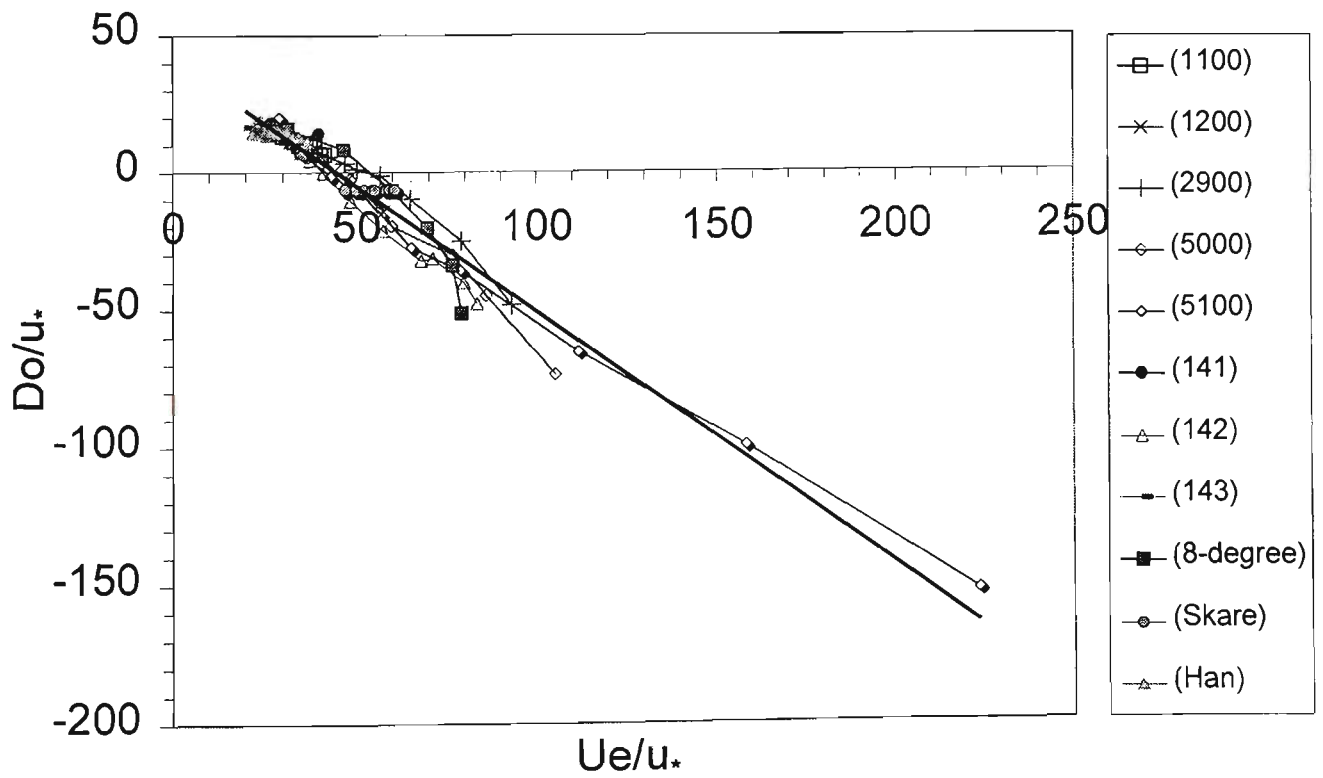
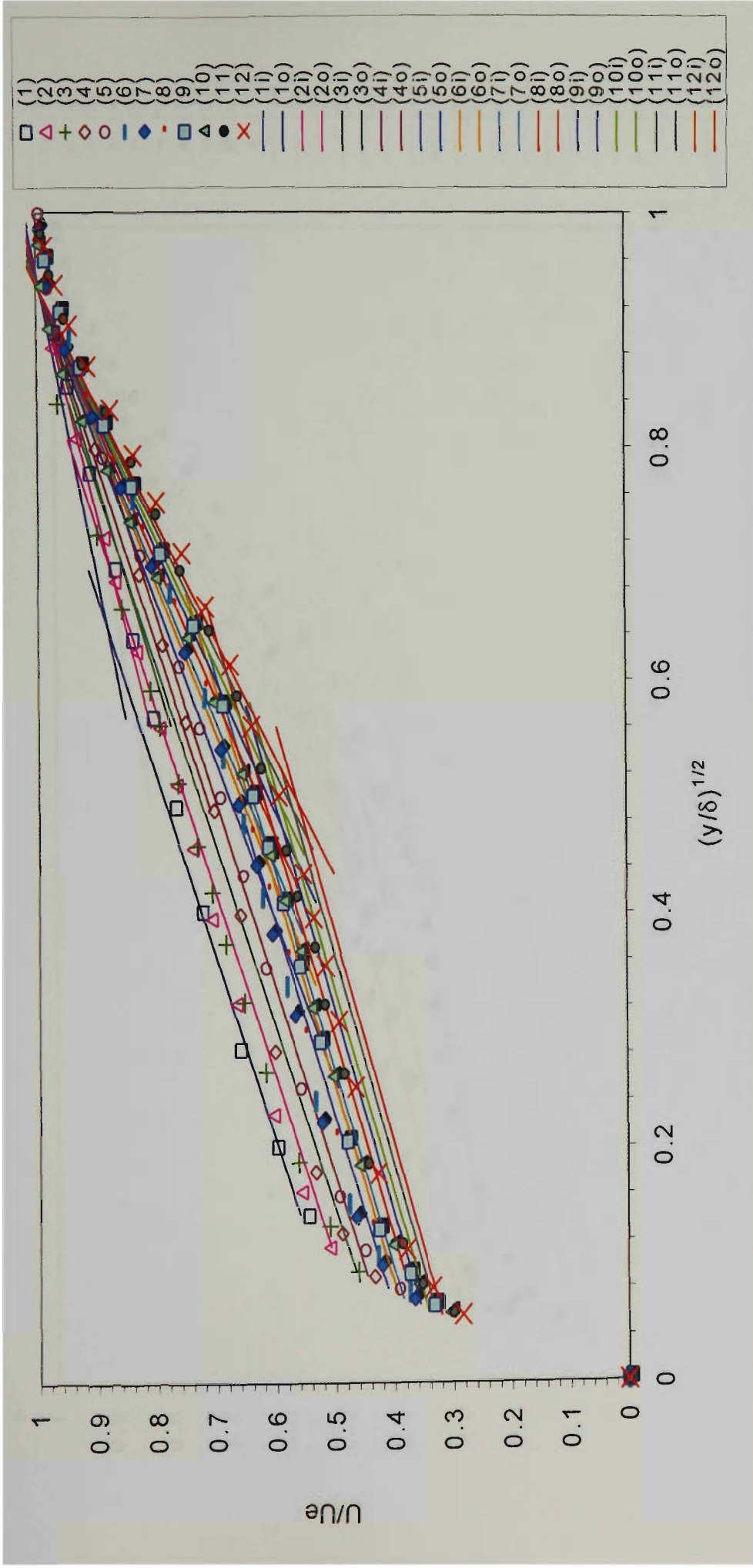
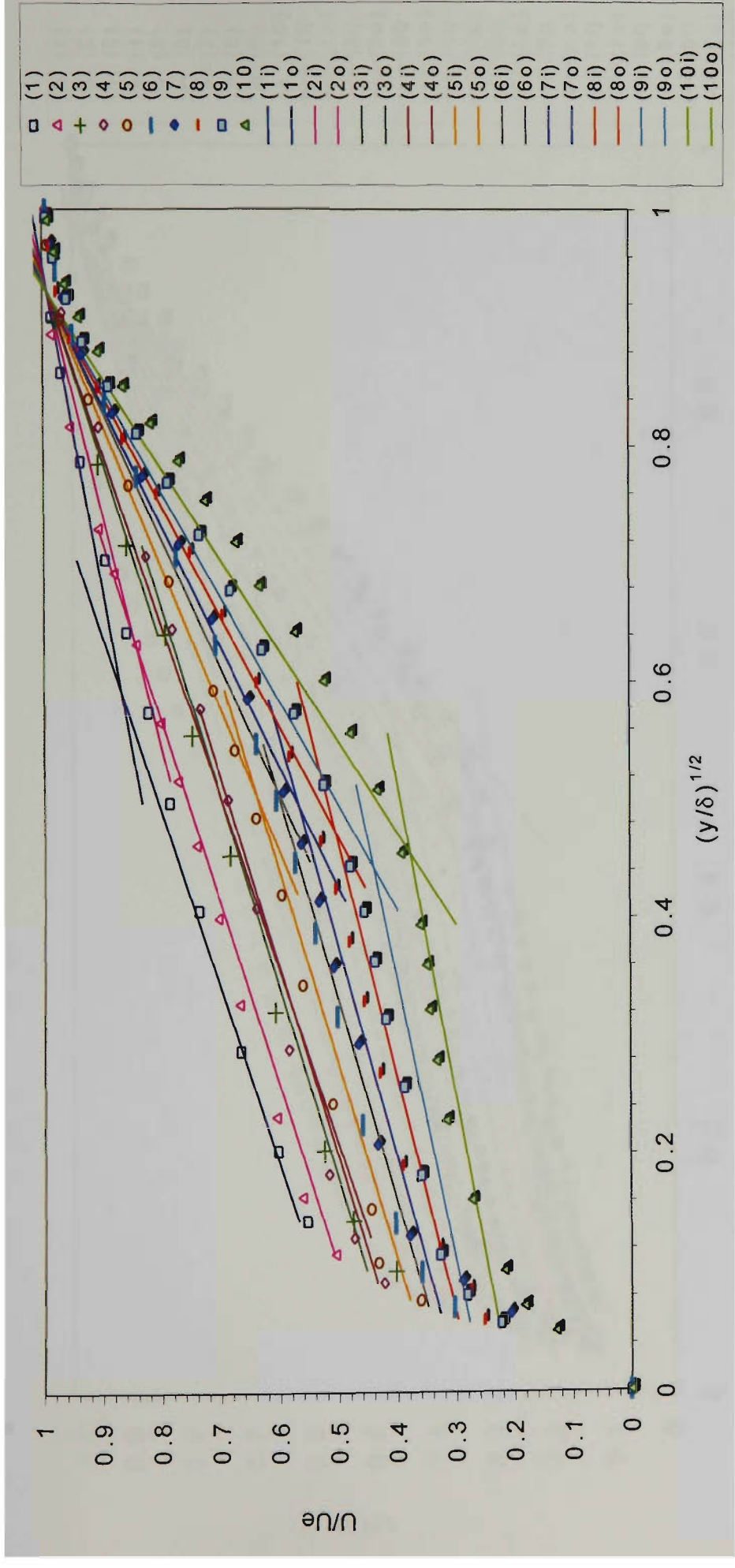


Figure 5.18 Outer half-power intercept. The solid line represents Equation 5.8.



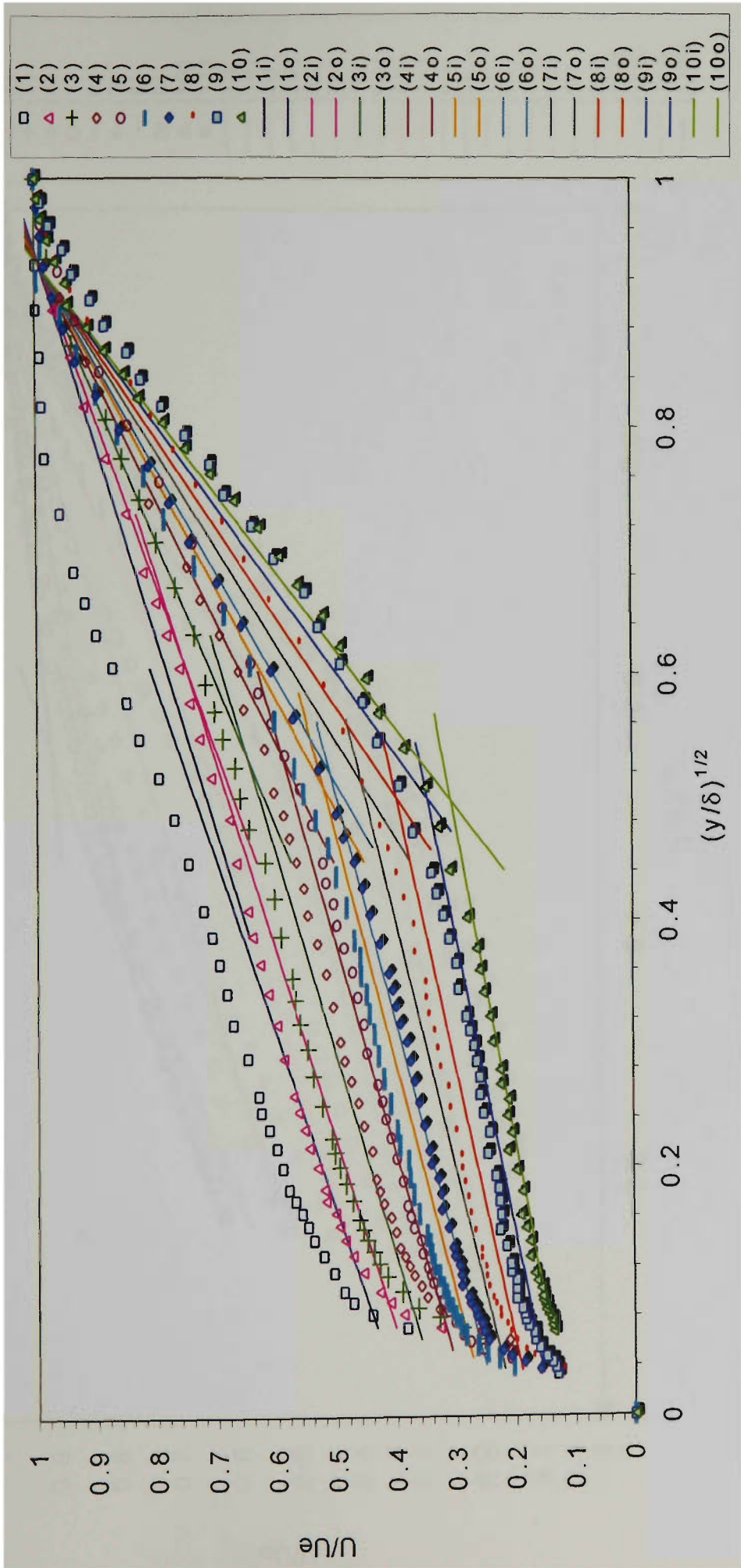
(a) Flow 1100.

Figure 5.19 Prediction of the half-power regions. The inner half-power lines are defined by Equations 5.1, 5.4 and 5.5. The outer half-power lines are defined by Equations 5.2, 5.7 and 5.8. Stations 1 to 12 correspond to 0.78, 1.28, 1.78, 2.28, 2.78, 3.13, 3.33, 3.53, 3.73, 3.93, 4.12, 4.33 m for the inlet, respectively.



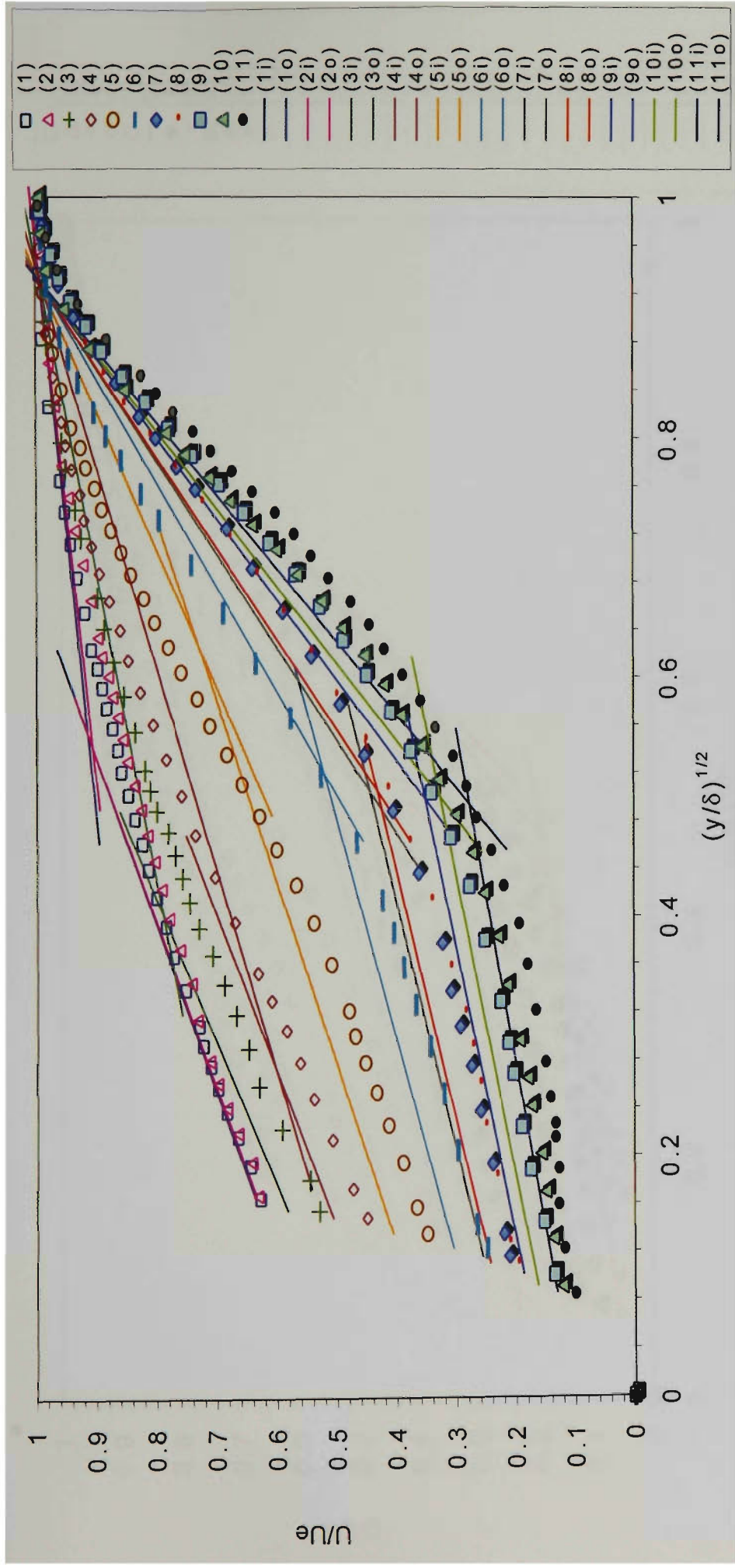
(b) Flow 1200.

Figure 5.19 Prediction of the half-power regions. The inner half-power lines are defined by Equations 5.1, 5.4 and 5.5. The outer half-power lines are defined by Equations 5.2, 5.7 and 5.8. Stations 1 to 10 correspond to 0.78, 1.28, 1.78, 2.28, 2.78, 3.13, 3.33, 3.53, 3.73, 3.93 m for the inlet, respectively.



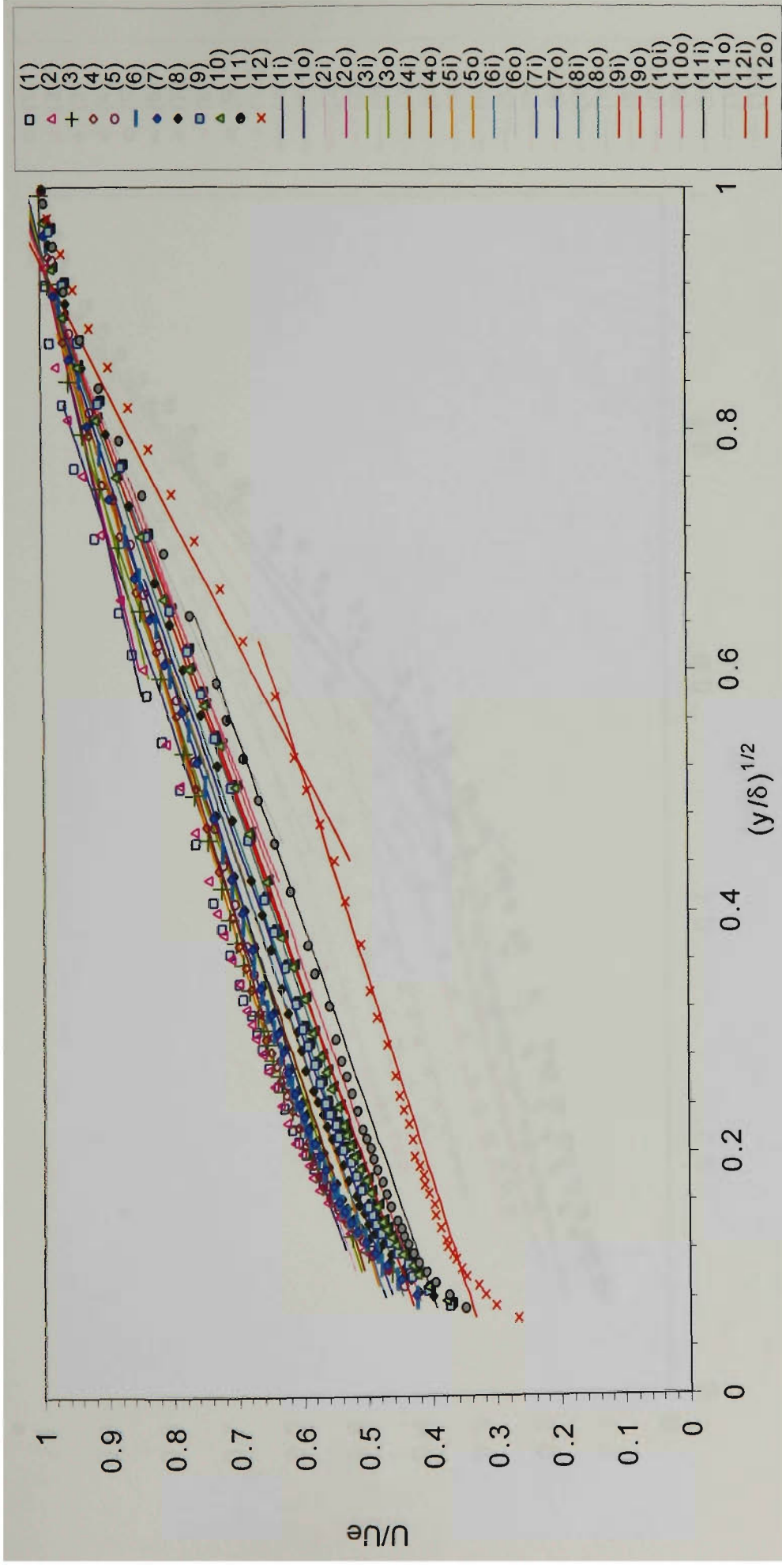
(c) Flow 2900.

Figure 5.19 Prediction of the half-power regions. The inner half-power lines are defined by Equations 5.1, 5.4 and 5.5. The outer half-power lines are defined by Equations 5.2, 5.7 and 5.8. Stations 1 to 10 correspond to 0.76, 1.22, 1.68, 2.13, 2.60, 3.05, 3.51, 3.81, 4.27, 4.57, m for the inlet, respectively.



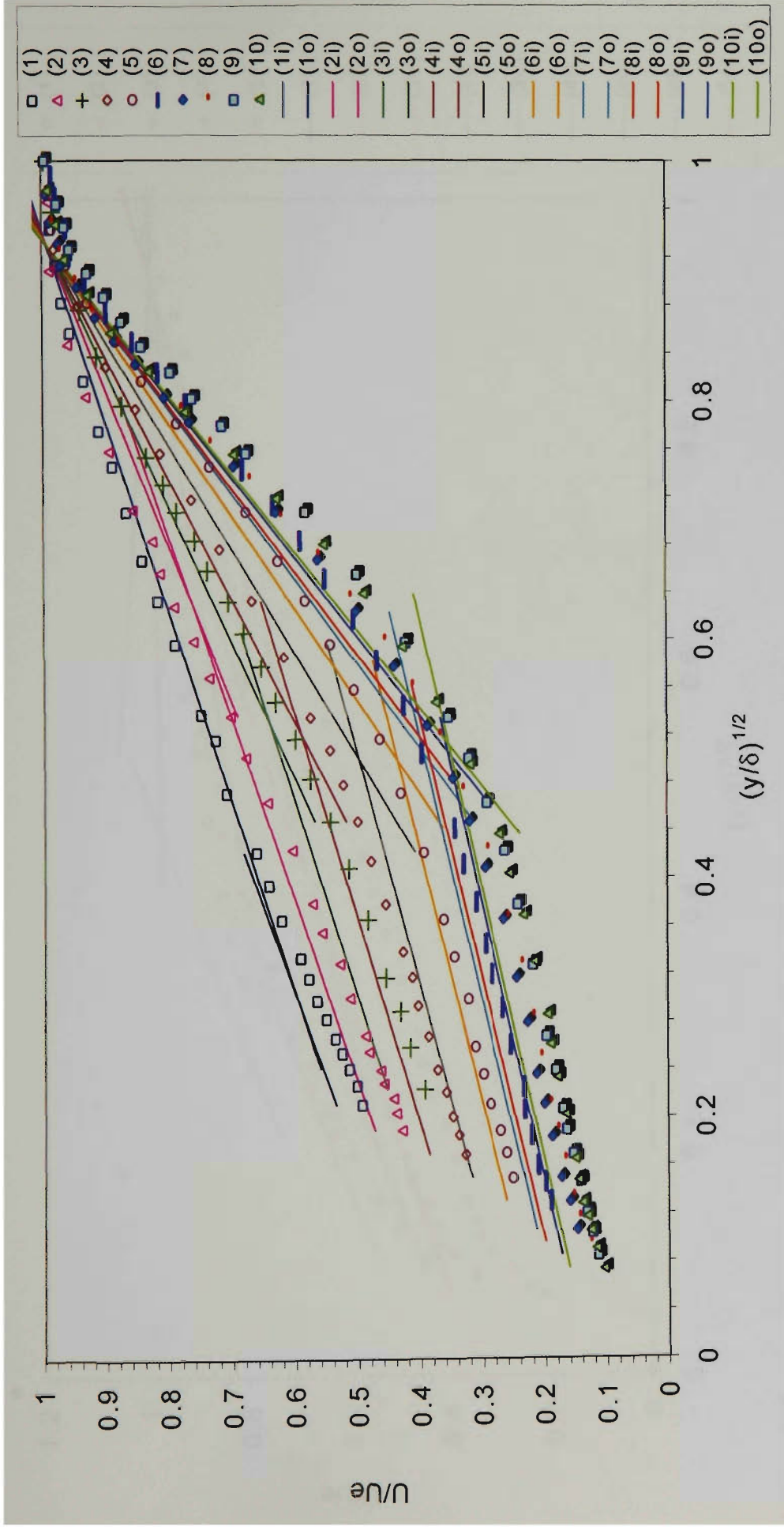
(d) Flow 5000.

Figure 5.19 Prediction of the half-power regions. The inner half-power lines are defined by Equations 5.1, 5.4 and 5.5. The outer half-power lines are defined by Equations 5.2, 5.7 and 5.8. Stations 1 to 11 correspond to 0.12, 0.16, 0.21, 0.24, 0.30, 0.38, 0.44, 0.47, 0.53, 0.58, 0.64 m for the inlet, respectively.



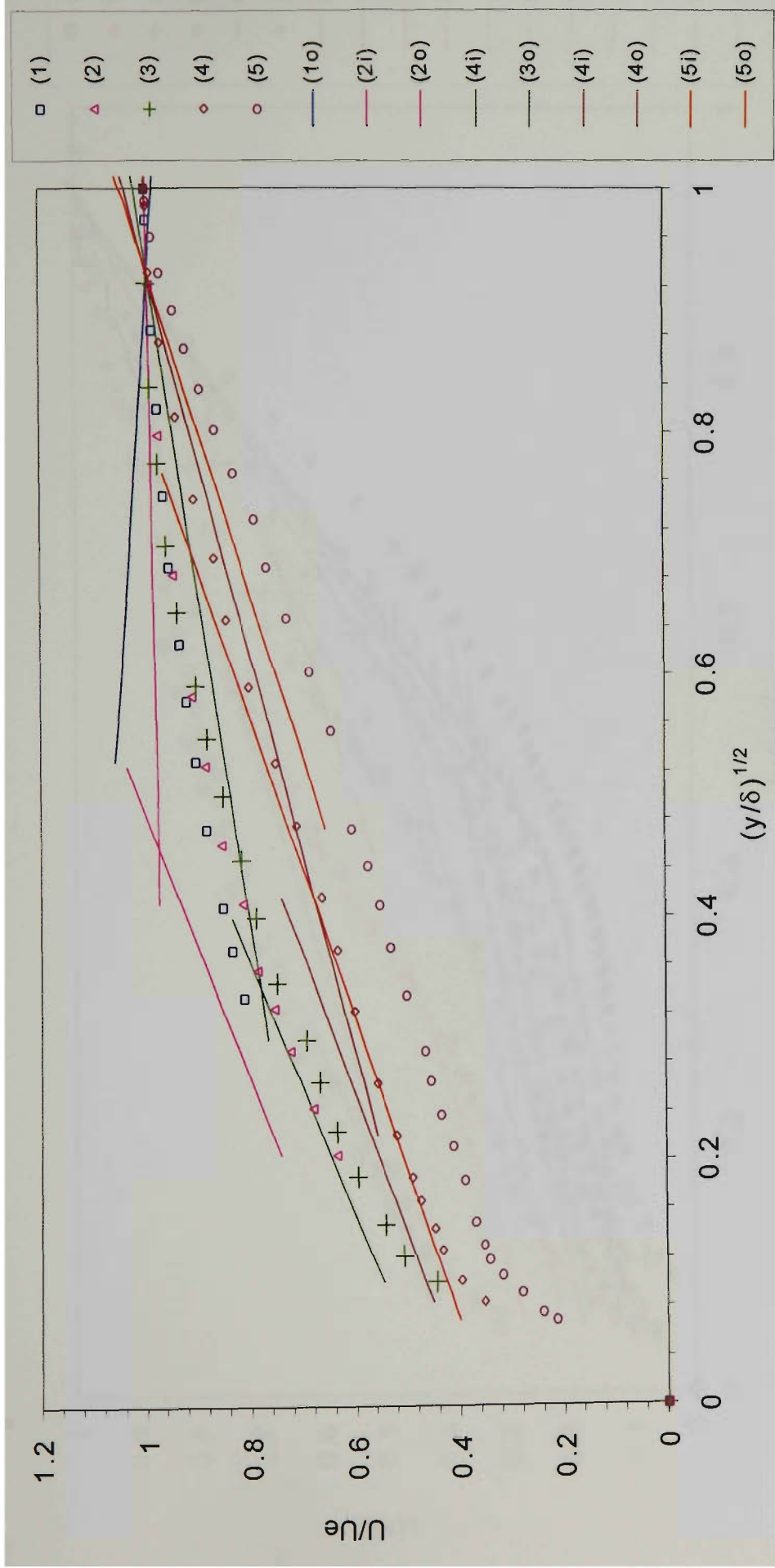
(f) Flow 141.

Figure 5.19 Prediction of the half-power regions. The inner half-power lines are defined by Equations 5.1, 5.4 and 5.5. The outer half-power lines are defined by Equations 5.2, 5.7 and 5.8. Stations 1 to 12 correspond to 0.86, 1.16, 1.44, 1.76, 2.10, 2.26, 2.40, 2.56, 2.72, 2.87, 3.04, 3.40 m for the inlet, respectively.



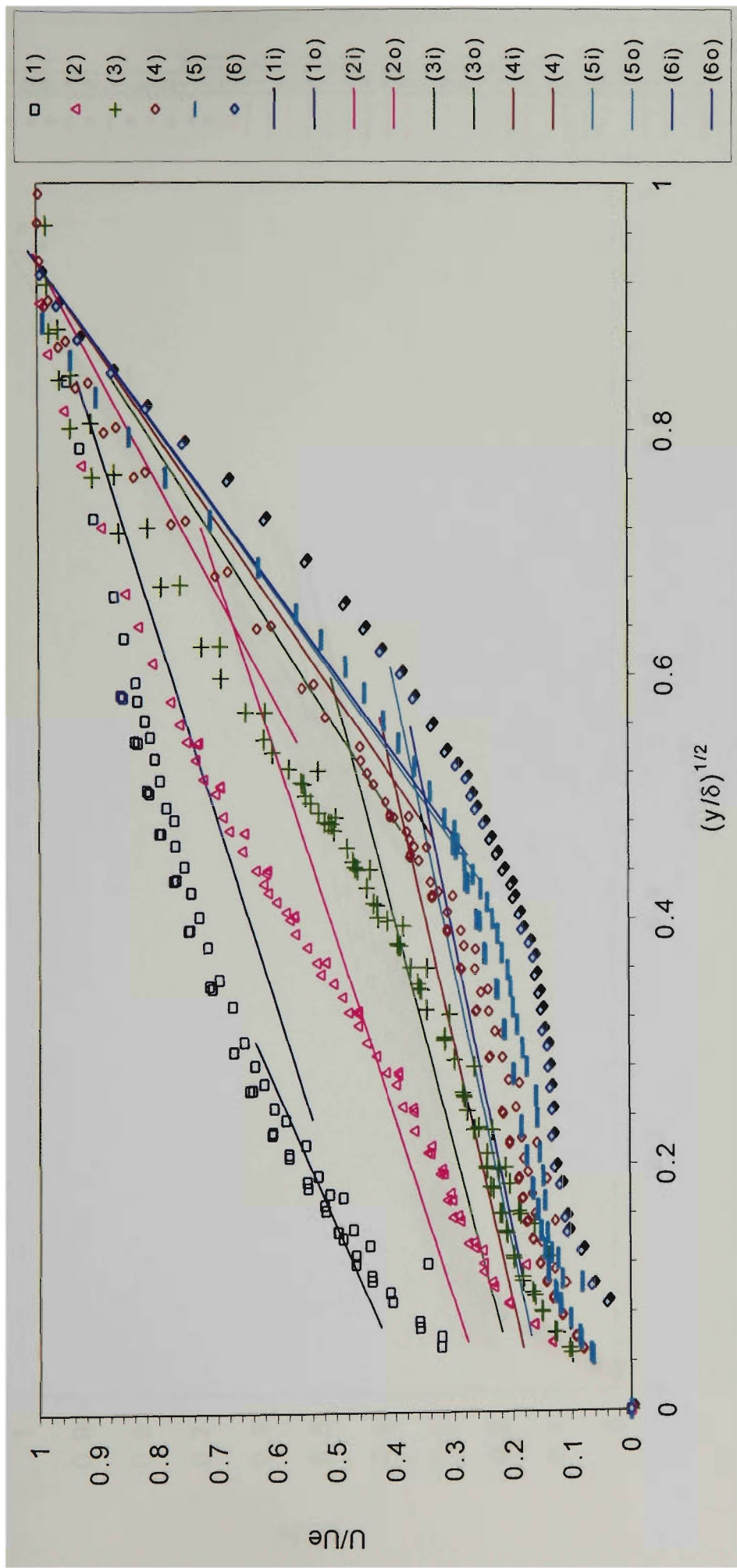
(g) Flow 142.

Figure 5.19 Prediction of the half-power regions. The inner half-power lines are defined by Equations 5.1, 5.4 and 5.5. The outer half-power lines are defined by Equations 5.2, 5.7 and 5.8. Stations 1 to 10 correspond to 0.1, 0.19, 0.29, 0.38, 0.57, 0.76, 1.05, 1.24, 1.53, 1.81 m for the inlet, respectively.



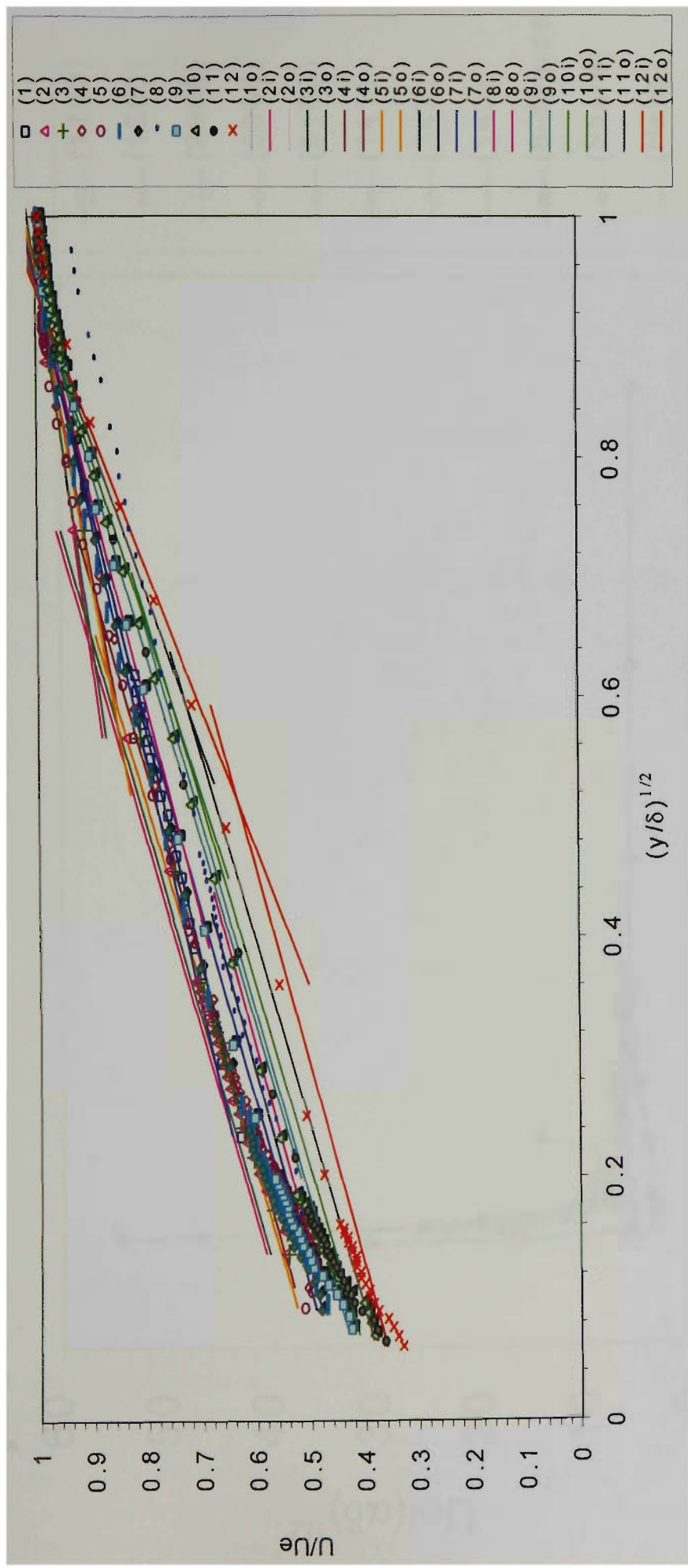
(h) Flow 143.

Figure 5.19 Prediction of the half-power regions. The inner half-power lines are defined by Equations 5.1, 5.4 and 5.5. The outer half-power lines are defined by Equations 5.2, 5.7 and 5.8. Stations 1 to 5 correspond to -0.06, 0.10, 0.57, 1.05, 1.81 m for the inlet, respectively. At station 1, the inner half-power line is not shown, since $\alpha < 0$ for this station.



(i) Flow 8-degree.

Figure 5.19 Prediction of the half-power regions. The inner half-power lines are defined by Equations 5.1, 5.4 and 5.5. The outer half-power lines are defined by Equations 5.2, 5.7 and 5.8. Stations 1 to 6 correspond to 0.06, 0.18, 0.30, 0.42, 0.54, 0.66 m for the inlet, respectively.



(k) Flow Han.

Figure 5.19 Prediction of the half-power regions. The inner half-power lines are defined by Equations 5.1, 5.4 and 5.5. The outer half-power lines are defined by Equations 5.2, 5.7 and 5.8. Stations 1 to 12 correspond to 0.26, 1.09, 1.25, 1.87, 2.34, 2.42, 2.67, 2.83, 3.32, 3.70, 3.90, 4.35 m for the inlet, respectively. At station 1, the inner half-power line is not shown, since $\alpha < 0$ for this station.

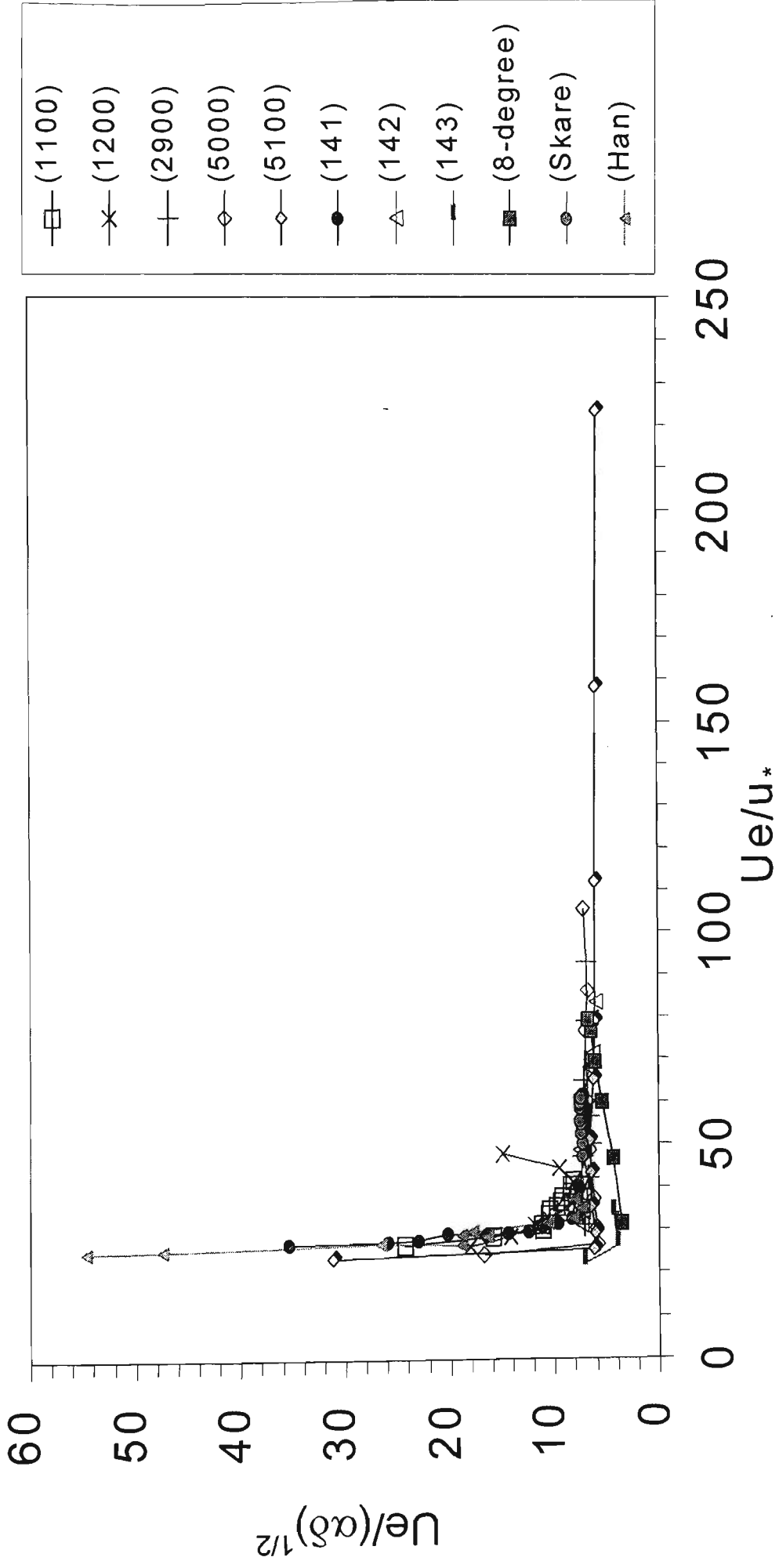
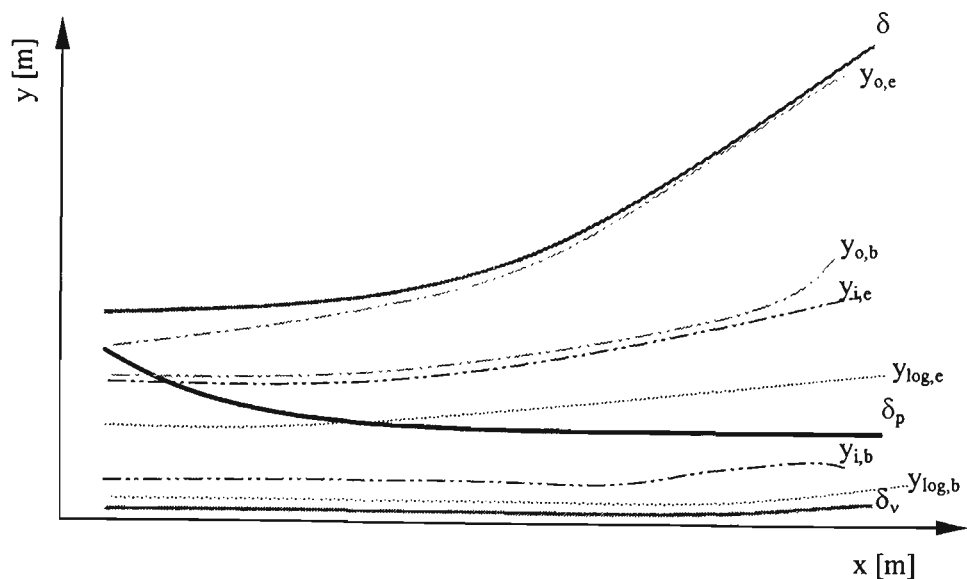
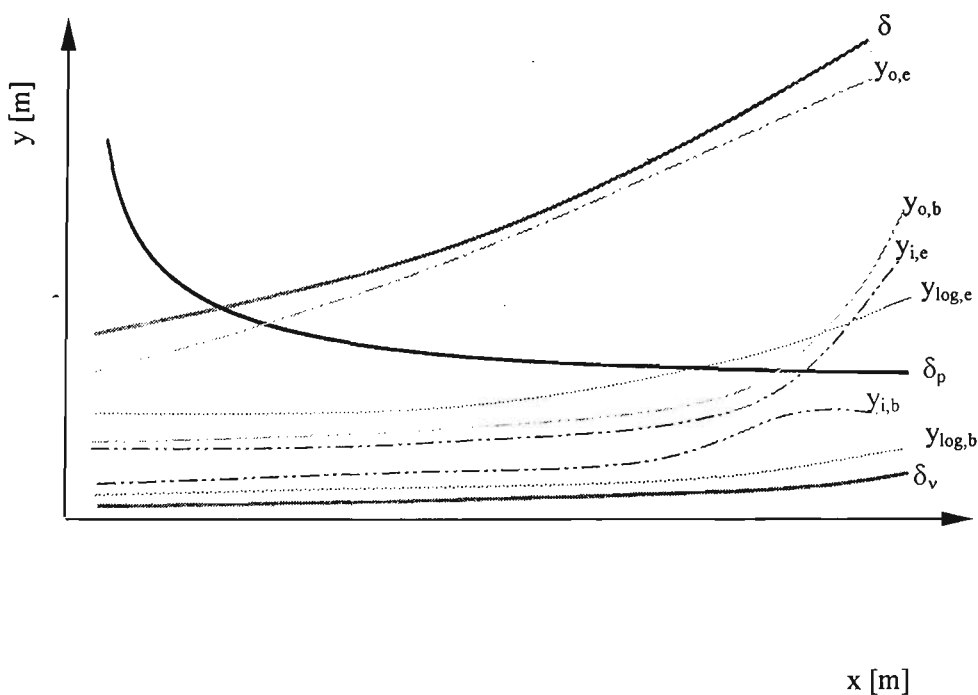


Figure 5.20 Equilibrium and moving equilibrium behaviour.

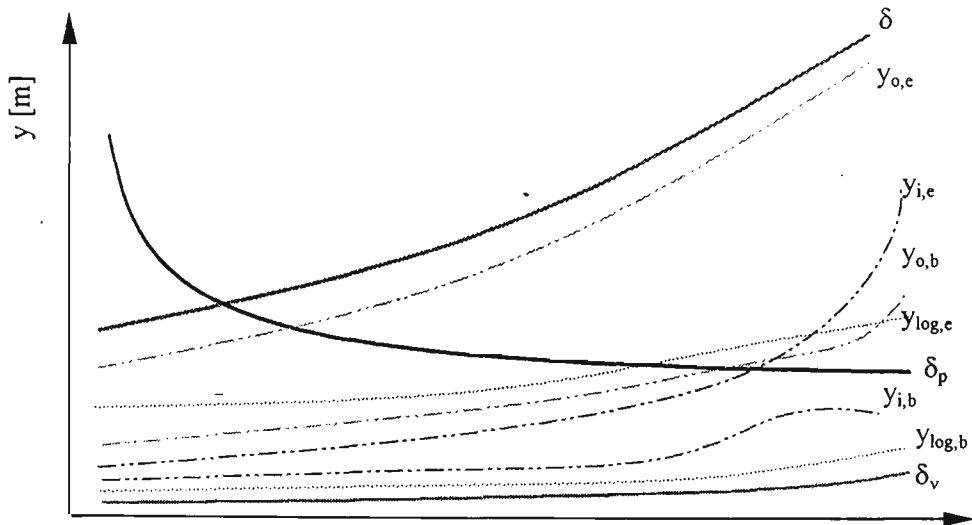


(a) Length scales in Flows 1100, 1200, 2900, 5000, 5100, 142, 143, 8-degree and Skåre.



(b) Length scales in Flow 141.

Figure 5.21 Length scales. The viscous length scale, pressure gradient length scale and boundary layer thickness are denoted as δ_v , δ_p and δ , respectively. The beginning and end of the logarithmic regions are denoted as $y_{\log,b}$ and $y_{\log,e}$, respectively. The beginning and end of the inner half power regions are denoted as $y_{i,b}$ and $y_{i,e}$, respectively. The beginning and end of the outer half power regions are denoted as $y_{o,b}$ and $y_{o,e}$, respectively.



(c)) Length scales in Flow Han.

Figure 5.21 Length scales. The viscous length scale, pressure gradient length scale and boundary layer thickness are denoted as δ_v , δ_p and δ , respectively. The beginning and end of the logarithmic regions are denoted as $y_{\log,b}$ and $y_{\log,e}$, respectively. The beginning and end of the inner half power regions are denoted as $y_{i,b}$ and $y_{i,e}$, respectively. The beginning and end of the outer half power regions are denoted as $y_{o,b}$ and $y_{o,e}$, respectively.

Chapter 6. Conclusions

The conclusions of this study can be summarized as follows:

1. A flexible setup has been prepared in a wind tunnel to allow thorough experimental examination of increasing adverse pressure gradient turbulent flows. This setup has a flexible top placed inside the test section. The false bottom with static pressure taps allows monitoring of the pressure distribution. The same setup can also be used to generate decreasing adverse pressure gradient cases.
2. A calibration rig has been prepared consisting of a fully-developed turbulent pipe flow setup. This rig can be used for the calibration of Preston tubes and x-wire probes for hot-wire anemometry measurements.
3. One increasing adverse pressure gradient case has been examined in the wind tunnel for its mean flow characteristics. Subsequently, these results have been compared with the mean flow profiles of ten other adverse pressure gradient flows from the literature.
4. For the case generated in the wind tunnel, similar friction velocity values are obtained using Preston's method (Preston, 1954) with Patel's correction (Patel, 1965) and using Clauser plots (Clauser, 1954).

5. The Frei and Thomann (1980) correction was not needed on the friction velocity values obtained using Preston's method.

6. The eleven flows examined indicate the presence of inner and outer half-power regions in the mean velocity profiles. Within these regions, the mean velocity is given as follows:

$$\frac{U}{u_*} = \frac{C_i}{u_*} \left(\frac{y}{\delta} \right)^{\frac{1}{2}} + \frac{D_i}{u_*} \quad \text{inner half-power profile, and}$$

$$\frac{U}{U_e} = \frac{C_o}{U_e} \left(\frac{y}{\delta} \right)^{\frac{1}{2}} + \frac{D_o}{U_e} \quad \text{outer half-power profile.}$$

7. The inner and outer half-power parameters can be expressed approximately as follows:

$$\frac{C_i}{\sqrt{\alpha\delta}} = 15.28 \frac{u_*}{\sqrt{\alpha\delta}} + 1.52,$$

$$\frac{D_i}{\sqrt{\alpha\delta}} = 12.57 \frac{u_*}{\sqrt{\alpha\delta}} - 0.13,$$

$$\frac{C_o}{u_*} = 2.06 \frac{U_e}{u_*} - 44.22, \text{ and}$$

$$\frac{D_o}{u_*} = -0.92 \frac{U_e}{u_*} + 41.14.$$

8. The resulting predicted half-power profiles follow the experimental trends, provided that the given adverse pressure gradient flow is in moving equilibrium, defined by

$\frac{U_e}{\sqrt{\alpha\delta}} > 6$ (Kader and Yaglom, 1978). Judging by the two increasing adverse pressure cases, this result appears to be independent of the type of adverse pressure gradient.

9. In decreasing adverse pressure gradient flows, the inner half-power region extends from within the logarithmic region to above the pressure gradient length scale. After a short overlapping region, it is followed by the outer half-power region almost to the edge of the boundary layer.

10. In increasing adverse pressure gradient flows, the inner half-power region remains fully within the logarithmic law region. Consequently, the outer half-power region starts below the pressure gradient length scale, but similar to decreasing adverse pressure gradient cases, it extends almost to the boundary layer's edge.

REFERENCES

Abbott, I.H. and Von Doenhoff, A.E. 1949 Theory of wing sections. McGraw-Hill.

Antonia, R.A. Browne, L.W.B. and Bisset, D. K. 1990 Effect of Reynolds number on the organised motion in a turbulent boundary layer, In Near-wall Turbulence, (eds. S.J. Kline and N.H. Afgan), Hemisphere Pub. Co.

Bisset, D.K. Antonia, R.A. and Browne, L.W.B. 1990 Spatial organisation of large structures in the far wake of a cylinder. *Journal of Fluid Mechanics*, vol.218, pp. 439-461.

Bradshaw, P. 1967 The turbulent structure of equilibrium turbulent boundary layers. *Journal of Fluid Mechanics*, vol. 29, pp. 625-645.

Bradshaw, P. 1976 *Complex Turbulent Flows, Theoretical and Applied Mechanics*. W.T. Koiler, ed., North Holland Publishing co., pp.103-113.

Brown, K.C. and Joubert, P.N. 1969 The measurement of skin friction in turbulent boundary layers with adverse pressure gradient. *Journal of Fluid Mechanics*, vol. 35, pp. 737-757.

Cockrell, D. Hill, P. Lumley, J. Morkovin, M. and Emmons, H. 1968 Report from the evaluation committee. In *Proc. Computation of Turbulent Boundary Layers*, AFOSR-

IFP-Stanford Conference (ed. S.J. Kline, M.V. Morkovin, G. Sovran and D.J. Cockrell), vol. 1, pp. 464-478.

Chukkapalli, G. and Turan, Ö.F. 1992 An improve k- ϵ turbulence model for prediction of adverse pressure gradient turbulent flows. Preprint Volume of the Thirteenth Symposium on Turbulence (ed. X B Reed, G.K. Patterson and J.L. Zakin), Department of Chemical Engineering, University of Missouri-Rolla, Sept. 21-23, pp. A28-1 – A28-10. F.

Chukkapalli, G. and Turan, Ö.F. 1995 Structural parameters and prediction of adverse pressure gradient turbulent flows: An improved k- ϵ model. ASME Journal of Fluids Engineering, vol. 117, pp. 424-432.

Clauser, F.H. 1954 Turbulent boundary layers in adverse pressure gradients. Journal of Aeronautical Science, Feb.

Coles, D.E. 1955 The law of the wall in turbulent shear flow. 50 Jahre Grenzschichtforschung, Eine Festschrift in Originalbeiträgen, pp. 153-163.

Coles, D.E. 1956 The law of the wake in the turbulent boundary layer. Journal of Fluid Mechanics, vol. 1,(2) pp. 191-226.

Coles, D.E. and Hurst, E.A. 1968 Computation of turbulent boundary layers – 1968 AFOSR –IFP – Stanford Conference, 1968.

Dang, T. 1987 Experimental investigation of the hot-film anemometry in fully-developed turbulent pipe flow. M.Sc. Thesis, Mechanical Engineering Department, University of Manitoba.

East, L.F. and Sawyer, W.G. 1979 An investigation of the structure of equilibrium turbulent boundary layers. In *Turbulent Boundary Layers: Experiment Theory and Modeling*, AGARD CP-271, 6.1-6.19

Feri, D. and Thomann, H. 1980 Direct measurements of skin friction in a turbulent boundary layer with a strong adverse pressure gradient. *Journal of Fluid Mechanics*, vol. 101, pp. 79-95.

Gerhart, P.M. and Gross, R.J. 1985 *Fundamentals of fluid mechanics*. Addison-Wesley Publishing Company, 1st ed. Ch. 7 and 9.

George, W.K., Beuther, P.D. and Arndt R.E.A. 1984 Pressure Spectra in Turbulent Free Shear Flows. *Journal of Fluid Mechanics*, vol. 148, pp. 155-191.

Goldstein, S. 1965 *Modern Developments in Fluid Dynamics*, vol.2, Dover.

Granville, P.S. 1989 A modified Van Driest formula for the mixing length of turbulent boundary layers in pressure gradients. *ASME Journal of Fluids Engineering*, vol. 111, pp. 94-97.

Hayakawa, A.M. and Hussain, F. 1989 Three-dimensionality of organisation structures in a plane turbulent wake. *Journal of Fluid Mechanics*, vol. 206, pp. 375-404.

Hinze, J.O. 1975 *Turbulence*. McGraw-Hill, 2nd ed., Ch. 7.

Kader, B.A. and Yaglom, A.M. 1978 Similarity treatment of moving equilibrium turbulent boundary layers in adverse pressure gradients. *Journal of Fluid Mechanics*, vol. 89, pp. 305-342.

Kassab, S.Z. 1986 *Turbulence structure in axisymmetric wall-bounded shear flow*. Ph.D. Thesis, University of Manitoba.

Kim, J. Moin, P. and Moser, R. 1987 Turbulence statistics in fully developed channel flow at low Reynolds number. *Journal of Fluid Mechanics*, vol. 117, pp. 133-166.

Kline, S.J. Cantwell, B.J. and Lilley, G.M. 1981 1980-81 AFOSR – HTTM – Stanford Conference on Complex Turbulent Flows.

Kopp, G.A. and Turan, Ö.F. 1992 Two half power regions in turbulent decreasing adverse pressure gradient flows. Preprint Volume, Thirteenth Symposium on Turbulence (Ed. XB Reed, G.K. Patterson and J.L. Zakin, Department of Chemical Engineering, University of Missouri-Rolla, September, 21-23) pp. B36-1 - B36-10.

Lai, Y.G. So, R.M.C. and Hwang, B.C. 1989 Calculation of planar and conical diffuser flows. *American Institute of Aeronautics and Astronautics Journal*, vol. 27, pp. 542-548.

Moser, R.D. Kim, J. and Mansour, N.N. 1999 Direct numerical simulation of turbulent channel flow up to $Re_\tau = 590$. *Physics of Fluids*, vol. 11 (4), pp. 943-945.

Musker, A.J. 1979 Explicit expression for the smooth wall velocity distribution in a turbulent boundary layer. *American Institute of Aeronautics and Astronautics Journal*, vol. 17, pp. 655-657.

McDonald, H. 1969 The effect of pressure gradient on the law of the wall in turbulent flow. *Journal of Fluid Mechanics*, vol. 35; part2, pp. 311-336.

Ozimek, L.G. 1985 Comparison of analog and digital data for measurements of turbulence parameters, M.Sc. Thesis, University of Manitoba.

Perry, A.E. 1966 Turbulent boundary layers in decreasing adverse pressure gradients. *Journal of Fluid Mechanics*, vol. 26, part3, pp. 481-506.

Perry, A.E. Bell, J.B. and Joubert, P.N. 1966 Velocity and temperature profiles in adverse pressure gradient turbulent boundary layers. *Journal of Fluid Mechanics*, vol. 25, part 2, pp. 299-320.

Perry, A.E and Schofield, W.H. 1973 Mean velocity and shear stress distributions in turbulent boundary layers. *Physics of Fluids*, vol. 16(12), pp. 2068-2074.

Preston, J.H. 1950 The Three-quarter radius pitot tube flow meter. *The Engineer*, vol. 190, pp. 400-402.

Preston, J.H. 1954 The determination of turbulent skin friction by means of pitot tubes. *Journal of the Royal Aeronautical Society*, vol. 58, pp. 109-121.

Pauley, L.L. Moin, P. and Reynolds, W.C. 1990 The structure of two-dimensional separation. *Journal of Fluid Mechanics*, vol. 220, pp. 397-411.

Sandborn, V.A. and Slogar, R.J. 1955 N.A.C.A. Technical Note, No. 3264.

Samuel, A.E. and Joubert, P.N. 1974 A boundary layer developing in an increasingly adverse pressure gradient. *Journal of Fluid Mechanics*, vol. 66 (3), pp. 481-505.

Selby, G.V. Lin, J.C. and Howard, F.G. 1990 Turbulent flow separation control over a backward facing ramp via transverse and swept grooves. *ASME Journal of Fluids Engineering*, vol. 112, pp. 238-240.

Shåre, P.E. and Krogstad, P.-Å. 1994 A turbulent equilibrium boundary layer near separation. *Journal of Fluid Mechanics*, vol. 272, pp. 319-348.

Shåre, P.E. 1994 Experimental investigation of an equilibrium boundary layer in strong adverse pressure gradient. Ph.D. thesis. University of Trondheim, The Norwegian Institute of Technology, Norway.

Simpson, R.L. 1981 A review of some phenomena in turbulent flow separation. ASME Journal of Fluids Engineering, vol. 103, pp. 520-533.

Simpson, R.L. 1983 A model of for the backflow mean velocity profile. American Institute of Aeronautics and Astronautics Journal, vol. 21, pp. 142-143.

Simpson, R.L. and Shivaprasad, B.G. 1983 The structure of a separating turbulent boundary layer. Part 5. Frequency effect on periodic unsteady free-stream flows. Journal of Fluid Mechanics, vol. 131, pp. 319-339.

Stratford, B.S. 1959 The prediction of separation of the turbulent boundary layer. Journal of Fluid Mechanics, vol. 5, pp. 1-16.

Stropky, D.M. Djilali, N. Gartshore, I.S. and Salcudean, M. 1990 Application of momentum integral methods and linearized potential theory for predicting separation bubble characteristics. ASME Journal of Fluids Engineering, vol. 112, pp. 416-424.

Tennekes, H. and Lumley, J.L. 1972 A first course in turbulence. The Massachusetts Institute of Technology Press, ch.1 & 5.

Townsend, A.A. 1960 Equilibrium layers and wall turbulence. *Journal of Fluid Mechanics*, vol. 11, pp. 97-120.

Townsend, A.A. 1976 *The structure of turbulent shear flow*. Cambridge University Press, 2nd ed., ch. 7.

Turan, Ö.F. Azad, R.S. and Kassab, S.Z. 1987 Experimental and theoretical evaluation of the K^{-1} spectral law. *Physics of Fluids*, vol. 30(11), pp. 3463-3474.

Turan, Ö.F. 1988 A new method of evaluating turbulence dissipation. Ph.D. thesis. University of Manitoba, Canada.

Turan, Ö.F. and Azad, R.S. 1989 Effect of hot-wire probe defects on a new method of evaluating turbulence dissipation. *Journal of Physics E: Scientific Instruments*, vol. 22, pp. 254-261.

Turan, Ö.F. and Azad, R.S. 1993 Comparison of the zero-wire length dissipation technique with spectral corrections and the effect of high turbulence intensity. *Experimental Thermal and Fluid Science*, vol. 6, pp. 292-308.

White, F.M. 1994 *Fluid mechanics*. McGraw-Hill, 3rd ed., Ch. 7.

Wilcox, D.C. 1993 *Turbulence Modeling for CFD*. DCW Industries, Inc., 1st ed., Ch. 2.

Appendix A. Preliminary Tests in the Wind Tunnel

In the following, 20 trial cases are presented each corresponding to a different flexible top shape in the test section. For each case, in Table (a), the coordinates of the flexible top are given. In Table (b), the corresponding pressure distribution, and its first and second streamwise derivatives are listed. In Figure (a), the values listed in Table (a) are plotted to illustrate the flexible top shape. In Figures (b), (c) and (d), respectively, the corresponding pressure distribution and its first and second streamwise derivatives are plotted against the longitudinal coordinate, x . The chosen case in Chapter 4 is Case 19.

x [mm]	y [mm]
0	740
75	720
670	580
1260	455
1760	385
1990	360
2260	350
2770	380
3270	450
3850	570
4445	705
4670	780

Table A.1. (a)

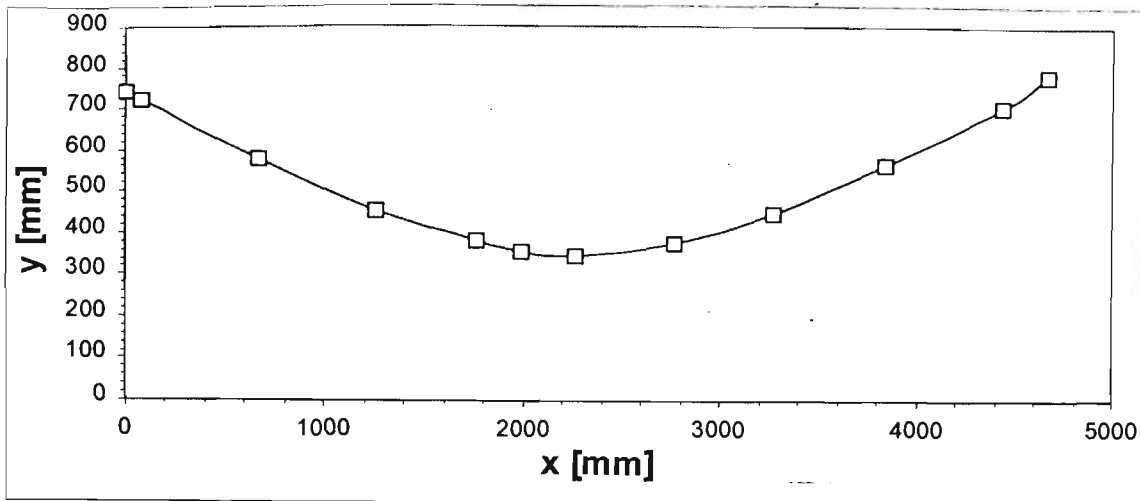


Figure A.1. (a)

x [mm]	P [mmH ₂ O]	dP/dx [mmH ₂ O/mm]	d ² P/dx ² [mmH ₂ O/mm ²]
100	16.7	0.0664	-1.1E-05
250	16.6	-0.0027	-0.00024
400	15.9	-0.0070	-2.9E-05
550	14.5	-0.0113	-2.9E-05
700	12.5	-0.0157	-2.3E-05
850	9.8	-0.0183	-2.3E-05
1000	7.0	-0.0227	-0.00002
1150	3.0	-0.0243	-1.9E-05
1300	-0.3	-0.0283	-4.6E-05
1450	-5.5	-0.0380	-7.6E-05
1600	-11.7	-0.0510	-0.00012
1750	-20.8	-0.0750	-0.00017
1900	-34.2	-0.1030	-7.3E-05
2050	-51.7	-0.0970	0.000192
2200	-63.3	-0.0454	0.000379
2352	-65.4	0.0175	0.000346
2502	-58.0	0.0590	0.000144
2652	-47.7	0.0607	-3.1E-05
2802	-39.8	0.0497	-6E-05
2952	-32.8	0.0427	-5.2E-05
3102	-27.0	0.0340	-0.00005
3252	-22.6	0.0277	-3.3E-05
3402	-18.7	0.0240	-2.6E-05
3552	-15.4	0.0200	-2.4E-05
3702	-12.7	0.0167	-0.00002
3852	-10.4	0.0140	-2.1E-05
4002	-8.5	0.0103	-1.7E-05
4152	-7.3	0.0090	-1.1E-05
4302	-5.8	0.0070	-1.3E-05
4452	-5.2	0.0050	-1E-05
4602	-4.3	0.0040	-2E-05
4752	-4.0	-0.0009	8.69E-07

Table A.1. (b)

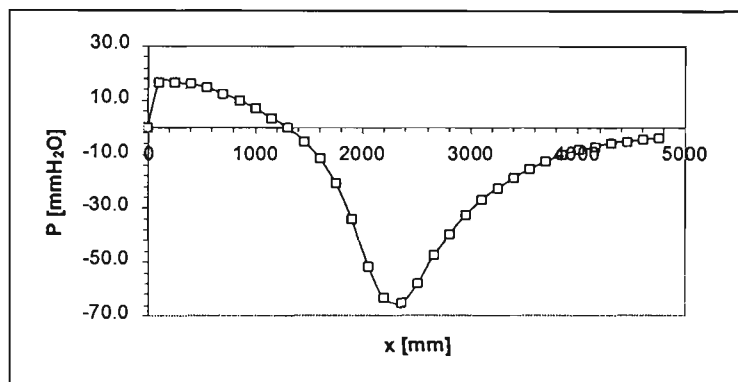


Figure A.1. (b)

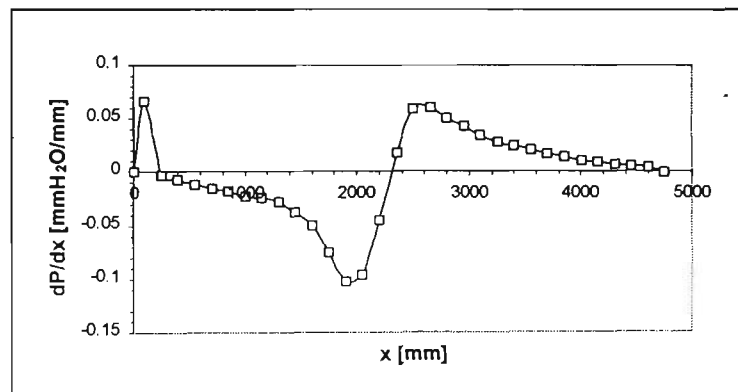


Figure A.1. (c)

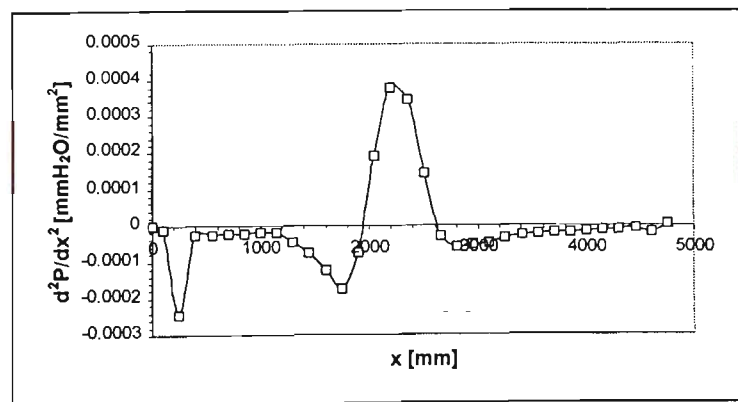


Figure A.1. (d)

x [mm]	y [mm]
0	745
615	505
1200	375
1700	345
2225	355
2765	405
3283	483
3868	575
4472	703
4672	728

Table A.2. (a)

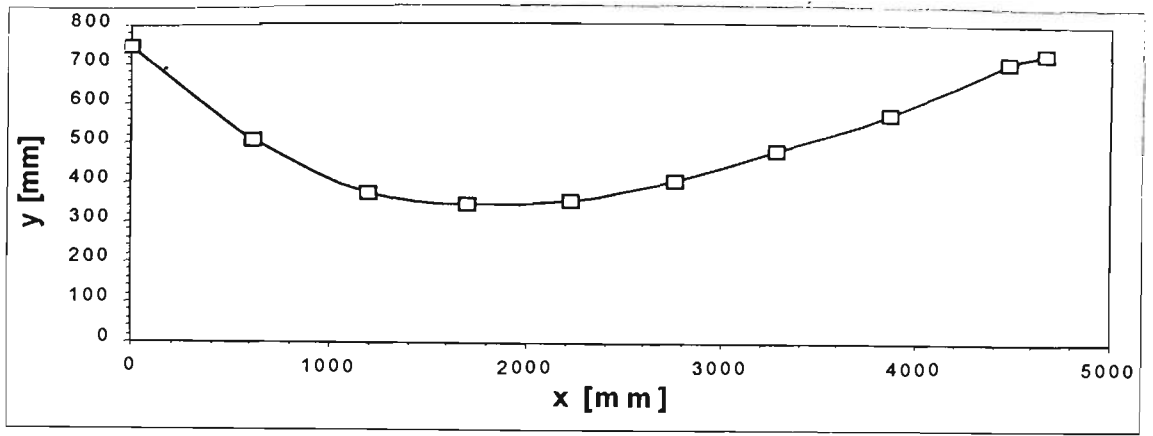


Figure A.2. (a)

x [mm]	P [mmH ₂ O]	dP/dx [mmH ₂ O/mm]	d ² P/dx ² [mmH ₂ O/mm ²]
100	8.0	0.0308	-3.5E-05
250	7.7	-0.0087	-0.00017
400	5.4	-0.0190	-0.00006
550	2.0	-0.0267	-5.1E-05
700	-2.6	-0.0343	-0.00004
850	-8.3	-0.0387	-1.9E-05
1000	-14.2	-0.0400	8.89E-06
1150	-20.3	-0.0360	2.56E-05
1300	-25.0	-0.0323	2.33E-05
1450	-30.0	-0.0290	2.22E-06
1600	-33.7	-0.0317	-5.7E-05
1750	-39.5	-0.0460	-7.4E-05
1900	-47.5	-0.0540	3.11E-05
2050	-55.7	-0.0367	0.00019
2200	-58.5	0.0030	0.00025
2352	-54.8	0.0387	0.000178
2502	-46.8	0.0567	4.75E-05
2652	-37.8	0.0530	-5.3E-05
2802	-30.9	0.0407	-6.8E-05
2952	-25.6	0.0327	-4.7E-05
3102	-21.1	0.0267	-3.8E-05
3252	-17.6	0.0213	-0.00003
3402	-14.7	0.0177	-2.2E-05
3552	-12.3	0.0147	-1.7E-05
3702	-10.3	0.0127	-1.3E-05
3852	-8.5	0.0107	-1.4E-05
4002	-7.1	0.0083	-0.00001
4152	-6.0	0.0077	-7.8E-06
4302	-4.8	0.0060	-1.2E-05
4452	-4.2	0.0040	-1.1E-05
4602	-3.6	0.0027	-1.6E-05
4752	-3.4	-0.0008	5.79E-07

Table A.2. (b)

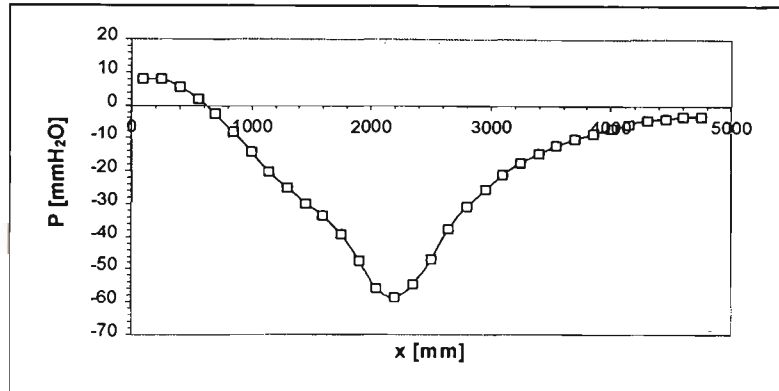


Figure A.2. (b)

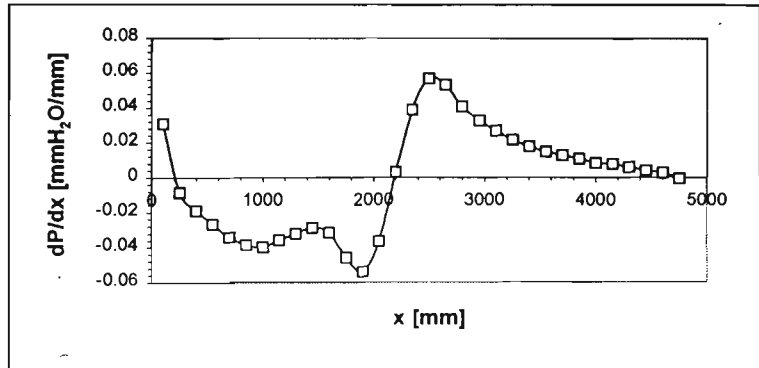


Figure A.2. (c)

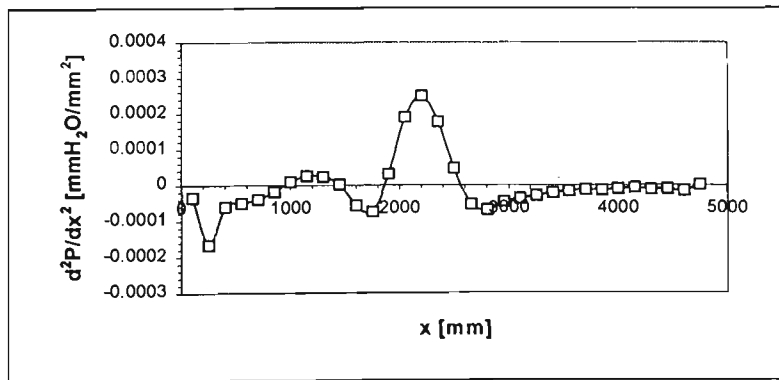


Figure A.2. (d)

CASE 3

x [mm]	y [mm]
0	745
143	710
615	500
1193	335
1703	325
2226	405
2765	525
3280	625
3865	688
4470	700
4640	695

Table A.3. (a)

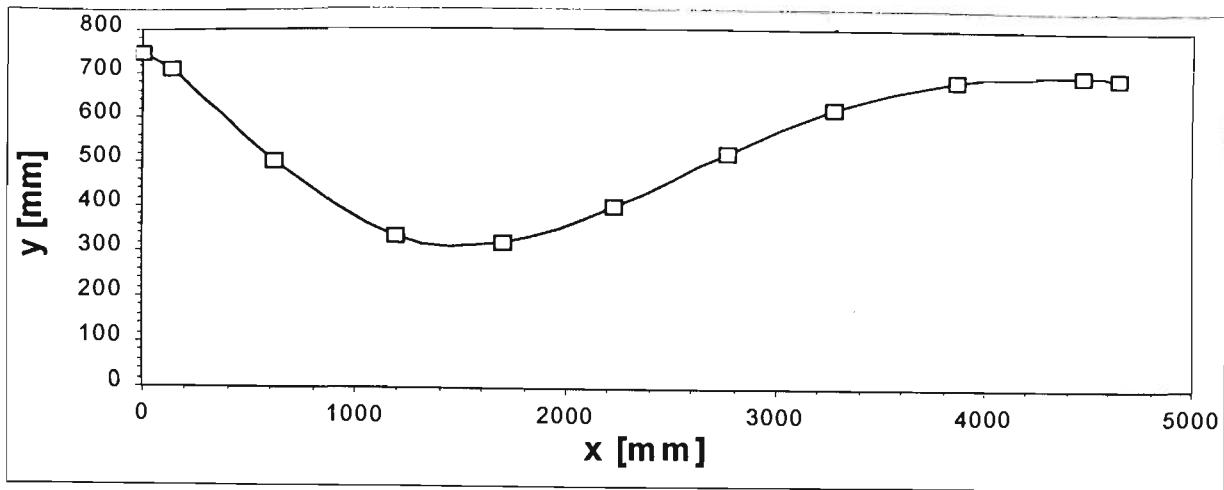


Figure A.3. (a)

x [mm]	P [mmH ₂ O]	dP/dx [mmH ₂ O/mm]	d ² P/dx ² [mmH ₂ O/mm ²]
100	6.3	0.0216	-4.8E-05
250	5.4	-0.0120	-0.00015
400	2.7	-0.0237	-7.7E-05
550	-1.7	-0.0350	-0.00008
700	-7.8	-0.0477	-7.4E-05
850	-16.0	-0.0573	-4.1E-05
1000	-25.0	-0.0600	1.33E-05
1150	-34.0	-0.0533	5.56E-05
1300	-41.0	-0.0433	0.000101
1450	-47.0	-0.0230	0.000148
1600	-47.9	0.0010	0.000128
1750	-46.7	0.0153	8.78E-05
1900	-43.3	0.0273	6.44E-05
2050	-38.5	0.0347	2.15E-05
2200	-32.9	0.0338	-2.2E-05
2352	-28.3	0.0281	-3.7E-05
2502	-24.4	0.0227	-3.4E-05
2652	-21.5	0.0180	-2.1E-05
2802	-19.0	0.0163	-8.9E-06
2952	-16.6	0.0153	-4.4E-06
3102	-14.4	0.0150	-2.2E-06
3252	-12.1	0.0147	-0.00001
3402	-10.0	0.0120	-1.4E-05
3552	-8.5	0.0103	-1.1E-05
3702	-6.9	0.0087	-1E-05
3852	-5.9	0.0073	-5.6E-06
4002	-4.7	0.0070	-0.00001
4152	-3.8	0.0043	-1.2E-05
4302	-3.4	0.0033	-8.9E-06
4452	-2.8	0.0017	-1.3E-05
4602	-2.9	-0.0007	-7.7E-06
4752	-3.0	-0.0006	-1.4E-07

Table A.3. (b)

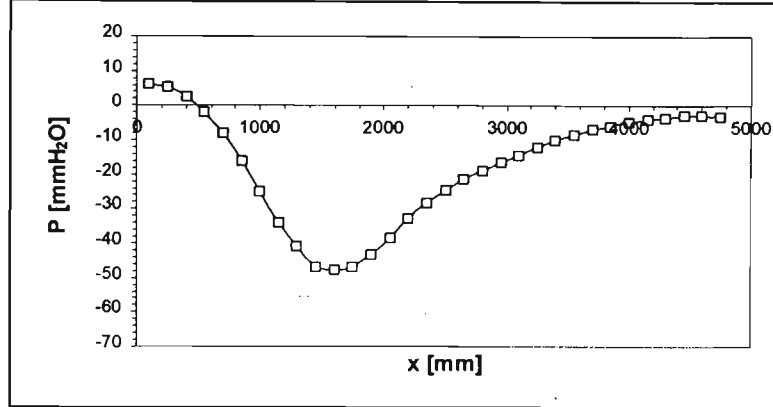


Figure A.3. (b)

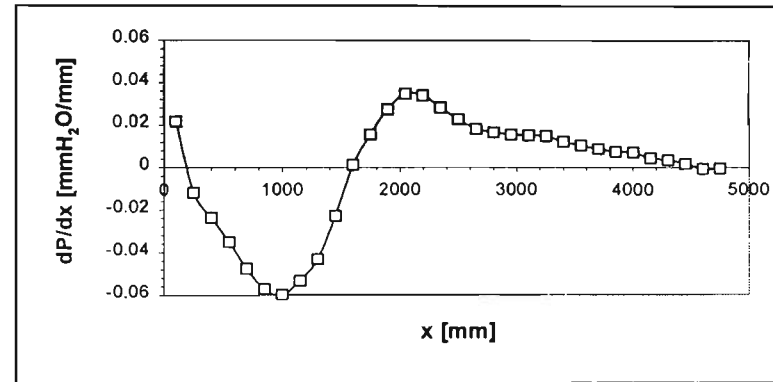


Figure A.3. (c)

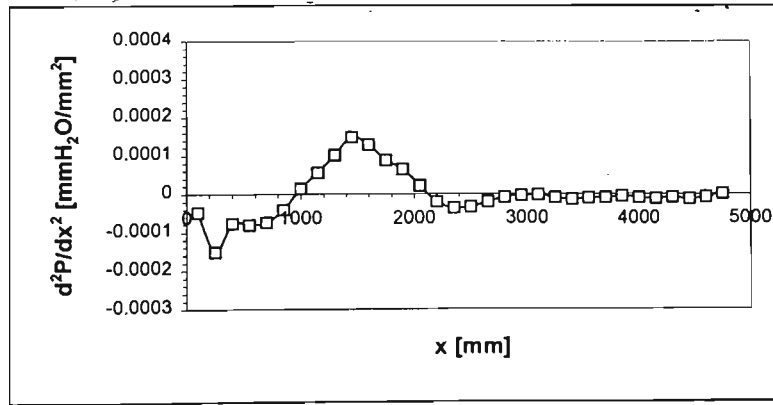


Figure A.3. (d)

CASE 4

x [mm]	y [mm]
0	335
143	335
615	335
1193	330
1703	325
2226	386
2765	525
3280	625
3865	688
4470	700
4640	695

Table A.4. (a)

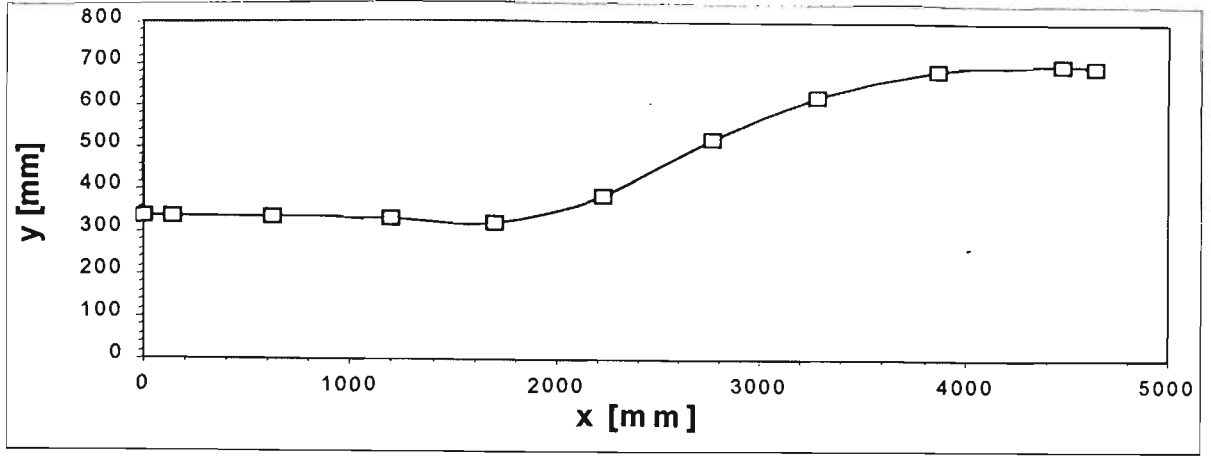


Figure A.4. (a)

x [mm]	P [mmH ₂ O]	dP/dx [mmH ₂ O/mm]	d ² P/dx ² [mmH ₂ O/mm ²]
100	-20.5	-0.0732	8.53E-05
250	-18.3	0.0213	0.000326
400	-14.1	0.0247	-1.6E-05
550	-10.9	0.0167	-5.9E-05
700	-9.1	0.0070	-5.2E-05
850	-8.8	0.0010	-0.00002
1000	-8.8	0.0010	1.11E-05
1150	-8.5	0.0043	1.67E-05
1300	-7.5	0.0060	-8.7E-21
1450	-6.7	0.0043	-3.9E-05
1600	-6.2	-0.0057	-7.1E-05
1750	-8.4	-0.0170	-5.4E-05
1900	-11.3	-0.0220	-0.00001
2050	-15.0	-0.0200	7E-05
2200	-17.3	-0.0010	0.000116
2352	-15.3	0.0149	4.85E-05
2502	-12.8	0.0137	-2.1E-05
2652	-11.2	0.0087	-2.3E-05
2802	-10.2	0.0067	-6.7E-06
2952	-9.2	0.0067	1.11E-06
3102	-8.2	0.0070	-1.2E-20
3252	-7.1	0.0067	0
3402	-6.2	0.0070	-2.2E-06
3552	-5.0	0.0060	-1.2E-05
3702	-4.4	0.0033	-1.1E-05
3852	-4.0	0.0027	-2.2E-06
4002	-3.6	0.0027	-1.1E-06
4152	-3.2	0.0023	-3.3E-06
4302	-2.9	0.0017	-1.1E-06
4452	-2.7	0.0020	1.11E-06
4602	-2.3	0.0020	-8.3E-06
4752	-2.1	-0.0005	4.35E-07

Table A.4. (b)

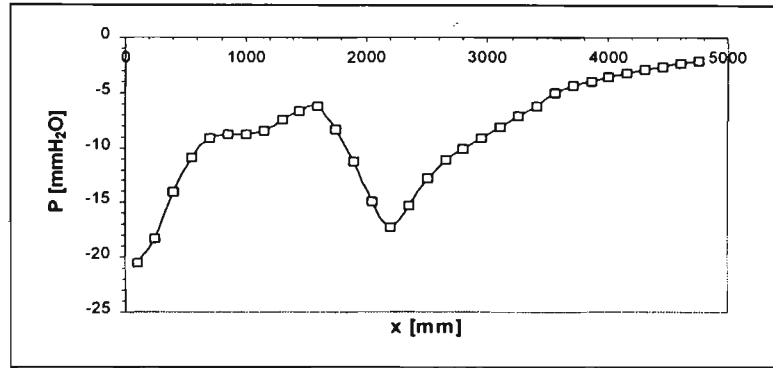


Figure A.4. (b)

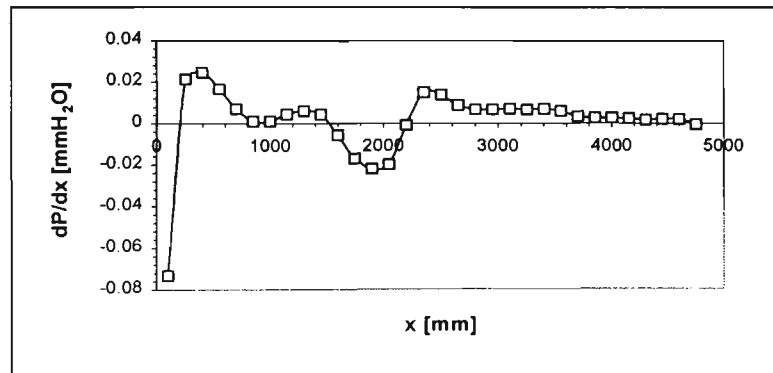


Figure A.4. (c)

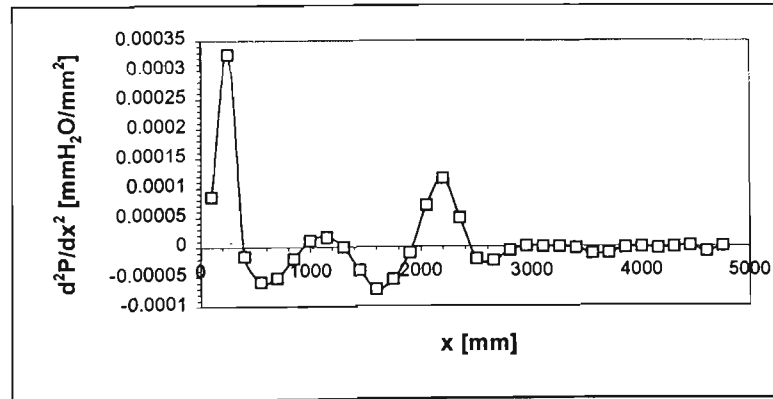


Figure A.4. (d)

CASE 5

x [mm]	y [mm]
0	321
143	316
615	316
1193	304
1703	310
2226	310
2765	382
3280	450
3865	566
4470	718
4640	765

Table A.5. (a)

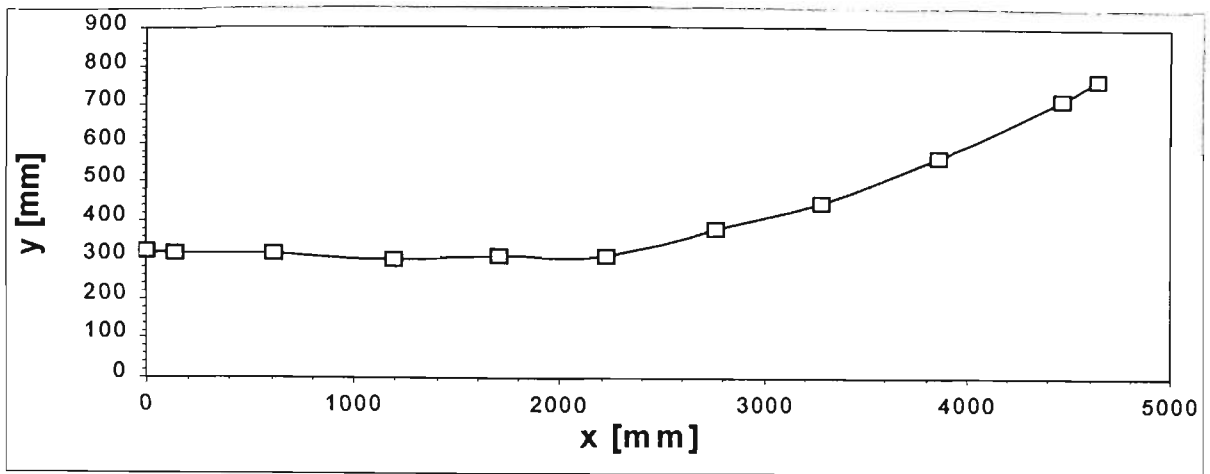


Figure A.5. (a)

x [mm]	P [mmH ₂ O]	dP/dx [mmH ₂ O/mm]	d ² P/dx ² [mmH ₂ O/mm ²]
100	-25.4	-0.0868	0.000105
250	-21.7	0.0263	0.000367
400	-17.5	0.0233	-4.8E-05
550	-14.7	0.0120	-0.00007
700	-13.9	0.0023	-4.3E-05
850	-14.0	-0.0010	-1E-05
1000	-14.2	-0.0007	1E-05
1150	-14.2	0.0020	1.11E-05
1300	-13.6	0.0027	1.11E-06
1450	-13.4	0.0023	-1.2E-05
1600	-12.9	-0.0010	-0.00002
1750	-13.7	-0.0037	-1.1E-05
1900	-14.0	-0.0043	4.44E-06
2050	-15.0	-0.0023	2.22E-05
2200	-14.7	0.0023	3.29E-05
2352	-14.3	0.0076	3.43E-05
2502	-12.4	0.0127	1.46E-05
2652	-10.5	0.0120	-7.8E-06
2802	-8.8	0.0103	-1.2E-05
2952	-7.4	0.0083	-1.3E-05
3102	-6.3	0.0063	-1.2E-05
3252	-5.5	0.0047	-5.8E-21
3402	-4.9	0.0063	-1.1E-06
3552	-3.6	0.0043	-1.6E-05
3702	-3.6	0.0017	-3.3E-06
3852	-3.1	0.0033	3.33E-06
4002	-2.6	0.0027	-3.3E-06
4152	-2.3	0.0023	-2.2E-06
4302	-1.9	0.0020	-2.2E-06
4452	-1.7	0.0017	-1.1E-06
4602	-1.4	0.0017	-6.6E-06
4752	-1.2	-0.0003	3.62E-07

Table A.5. (b)

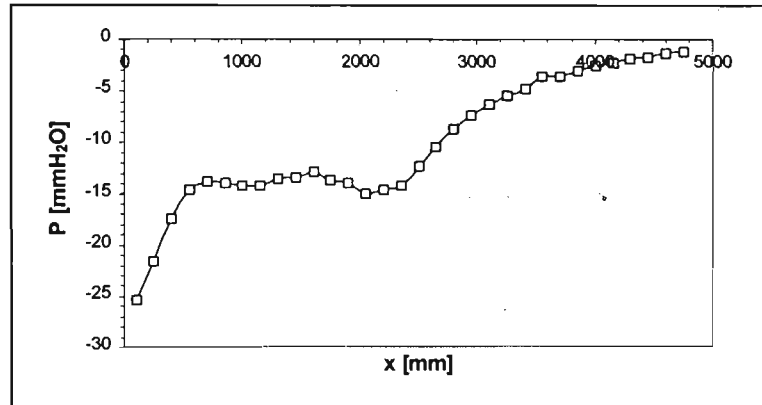


Figure A.5. (b)

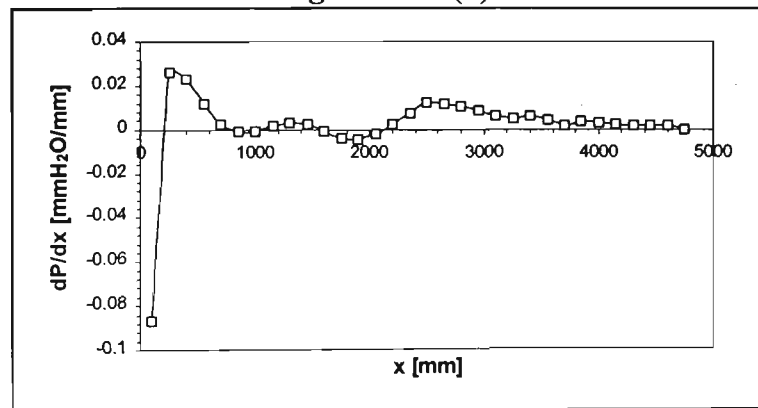


Figure A.5. (c)

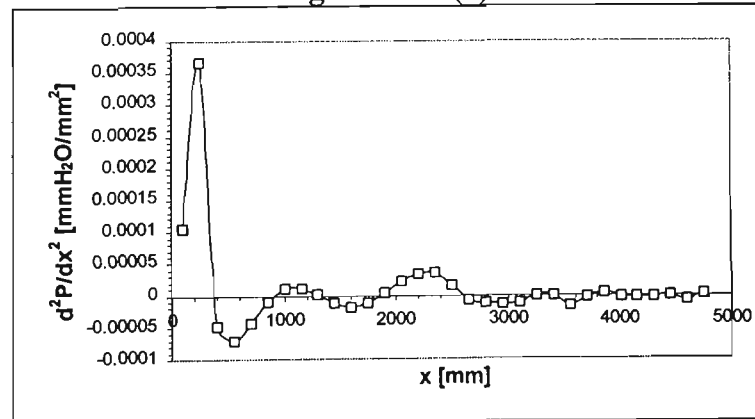


Figure A.5. (d)

CASE 6

x [mm]	y [mm]
0	316
143	320
615	316
1193	296
1703	316
2226	306
2765	462
3280	476.5
3865	573
4470	724
4640	804

Table A.6. (a)

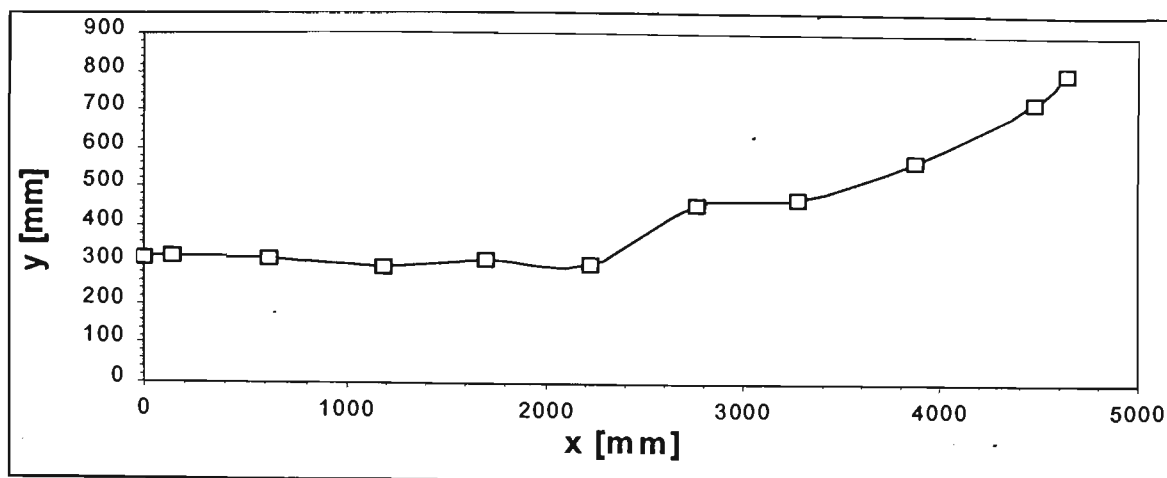


Figure A.6. (a)

x [mm]	P [mmH ₂ O]	dP/dx [mmH ₂ O/mm]	d ² P/dx ² [mmH ₂ O/mm ²]
100	-17.8	-0.0596	0.000068
250	-14.9	0.0170	0.000233
400	-12.7	0.0103	-4.4E-05
550	-11.8	0.0037	-3.8E-05
700	-11.6	-0.0010	-2.4E-05
850	-12.1	-0.0037	-3.3E-06
1000	-12.7	-0.0020	0.00002
1150	-12.7	0.0023	1.78E-05
1300	-12.0	0.0033	1.11E-06
1450	-11.7	0.0027	-1.9E-05
1600	-11.2	-0.0023	-4.2E-05
1750	-12.4	-0.0100	-3.2E-05
1900	-14.2	-0.0120	1E-05
2050	-16.0	-0.0070	5.77E-05
2200	-16.3	0.0053	6.7E-05
2352	-14.4	0.0132	2.99E-05
2502	-12.3	0.0143	-3E-06
2652	-10.1	0.0123	-1.6E-05
2802	-8.6	0.0097	-1.2E-05
2952	-7.2	0.0087	-1E-05
3102	-6.0	0.0067	-1.3E-05
3252	-5.2	0.0047	-5.6E-06
3402	-4.6	0.0050	-1.1E-06
3552	-3.7	0.0043	-6.7E-06
3702	-3.3	0.0030	-4.4E-06
3852	-2.8	0.0030	-1.1E-06
4002	-2.4	0.0027	-2.2E-06
4152	-2.0	0.0023	-3.3E-06
4302	-1.7	0.0017	-4.4E-06
4452	-1.5	0.0010	-2.2E-06
4602	-1.4	0.0010	-4.3E-06
4752	-1.2	-0.0003	2.17E-07

Table A.6. (b)

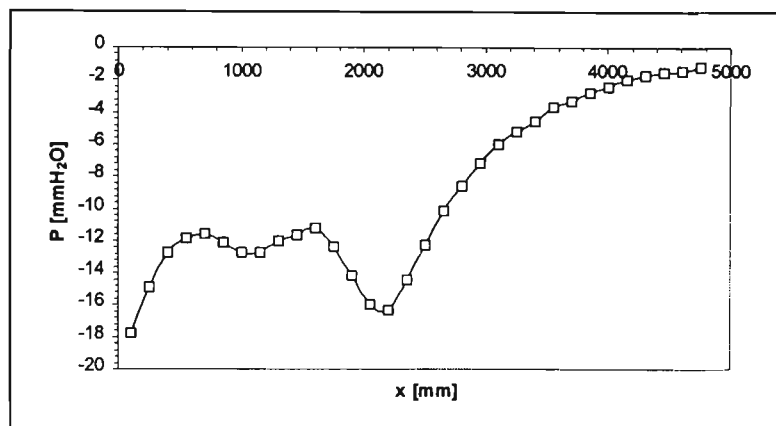


Figure A.6. (b)

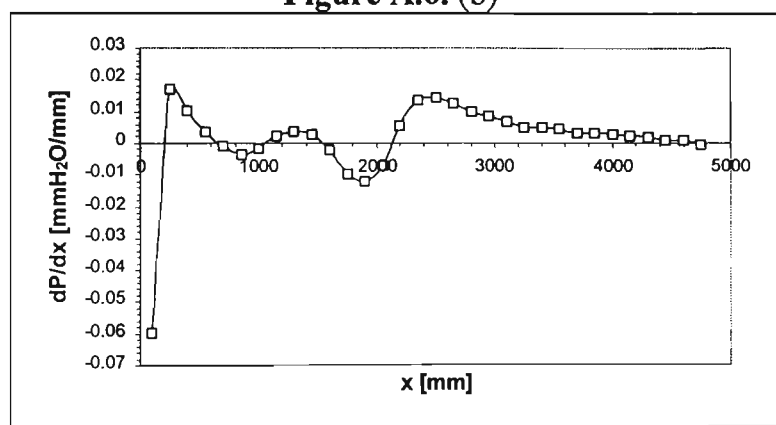


Figure A.6. (c)

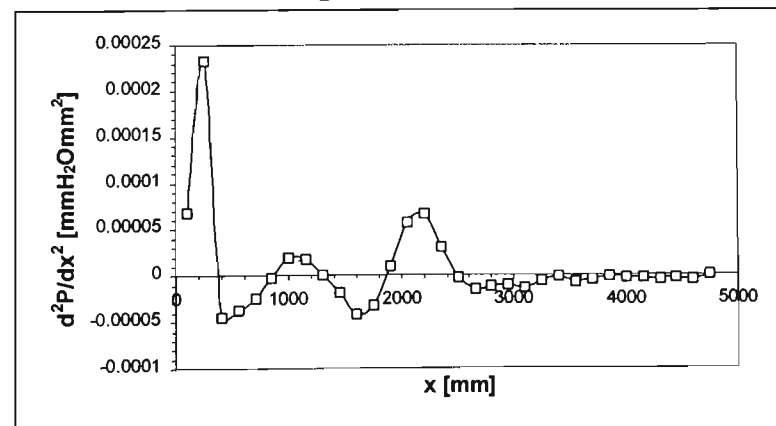


Figure A.6. (d)

CASE 7

x [mm]	y [mm]
0	742
143	566
615	487
1193	441
1703	448
2226	462
2765	482
3280	511
3865	573
4470	699
4640	772

Table A.7. (a)

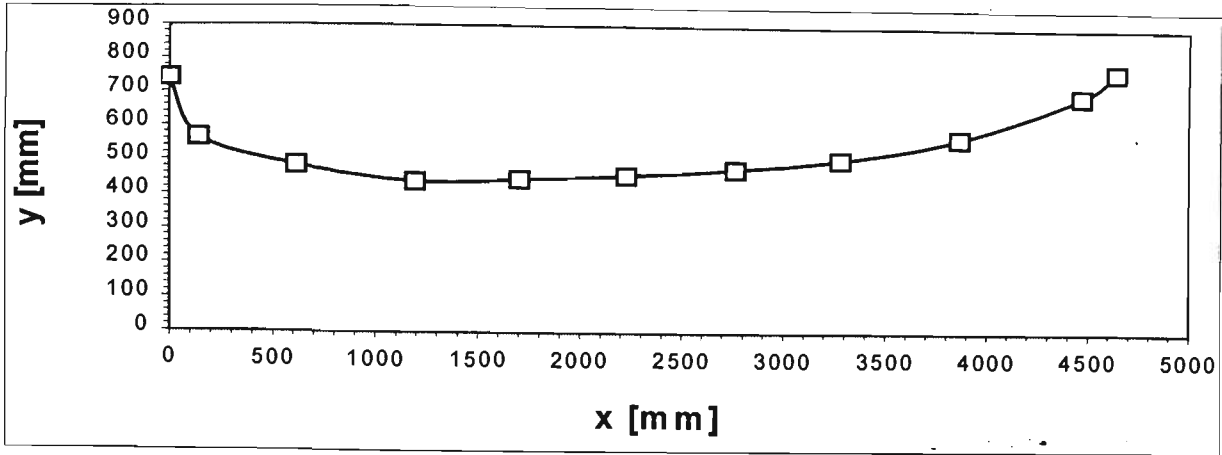


Figure A.7. (a)

x [mm]	P [mmH ₂ O]	dP/dx [mmH ₂ O/mm]	d ² P/dx ² [mmH ₂ O/mm ²]
100	4.5	0.0192	2.27E-05
250	4.8	0.0057	-2.7E-05
400	6.2	0.0110	2.33E-05
550	8.1	0.0127	6.67E-06
700	10.0	0.0130	-1.1E-06
850	12.0	0.0123	-1.2E-05
1000	13.7	0.0093	-2.9E-05
1150	14.8	0.0037	-2.9E-05
1300	14.8	0.0007	-1.3E-05
1450	15.0	-0.0003	-2.2E-06
1600	14.7	0.0000	7.78E-06
1750	15.0	0.0020	7.78E-06
1900	15.3	0.0023	1.11E-06
2050	15.7	0.0023	-7.8E-06
2200	16.0	0.0000	-1.6E-05
2352	15.7	-0.0026	-2E-05
2502	15.2	-0.0060	-2.2E-05
2652	13.9	-0.0093	-0.00001
2802	12.4	-0.0090	6.67E-06
2952	11.2	-0.0073	8.89E-06
3102	10.2	-0.0063	4.44E-06
3252	9.3	-0.0060	2.22E-06
3402	8.4	-0.0057	-2E-20
3552	7.6	-0.0060	-2.2E-06
3702	6.6	-0.0063	-1.1E-06
3852	5.7	-0.0063	2.22E-06
4002	4.7	-0.0057	2.22E-06
4152	4.0	-0.0057	4.44E-06
4302	3.0	-0.0043	1.22E-05
4452	2.7	-0.0020	8.89E-06
4602	2.4	-0.0017	8.41E-06
4752	2.2	0.0005	-3.6E-07

Table A.7. (b)

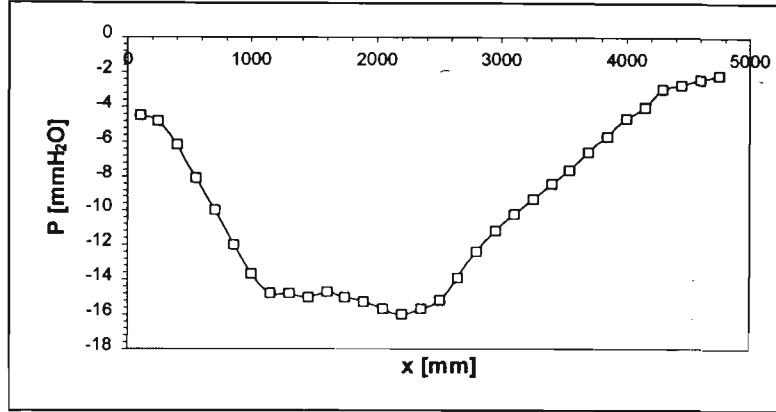


Figure A.7. (b)

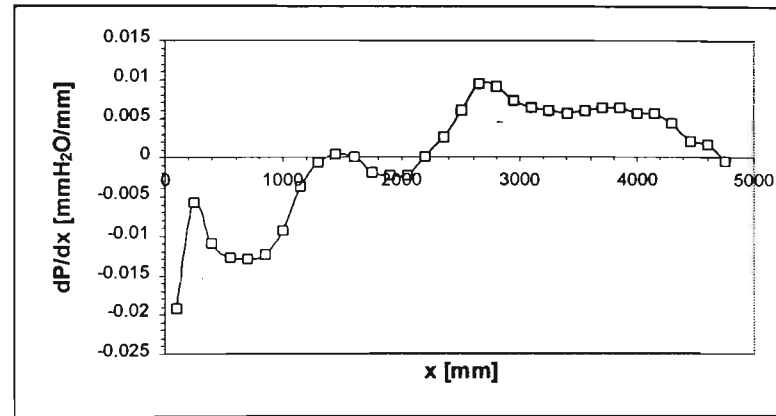


Figure A.7. (c)

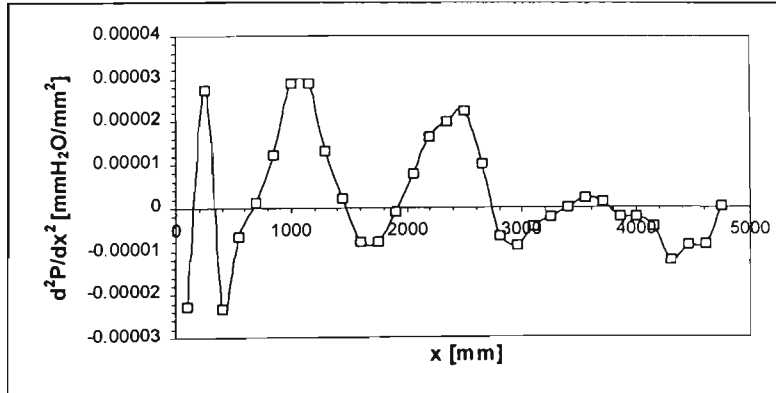


Figure A.7. (d)

CASE 8

x [mm]	y [mm]
0	436
143	436
615	436
1193	441
1703	448
2226	462
2765	482
3280	511
3865	573
4470	699
4640	772

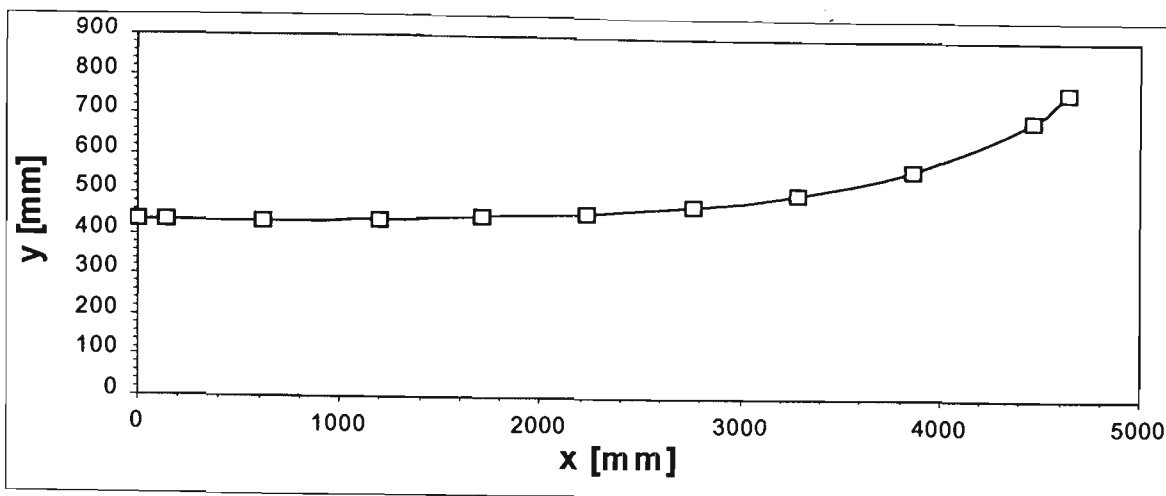


Table A.8. (a)

Figure A.8. (a)

x [mm]	P [mmH ₂ O]	dP/dx [mmH ₂ O/mm]	d ² P/dx ² [mmH ₂ O/mm ²]
100	-11.0	-0.0388	2.13E-05
250	-9.7	0.0053	0.000133
400	-9.4	0.0010	-1.8E-05
550	-9.4	0.0000	-5.6E-06
700	-9.4	-0.0007	-2.2E-06
850	-9.6	-0.0007	1.11E-06
1000	-9.6	-0.0003	4.44E-06
1150	-9.7	0.0007	6.67E-06
1300	-9.4	0.0017	3.33E-06
1450	-9.2	0.0017	-3.3E-06
1600	-8.9	0.0007	-8.9E-06
1750	-9.0	-0.0010	-6.7E-06
1900	-9.2	-0.0013	-2E-20
2050	-9.4	-0.0010	4.44E-06
2200	-9.5	0.0000	9.89E-06
2352	-9.4	0.0020	1.21E-05
2502	-8.9	0.0037	8.93E-06
2652	-8.3	0.0047	4.44E-06
2802	-7.5	0.0050	-1.1E-06
2952	-6.8	0.0043	-2.2E-06
3102	-6.2	0.0043	-1.1E-06
3252	-5.5	0.0040	-2.2E-06
3402	-5.0	0.0037	-2.2E-06
3552	-4.4	0.0033	-2.2E-06
3702	-4.0	0.0030	2.22E-06
3852	-3.5	0.0040	2.22E-06
4002	-2.8	0.0037	-3.3E-06
4152	-2.4	0.0030	-4.4E-06
4302	-1.9	0.0023	-5.6E-06
4452	-1.7	0.0013	-4.4E-06
4602	-1.5	0.0010	-5.5E-06
4752	-1.4	-0.0003	2.17E-07

Table A.8. (b)

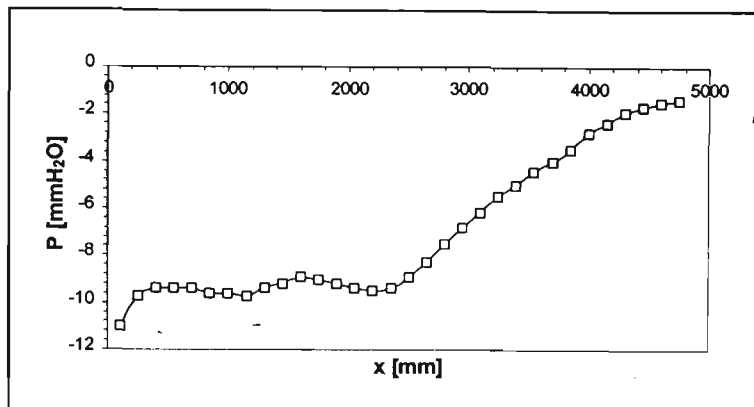


Figure A.8. (b)

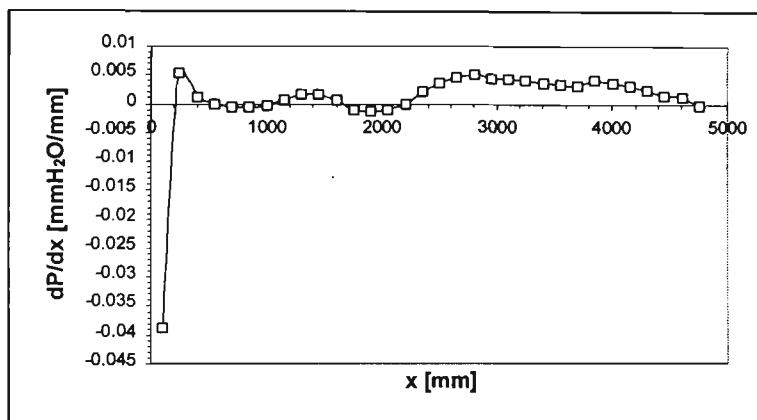


Figure A.8. (c)

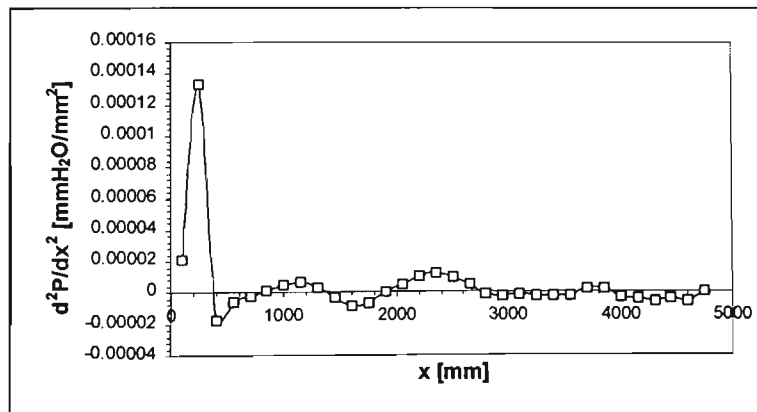


Figure A.8. (d)

CASE 9

x [mm]	y [mm]
0	300
143	295
615	298
1193	301
1703	318
2226	348
2765	405
3280	472
3865	570
4470	710
4640	772

Table A.9. (a)

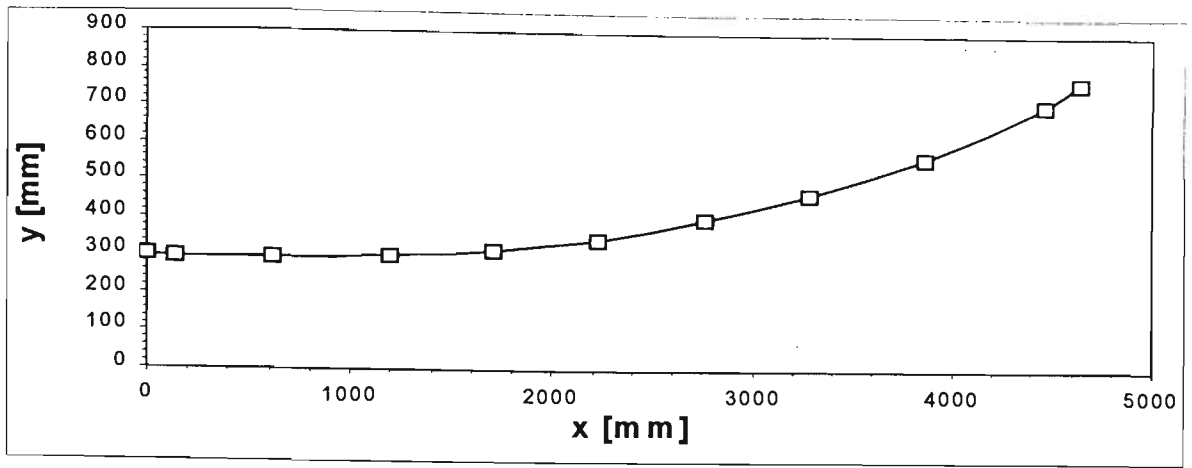


Figure A.9. (a)

x [mm]	P [mmH ₂ O]	dP/dx [mmH ₂ O/mm]	d ² P/dx ² [mmH ₂ O/mm ²]
100	-14.0	-0.0568	-8E-06
250	-14.2	-0.0020	0.000182
400	-14.6	-0.0023	4.44E-06
550	-14.9	-0.0007	1.11E-06
700	-14.8	-0.0020	-8.9E-06
850	-15.5	-0.0033	3.33E-06
1000	-15.8	-0.0010	2.11E-05
1150	-15.8	0.0030	2.33E-05
1300	-14.9	0.0060	1.11E-05
1450	-14.0	0.0063	-6.7E-06
1600	-13.0	0.0040	-1.3E-05
1750	-12.8	0.0023	-4.4E-06
1900	-12.3	0.0027	4.44E-06
2050	-12.0	0.0037	8.77E-06
2200	-11.2	0.0053	9.79E-06
2352	-10.4	0.0066	1.12E-05
2502	-9.2	0.0087	1.01E-05
2652	-7.8	0.0097	-1.1E-06
2802	-6.3	0.0083	-1.1E-05
2952	-5.3	0.0063	-8.9E-06
3102	-4.4	0.0057	-5.6E-06
3252	-3.6	0.0047	-5.6E-06
3402	-3.0	0.0040	-3.3E-06
3552	-2.4	0.0037	-3.3E-06
3702	-1.9	0.0030	-4.4E-06
3852	-1.5	0.0023	-5.1E-06
4002	-1.2	0.0015	-4.2E-06
4152	-1.1	0.0011	-2.4E-06
4302	-0.9	0.0007	-2.7E-06
4452	-0.8	0.0003	-1.8E-06
4602	-0.8	0.0002	-1.5E-06
4752	-0.8	-0.0002	4.35E-08

Table A.9. (b)

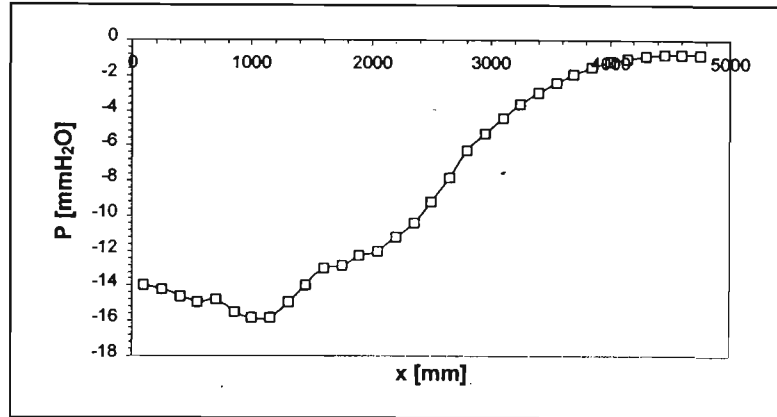


Figure A.9. (b)

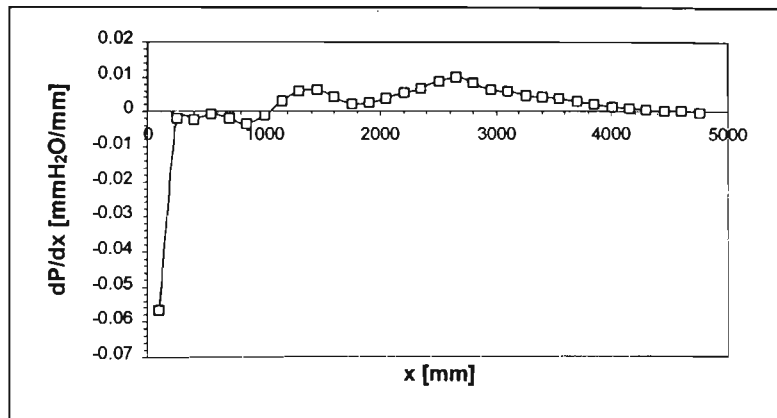


Figure A.9. (c)

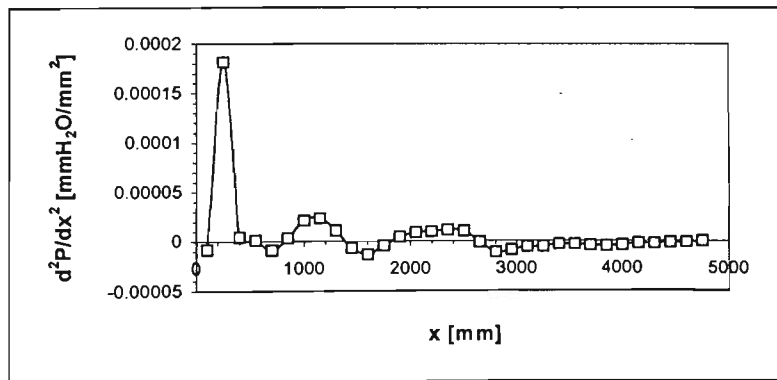


Figure A.9. (d)

CASE 10

x [mm]	y [mm]
0	300
143	295
615	301
1193	250
1703	263
2226	290
2765	405
3280	472
3865	570
4470	710
4640	772

Table A.10. (a)

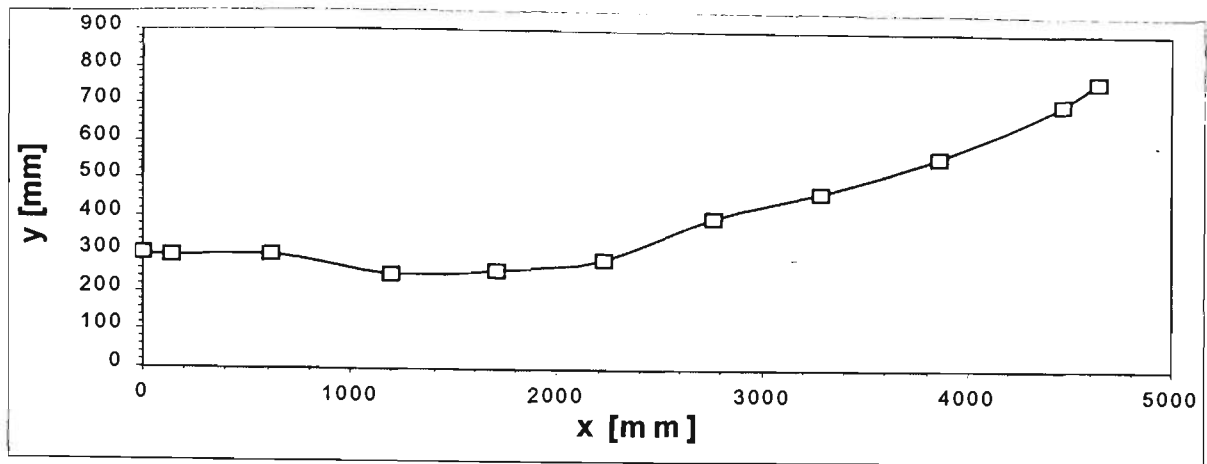


Figure A.10. (a)

x [mm]	P [mmH ₂ O]	dP/dx [mmH ₂ O/mm]	d ² P/dx ² [mmH ₂ O/mm ²]
100	-8.9	-0.0360	-4E-06
250	-9.0	-0.0010	0.000114
400	-9.2	-0.0017	-1.1E-05
550	-9.5	-0.0043	-3.3E-05
700	-10.5	-0.0117	-4.3E-05
850	-13.0	-0.0173	-1.8E-05
1000	-15.7	-0.0170	2.11E-05
1150	-18.1	-0.0110	4.33E-05
1300	-19.0	-0.0040	4.11E-05
1450	-19.3	0.0013	2.89E-05
1600	-18.6	0.0047	1.89E-05
1750	-17.9	0.0070	1.67E-05
1900	-16.5	0.0097	1.56E-05
2050	-15.0	0.0117	1.3E-05
2200	-13.0	0.0136	7.42E-06
2352	-10.9	0.0139	-1.9E-06
2502	-8.8	0.0130	-1.2E-05
2652	-7.0	0.0103	-1.7E-05
2802	-5.7	0.0080	-1.3E-05
2952	-4.6	0.0063	-8.9E-06
3102	-3.8	0.0053	-6.7E-06
3252	-3.0	0.0043	-7.8E-06
3402	-2.5	0.0030	-5.6E-06
3552	-2.1	0.0027	-2.8E-06
3702	-1.7	0.0022	-2.8E-06
3852	-1.5	0.0018	-2.7E-06
4002	-1.2	0.0014	-2.9E-06
4152	-1.0	0.0010	-1.9E-06
4302	-0.9	0.0008	-2.2E-06
4452	-0.8	0.0003	-3E-06
4602	-0.8	-0.0001	-1.6E-06
4752	-0.8	-0.0002	-2.2E-08

Table A.10. (b)

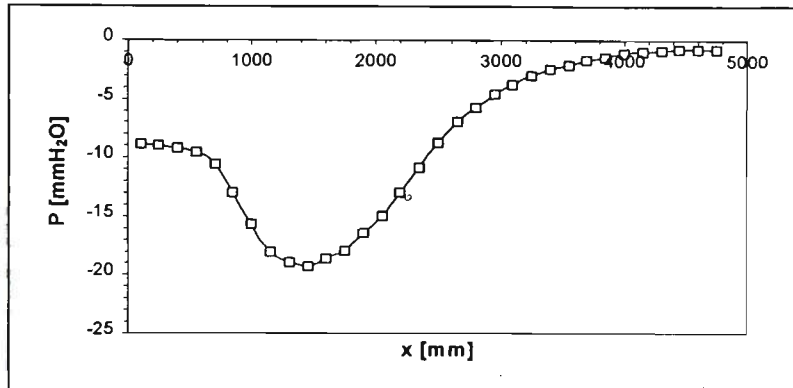


Figure A.10. (b)

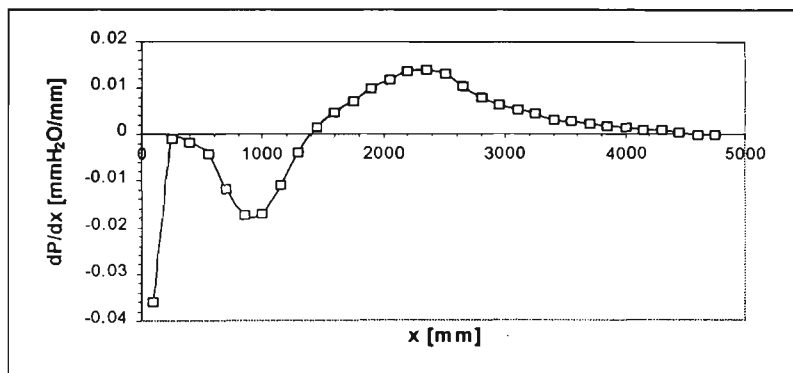


Figure A.10. (c)

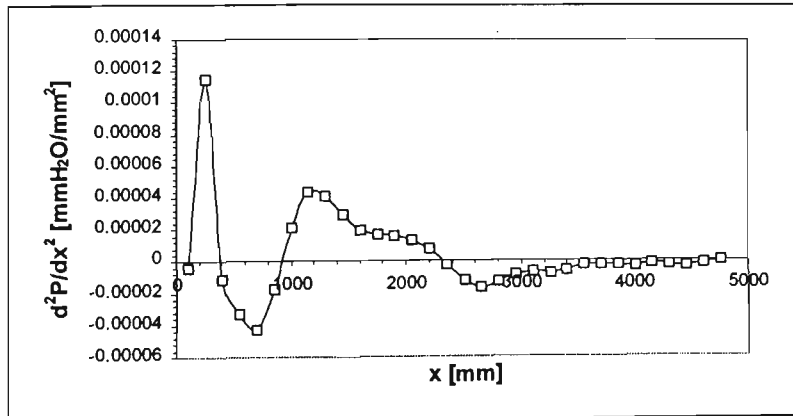


Figure A.10. (d)

CASE II

x [mm]	y [mm]
0	300
143	295
615	301
1193	286
1703	290
2226	320
2765	405
3280	472
3865	570
4470	710
4640	772

Table A.11. (a)

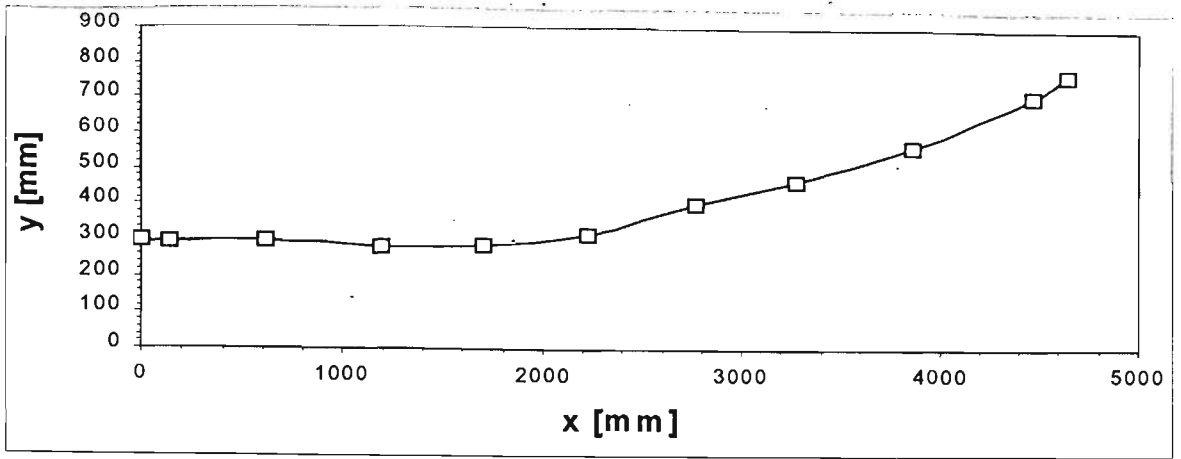


Figure A.11. (a)

x [mm]	P [mmH ₂ O]	dP/dx [mmH ₂ O/mm]	d ² P/dx ² [mmH ₂ O/mm ²]
100	-11.4	-0.0460	-4E-06
250	-11.5	-0.0010	0.00015
400	-11.7	-0.0010	-1.1E-06
550	-11.8	-0.0013	-7.8E-06
700	-12.1	-0.0033	-0.00001
850	-12.8	-0.0043	-1.1E-06
1000	-13.4	-0.0037	7.78E-06
1150	-13.9	-0.0020	7.78E-06
1300	-14.0	-0.0013	4.44E-06
1450	-14.3	-0.0007	2.02E-20
1600	-14.2	-0.0013	-3.3E-06
1750	-14.7	-0.0017	6.67E-06
1900	-14.7	0.0007	0.00002
2050	-14.5	0.0043	2.98E-05
2200	-13.4	0.0096	2.84E-05
2352	-11.6	0.0129	1.24E-05
2502	-9.5	0.0133	-4.2E-06
2652	-7.6	0.0117	-1.3E-05
2802	-6.0	0.0093	-1.7E-05
2952	-4.8	0.0067	-1.6E-05
3102	-4.0	0.0047	-8.9E-06
3252	-3.4	0.0040	-3.3E-06
3402	-2.8	0.0037	-3.3E-06
3552	-2.3	0.0030	-3.3E-06
3702	-1.9	0.0027	-2.2E-06
3852	-1.5	0.0023	-4.4E-06
4002	-1.2	0.0013	-3.9E-06
4152	-1.1	0.0012	-1.3E-06
4302	-0.9	0.0009	-3.3E-06
4452	-0.8	0.0002	-3.2E-06
4602	-0.8	0.0000	-1.1E-06
4752	-0.8	-0.0002	-7.2E-09

Table A.11. (b)

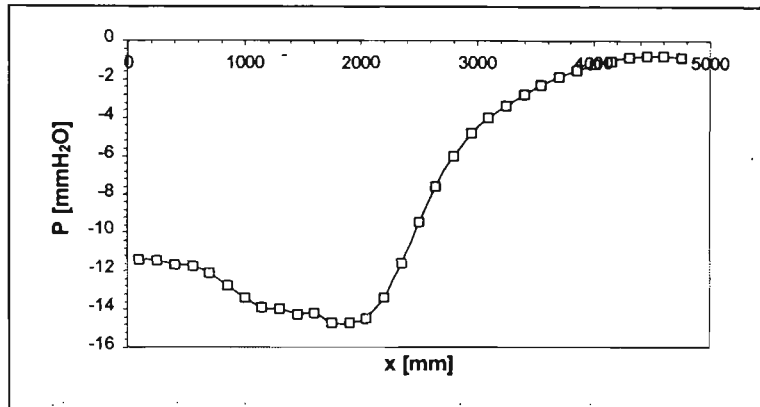


Figure A.11. (b)

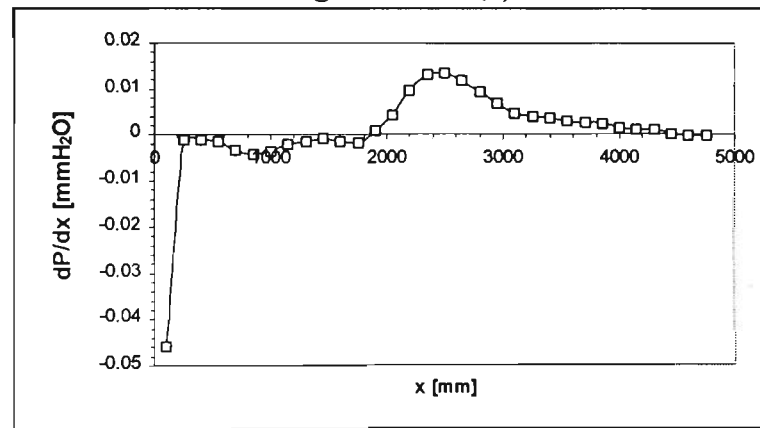


Figure A.11. (c)

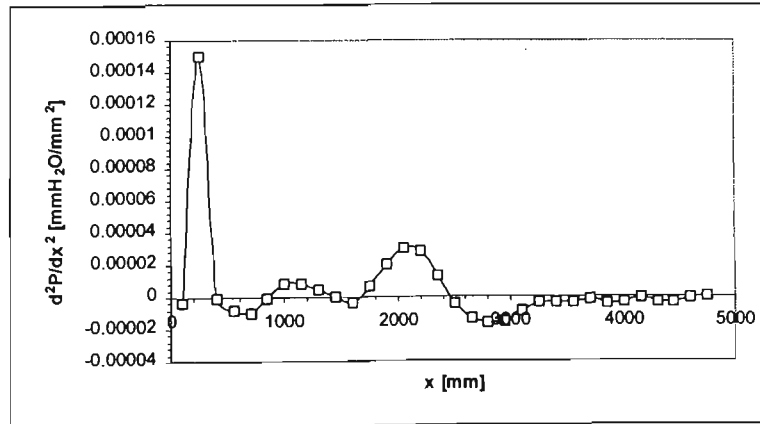


Figure A.11. (d)

CASE 12

x [mm]	y [mm]
0	305
143	310
615	310
1193	315
1703	340
2226	370
2765	420
3280	470
3865	560
4470	710
4640	772

Table A.12. (a)

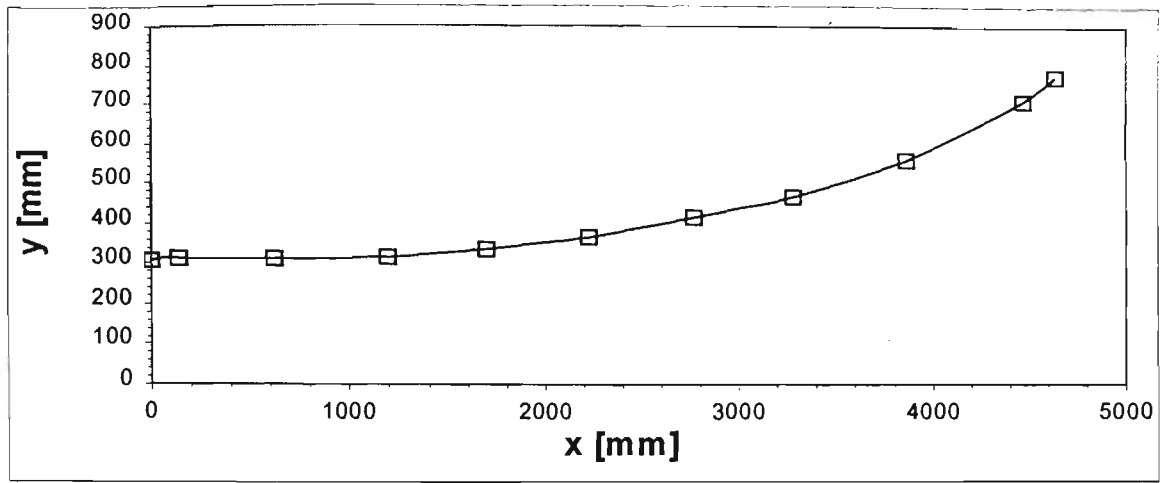


Figure A.12. (a)

x [mm]	P [mmH ₂ O]	dP/dx [mmH ₂ O/mm]	d ² P/dx ² [mmH ₂ O/mm ²]
100	-15.3	-0.0624	-8E-06
250	-15.6	-0.0020	0.000208
400	-15.9	0.0000	1.44E-05
550	-15.6	0.0023	4.44E-06
700	-15.2	0.0013	-7.8E-06
850	-15.2	0.0000	1.11E-06
1000	-15.2	0.0017	1.56E-05
1150	-14.7	0.0047	1.33E-05
1300	-13.8	0.0057	1.11E-06
1450	-13.0	0.0050	-4.4E-06
1600	-12.3	0.0043	-4.4E-06
1750	-11.7	0.0037	-2.2E-06
1900	-11.2	0.0037	1.11E-06
2050	-10.6	0.0040	4.33E-06
2200	-10.0	0.0050	8.68E-06
2352	-9.1	0.0066	6.73E-06
2502	-8.0	0.0070	1.47E-07
2652	-7.0	0.0067	-3.3E-06
2802	-6.0	0.0060	-5.6E-06
2952	-5.2	0.0050	-6.7E-06
3102	-4.5	0.0040	-4.4E-06
3252	-4.0	0.0037	0
3402	-3.4	0.0040	0
3552	-2.8	0.0037	-3.3E-06
3702	-2.3	0.0030	-3.3E-06
3852	-1.9	0.0027	-2.2E-06
4002	-1.5	0.0023	-3.2E-06
4152	-1.2	0.0017	-4.3E-06
4302	-1.0	0.0010	-4.1E-06
4452	-0.9	0.0005	-3.2E-06
4602	-0.9	0.0001	-2.2E-06
4752	-0.9	-0.0002	1.45E-08

Table A.12. (b)

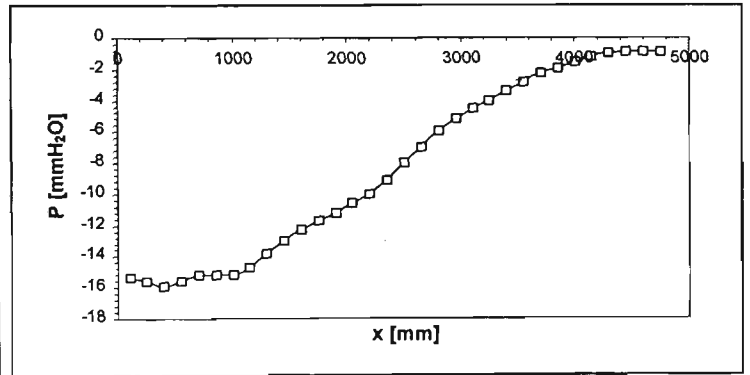


Figure A.12. (b)

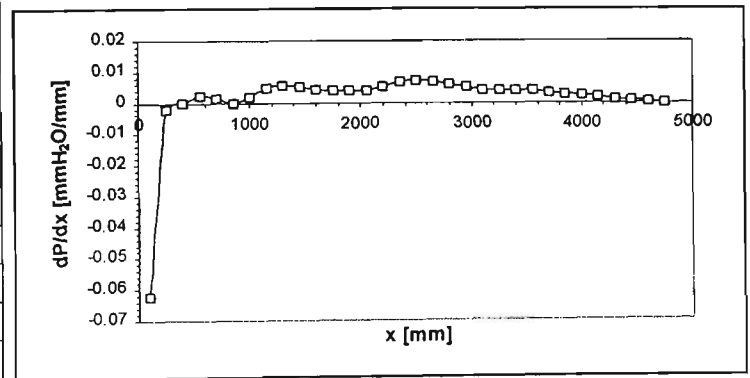


Figure A.12. (c)

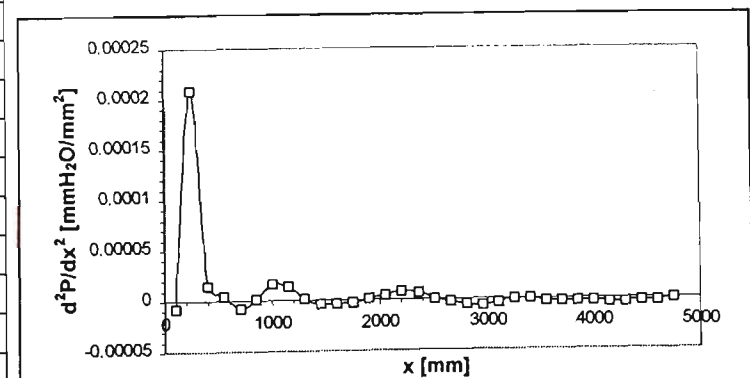


Figure A.12. (d)

CASE 13

x [mm]	y [mm]
7	385
143	383
615	392
1193	398
1703	415
2226	420
2765	460
3280	495
3865	558
4518	660
4640	733

Table A.13. (a)

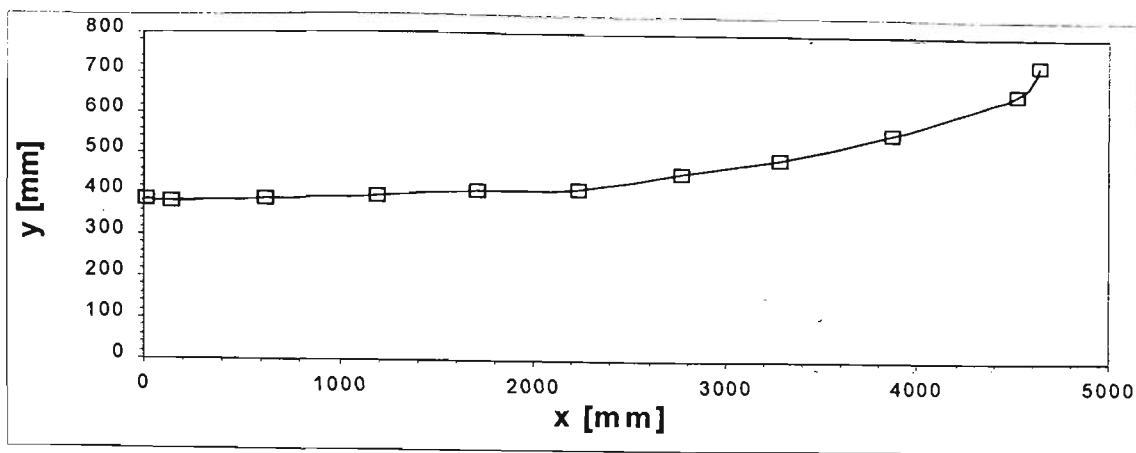


Figure A.13. (a)

x [mm]	P [mmH ₂ O]	dP/dx [mmH ₂ O/mm]	d ² P/dx ² [mmH ₂ O/mm ²]
100	-14.8	-0.0536	2.67E-05
250	-13.4	0.0067	0.00019
400	-12.8	0.0033	-1.6E-05
550	-12.4	0.0020	-8.9E-06
700	-12.2	0.0007	-4.4E-06
850	-12.2	0.0007	3.33E-06
1000	-12.0	0.0017	5.56E-06
1150	-11.7	0.0023	2.22E-06
1300	-11.3	0.0023	-1.1E-06
1450	-11.0	0.0020	-4.4E-06
1600	-10.7	0.0010	-6.7E-06
1750	-10.7	0.0000	-3.3E-06
1900	-10.7	0.0000	1.11E-06
2050	-10.7	0.0003	5.52E-06
2200	-10.6	0.0017	6.57E-06
2352	-10.2	0.0023	7.76E-06
2502	-9.9	0.0040	1.34E-05
2652	-9.0	0.0063	5.56E-06
2802	-8.0	0.0057	-6.7E-06
2952	-7.3	0.0043	-4.4E-06
3102	-6.7	0.0043	0
3252	-6.0	0.0043	-1.1E-06
3402	-5.4	0.0040	-2.2E-06
3552	-4.8	0.0037	1.11E-06
3702	-4.3	0.0043	1.11E-06
3852	-3.5	0.0040	-3.3E-06
4002	-3.1	0.0033	-2.2E-06
4152	-2.5	0.0033	-2.2E-06
4302	-2.1	0.0027	-5.6E-06
4452	-1.7	0.0017	-5.6E-06
4602	-1.6	0.0010	-6.7E-06
4752	-1.4	-0.0003	2.17E-07

Table A.13. (b)

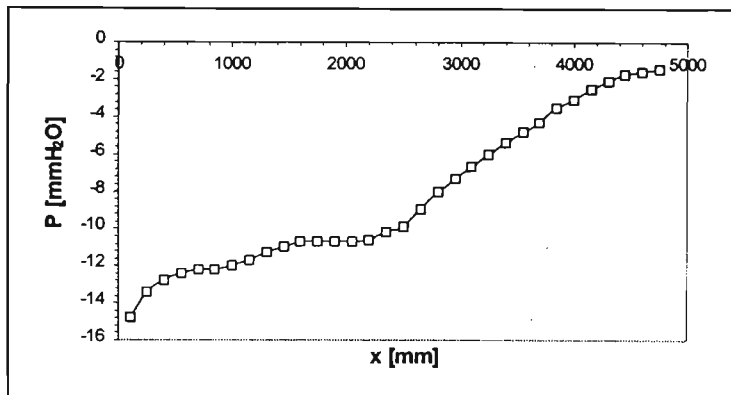


Figure A.13. (b)

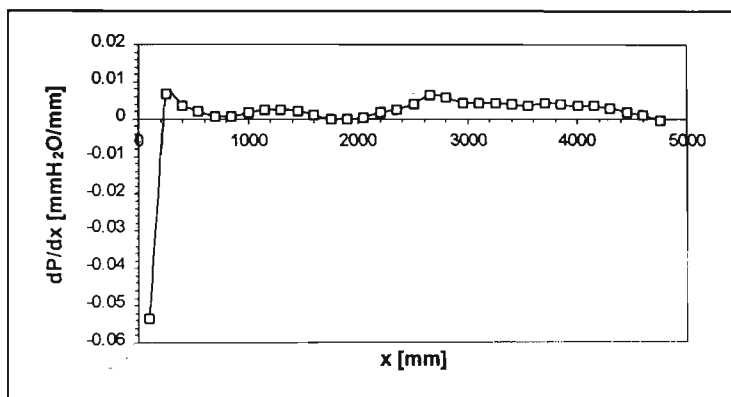


Figure A.13. (c)

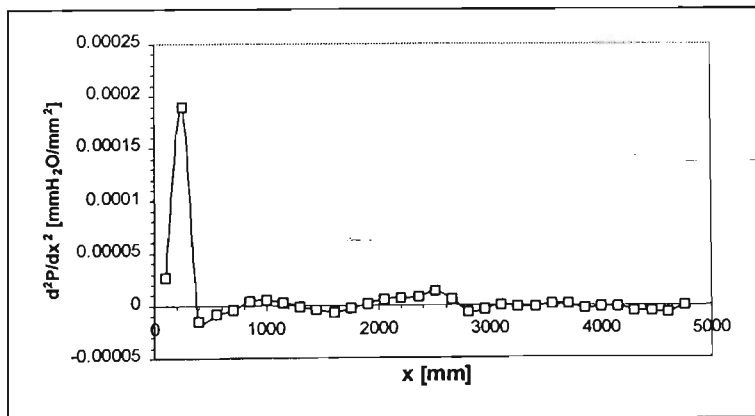


Figure A.13. (d)

CASE 14

x [mm]	y [mm]
0	370
143	355
615	350
1193	344
1703	355
2226	398
2765	432
3280	470
3865	540
4470	650
4640	705

Table A.14. (a)

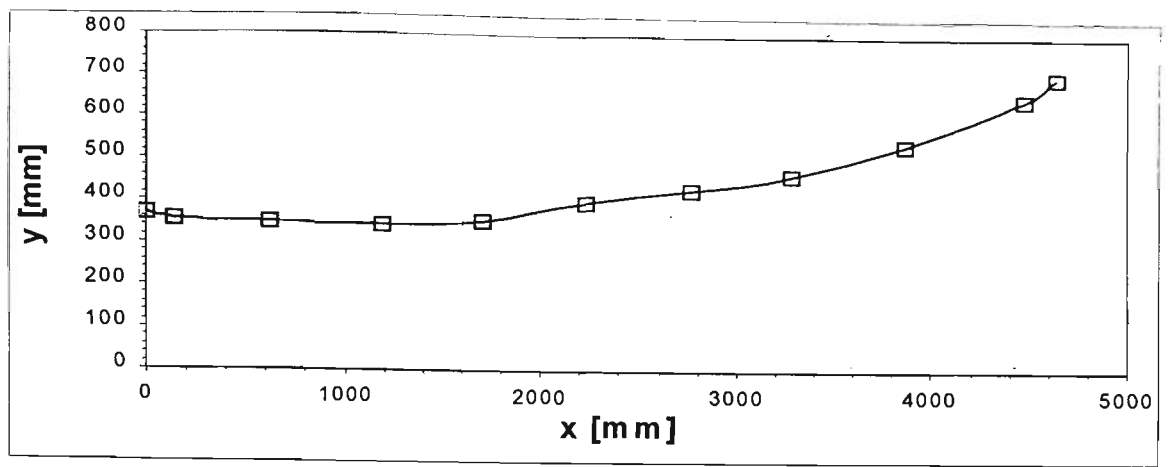


Figure A.14. (a)

x [mm]	P [mmH ₂ O]	dP/dx [mmH ₂ O/mm]	d ² P/dx ² [mmH ₂ O/mm ²]
100	-11.8	-0.0468	-4E-06
250	-11.7	-0.0010	0.000146
400	-12.1	-0.0030	-6.7E-06
550	-12.6	-0.0030	0
700	-13.0	-0.0030	1.11E-06
850	-13.5	-0.0027	5.56E-06
1000	-13.8	-0.0013	1.22E-05
1150	-13.9	0.0010	8.89E-06
1300	-13.5	0.0013	1.11E-06
1450	-13.5	0.0013	2.22E-06
1600	-13.1	0.0020	0
1750	-12.9	0.0013	0
1900	-12.7	0.0020	4.44E-06
2050	-12.3	0.0027	4.37E-06
2200	-11.9	0.0033	7.62E-06
2352	-11.3	0.0050	1.11E-05
2502	-10.4	0.0067	7.89E-06
2652	-9.3	0.0073	8.67E-21
2802	-8.2	0.0067	-4.4E-06
2952	-7.3	0.0060	-3.3E-06
3102	-6.4	0.0057	-3.3E-06
3252	-5.6	0.0050	-3.3E-06
3402	-4.9	0.0047	-2.2E-06
3552	-4.2	0.0043	-2.2E-06
3702	-3.6	0.0040	-2.2E-06
3852	-3.0	0.0037	-3.3E-06
4002	-2.5	0.0030	-3.3E-06
4152	-2.1	0.0027	-2.2E-06
4302	-1.7	0.0023	-3.3E-06
4452	-1.4	0.0017	-4.4E-06
4602	-1.2	0.0010	-6.4E-06
4752	-1.1	-0.0003	2.17E-07

Table A.14. (b)

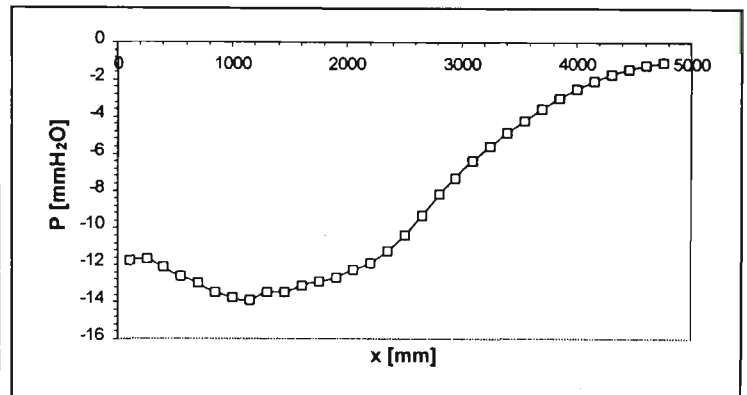


Figure A.14. (b)

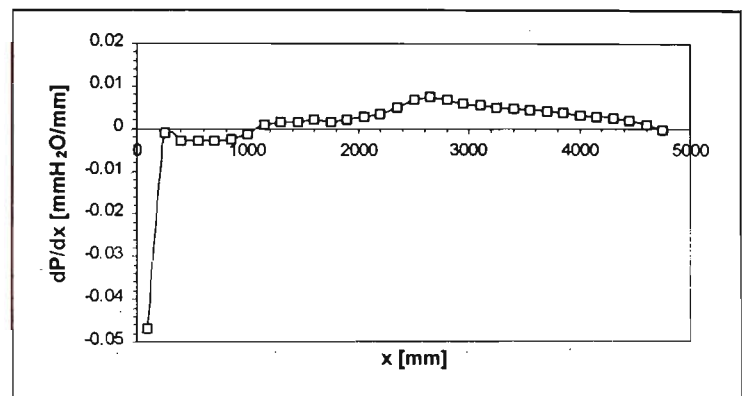


Figure A.14. (c)

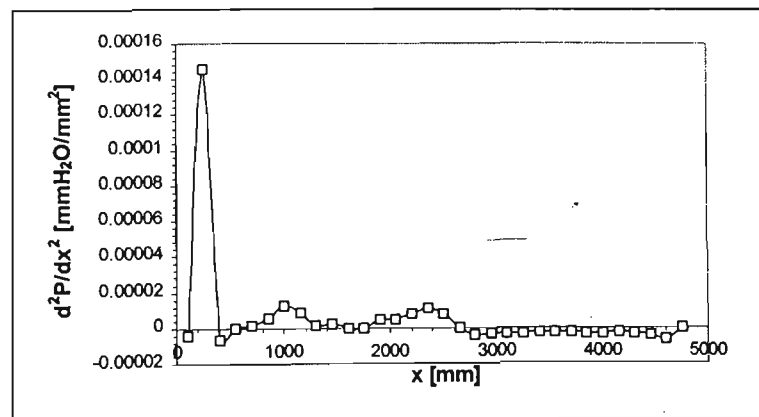


Figure A.14. (d)

CASE 15

x [mm]	y [mm]
0	367.9
143	371.5
615	383.4
1193	398
1703	410.8
2226	424
2765	443
3280	477
3865	562
4470	727
4640	785

Table A.15. (a)

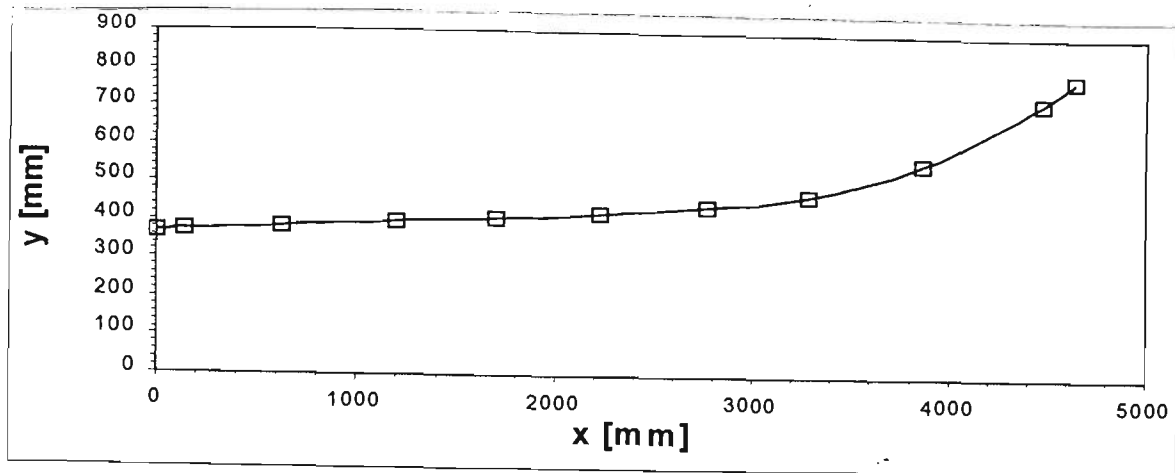


Figure A.15. (a)

x [mm]	P [mmH ₂ O]	dP/dx [mmH ₂ O/m]	d ² P/dx ² [mmH ₂ O/mm ²]
100	-13.8	-0.0480	3.73E-05
250	-12.0	0.0093	0.000178
400	-11.0	0.0053	-2.2E-05
550	-10.4	0.0027	-1.6E-05
700	-10.2	0.0007	-6.7E-06
850	-10.2	0.0007	-2E-20
1000	-10.0	0.0007	3.33E-06
1150	-10.0	0.0017	6.67E-06
1300	-9.5	0.0027	3.33E-06
1450	-9.2	0.0027	-2E-20
1600	-8.7	0.0027	-3.3E-06
1750	-8.4	0.0017	-4.4E-06
1900	-8.2	0.0013	-2.2E-06
2050	-8.0	0.0010	-2.2E-06
2200	-7.9	0.0007	-2.2E-08
2352	-7.8	0.0010	4.43E-06
2502	-7.6	0.0020	6.69E-06
2652	-7.2	0.0030	3.33E-06
2802	-6.7	0.0030	1.01E-20
2952	-6.3	0.0030	1.11E-06
3102	-5.8	0.0033	-1E-20
3252	-5.3	0.0030	1.11E-06
3402	-4.9	0.0037	4.44E-06
3552	-4.2	0.0043	1.11E-06
3702	-3.6	0.0040	-1.1E-06
3852	-3.0	0.0040	-2.2E-06
4002	-2.4	0.0033	-4.4E-06
4152	-2.0	0.0027	-3.3E-06
4302	-1.6	0.0023	-4.4E-06
4452	-1.3	0.0013	-5.6E-06
4602	-1.2	0.0007	-5.3E-06
4752	-1.1	-0.0003	1.45E-07

Table A.15. (b)

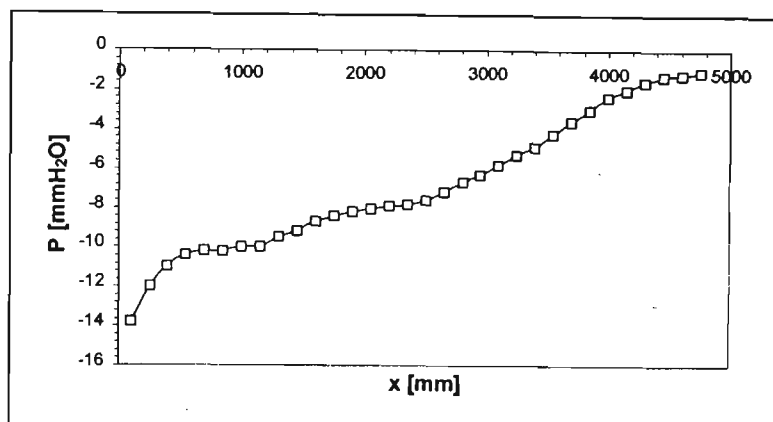


Figure A.15. (a)

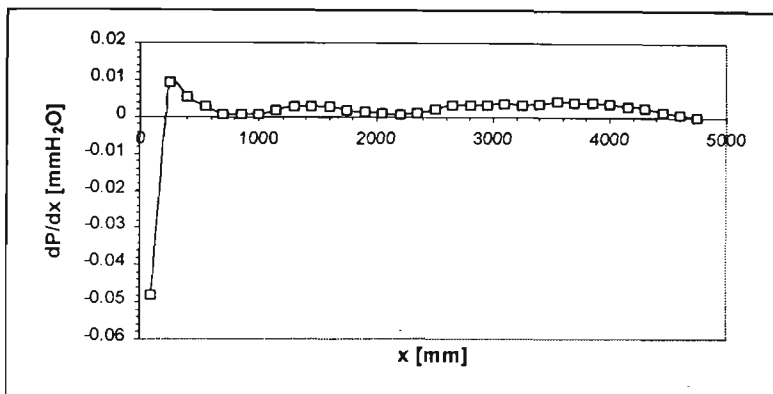


Figure A.15. (b)

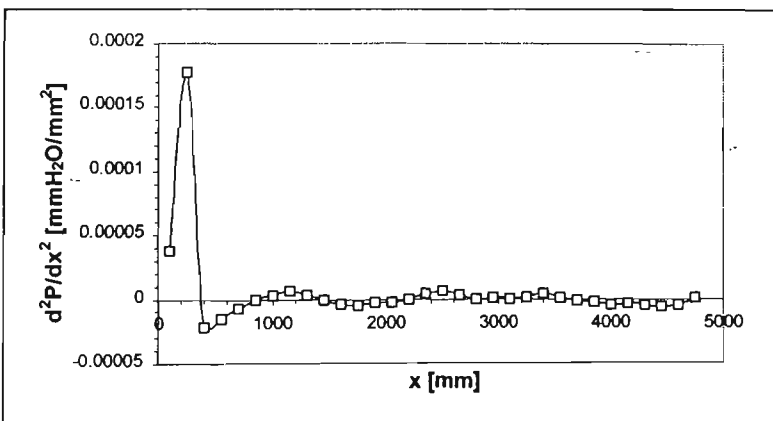


Figure A.15. (c)

CASE 16

x [mm]	y [mm]
0	413
143	416
615	426
1193	438
1703	449
2226	462
2765	482
3280	511
3865	573
4470	699
4640	772

Table A.16. (a)

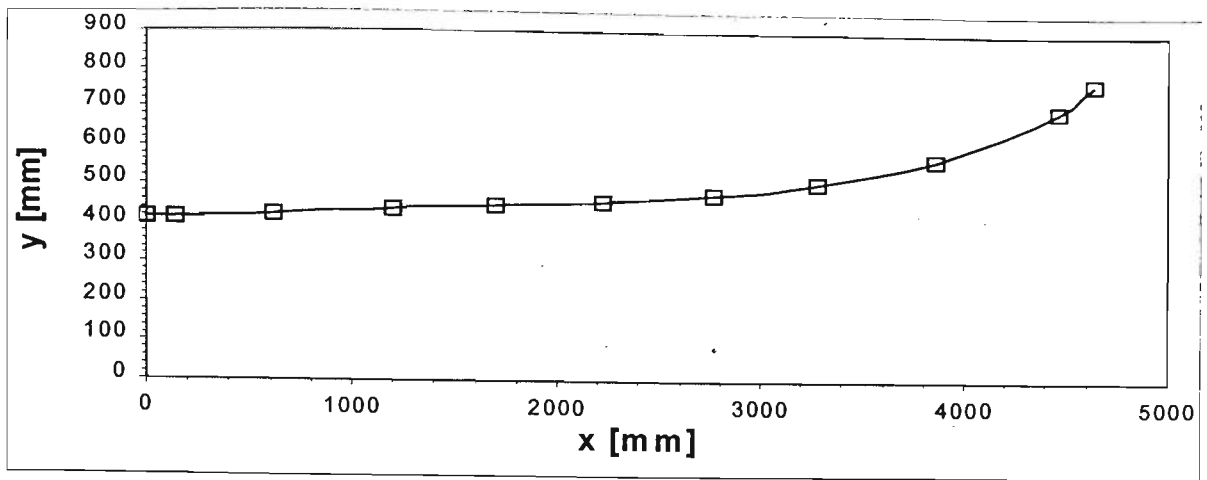


Figure A.16. (a)

x [mm]	P [mmH ₂ O]	dP/dx [mmH ₂ O/mm]	d ² P/dx ² [mmH ₂ O/mm ²]
100	-13.0	-0.0452	2.93E-05
250	-11.3	0.0073	0.000161
400	-10.8	0.0030	-1.8E-05
550	-10.4	0.0020	-7.8E-06
700	-10.2	0.0007	-4.4E-06
850	-10.2	0.0007	2.22E-06
1000	-10.0	0.0013	3.33E-06
1150	-9.8	0.0017	-1.1E-06
1300	-9.5	0.0010	-3.3E-06
1450	-9.5	0.0007	-1.1E-06
1600	-9.3	0.0007	-1.1E-06
1750	-9.3	0.0003	1.11E-06
1900	-9.2	0.0010	2.22E-06
2050	-9.0	0.0010	2.19E-06
2200	-8.9	0.0017	5.46E-06
2352	-8.5	0.0026	2.24E-06
2502	-8.1	0.0023	-1.1E-06
2652	-7.8	0.0023	2.22E-06
2802	-7.4	0.0030	3.33E-06
2952	-6.9	0.0033	1.01E-20
3102	-6.4	0.0030	-2.2E-06
3252	-6.0	0.0027	2.22E-06
3402	-5.6	0.0037	3.33E-06
3552	-4.9	0.0037	1.01E-20
3702	-4.5	0.0037	1.11E-06
3852	-3.8	0.0040	-1.1E-06
4002	-3.3	0.0033	-2.2E-06
4152	-2.8	0.0033	-2.2E-06
4302	-2.3	0.0027	-4.4E-06
4452	-2.0	0.0020	-4.4E-06
4602	-1.7	0.0013	-7.9E-06
4752	-1.6	-0.0004	2.9E-07

Table A.16. (b)

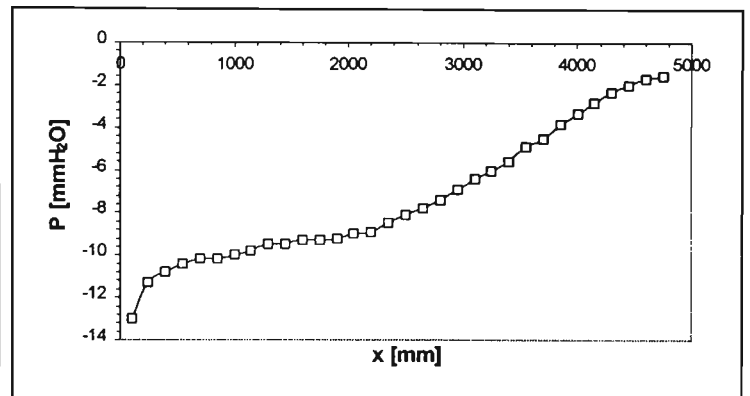


Figure A.16. (b)

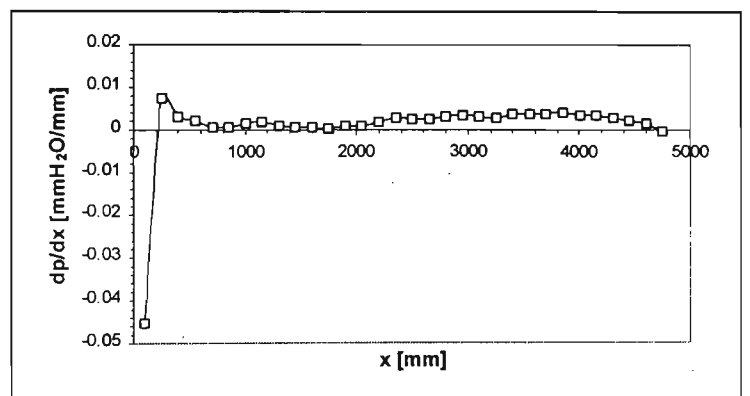


Figure A.16. (c)

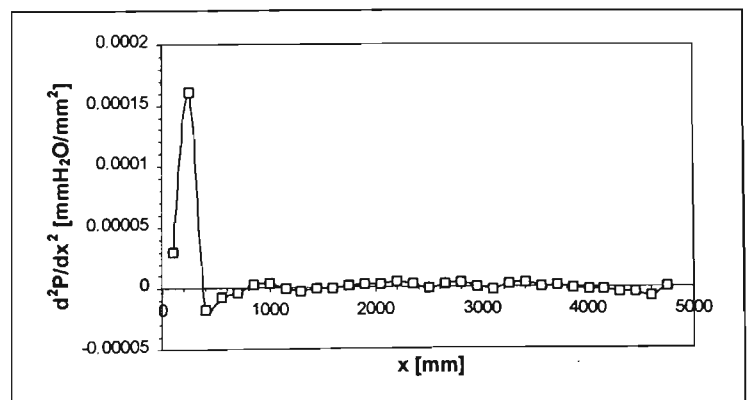


Figure A.16. (d)

x [mm]	y [mm]
0	425
143	426
615	431
1193	440
1703	448.5
2226	462
2765	482
3280	511
3865	573
4470	699
4640	772

Table A.17. (a)

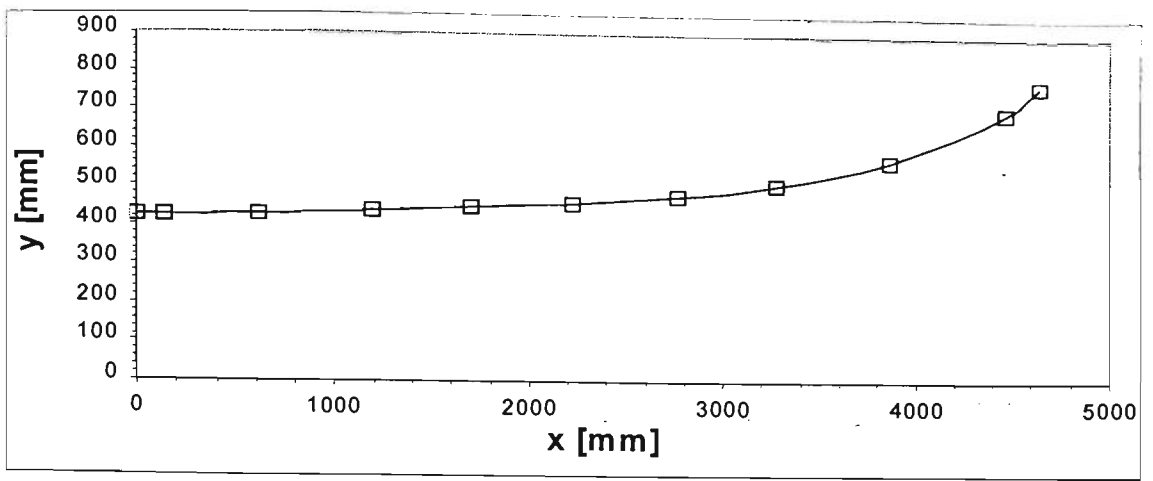


Figure A.17. (a)

x [mm]	P [mmH ₂ O]	dP/dx [mmH ₂ O/mm]	d ² P/dx ² [mmH ₂ O/mm ²]
100	-12.3	-0.0420	3.47E-05
250	-10.5	0.0087	0.000153
400	-9.7	0.0040	-2.3E-05
550	-9.3	0.0017	-1.1E-05
700	-9.2	0.0007	-3.3E-06
850	-9.1	0.0007	-2E-20
1000	-9.0	0.0007	1.11E-06
1150	-8.9	0.0010	2.22E-06
1300	-8.7	0.0013	1.11E-06
1450	-8.5	0.0013	-2.2E-06
1600	-8.3	0.0007	-2.2E-06
1750	-8.3	0.0007	1.11E-06
1900	-8.1	0.0010	1.11E-06
2050	-8.0	0.0010	-2.2E-08
2200	-7.8	0.0010	1.07E-06
2352	-7.7	0.0013	3.33E-06
2502	-7.4	0.0020	3.36E-06
2652	-7.1	0.0023	2.22E-06
2802	-6.7	0.0027	2.22E-06
2952	-6.3	0.0030	1.11E-06
3102	-5.8	0.0030	-1.1E-06
3252	-5.4	0.0027	1.01E-20
3402	-5.0	0.0030	2.22E-06
3552	-4.5	0.0033	-1.1E-06
3702	-4.0	0.0027	1.11E-06
3852	-3.7	0.0037	4.44E-06
4002	-2.9	0.0040	-3.3E-06
4152	-2.5	0.0027	-5.6E-06
4302	-2.1	0.0023	-3.3E-06
4452	-1.8	0.0017	-2.2E-06
4602	-1.6	0.0017	-6.7E-06
4752	-1.3	-0.0003	3.62E-07

Table A.17. (b)

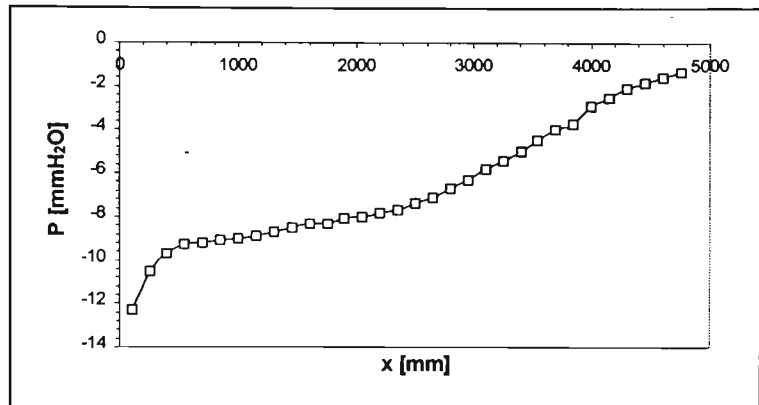


Figure A.17. (b)

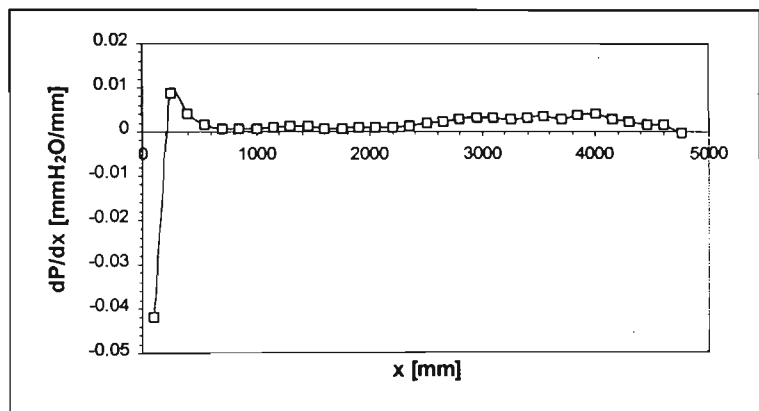


Figure A.17. (c)

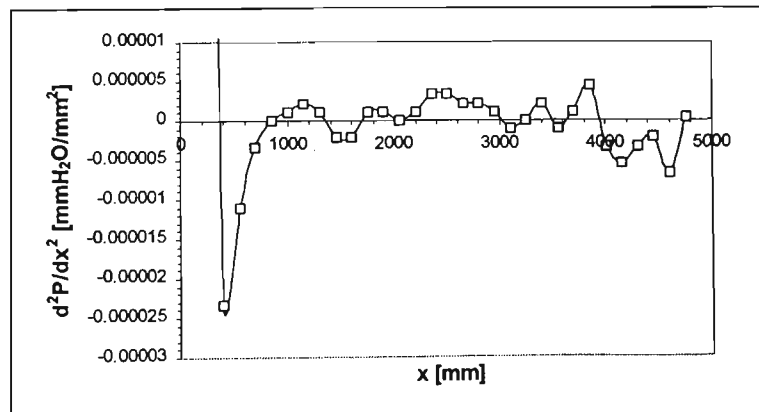


Figure A.17. (d)

CASE 18

x [mm]	y [mm]
0	425
143	426
615	431
1193	440
1703	448.5
2226	462
2765	482
3280	511
3865	573
4470	699
4640	772

Table A.18. (a)

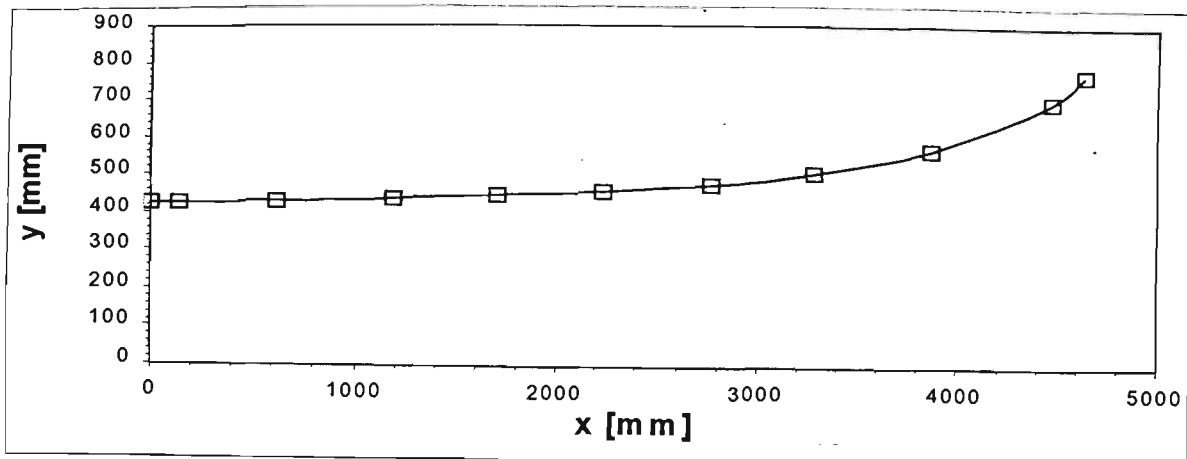


Figure A.18. (a)

x [mm]	P [mmH ₂ O]	dP/dx [mmH ₂ O/mm]	d ² P/dx ² [mmH ₂ O/mm ²]
100	-12.4	-0.0412	0.000036
250	-10.3	0.0090	0.000147
400	-9.7	0.0030	-2.4E-05
550	-9.4	0.0017	-7.8E-06
700	-9.2	0.0007	-3.3E-06
850	-9.2	0.0007	1.11E-06
1000	-9.0	0.0010	2.22E-06
1150	-8.9	0.0013	1.11E-06
1300	-8.6	0.0013	-1.1E-06
1450	-8.5	0.0010	-2.2E-06
1600	-8.3	0.0007	-2.2E-06
1750	-8.3	0.0003	1.11E-06
1900	-8.2	0.0010	3.33E-06
2050	-8.0	0.0013	2.19E-06
2200	-7.8	0.0017	-2.9E-08
2352	-7.5	0.0013	-1.1E-06
2502	-7.4	0.0013	3.36E-06
2652	-7.1	0.0023	5.56E-06
2802	-6.7	0.0030	2.22E-06
2952	-6.2	0.0030	-2.2E-06
3102	-5.8	0.0023	-2.2E-06
3252	-5.5	0.0023	0
3402	-5.1	0.0023	2.22E-06
3552	-4.8	0.0030	6.67E-06
3702	-4.2	0.0043	3.33E-06
3852	-3.5	0.0040	-3.3E-06
4002	-3.0	0.0033	-2.2E-06
4152	-2.5	0.0033	-3.3E-06
4302	-2.0	0.0023	-5.6E-06
4452	-1.8	0.0017	-3.3E-06
4602	-1.5	0.0013	-6.6E-06
4752	-1.4	-0.0003	2.9E-07

Table A.18. (b)

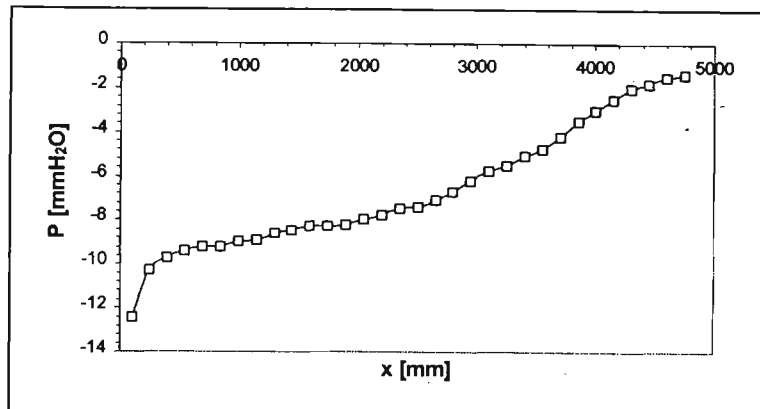


Figure A.18. (b)

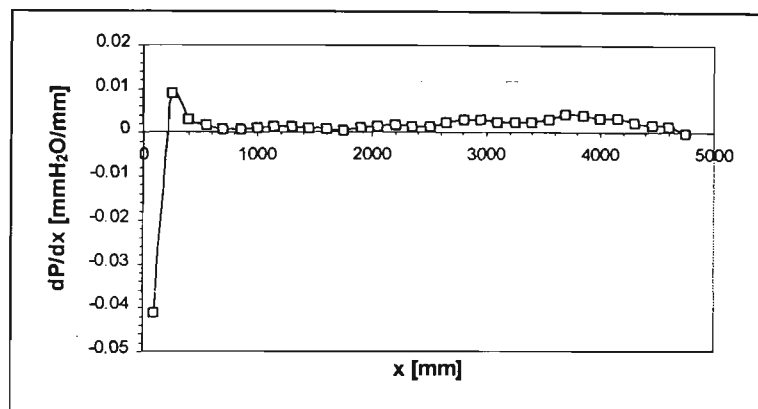


Figure A.18. (c)

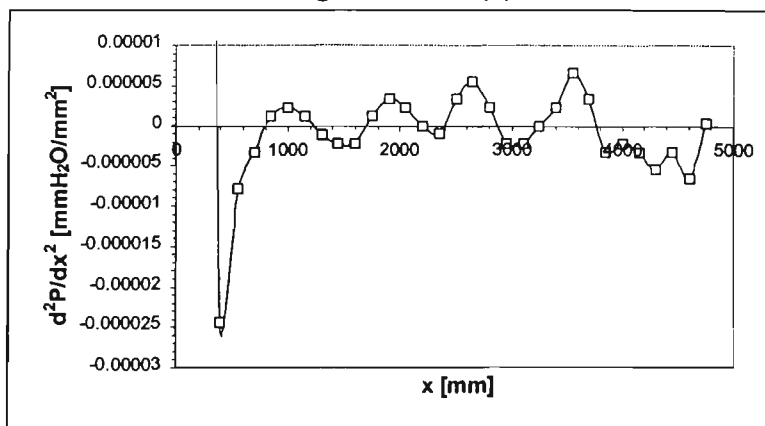


Figure A.18. (d)

CASE 19

x [mm]	y [mm]
0	425
143	425
615	430
1193	440
1703	448
2226	457
2765	480
3280	511
3865	571
4470	700
4640	751

Table A.19. (a)

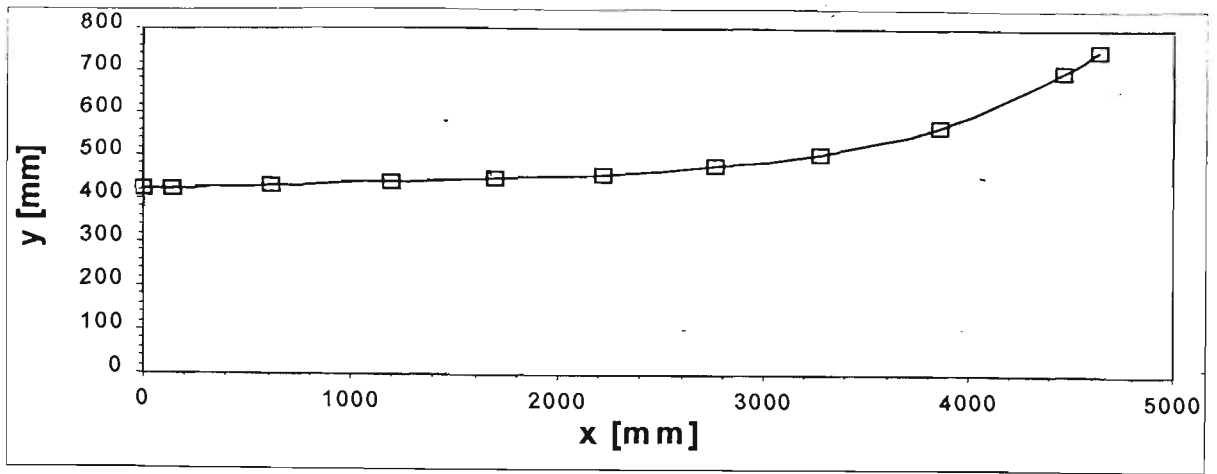


Figure A.19. (a)

x [mm]	P [mmH ₂ O]	dP/dx [mmH ₂ O/mm]	d ² P/dx ² [mmH ₂ O/mm ²]
100	-16.2	-0.0588	2.67E-05
250	-14.7	0.0067	0.0002
400	-14.2	0.0013	-1.9E-05
550	-14.3	0.0010	3.33E-06
700	-13.9	0.0023	1.11E-06
850	-13.6	0.0013	-5.6E-06
1000	-13.5	0.0007	1.11E-06
1150	-13.4	0.0017	2.22E-06
1300	-13.0	0.0013	-5.6E-06
1450	-13.0	0.0000	-7.8E-06
1600	-13.0	-0.0010	-2.2E-06
1750	-13.3	-0.0007	3.33E-06
1900	-13.2	0.0000	5.56E-06
2050	-13.3	0.0010	8.83E-06
2200	-12.9	0.0026	8.75E-06
2352	-12.5	0.0036	4.47E-06
2502	-11.8	0.0040	-1E-06
2652	-11.3	0.0033	-1.1E-06
2802	-10.8	0.0037	3.33E-06
2952	-10.2	0.0043	3.33E-06
3102	-9.5	0.0047	-2.2E-06
3252	-8.8	0.0037	-1.1E-06
3402	-8.4	0.0043	6.67E-06
3552	-7.5	0.0057	3.33E-06
3702	-6.7	0.0053	1.11E-06
3852	-5.9	0.0060	2.22E-06
4002	-4.9	0.0060	-3.3E-06
4152	-4.1	0.0050	-5.6E-06
4302	-3.4	0.0043	-5.6E-06
4452	-2.8	0.0033	-7.8E-06
4602	-2.4	0.0020	-1.3E-05
4752	-2.2	-0.0005	4.35E-07

Table A.19. (b)

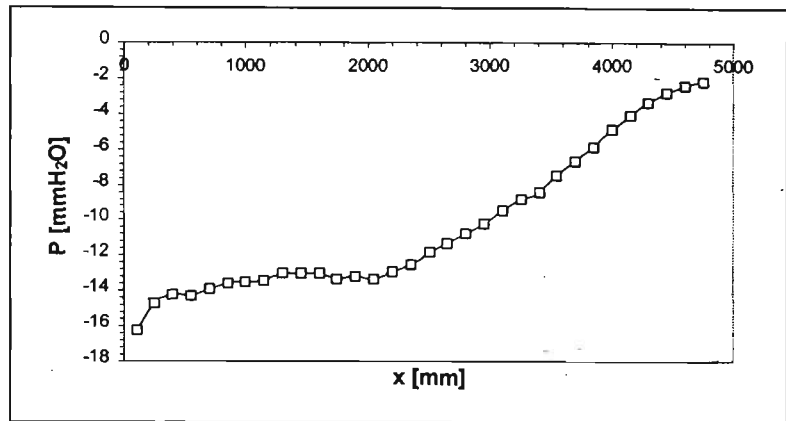


Figure A.19. (b)

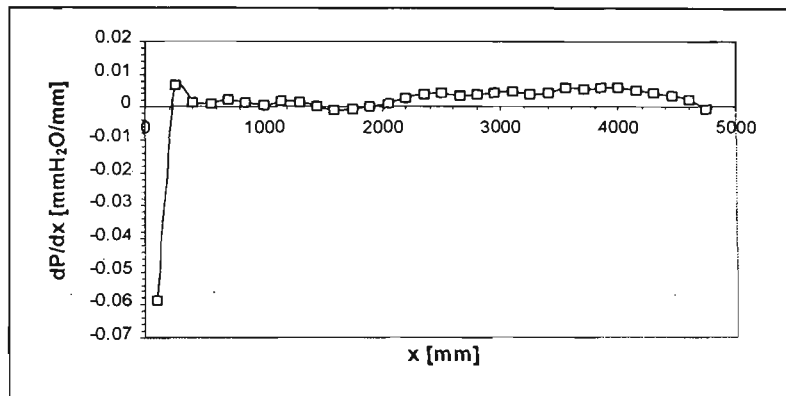


Figure A.19. (c)

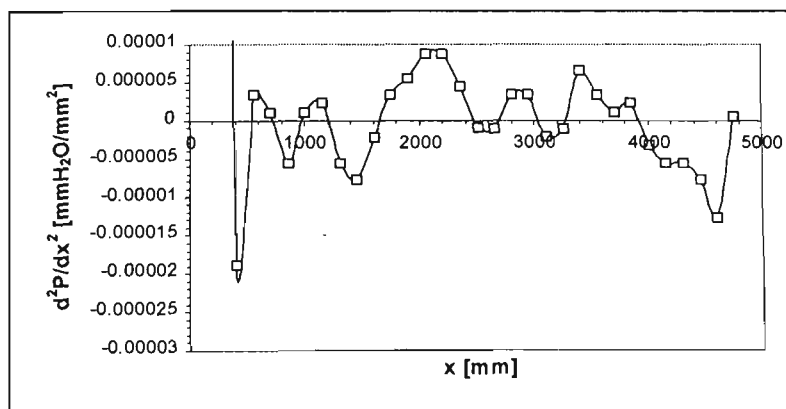


Figure A.19. (d)

CASE 20

x [mm]	y [mm]
0	435
143	435
615	445
1193	457
1703	448
2226	457
2765	480
3280	511
3865	571
4470	700
4640	751

Table A.20. (a)

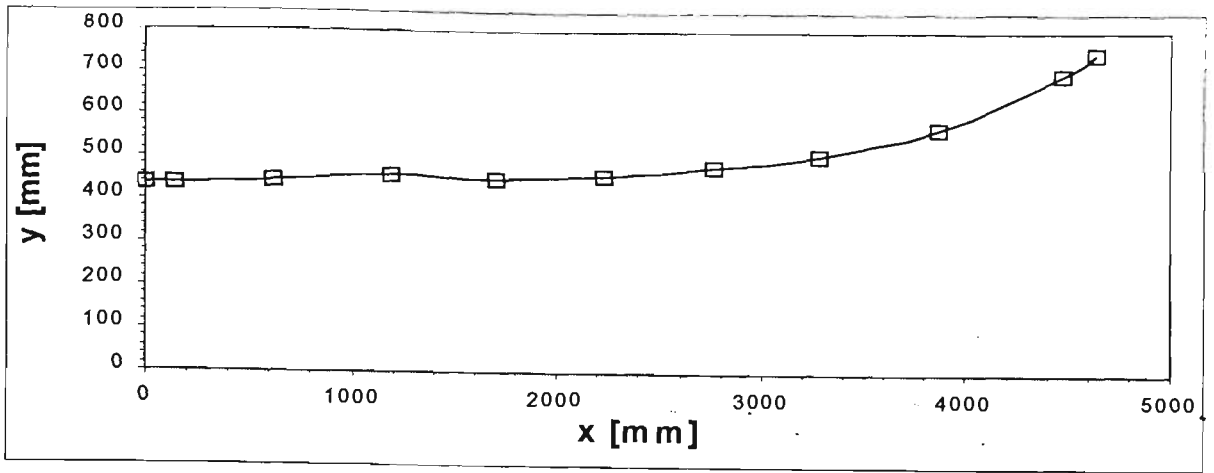


Figure A.20. (a)

x [mm]	P [mmH ₂ O]	dP/dx [mmH ₂ O/mm]	d ² P/dx ² [mmH ₂ O/mm ²]
100	-14.3	-0.0588	-5.3E-06
250	-14.7	-0.0013	0.000195
400	-14.7	-0.0003	5.56E-06
550	-14.8	0.0003	3.33E-06
700	-14.6	0.0007	-4.4E-06
850	-14.6	-0.0010	-5.6E-06
1000	-14.9	-0.0010	7.78E-06
1150	-14.9	0.0013	1.22E-05
1300	-14.5	0.0027	3.33E-06
1450	-14.1	0.0023	-2.2E-06
1600	-13.8	0.0020	2.02E-20
1750	-13.5	0.0023	-1.1E-06
1900	-13.1	0.0017	-2.2E-06
2050	-13.0	0.0017	3.27E-06
2200	-12.6	0.0026	6.54E-06
2352	-12.2	0.0036	6.68E-06
2502	-11.5	0.0047	-1E-06
2652	-10.8	0.0033	-4.4E-06
2802	-10.5	0.0033	3.33E-06
2952	-9.8	0.0043	2.22E-06
3102	-9.2	0.0040	-2.2E-06
3252	-8.6	0.0037	1.11E-06
3402	-8.1	0.0043	3.33E-06
3552	-7.3	0.0047	4.44E-06
3702	-6.7	0.0057	5.56E-06
3852	-5.6	0.0063	-2.9E-21
4002	-4.8	0.0057	-3.3E-06
4152	-3.9	0.0053	-5.6E-06
4302	-3.2	0.0040	-7.8E-06
4452	-2.7	0.0030	-6.7E-06
4602	-2.3	0.0020	-1.2E-05
4752	-2.1	-0.0005	4.35E-07

Table A.20. (b)

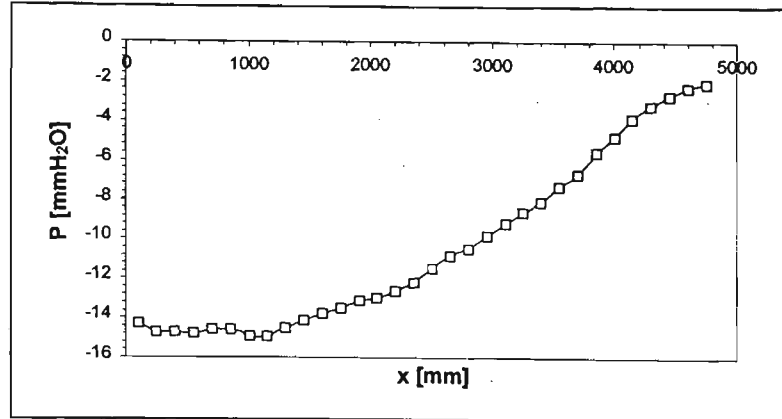


Figure A.20. (b)

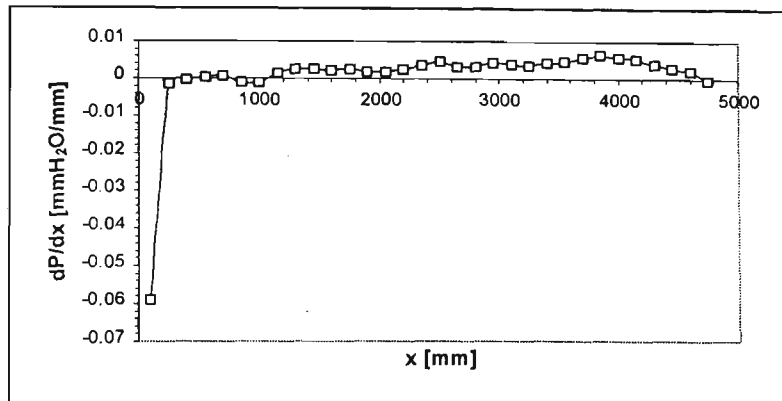


Figure A.20. (c)

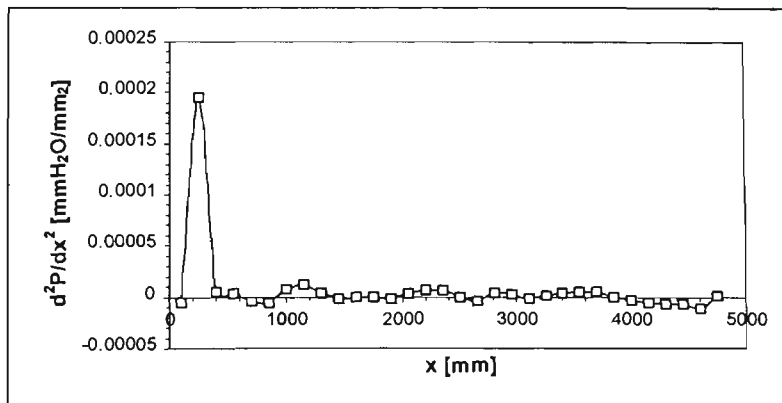


Figure A.20. (d)

Appendix B. Mean Velocity Profiles

The experimental values of y^+ , U^+ , y/δ and U/U_e are listed in Tables B.1 to B.12

for the 12 streamwise locations indicated in Chapter 4.

y^+	U^+	y/δ	U/U_e
31.67	13.79	0.05	0.63
41.17	13.92	0.07	0.64
50.67	14.56	0.09	0.66
60.17	14.74	0.10	0.67
69.67	15.17	0.12	0.69
79.17	15.34	0.14	0.70
88.67	15.63	0.15	0.71
98.17	15.81	0.17	0.72
107.67	16.03	0.19	0.73
117.17	16.15	0.20	0.74
126.67	16.37	0.22	0.75
136.17	16.53	0.24	0.76
145.67	16.70	0.25	0.76
155.17	16.97	0.27	0.77
164.67	17.12	0.29	0.78
174.17	17.39	0.30	0.79
183.67	17.49	0.32	0.80
193.17	17.64	0.33	0.81
202.67	17.75	0.35	0.81
212.17	17.95	0.37	0.82
221.67	18.00	0.38	0.82
348.97	19.95	0.60	0.91
538.97	21.61	0.93	0.99
557.97	21.73	0.97	0.99
576.97	21.77	1.00	0.99
595.97	21.81	1.03	1.00
614.97	21.86	1.07	1.00
633.97	21.90	1.10	1.00
652.97	21.94	1.13	1.00
671.97	21.94	1.16	1.00
690.97	21.94	1.20	1.00
709.97	21.94	1.23	1.00
728.97	21.94	1.26	1.00
918.97	21.94	1.59	1.00

1298.97	21.94	2.25	1.00
1678.97	21.90	2.91	1.00
2058.97	21.90	3.57	1.00
2438.97	21.90	4.23	1.00
2818.97	21.90	4.89	1.00
3198.97	21.90	5.54	1.00
3578.97	21.90	6.20	1.00
3958.97	21.90	6.86	1.00
5858.97	21.90	10.15	1.00
7758.97	21.86	13.45	1.00
9658.97	21.86	16.74	1.00
11558.97	21.81	20.03	1.00
13458.97	21.86	23.33	1.00
15358.97	21.90	26.62	1.00
17258.97	21.90	29.91	1.00
19158.97	21.90	33.21	1.00
21058.97	21.90	36.50	1.00
22958.97	21.94	39.79	1.00
24858.97	21.90	43.09	1.00
25048.97	21.90	43.41	1.00
25238.97	21.90	43.74	1.00
25428.97	21.90	44.07	1.00
25618.97	21.86	44.40	1.00
25808.97	21.86	44.73	1.00
25998.97	21.77	45.06	0.99
26188.97	21.48	45.39	0.98
26378.97	20.18	45.72	0.92

Table B.1. $x = 262$ mm. $u_* = 0.95$ m/s,

$\delta = 0.0091$ mm and $U_e = 20.8$ m/s.

y^+	U^+	y/δ	U/U_e
27.33	13.79	0.02	0.55
35.53	13.88	0.02	0.55
43.73	14.23	0.03	0.57
51.93	14.73	0.04	0.59
60.13	15.06	0.04	0.60
68.33	15.29	0.05	0.61
76.53	15.61	0.05	0.62
84.73	15.76	0.06	0.63
92.93	15.99	0.06	0.64
101.13	16.29	0.07	0.65
109.33	16.37	0.08	0.65
117.53	16.52	0.08	0.66
125.73	16.66	0.09	0.66
133.93	16.81	0.09	0.67
142.13	16.95	0.10	0.67
150.33	17.09	0.10	0.68
158.53	17.30	0.11	0.69
166.73	17.44	0.12	0.69
174.93	17.58	0.12	0.70
183.13	17.72	0.13	0.71
191.33	17.92	0.13	0.71
301.21	19.17	0.21	0.76
465.21	21.04	0.32	0.84
793.21	23.49	0.55	0.94
1121.21	24.75	0.77	0.99
1449.21	25.09	1.00	1.00
1613.21	25.09	1.11	1.00
1646.01	25.14	1.14	1.00
1678.81	25.14	1.16	1.00
1711.61	25.14	1.18	1.00
1744.41	25.14	1.20	1.00
1777.21	25.14	1.23	1.00
1941.21	25.14	1.34	1.00
2105.21	25.09	1.45	1.00
2433.21	25.14	1.68	1.00
2761.21	25.09	1.91	1.00
3089.21	25.09	2.13	1.00
3417.21	25.09	2.36	1.00
5057.21	25.04	3.49	1.00
6697.21	25.09	4.62	1.00
8337.21	25.04	5.75	1.00
9977.21	25.04	6.88	1.00

11617.21	25.04	8.02	1.00
13257.21	25.09	9.15	1.00
14897.21	25.04	10.28	1.00
16537.21	25.09	11.41	1.00
18177.21	25.14	12.54	1.00
19817.21	25.14	13.67	1.00
21457.21	25.09	14.81	1.00
21621.21	25.09	14.92	1.00
21785.21	25.04	15.03	1.00
21949.21	24.99	15.15	0.99
22277.21	24.50	15.37	0.98
22605.21	23.13	15.60	0.92
22933.21	20.92	15.82	0.83
23097.21	19.61	15.94	0.78

Figure B.2. $x = 1089$ mm. $u^* = 0.82$ m/s,

$\delta = 0.0265$ mm and $U_e = 20.6$ m/s.

y^+	U^+	y/δ	U/U_e
27.00	13.79	0.02	0.54
35.10	13.88	0.02	0.55
43.20	14.50	0.03	0.57
51.30	14.67	0.04	0.58
59.40	15.09	0.04	0.59
67.50	15.41	0.05	0.61
75.60	15.65	0.05	0.62
83.70	15.89	0.06	0.62
91.80	16.04	0.06	0.63
99.90	16.20	0.07	0.64
108.00	16.35	0.08	0.64
116.10	16.50	0.08	0.65
124.20	16.73	0.09	0.66
132.30	16.87	0.09	0.66
140.40	16.95	0.10	0.67
148.50	17.17	0.10	0.68
156.60	17.31	0.11	0.68
164.70	17.38	0.12	0.68
172.80	17.53	0.12	0.69
180.90	17.74	0.13	0.70
189.00	17.88	0.13	0.70
297.54	19.09	0.21	0.75
459.54	20.65	0.32	0.81
783.54	23.20	0.55	0.91
1107.54	24.81	0.77	0.98
1431.54	25.36	1.00	1.00
1674.54	25.45	1.17	1.00
1755.54	25.45	1.23	1.00
1917.54	25.45	1.34	1.00
2079.54	25.45	1.45	1.00
2241.54	25.45	1.57	1.00
2403.54	25.45	1.68	1.00
2727.54	25.40	1.91	1.00
3051.54	25.40	2.13	1.00
3375.54	25.40	2.36	1.00
4995.54	25.40	3.49	1.00
6615.54	25.40	4.62	1.00
8235.54	25.40	5.75	1.00
9855.54	25.36	6.88	1.00
11475.54	25.36	8.02	1.00
13095.54	25.36	9.15	1.00
14715.54	25.40	10.28	1.00

16335.54	25.40	11.41	1.00
17955.54	25.45	12.54	1.00
19575.54	25.45	13.67	1.00
21195.54	25.45	14.81	1.00
21357.54	25.45	14.92	1.00
21519.54	25.40	15.03	1.00
21681.54	25.36	15.15	1.00
22005.54	25.31	15.37	1.00
22329.54	24.91	15.60	0.98
22491.54	23.94	15.71	0.94
22653.54	22.11	15.82	0.87
22815.54	21.13	15.94	0.83
22977.54	19.60	16.05	0.77
23139.54	17.74	16.16	0.70

Figure B.3. $x = 1245$ mm. $u_* = 0.81$ m/s,

$\delta = 0.0265$ mm and $U_e = 20.6$ m/s.

y^+	U^+	y/δ	U/U_e
25.00	13.67	0.01	0.51
32.50	13.67	0.02	0.51
40.00	13.67	0.02	0.51
47.50	13.67	0.02	0.51
55.00	13.88	0.03	0.52
62.50	14.39	0.03	0.53
70.00	14.59	0.03	0.54
77.50	14.89	0.04	0.55
85.00	15.18	0.04	0.56
92.50	15.37	0.04	0.57
100.00	15.65	0.05	0.58
107.50	16.01	0.05	0.59
115.00	16.19	0.06	0.60
122.50	16.28	0.06	0.60
125.50	16.46	0.06	0.61
130.00	16.55	0.06	0.61
137.50	16.64	0.07	0.62
145.00	16.72	0.07	0.62
152.50	16.98	0.07	0.63
160.00	17.15	0.08	0.64
167.50	17.24	0.08	0.64
175.00	17.40	0.08	0.65
253.00	18.30	0.12	0.68
325.00	19.22	0.16	0.71
475.00	20.47	0.23	0.76
575.50	21.16	0.28	0.79
725.50	22.17	0.35	0.82
875.50	23.13	0.42	0.86
1025.50	23.87	0.49	0.89
1175.50	24.59	0.57	0.91
1325.50	25.46	0.64	0.95
1475.50	25.91	0.71	0.96
1625.50	26.30	0.78	0.98
1775.50	26.57	0.86	0.99
1925.50	26.74	0.93	0.99
2075.50	26.79	1.00	0.99
2105.50	26.84	1.01	1.00
2135.50	26.84	1.03	1.00
2165.50	26.90	1.04	1.00
2195.50	26.90	1.06	1.00
2225.50	26.90	1.07	1.00
2375.50	26.95	1.14	1.00
2525.50	26.95	1.22	1.00

2675.50	26.95	1.29	1.00
2825.50	26.95	1.36	1.00
2975.50	26.95	1.43	1.00
3125.50	26.95	1.51	1.00
4625.50	26.90	2.23	1.00
6125.50	26.90	2.95	1.00
7625.50	26.90	3.67	1.00
9125.50	26.90	4.40	1.00
10625.50	26.90	5.12	1.00
12125.50	26.95	5.84	1.00
13625.50	26.90	6.56	1.00
15125.50	26.95	7.29	1.00
16625.50	26.95	8.01	1.00
18125.50	26.95	8.73	1.00
19625.50	26.95	9.46	1.00
19640.50	26.95	9.46	1.00
19655.50	26.95	9.47	1.00
19670.50	26.95	9.48	1.00
19685.50	26.95	9.48	1.00
19760.50	26.95	9.52	1.00
19835.50	26.95	9.56	1.00
19910.50	26.95	9.59	1.00
19985.50	26.90	9.63	1.00
20060.50	26.90	9.67	1.00
20135.50	26.90	9.70	1.00
20210.50	26.79	9.74	0.99
20285.50	26.74	9.77	0.99
20360.50	26.68	9.81	0.99
20435.50	26.57	9.85	0.99
20675.50	26.13	9.96	0.97
20825.50	25.80	10.03	0.96
20975.50	25.11	10.11	0.93
21125.50	24.65	10.18	0.92
21275.50	23.93	10.25	0.89
21425.50	23.13	10.32	0.86
21575.50	22.04	10.40	0.82
21725.50	21.16	10.47	0.79
21875.50	20.04	10.54	0.74
22025.50	18.61	10.61	0.69

Figure B.4. $x = 1867$ mm. $u_* = 0.75$ m/s,

$\delta = 0.0415$ mm and $U_e = 20.2$ m/s.

y^+	U^+	y/δ	U/U_e
24.67	13.73	0.01	0.51
32.07	13.40	0.01	0.50
39.47	13.18	0.01	0.49
46.87	13.18	0.02	0.49
54.27	13.18	0.02	0.49
61.67	13.18	0.02	0.49
69.07	13.18	0.02	0.49
76.47	13.52	0.03	0.51
83.87	13.95	0.03	0.52
91.27	14.27	0.03	0.53
98.67	14.58	0.03	0.54
106.07	14.88	0.04	0.56
113.47	14.98	0.04	0.56
120.87	15.18	0.04	0.57
128.27	15.47	0.05	0.58
135.67	15.56	0.05	0.58
143.07	15.85	0.05	0.59
150.47	15.94	0.05	0.60
157.87	16.04	0.06	0.60
165.27	16.40	0.06	0.61
172.67	16.49	0.06	0.62
320.67	18.13	0.11	0.68
468.67	19.40	0.17	0.73
616.67	20.30	0.22	0.76
764.67	21.16	0.27	0.79
912.67	22.06	0.32	0.82
1060.67	22.59	0.37	0.84
1208.67	23.24	0.43	0.87
1356.67	23.81	0.48	0.89
1504.67	24.49	0.53	0.92
1652.67	24.97	0.58	0.93
1800.67	25.27	0.63	0.94
1948.67	25.74	0.69	0.96
2096.67	26.08	0.74	0.97
2244.67	26.25	0.79	0.98
2259.47	26.31	0.80	0.98
2274.27	26.37	0.80	0.99
2289.07	26.37	0.81	0.99
2303.87	26.31	0.81	0.98
2318.67	26.37	0.82	0.99
2333.47	26.42	0.82	0.99
2348.27	26.42	0.83	0.99

2363.07	26.42	0.83	0.99
2377.87	26.42	0.84	0.99
2392.67	26.42	0.84	0.99
2540.67	26.48	0.90	0.99
2688.67	26.59	0.95	0.99
2836.67	26.65	1.00	1.00
2984.67	26.70	1.05	1.00
3132.67	26.70	1.10	1.00
3280.67	26.70	1.16	1.00
3428.67	26.70	1.21	1.00
4464.67	26.70	1.57	1.00

Figure B.5. $x = 2335$ mm. $u_* = 0.75$ m/s,

$\delta = 0.0575$ mm and $U_e = 19.8$ m/s.

y^+	U^+	y/δ	U/U_e
22.67	13.68	0.01	0.47
31.73	14.31	0.01	0.49
38.53	14.31	0.02	0.49
45.33	14.91	0.02	0.51
52.13	15.15	0.02	0.52
58.93	15.38	0.02	0.53
65.73	15.72	0.03	0.54
72.53	16.05	0.03	0.55
79.33	16.16	0.03	0.56
86.13	16.38	0.03	0.57
92.93	16.59	0.04	0.57
99.73	16.80	0.04	0.58
106.53	16.91	0.04	0.58
113.33	17.11	0.05	0.59
126.93	17.42	0.05	0.60
140.53	17.62	0.06	0.61
154.13	17.82	0.06	0.62
167.73	18.21	0.07	0.63
303.73	19.97	0.12	0.69
439.73	21.25	0.18	0.73
575.73	22.23	0.23	0.77
711.73	23.01	0.29	0.79
847.73	23.84	0.34	0.82
983.73	24.64	0.40	0.85
1119.73	25.27	0.45	0.87
1255.73	25.76	0.51	0.89
1391.73	26.43	0.56	0.91
1527.73	26.96	0.62	0.93
1663.73	27.22	0.67	0.94
1799.73	27.86	0.73	0.96
1935.73	28.12	0.78	0.97
2071.73	28.49	0.84	0.98
2207.73	28.61	0.89	0.99
2343.73	28.67	0.95	0.99
2479.73	28.92	1.00	1.00
2506.93	28.92	1.01	1.00
2534.13	28.92	1.02	1.00
2561.33	28.92	1.03	1.00
2588.53	28.92	1.04	1.00
2615.73	28.98	1.05	1.00
2642.93	28.98	1.07	1.00
2670.13	28.98	1.08	1.00

2697.33	28.98	1.09	1.00
2724.53	28.98	1.10	1.00
2751.73	28.98	1.11	1.00
4111.73	29.04	1.66	1.00

Figure B.6. $x = 2422$ mm. $u_* = 0.68$ m/s,

$\delta = 0.0547$ mm and $U_e = 19.7$ m/s.

y^+	U^+	y/δ	U/U_e
23.00	13.64	0.01	0.48
29.90	13.77	0.01	0.49
36.80	14.01	0.01	0.50
43.70	14.38	0.02	0.51
50.60	14.73	0.02	0.52
57.50	15.07	0.02	0.53
64.40	15.19	0.02	0.54
71.30	15.52	0.03	0.55
78.20	15.74	0.03	0.56
85.10	16.06	0.03	0.57
92.00	16.17	0.03	0.57
98.90	16.28	0.04	0.58
105.80	16.49	0.04	0.58
112.70	16.59	0.04	0.59
119.60	16.69	0.04	0.59
126.50	16.90	0.05	0.60
133.40	17.10	0.05	0.61
140.30	17.20	0.05	0.61
147.20	17.20	0.05	0.61
154.10	17.30	0.06	0.61
161.00	17.40	0.06	0.62
239.66	18.35	0.09	0.65
391.46	19.88	0.14	0.70
529.46	20.72	0.19	0.73
667.46	21.53	0.24	0.76
805.46	22.39	0.29	0.79
943.46	23.07	0.34	0.82
1081.46	23.73	0.39	0.84
1219.46	24.23	0.44	0.86
1357.46	24.79	0.49	0.88
1495.46	25.27	0.54	0.89
1633.46	26.00	0.58	0.92
1771.46	26.33	0.63	0.93
1909.46	26.53	0.68	0.94
2047.46	27.04	0.73	0.96
2185.46	27.35	0.78	0.97
2323.46	27.60	0.83	0.98
2461.46	27.79	0.88	0.98
2599.46	27.91	0.93	0.99
2613.26	27.91	0.94	0.99
2627.06	27.97	0.94	0.99
2640.86	28.03	0.95	0.99
2654.66	28.09	0.95	0.99
2668.46	28.09	0.96	0.99
2682.26	28.09	0.96	0.99

2696.06	28.16	0.97	1.00
2709.86	28.09	0.97	0.99
2723.66	28.09	0.98	0.99
2792.66	28.09	1.00	0.99
2875.46	28.16	1.03	1.00
2903.06	28.16	1.04	1.00
2932.04	28.22	1.05	1.00
2961.02	28.22	1.06	1.00
2985.86	28.22	1.07	1.00
3013.46	28.22	1.08	1.00
3041.06	28.28	1.09	1.00
3068.66	28.22	1.10	1.00
3151.46	28.22	1.13	1.00
3220.46	28.22	1.15	1.00
3289.46	28.22	1.18	1.00
4255.46	28.28	1.52	1.00
5635.46	28.28	2.02	1.00
7015.46	28.22	2.51	1.00
8395.46	28.22	3.01	1.00
9775.46	28.22	3.50	1.00
11155.46	28.22	3.99	1.00
12535.46	28.22	4.49	1.00
13915.46	28.28	4.98	1.00
15295.46	28.22	5.48	1.00
16675.46	28.22	5.97	1.00
18055.46	28.28	6.47	1.00
18193.46	28.28	6.51	1.00
18331.46	28.34	6.56	1.00
18469.46	28.34	6.61	1.00
18607.46	28.28	6.66	1.00
18745.46	28.22	6.71	1.00
18883.46	28.22	6.76	1.00
19021.46	28.09	6.81	0.99
19159.46	28.03	6.86	0.99
19297.46	27.79	6.91	0.98
19435.46	27.60	6.96	0.98
19711.46	26.97	7.06	0.95
19987.46	26.14	7.16	0.92
20263.46	25.13	7.26	0.89
20539.46	24.02	7.35	0.85
20815.46	22.54	7.45	0.80
21091.46	21.05	7.55	0.74
21367.46	18.82	7.65	0.67
21643.46	13.00	7.75	0.46

Figure B.7. $x = 2669$ mm. $u_* = 0.69$ m/s,
 $\delta = 0.0607$ mm and $U_e = 19.5$ m/s.

y^+	U^+	y/δ	U/U_e
42.67	15.33	0.02	0.52
55.47	15.46	0.03	0.52
68.27	15.46	0.04	0.52
81.07	15.72	0.04	0.53
93.87	15.84	0.05	0.53
106.67	16.46	0.05	0.55
119.47	16.82	0.06	0.57
132.27	17.17	0.07	0.58
145.07	17.51	0.07	0.59
157.87	17.51	0.08	0.59
170.67	17.85	0.09	0.60
183.47	18.18	0.09	0.61
196.27	18.62	0.10	0.63
209.07	18.51	0.11	0.62
221.87	19.04	0.11	0.64
234.67	18.83	0.12	0.63
247.47	19.14	0.13	0.64
260.27	19.25	0.13	0.65
273.07	19.66	0.14	0.66
285.87	19.66	0.15	0.66
298.67	19.76	0.15	0.67
311.47	19.76	0.16	0.67
324.27	19.96	0.17	0.67
337.07	20.06	0.17	0.68
349.87	20.16	0.18	0.68
362.67	20.26	0.19	0.68
375.47	20.35	0.19	0.69
388.27	20.55	0.20	0.69
401.07	20.65	0.21	0.70
413.87	20.74	0.21	0.70
426.67	20.93	0.22	0.71
490.67	21.22	0.25	0.71
554.67	21.77	0.28	0.73
618.67	22.05	0.32	0.74
682.67	22.49	0.35	0.76
746.67	22.93	0.38	0.77
810.67	23.28	0.42	0.78
874.67	23.53	0.45	0.79
938.67	23.95	0.48	0.81
1002.67	24.28	0.51	0.82
1066.67	24.69	0.55	0.83

1130.67	24.85	0.58	0.84
1194.67	25.17	0.61	0.85
1258.67	25.25	0.65	0.85
1322.67	25.64	0.68	0.86
1450.67	26.10	0.74	0.88
1514.67	26.48	0.78	0.89
1578.67	26.78	0.81	0.90
1706.67	27.29	0.88	0.92
1770.67	27.51	0.91	0.93
1834.67	27.66	0.94	0.93
1962.67	28.01	1.01	0.94
2026.67	28.30	1.04	0.95
2090.67	28.30	1.07	0.95
2218.67	28.58	1.14	0.96
2282.67	28.72	1.17	0.97
2346.67	28.85	1.20	0.97
2474.67	29.06	1.27	0.98
2538.67	29.20	1.30	0.98
2602.67	29.27	1.33	0.99
2730.67	29.33	1.40	0.99
2794.67	29.40	1.43	0.99
2858.67	29.47	1.47	0.99
2922.67	29.54	1.50	0.99
2986.67	29.60	1.53	1.00
3114.67	29.60	1.60	1.00
3178.67	29.60	1.63	1.00
3242.67	29.60	1.66	1.00
3370.67	29.60	1.73	1.00
3498.67	29.60	1.79	1.00
3626.67	29.60	1.86	1.00
3754.67	29.60	1.93	1.00
3882.67	29.60	1.99	1.00

Figure B.8. $x = 2825$ mm. $u_* = 0.64$ m/s,
 $\delta = 0.0457$ mm and $U_e = 19.0$ m/s.

y^+	U^+	y/δ	U/U_e
19.33	13.36	0.01	0.43
25.13	13.54	0.01	0.43
30.93	13.89	0.01	0.44
36.73	14.24	0.01	0.46
42.53	14.74	0.01	0.47
48.33	15.07	0.01	0.48
54.13	15.54	0.02	0.50
59.93	15.70	0.02	0.50
65.73	15.85	0.02	0.51
71.53	16.15	0.02	0.52
77.33	16.30	0.02	0.52
83.13	16.45	0.02	0.53
88.93	16.74	0.03	0.54
94.73	16.89	0.03	0.54
100.53	17.03	0.03	0.54
106.33	17.03	0.03	0.54
112.13	17.17	0.03	0.55
117.93	17.31	0.03	0.55
123.73	17.45	0.04	0.56
129.53	17.59	0.04	0.56
135.33	17.73	0.04	0.57
213.05	18.92	0.06	0.60
329.05	20.16	0.10	0.64
561.05	21.78	0.16	0.70
793.05	23.29	0.23	0.74
1257.05	24.41	0.37	0.78
1489.05	25.48	0.44	0.81
1721.05	26.32	0.51	0.84
1953.05	27.31	0.57	0.87
2185.05	28.27	0.64	0.90
2417.05	29.12	0.71	0.93
2614.25	29.78	0.77	0.95
2881.05	30.42	0.85	0.97
2939.05	30.66	0.86	0.98
2997.05	30.90	0.88	0.99
3113.05	30.90	0.91	0.99
3229.05	30.97	0.95	0.99
3345.05	31.05	0.98	0.99
3403.05	31.21	1.00	1.00
3461.05	31.21	1.02	1.00
3519.05	31.29	1.03	1.00
3577.05	31.29	1.05	1.00

3635.05	31.29	1.07	1.00
4737.05	31.29	1.39	1.00
5897.05	31.29	1.73	1.00
7057.05	31.21	2.07	1.00
8217.05	31.29	2.41	1.00
9377.05	31.21	2.76	1.00
10537.05	31.21	3.10	1.00
11697.05	31.29	3.44	1.00
12857.05	31.29	3.78	1.00
14017.05	31.29	4.12	1.00
15177.05	31.36	4.46	1.00
15235.05	31.36	4.48	1.00
16337.05	31.36	4.80	1.00
16453.05	31.29	4.83	1.00
16569.05	31.29	4.87	1.00
16685.05	31.21	4.90	1.00
16801.05	31.13	4.94	0.99
16917.05	31.05	4.97	0.99
17033.05	30.97	5.01	0.99
17149.05	30.90	5.04	0.99
17265.05	30.66	5.07	0.98
17381.05	30.34	5.11	0.97
17497.05	29.94	5.14	0.96
17729.05	29.03	5.21	0.93
17961.05	28.27	5.28	0.90
18193.05	27.22	5.35	0.87
18425.05	25.85	5.41	0.83
18657.05	24.51	5.48	0.78
18889.05	23.29	5.55	0.74
19121.05	21.78	5.62	0.70
19237.05	20.64	5.65	0.66
19353.05	19.92	5.69	0.64
19469.05	18.92	5.72	0.60
19585.05	17.59	5.76	0.56
19643.05	17.03	5.77	0.54

Figure B.9. $x = 3317$ mm. $u_* = 0.58$ m/s,
 $\delta = 0.0880$ mm and $U_e = 18.2$ m/s.

y^+	U^+	y/δ	U/U_e
17.67	12.75	0.00	0.39
22.97	12.98	0.01	0.39
28.27	13.20	0.01	0.40
33.57	13.42	0.01	0.41
38.87	14.26	0.01	0.43
44.17	14.66	0.01	0.44
49.47	15.05	0.01	0.46
54.77	15.24	0.02	0.46
60.07	15.43	0.02	0.47
65.37	15.62	0.02	0.47
70.67	15.99	0.02	0.48
75.97	15.99	0.02	0.48
81.27	16.17	0.02	0.49
86.57	16.35	0.02	0.50
91.87	16.52	0.03	0.50
97.17	16.70	0.03	0.51
102.47	16.70	0.03	0.51
107.77	16.87	0.03	0.51
113.07	17.04	0.03	0.52
118.37	17.38	0.03	0.53
123.67	17.55	0.03	0.53
194.69	17.71	0.05	0.54
300.69	19.73	0.08	0.60
512.69	21.42	0.14	0.65
724.69	22.48	0.20	0.68
936.69	23.86	0.26	0.72
1148.69	24.93	0.32	0.76
1360.69	26.07	0.38	0.79
1572.69	26.95	0.44	0.82
1784.69	27.90	0.50	0.84
1996.69	28.92	0.56	0.88
2208.69	29.62	0.62	0.90
2420.69	30.39	0.67	0.92
2632.69	30.96	0.73	0.94
2738.69	31.24	0.76	0.95
2791.69	31.61	0.78	0.96
2844.69	31.61	0.79	0.96
2897.69	31.70	0.81	0.96
2950.69	31.79	0.82	0.96
3003.69	31.88	0.84	0.97
3056.69	32.16	0.85	0.97
3109.69	32.16	0.87	0.97
3162.69	32.34	0.88	0.98

3215.69	32.43	0.90	0.98
3268.69	32.43	0.91	0.98
3321.69	32.52	0.93	0.98
3374.69	32.52	0.94	0.98
3480.69	32.69	0.97	0.99
3586.69	32.87	1.00	1.00
3692.69	32.96	1.03	1.00
3798.69	32.96	1.06	1.00
3904.69	32.96	1.09	1.00
4010.69	32.96	1.12	1.00
4116.69	32.96	1.15	1.00
4222.69	32.96	1.18	1.00
4328.69	32.96	1.21	1.00
5388.69	32.96	1.50	1.00
6448.69	32.96	1.80	1.00
7508.69	32.96	2.09	1.00
8568.69	32.96	2.39	1.00
9628.69	32.96	2.68	1.00
10688.69	32.96	2.98	1.00
11748.69	32.96	3.28	1.00
12808.69	32.96	3.57	1.00
13868.69	33.05	3.87	1.00
14928.69	33.05	4.16	1.00
15458.69	33.05	4.31	1.00
15988.69	32.78	4.46	0.99
16094.69	32.69	4.49	0.99
16200.69	32.52	4.52	0.98
16306.69	32.25	4.55	0.98
16412.69	32.07	4.58	0.97
16518.69	31.88	4.61	0.97
16730.69	31.05	4.66	0.94
16942.69	30.39	4.72	0.92
17154.69	29.42	4.78	0.89
17366.69	28.21	4.84	0.85
17578.69	27.16	4.90	0.82
17790.69	25.96	4.96	0.79
18002.69	24.58	5.02	0.74
18214.69	23.24	5.08	0.70
18426.69	21.42	5.14	0.65
18638.69	19.87	5.20	0.60
18744.69	18.20	5.23	0.55
18797.69	17.21	5.24	0.52

Figure B.10. $x = 3702$ mm. $u_* = 0.53$ m/s,
 $\delta = 0.1015$ mm and $U_e = 17.5$ m/s.

y^+	U^+	y/δ	U/U_e
16.33	12.58	0.00	0.36
21.23	13.11	0.01	0.38
26.13	13.37	0.01	0.39
31.03	14.11	0.01	0.41
35.93	14.58	0.01	0.42
40.83	14.82	0.01	0.43
45.73	15.04	0.01	0.44
50.63	15.27	0.01	0.44
55.53	15.49	0.01	0.45
60.43	15.71	0.02	0.46
65.33	15.92	0.02	0.46
70.23	16.13	0.02	0.47
75.13	16.34	0.02	0.47
80.03	16.34	0.02	0.47
84.93	16.55	0.02	0.48
89.83	16.75	0.02	0.49
94.73	16.96	0.02	0.49
99.63	17.15	0.03	0.50
104.53	17.35	0.03	0.50
109.43	17.35	0.03	0.50
114.33	17.55	0.03	0.51
179.99	18.30	0.05	0.53
277.99	19.73	0.07	0.57
571.99	21.86	0.15	0.63
1061.99	25.32	0.28	0.73
1551.99	27.63	0.41	0.80
2041.99	29.64	0.54	0.86
2531.99	31.85	0.67	0.92
3021.99	33.31	0.79	0.97
3511.99	34.12	0.92	0.99
3609.99	34.22	0.95	0.99
3707.99	34.22	0.97	0.99
3805.99	34.32	1.00	1.00
3903.99	34.32	1.03	1.00
4001.99	34.42	1.05	1.00
4099.99	34.42	1.08	1.00
4197.99	34.42	1.10	1.00
4295.99	34.42	1.13	1.00
4393.99	34.42	1.15	1.00
4491.99	34.42	1.18	1.00
4981.99	34.42	1.31	1.00

5961.99	34.42	1.57	1.00
6941.99	34.42	1.82	1.00
7921.99	34.32	2.08	1.00
8901.99	34.42	2.34	1.00
9881.99	34.42	2.60	1.00
10861.99	34.42	2.85	1.00
11841.99	34.42	3.11	1.00
12821.99	34.42	3.37	1.00
13801.99	34.42	3.63	1.00
14291.99	34.42	3.76	1.00
14781.99	34.42	3.88	1.00
14879.99	34.52	3.91	1.00
14977.99	34.42	3.94	1.00
15075.99	34.32	3.96	1.00
15173.99	34.42	3.99	1.00
15271.99	34.32	4.01	1.00
15369.99	34.22	4.04	0.99
15467.99	34.12	4.06	0.99
15565.99	33.92	4.09	0.98
15663.99	33.72	4.12	0.98
15761.99	33.52	4.14	0.97
16741.99	29.76	4.40	0.86
17721.99	23.94	4.66	0.69
18211.99	19.56	4.79	0.57
18505.99	15.71	4.86	0.46
19681.99	11.75	5.17	0.34

Figure B.11. $x = 3902$ mm. $u_* = 0.49$ m/s, $\delta = 0.1165$ mm and $U_e = 16.9$ m/s.

y^+	U^+	y/δ	U/U_e
14.33	12.18	0.00	0.33
18.63	12.53	0.00	0.34
22.93	12.88	0.01	0.35
27.23	13.22	0.01	0.36
31.53	13.87	0.01	0.38
35.83	14.18	0.01	0.39
40.13	14.49	0.01	0.39
44.43	14.49	0.01	0.39
48.73	14.79	0.01	0.40
53.03	15.09	0.01	0.41
57.33	15.09	0.01	0.41
61.63	15.38	0.02	0.42
65.93	15.38	0.02	0.42
70.23	15.38	0.02	0.42
74.53	15.66	0.02	0.43
78.83	15.66	0.02	0.43
83.13	15.94	0.02	0.43
87.43	15.94	0.02	0.43
91.73	16.22	0.02	0.44
96.03	16.22	0.02	0.44
100.33	16.49	0.03	0.45
157.95	17.52	0.04	0.48
243.95	18.74	0.06	0.51
501.95	20.54	0.13	0.56
931.95	24.10	0.24	0.66
1361.95	26.37	0.35	0.72
1791.95	28.92	0.46	0.79
2221.95	31.13	0.58	0.85
2651.95	33.05	0.69	0.90
3081.95	34.62	0.80	0.94
3511.95	36.12	0.91	0.98
3597.95	36.24	0.93	0.99
3683.95	36.36	0.96	0.99
3769.95	36.48	0.98	0.99
3855.95	36.60	1.00	1.00
3941.95	36.72	1.02	1.00
4027.95	36.72	1.04	1.00
4113.95	36.84	1.07	1.00
4371.95	36.84	1.13	1.00
4801.95	36.84	1.25	1.00
5231.95	36.96	1.36	1.01
5661.95	36.96	1.47	1.01
6091.95	36.84	1.58	1.00

6521.95	36.84	1.69	1.00
6951.95	36.84	1.80	1.00
7381.95	36.84	1.91	1.00
7811.95	36.84	2.03	1.00
8671.95	36.84	2.25	1.00
9531.95	36.96	2.47	1.01
10391.95	36.96	2.70	1.01
11251.95	36.96	2.92	1.01
12111.95	36.96	3.14	1.01
12971.95	37.08	3.36	1.01
13401.95	37.08	3.48	1.01
13831.95	37.08	3.59	1.01
14261.95	37.08	3.70	1.01
14691.95	36.84	3.81	1.00
14777.95	36.72	3.83	1.00
14863.95	36.60	3.85	1.00
14949.95	36.36	3.88	0.99
15035.95	36.24	3.90	0.99
15121.95	35.87	3.92	0.98
15551.95	34.36	4.03	0.94
16411.95	29.83	4.26	0.81
17271.95	23.35	4.48	0.64
18131.95	16.49	4.70	0.45
18561.95	15.09	4.81	0.41
18647.95	13.87	4.84	0.38
18733.95	13.55	4.86	0.37
18819.95	13.22	4.88	0.36
18905.95	12.88	4.90	0.35

Figure B.12. $x = 4346$ mm. $u_* = 0.43$ m/s, $\delta = 0.1345$ mm and $U_e = 15.8$ m/s.

Appendix C. Procedure to Obtain Half-Power Parameters

The procedure to obtain inner and outer parameters C_i , C_o , D_i and D_o is as follows:

1. Plot U^+ against y^+ . Then, pick the U^+ value where a profile starts to separate from the logarithmic law. The corresponding value of U^+ is referred as U_c^+ here ($U_c^+ \sim 20 \pm 5$).
2. In the U/U_e against $(y/\delta)^{1/2}$ plot, U/U_e values belong to the inner and outer regions based roughly on the value of the U_c^+ . U/U_e is in the inner region when U^+ is smaller than U_c^+ , and U/U_e is in the outer region when U^+ is greater than U_c^+ .
3. Draw two least squares best fits for the inner and outer regions of U/U_e against $(y/\delta)^{1/2}$. The two best fits of each profile emphasize the concave up or down shape of this part of the mean velocity profile.
4. When D_i is smaller than D_o (or C_i is greater than C_o), the two best fits form a concave down shape. When D_i is greater than D_o (or C_i smaller than C_o), the best fits form a concave up shape.
5. An angle θ can be defined as measured from the U^+ against y^+ plot. θ is measured from the origin where U_c^+ is crossing the first profile of the flows. When $\theta \leq 30^\circ \pm 5^\circ$, $D_i < D_o$ (or $C_i > C_o$) in the U/U_e against $(y/\delta)^{1/2}$ plots. θ is illustrated in Figure C.1.

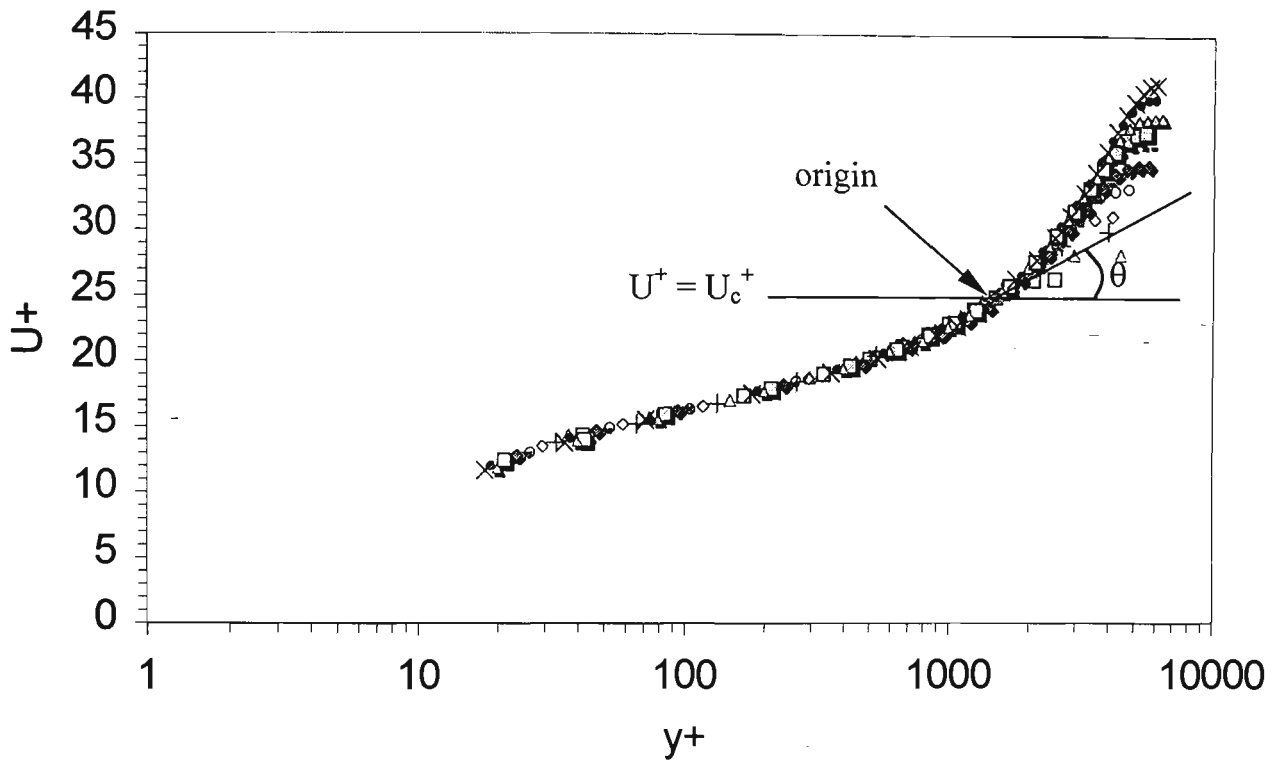


Figure C.1. U_c^+ and θ definitions to determine inner and outer half-power parameters.

Appendix D. Length scales.

In the following, viscous length scale, pressure gradient length scale and boundary layer thickness are denoted as δ_v , δ_p and δ , respectively. The beginning and end of the logarithmic regions are denoted as $y_{\log,b}$ and $y_{\log,e}$, respectively. The beginning and end of the inner half power regions are denoted as $y_{i,b}$ and $y_{i,e}$, respectively. The beginning and end of the outer half power regions are denoted as $y_{o,b}$ and $y_{o,e}$, respectively. The streamwise location of each of these 9 length scales are plotted in Figures D.1 to D.11 for the 11 adverse pressure gradient flows examined in Chapter 5.

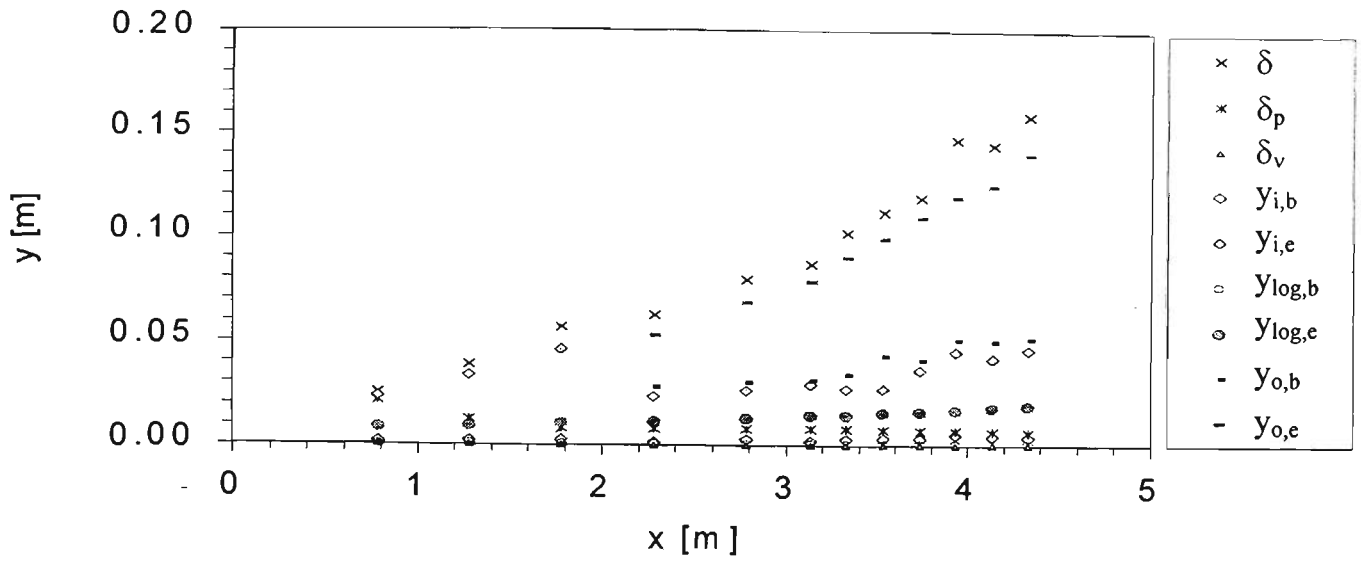


Figure D.1 Flow 1100.

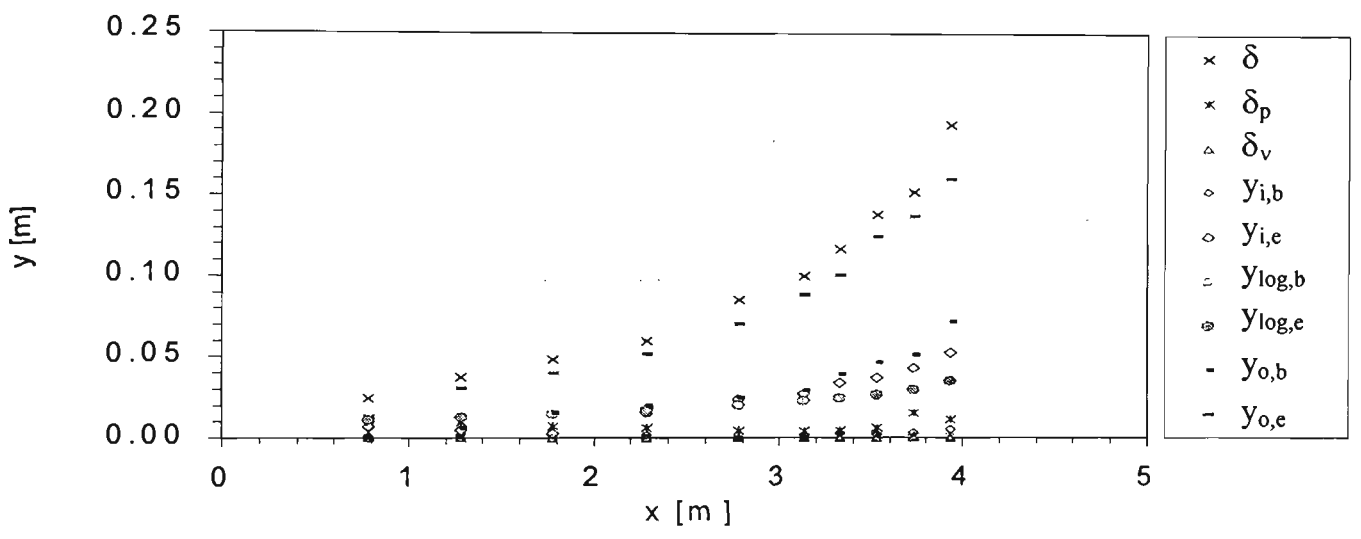


Figure D.2 Flow 1200.

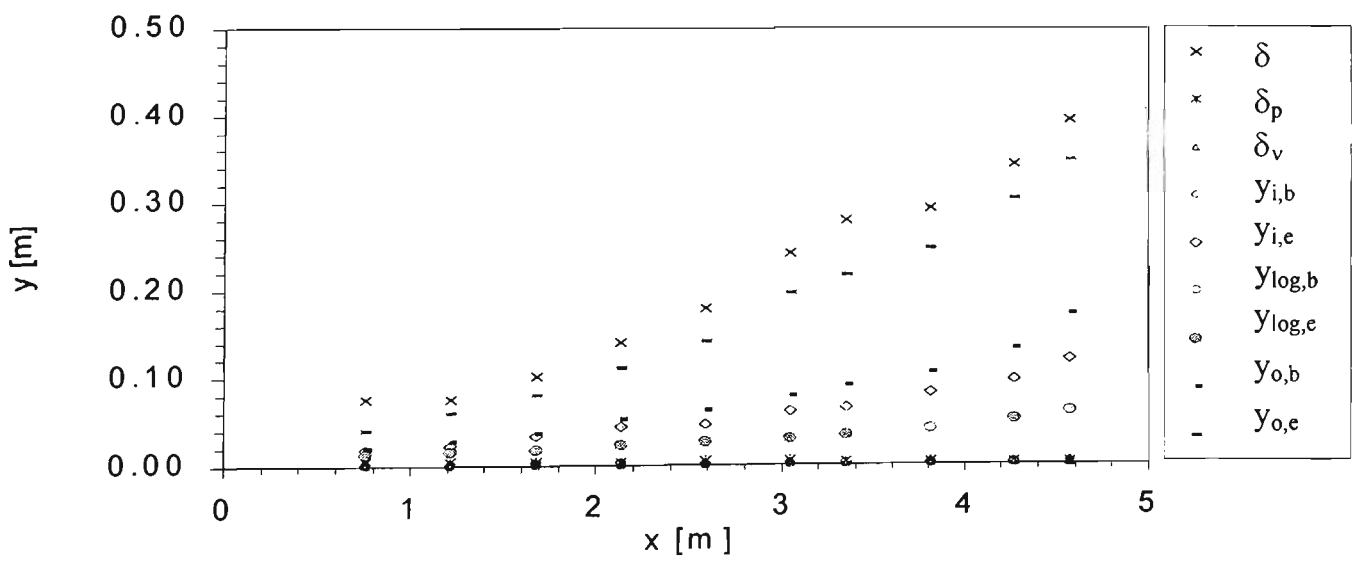


Figure D.3 Flow 2900.

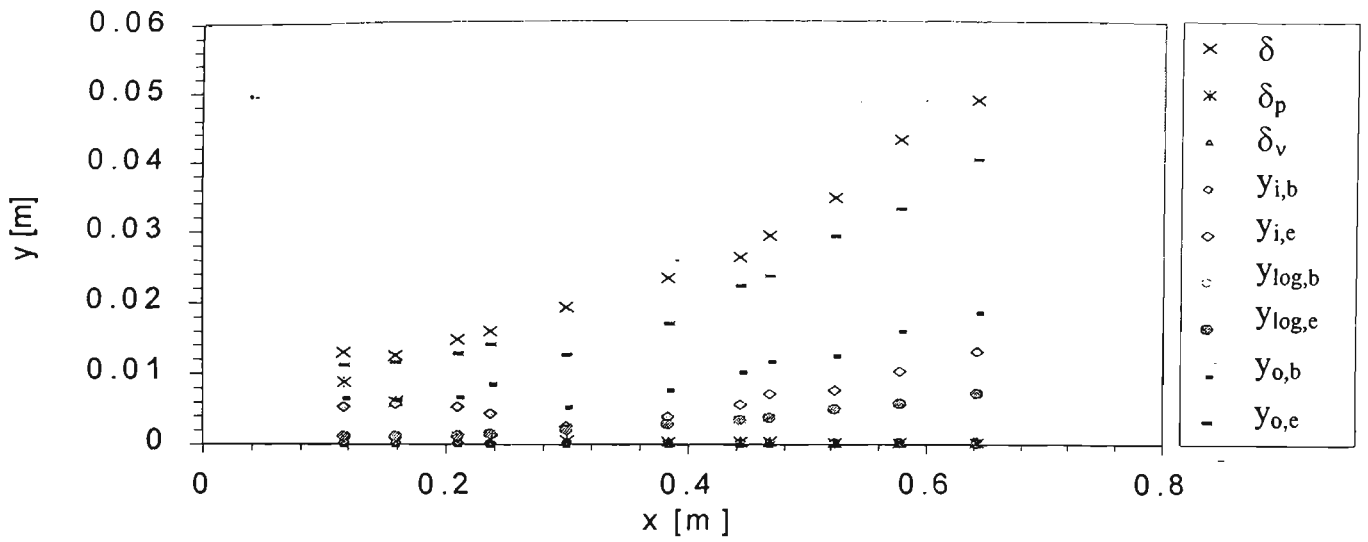


Figure D.4 Flow 5000.

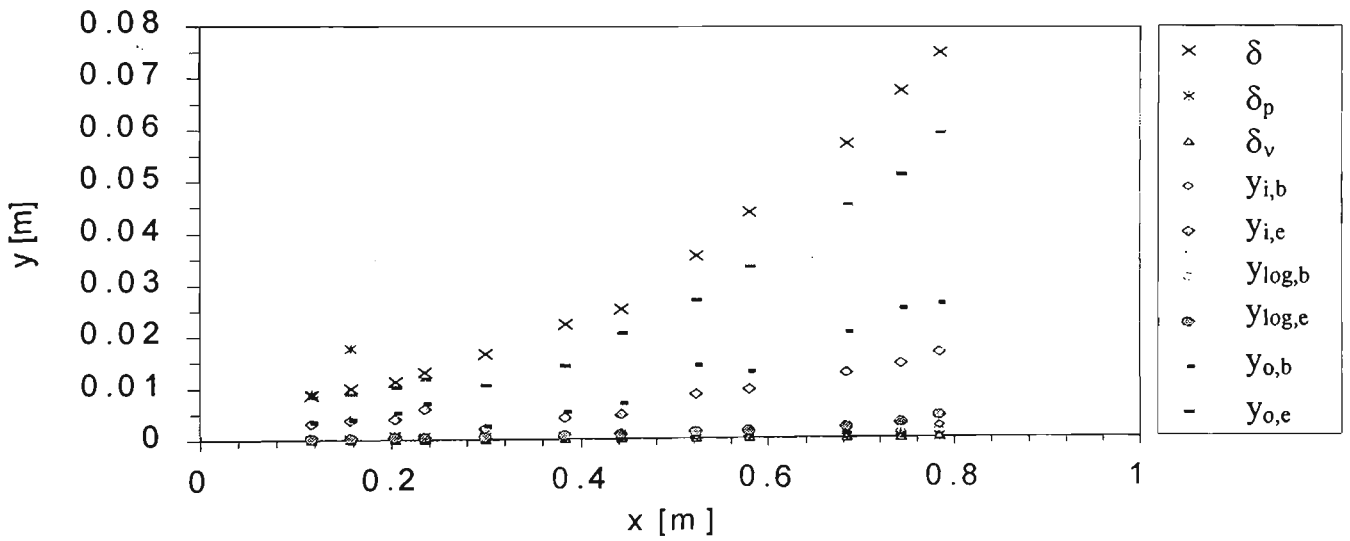


Figure D.5 Flow 5100.

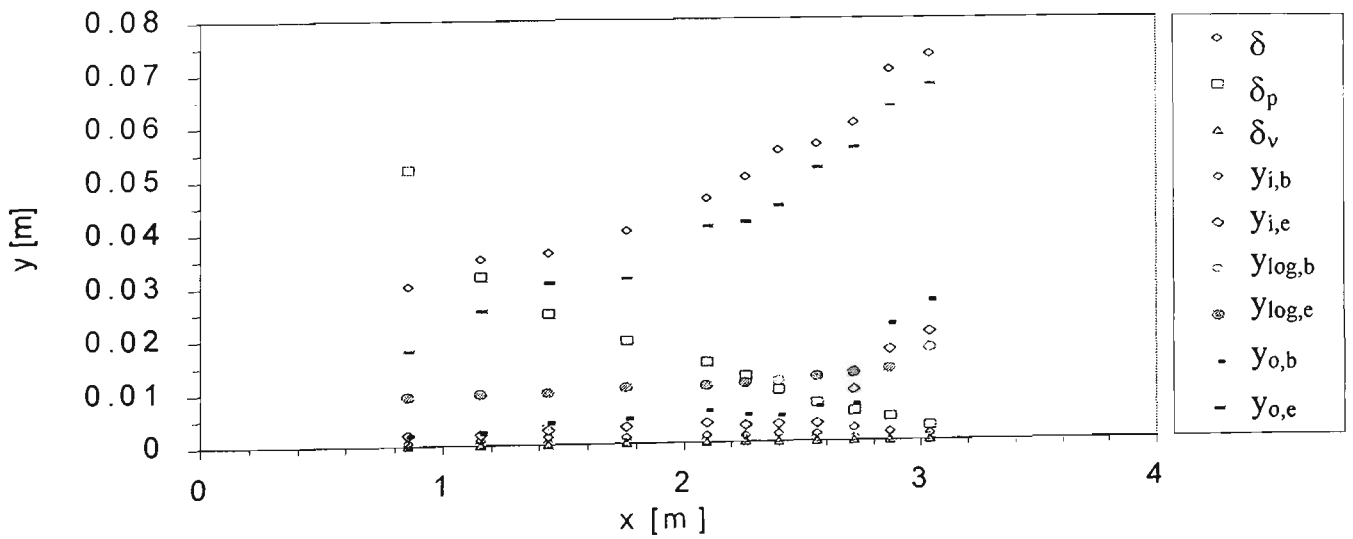


Figure D.6 Flow 141.

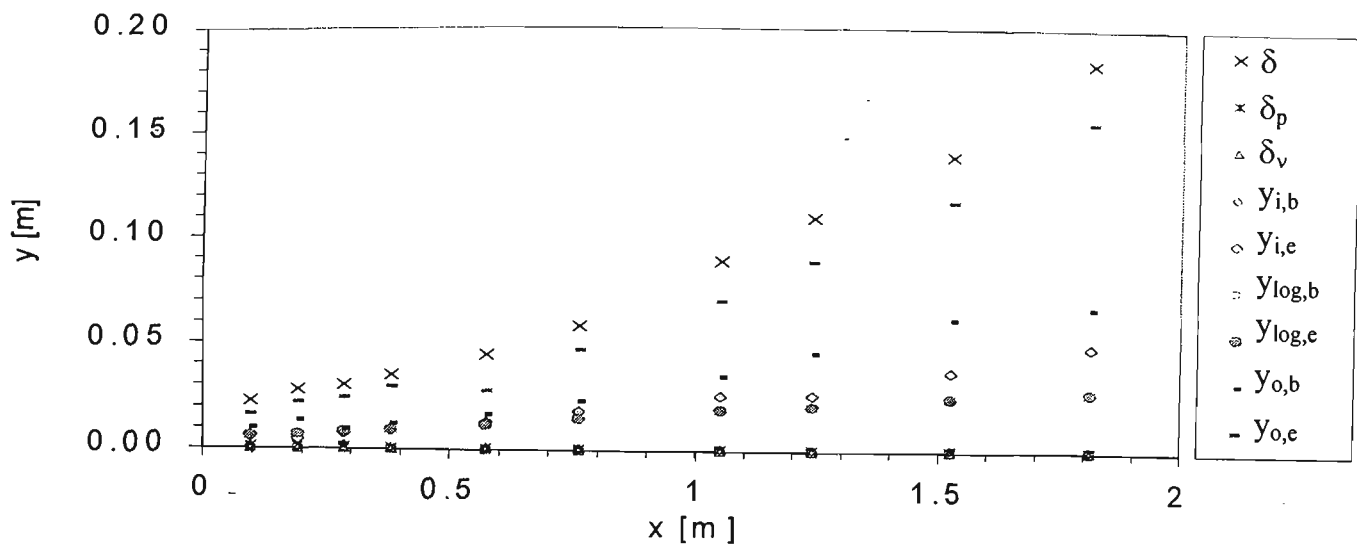


Figure D.7 Flow 142.

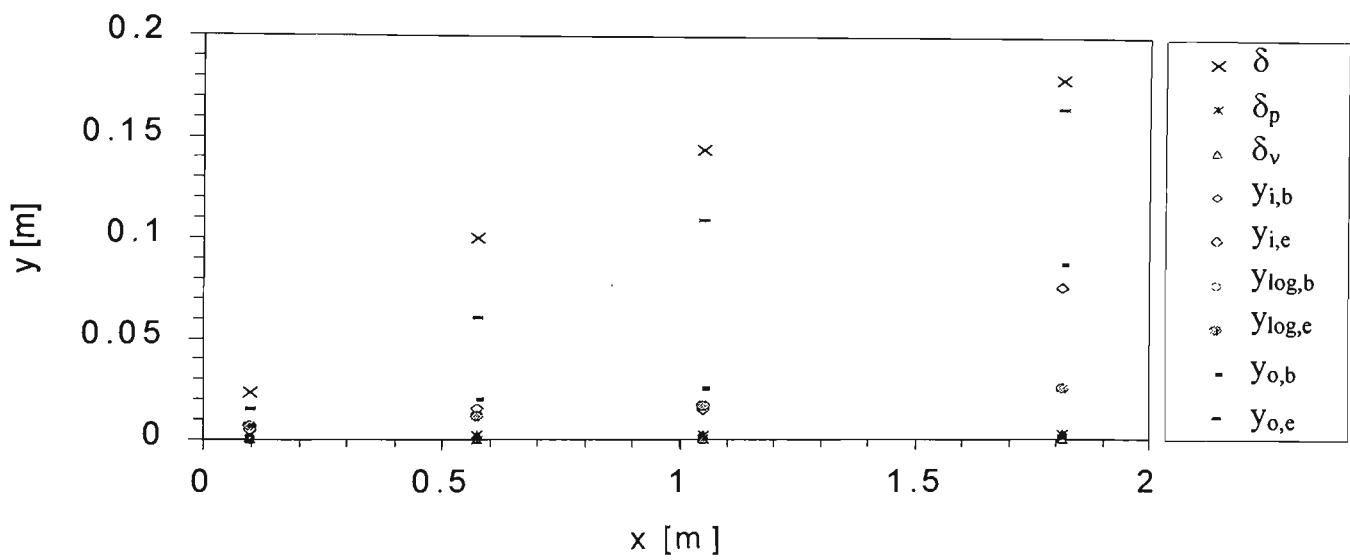


Figure D.8 Flow 143.

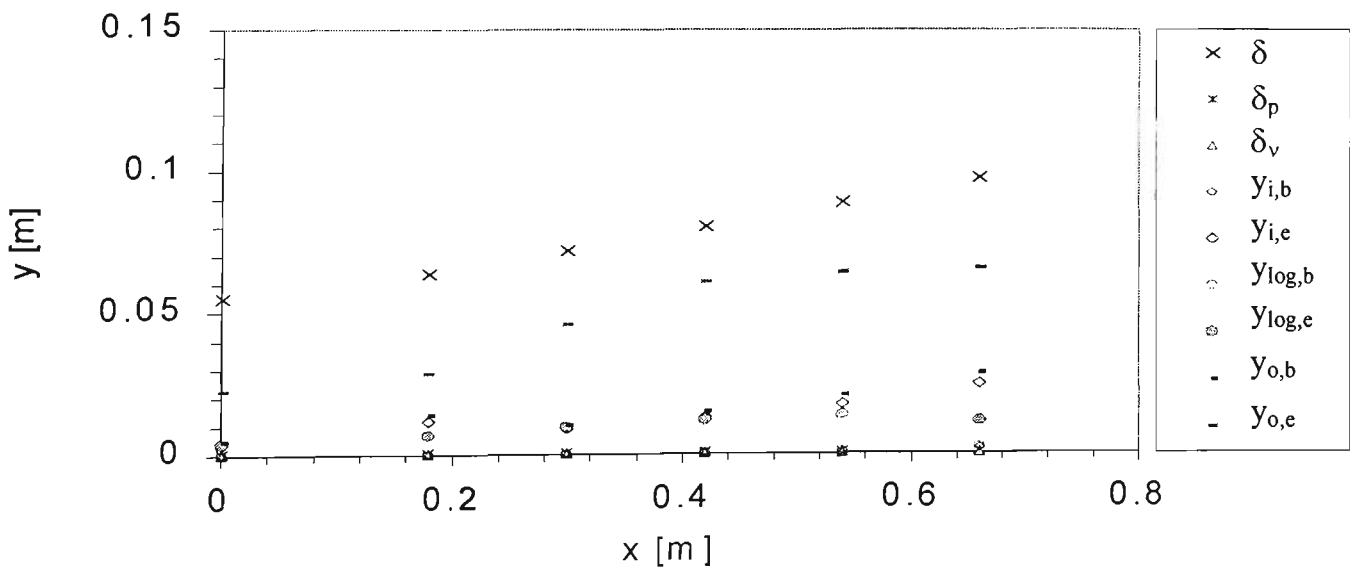


Figure D.9 Flow 8-degree.

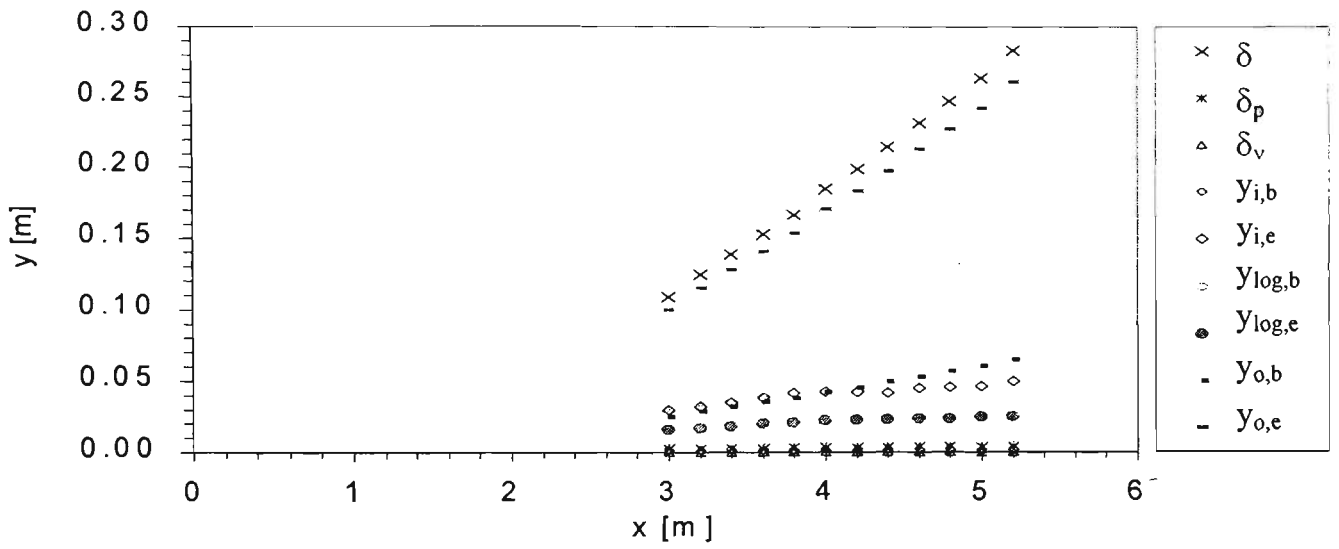


Figure D.10 Flow Skåre.

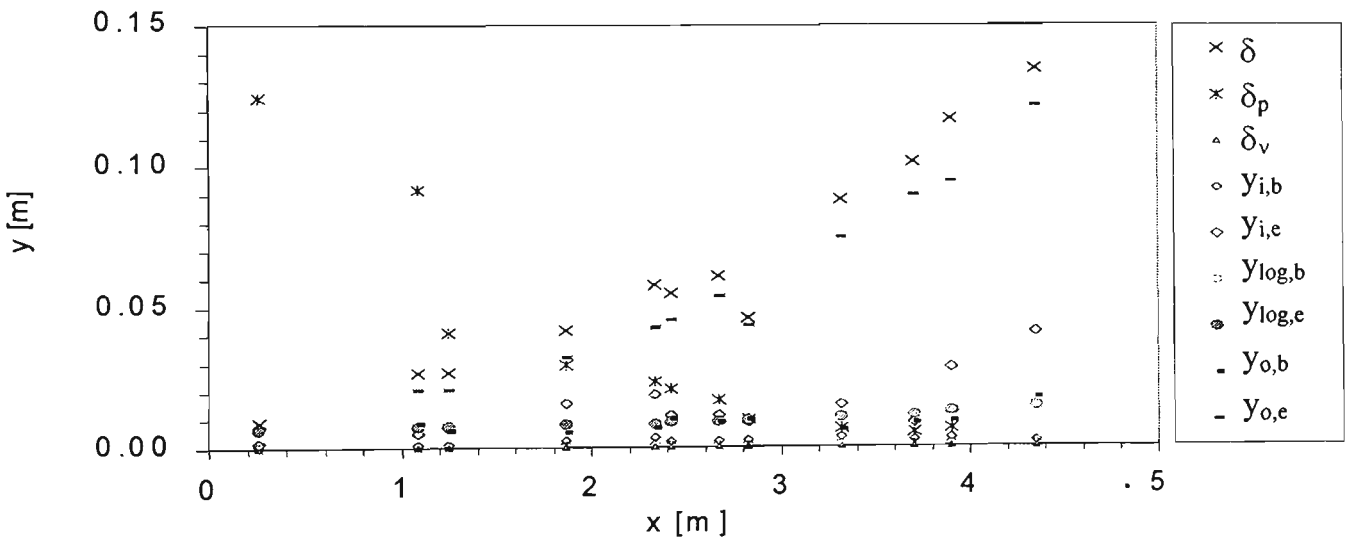


Figure D.11 Flow Han.